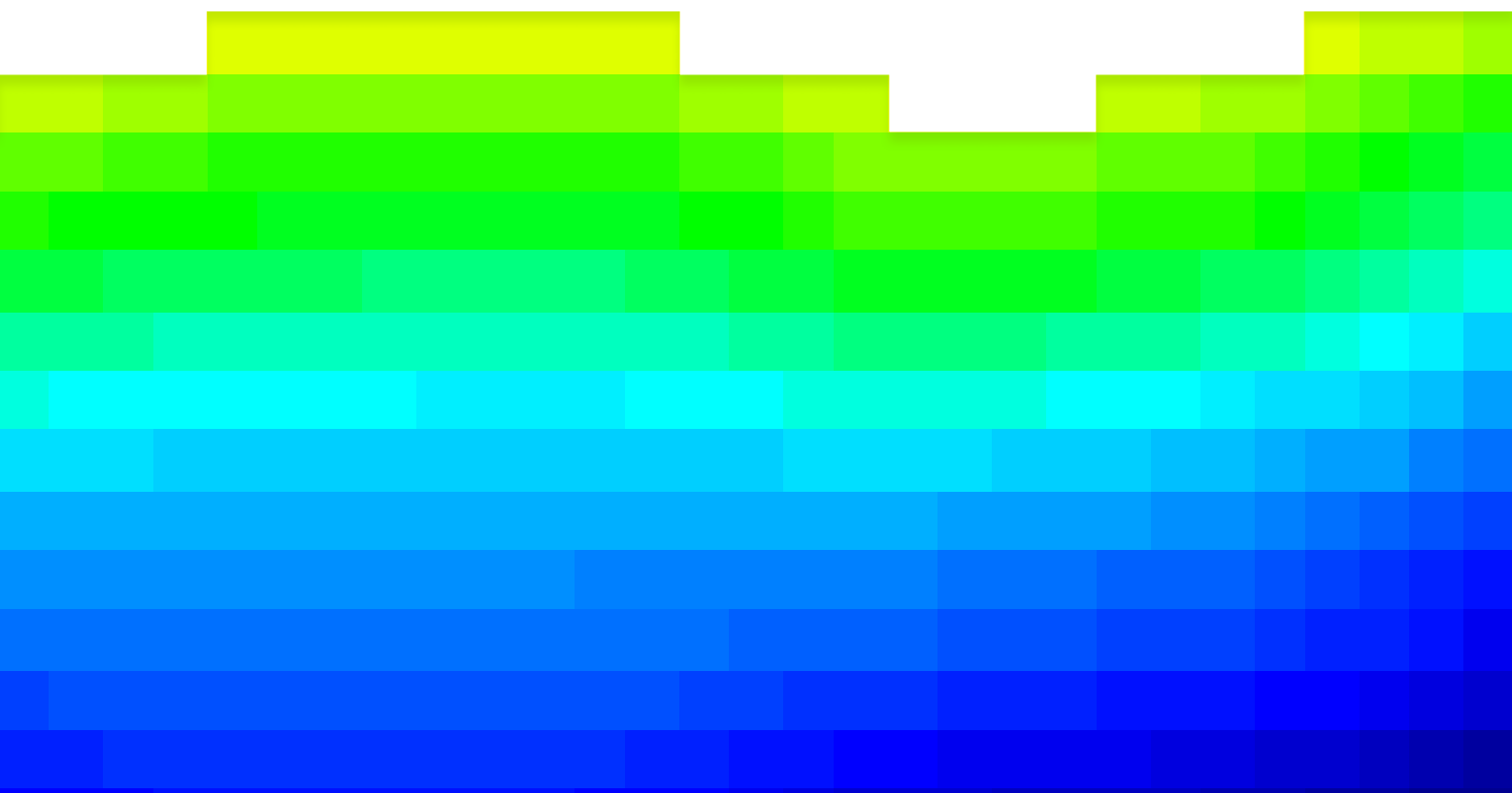


Master of Science thesis in Biomedical Engineering at the Delft University of Technology

# Material property characterisation of tissue engineered fibrous cap structures

An inverse Finite Element study

Daniel Janos Kurucz



# Material property characterisation of tissue engineered fibrous cap structures

An inverse Finite Element study

by

**Daniel Janos Kurucz**

In partial fulfillment of the requirements for the degree in

**Master of Science**  
in Biomedical Engineering

at Delft University of Technology,  
to be defended on Thursday, May 19, 2022 at 14:00 PM

Student number: 4917294

Supervisor:	Dr. ir. Frank Gijzen ir. Su Guvenir Torun Dr. Ali C. Akyildiz	Delft University of Technology Erasmus Medical Centre Erasmus Medical Centre
Thesis committee:	Dr. ir. Frank Gijzen Dr. Ali C. Akyildiz Lise Noel	Delft University of Technology Erasmus Medical Centre Delft University of Technology

An electronic version of this thesis is available at <http://repository.tudelft.nl>

# Declaration

I hereby declare that this thesis represents my own intellectual work, which has been done after the registration at Delft University of Technology for the degree of MSc (Master of Science) in Biomedical Engineering and has not been previously included in other thesis or dissertation submitted to this or other institution for a degree, diploma or other qualifications.

Signature:  \_\_\_\_\_

Date: May, 2022

## Acknowledgements

During this graduation project I had the opportunity to be part of the Biomedical Engineering research lab at Erasmus MC, an internationally recognised group in the field of arterial biomechanics. I am thankful that I was welcomed to the lab and especially grateful for the guidance of my supervisors; Dr. ir Frank Gijsen, Dr. Ali Akyildiz and Su Guvenir-Torun.

Dear Frank, thank you for overseeing and steering my project, starting from the first day of my internship until the day of my graduation. Your positive attitude towards my work, patience and support when I needed it kept me working towards the end of this project. Ali and Su, your all-time availability and quick solutions to any mechanical problem was inspirational and saved me many times when I found myself stuck with my project.

I would also like to thank my parents, my sister and my close friends for supporting me throughout my thesis and for always having my best interest at heart. Thank you for believing in me.

# Abstract

**Introduction:** Atherosclerosis is characterised by the buildup of plaque within the arterial wall and it is often the underlying cause effect of deaths related to cardiovascular diseases. Thin cap fibroatheromas are plaques with a high risk of causing clinical events due to rupture and espousal of thrombogenic components to the bloodstream. The rupture of the plaque is not yet fully understood and for this reason, tissue engineered plaques were created in a previous study to assess the rupture of the plaques based on the displacement field registered with Digital Image Correlation during a uniaxial tensile experiment. The knowledge of the material properties of the tissue-engineered fibrous cap structures makes it possible to link deformations to external loads and contributes to the understanding of plaque rupture. The study aims to create a pipeline for local mechanical property characterisation of tissue engineered fibrous plaque structures.

**Methods:** In this novel method inverse Finite Element Method (iFEM) was combined with the Differential Evolution machine learning algorithm to assess global and local mechanical properties of tissue engineered fibrous plaque structures. The method required three main steps. Step one was the implementation of the uniaxial tensile test into a computational model using ABAQUS version 2016 Finite Element Method (FEM) software. To couple loads and deformations the hyperelastic reduced polynomial function of second order was implemented in the FEM. The characterisation of the  $c_{10}[kPa]$  and  $c_{20}[kPa]$  parameters in the model is the main focus of this study. After the creation of the FEM, the computed displacement field and the previously registered DIC displacement field were implemented into the iFEM pipeline. Preliminary to the experimental data study, the pipeline was tested on a synthetically generated displacement field, in order to investigate the expected accuracy of the method. In step two the global mechanical properties of the fibrous plaque structures were investigated, using the assumption of homogeneous material property distribution in the samples. The resulting material properties after the global estimation served as an initial guess for the local estimation procedure. In step three the local material properties were investigated by creating sections with independently variable material properties, thus introducing heterogeneous distribution of material properties within the samples.

**Results:** The global mechanical property assessment was carried out successfully and the resulting material properties are within the range of previously reported stiffness values of plaques with a similar composition. Local mechanical properties were characterised using up to twelve independently variable material parameters to investigate the heterogeneous mechanical behaviour of the constructs.

**Conclusion:** During this project a new method was established to assess the local mechanical properties of tissue engineered fibrous cap structures. The pipeline shows high potential to be useful when investigating plaque rupture in a controlled environment using tissue engineered constructs. The knowledge of local material properties in combination with local deformations is a great addition to the understanding of plaque rupture.

# Contents

<b>Declaration</b>	<b>i</b>
<b>Acknowledgements</b>	<b>ii</b>
<b>Abstract</b>	<b>iii</b>
<b>1 Introduction</b>	<b>1</b>
1.1 Motivation of the study . . . . .	3
1.2 Goals of the study . . . . .	5
<b>2 Methods</b>	<b>6</b>
2.1 Finite Element Method . . . . .	6
2.1.1 Geometry . . . . .	6
2.1.2 Loads & Boundary conditions . . . . .	7
2.1.3 Material Model . . . . .	11
2.1.4 Discretization and mesh refinement . . . . .	13
2.2 Material property estimation . . . . .	16
2.2.1 Grid and objective function . . . . .	16
2.2.2 Differential evolution algorithm . . . . .	18
2.2.3 Global and local material property estimation . . . . .	19
2.3 Methods for synthetic data study . . . . .	20
2.3.1 Effect of grid size . . . . .	20
2.3.2 Noise . . . . .	20
2.3.3 Number of sections . . . . .	21
2.3.4 Differential evolution parameters . . . . .	21
<b>3 Results</b>	<b>24</b>
3.1 Results of synthetic data study . . . . .	24
3.1.1 Grid size . . . . .	24
3.1.2 Effect of noise . . . . .	28
3.1.3 Number of sections . . . . .	31
3.1.4 Differential evolution control parameters . . . . .	33
3.2 Results of experimental data study . . . . .	35
3.2.1 Global material properties . . . . .	35
3.2.2 Local material property estimation . . . . .	42
<b>4 Discussion</b>	<b>48</b>
4.1 Synthetic data study . . . . .	48
4.1.1 Grid study . . . . .	48
4.1.2 Noise study . . . . .	49
4.1.3 Section study . . . . .	49
4.1.4 DE control parameters . . . . .	50
4.2 Experimental data study . . . . .	51
4.2.1 Discussion global material properties . . . . .	51
4.2.2 Discussion local material properties . . . . .	53
4.3 Limitations . . . . .	54
4.4 Future recommendations . . . . .	55

<b>5</b>	<b>Conclusion</b>	<b>56</b>
	<b>Information on creating the TCFA</b>	<b>61</b>
A	Cell culturing . . . . .	61
B	Uniaxial tensile test . . . . .	62
C	Results of the study . . . . .	63
	<b>Supplementary information to the methods</b>	<b>65</b>
D	FEM of the fibrous cap + SI . . . . .	65
E	Different grid sizes applied to the computed displacement fields . . .	67
	E.1    Fibrous cap model . . . . .	67
	E.2    Fibrous cap + SI model . . . . .	71
F	Noise estimation . . . . .	72
	<b>Supplementary information on Differential evolution algorithm</b>	<b>74</b>
G	Working example of differential evolution . . . . .	74
H	Differential Evolution Algorithm . . . . .	75
	<b>Supplementary results to the synthetic data study</b>	<b>90</b>
I	Grid study . . . . .	90
	I.1    Estimation procedure . . . . .	90
	I.2    Resulting displacement fields . . . . .	93
J	Noise study . . . . .	97
	J.1    Estimation procedure . . . . .	97
	J.2    Resulting displacement fields . . . . .	102
K	Section Study . . . . .	125
	K.1    Estimation procedure . . . . .	125
	K.2    Resulting displacement fields . . . . .	134
L	DE control parameters . . . . .	146
	L.1    Estimation procedure . . . . .	146
	L.2    Resulting displacement fields . . . . .	152
	<b>Supplementary results to the experimental study</b>	<b>164</b>
M	Global estimation procedure . . . . .	164
	M.1    Fibrous cap . . . . .	164
	M.2    Fibrous cap + SI . . . . .	165
N	Local estimation . . . . .	167
	N.1    Fibrous cap . . . . .	167
	N.2    Fibrous cap + SI . . . . .	176
	N.3    Resulting displacement fields . . . . .	184

# List of Figures

1	The development of a thin cap fibroatheroma. Panel <b>a</b> shows the accumulation of LDL in the subendothelial space and the inflammatory response involving macrophages. Panel <b>b</b> shows the proliferation of SMC from the media to the subendothelial space and the accumulation of macrophages. Panel <b>c</b> shows the cell overturn of macrophages into fatty streaks and the formation of a fibrous cap. Panel <b>d</b> shows the effect of plaque failure. Exposed lipid cells cause blood coagulation and lead to the development of thrombus. . . . .	2
2	Tissue engineered fibrous cap (a) and fibrous cap + SI sample (b). . .	3
3	Samples clamped in for uniaxial tensile test, with speckle pattern applied to them for DIC. . . . .	3
4	Flowchart of iFEM, visualising the main steps of the procedure. Measured and computed output fields are compared to each other in the objective function. The optimization algorithm changes the material properties in the numerical model until the minimum difference is reached. . . . .	4
5	The geometries, positions of ROI, and the implemented geometries in ABAQUS. Panel A and B show the fibrous cap and fibrous cap + SI samples respectively. . . . .	7
6	Axial Stress [kPa] and stretch [-] during the uniaxial tension test for the fibrous cap sample. The curve beings after the pre-conditioning cycle, and starts from the pre-stretched, stress-free configuration. The curve shows nonlinear mechanical behaviour, and strain stiffening behaviour as expected from tissue materials. . . . .	8
7	Axial Stress [kPa] and stretch [-] during the uniaxial tension test for the fibrous cap+SI sample. The curve beings after the pre-conditioning cycle, and starts from the pre-stretched, stress-free configuration. The curve shows nonlinear mechanical behaviour, and strain stiffening behaviour as expected from tissue materials. . . . .	9
8	Panel A shows the axial stress along the clamp regions and panel B shows the restrictions for rigid body movements in the buffer regions and the restrictions for horizontal movement for the clamps. . . . .	10
9	Results of the curve fitting procedure for fibrous cap sample. Blue dashed data represents the stress-stretch curve from the experiment, the red line represents the fitted curve. The material parameters were taken from equation nr. 8, when $n = 2$ , the resulting $c_{10}$ and $c_{20}$ parameters were estimated as 97.86 kPa and 1069 kPa respectively, with 95% confidence bounds. . . . .	12
10	Results of the curve fitting procedure for fibrous cap + SI sample. Blue dashed data represents the stress-stretch curve from the experiment, the red line represents the fitted curve. The material parameters were taken from equation nr. 8, when $n = 2$ , the resulting $c_{10}$ and $c_{20}$ parameters were estimated as 93.66 kPa and 1037 kPa respectively, with 95% confidence bounds. . . . .	13

11	Result of mesh independency analysis. The X-axis shows the X-coordinates of the nodes along the upper edge of the ROI (in mm), and the Y-axis shows the corresponding displacement (in mm) at the corresponding node. . . . .	15
12	CPU time in sec for the models with different element sizes. X axis shows the element size in mm and Y axis shows the computational time in seconds, until compilation of the FEM. . . . .	15
13	Discretized model for the fibrous cap model. ROI includes elements with 0.2mm size, the surrounding tissue contains elements with 0.4 mm. . . . .	16
14	The grid applied to the ROI of the fibrous cap model. The dots represent the nodes from the Finite Element Model . . . . .	17
15	The main steps in DE. The procedure starts with the population initiation, followed by mutation and crossover, and finally the selection of the optimal parameters for the function. These parameters are propagated to the next generation where the procedure begins again.	18
16	The sections for the local material property estimations. Four different subdivisions were tested for both models. The ROIs were subdivided into two four and six sections. Panel A and B show the sections for fibrous cap and fibrous cap + SI models respectively. . . . .	19
17	Evolution of material properties throughout the optimization procedure. Upper and lower panels show the evolution of $c_{10}[kPa]$ and $c_{20}[kPa]$ respectively. X axes show the iteration number and Y axes show the material parameters implemented in the FEA. . . . .	25
18	Evolution of objective function for grid 1 throughout the optimization procedure. X axis shows the iteration number and Y axis shows the resulting objective function (NRMSEERR [-]) to the corresponding set of material properties. . . . .	26
19	This figure shows the difference between the GTD (left) and CD (right) using different grid sizes. The results belong to the loading step 1. . . . .	27
20	The average grid displacement along the upper edge of the ROI for different grid sizes. The curves show the distribution of displacements for the GTD data using different grid sizes and the resulting distribution from the computed displacement fields using the resulting material properties. . . . .	28
21	Distribution of displacement values along the upper edge of the ROI from the GTD (blue), and the altered GTD using 1 percent (red), and 2 percent (yellow) noise X axis shows the distance [mm] from the upper right corner of the ROI and y axis shows the average grid displacement values [mm]. . . . .	30
22	The difference between the grid displacement values for GTD and computed fields after estimation. Red and yellow curve belong to computed displacement using 1 and 2 percent noise respectively. The x axis shows the distance from the right upper corner of the ROI and the y axis shows the average grid displacement values [mm]. . . . .	31

23	Objective function values throughout the optimization procedures for different sections. X axes show the iteration numbers and y axes show the objective function value corresponding to the iteration number. . . . .	33
24	Boxplots for both material parameters throughout the procedure for fibrous cap (top) and fibrous cap + SI (bottom). . . . .	36
25	Visualisation of the experimental and computed displacement field in the ROI. The top row shows the distribution of the experimental data in each grid. The bottom row shows the computed displacements in each grid, using the resulting material properties at the end of the optimization. Different columns show the displacement fields at different loading levels. Due to the larger difference in the resulting displacement fields at step one, the colour bars show different scaling and range of values. . . . .	38
26	The distribution of absolute difference in mm along the selected line from the ROI for the fibrous cap model. Blue represents step 1 red and yellow represent step 2 and step 3 respectively. The X-axis shows the distance in mm along the second row in the ROI. The Y-axis shows the difference between the grid values from the experimental and computed fields. . . . .	40
27	The distribution of absolute difference in mm along the selected line for the fibrous cap + SI model. Blue represents step 1 red and yellow represent step 2 and step 3 respectively. The X-axis shows the distance in mm along the second row in the ROI The Y-axis shows the difference between the grid values from the experimental and computed fields. . . . .	41
28	Visual representation of the resulting $c_{10}$ values for each sections. The upper row shows the fibrous cap structure, the lower includes the sample with SI. Stiffness values are represented in kPa. . . . .	43
29	Visual comparisons of the resulting displacement fields with different sections. The top figure shows the experimental displacement field. Below that the figure shows the results for global, two, four, and six sections models. The range of displacement values agree the most at loading level three, therefore the visual comparison was based on this level. The colour bar on the right shows the range of values in mm. . . . .	44
30	The distribution of displacement values along the selected line from the experimental (blue), the globally estimated displacements (red), the locally estimated models (yellow, purple green), for two, four, and six sections. The top panel shows the distributions belonging to fibrous cap model, the bottom panel shows the distribution belonging to fibrous cap + SI model. The X-axis shows the position along the selected row along the ROI and Y axis show the average grid displacement [mm]. . . . .	47
31	The difference between the distributions when using different $c_{20}$ values.	52
32	The difference between the distributions when using different $c_{10}$ values.	53

## List of Tables

1	Material properties for fibrous cap and fibrous cap + SI models . . .	13
2	Number of columns and rows required to cover the ROI and the average number of data points in the grid elements in the GT displacement field. . . . .	20
3	The material parameters implemented in different sections, in order to represent heterogeneity in the model . . . . .	21
4	Investigated Differential evolution control parameters. . . . .	23
5	The results if the grid study. . . . .	24
6	Summary of the results of the noise study. The section includes the ROI, zero percent noise was included as reference, duration, generations, resulting objective function and material properties as well as the error between GTD and estimated material properties. . . . .	29
7	Results of section study. The results of the ROI with grid 3 and two percent noise are included as a reference. The table compares the estimation procedures with an increased number of sections. The comparison includes the duration of the procedure, the number of generations, the resulting objective function and the resulting material properties. . . . .	32
8	Results of DE control parameter study . . . . .	34
9	Summary of the results for global material property estimation. . . .	35
10	Summary of the results of local parameter estimation for both samples. The material properties marked with * belong to manually terminated procedure. . . . .	42
11	The deviations in percentage between GTD and estimated material properties for different sections. . . . .	50

# Nomenclature

## List of Abbreviations

CD	Computed Data
CVD	Cardiovascular Diseases
DE	Differential Evolution
DIC	Digital Image Correlation
FEM	Finite Element Method
GTD	Ground Truth Data
iFEM	inverse Finite Element Method
LDL	Low-density lipid
LRNC	Lipid rich necrotic core
NRMSERR	Normalised Root Means Square Error
ROI	Region Of Interest
SI	Soft Inclusion
SMC	Smooth muscle cell
TCFA	Thin Cap Fibrous Atheroma

## List of Symbols

$(\bar{u}^{meas})$	Mean of the measured grid displacement values [mm]
$\bar{I}_1$	First invariant of the deviatoric strain tensor [-]
$\Delta L$	Actuator displacement [mm]
$\lambda_i$	principal stretches [-]
$\lambda_U$	axial stretch [-]
$\mu_0$	Initial shear modulus [kPa]
$\sigma$	Axial stress [kPa]
$c_{10}$	First material parameter from second order reduced polynomial function [kPa]
$c_{20}$	Second material parameter from second order reduced polynomial function [kpa]
$F_a$	Actuator force [mN]
$J^{el}$	elastic volume ratio

---

$K_0$	initial bulk modulus [1/kPa]
$L_0$	Initial gauge length of the TCFA [mm]
$u_{ij}$	Offspring vector
$u_i^{comp}$	Computed average displacement per grid element [mm]
$u_i^{meas}$	Measured average displacement per grid element [mm]
$v_{i,j}$	Trial vector
A	Cross sectional area [mm]
CR	Crossover probability
F	Mutation factor
pop	population size in DE algorithm
U	Strain-energy function

## 1 Introduction

Cardiovascular diseases (CVD) are the major cause of death in the western world, accounting for 17.3 million deaths worldwide, according to the 2013 Global Burden of Disease study [1]. Atherosclerosis is the common underlying pathological condition that leads to the two major cause effects of CVD-related deaths: Ischemic heart disease and stroke [2].

Atherosclerosis causes the thickening of large arteries due to the formation of a plaque in the inner arterial layer, the intima. Pathological observations show that atherosclerotic plaques occur within curvatures and bifurcations of arteries, they develop in the aorta in the first decade, in the coronary in the second decade, and at the cerebral in the third to fourth decades [3, 4]. The driving mechanism behind the formation of a plaque is the accumulation of low-density lipids (LDL) within the arterial walls, which leads to an immune response involving macrophages. Further steps involve the migration of smooth muscle cells (SMC) from the media layer and the turnover of LDL to a fatty streak. During the development of the disease the wall components undergo structural changes until the plaque develops into a complex structure, containing thrombogenic components [4–6].

Atherosclerosis or even the presence of plaque does not necessarily result in complications. The thickened portion of the intima results in restricted blood flow in the affected arteries, but stenosis alone is rarely responsible for clinical events. The formation of a thrombus attached to the surface of the lumen is more often the underlying reason for ischemic heart disease and stroke. The thrombosis is the result of the exposed plaque components to the bloodstream, therefore it is important to look into the characteristics of plaques that are prone to cause complications [7].

The term vulnerable plaque has been used to refer to plaques that are prone to rupture, thus exposing thrombogenic components to the bloodstream [8]. However, retrospective pathological studies have suggested that plaque rupture is not the only histological mechanism resulting in thrombosis. Plaque erosion and calcification can also lead to plaque-related thrombosis. Therefore the term vulnerable plaque describes plaques "which are prone to thrombose" [9]. From these three mechanisms, both the rupture and erosion of the plaque cause the majority of clinical events [10]. Vulnerable plaques have unique characteristics: the combination of a fibrous cap with an underlying lipid-rich necrotic core (LRNC) embedded in collagenous matrix (Type I and III) are the hallmark of vulnerable plaques [8]. Figure 1 show the development of an initial lesion (Figure 1/a), followed by the cellular turnover resulting in foam cells, a fatty streak and a fibrous cap (Figure 1/ b-c), and finally the rupture of plaque (Figure 1/d). The specific class of vulnerable plaques which have an elevated risk to rupture are known as thin cap fibrous atheromas (TCFA) [11].

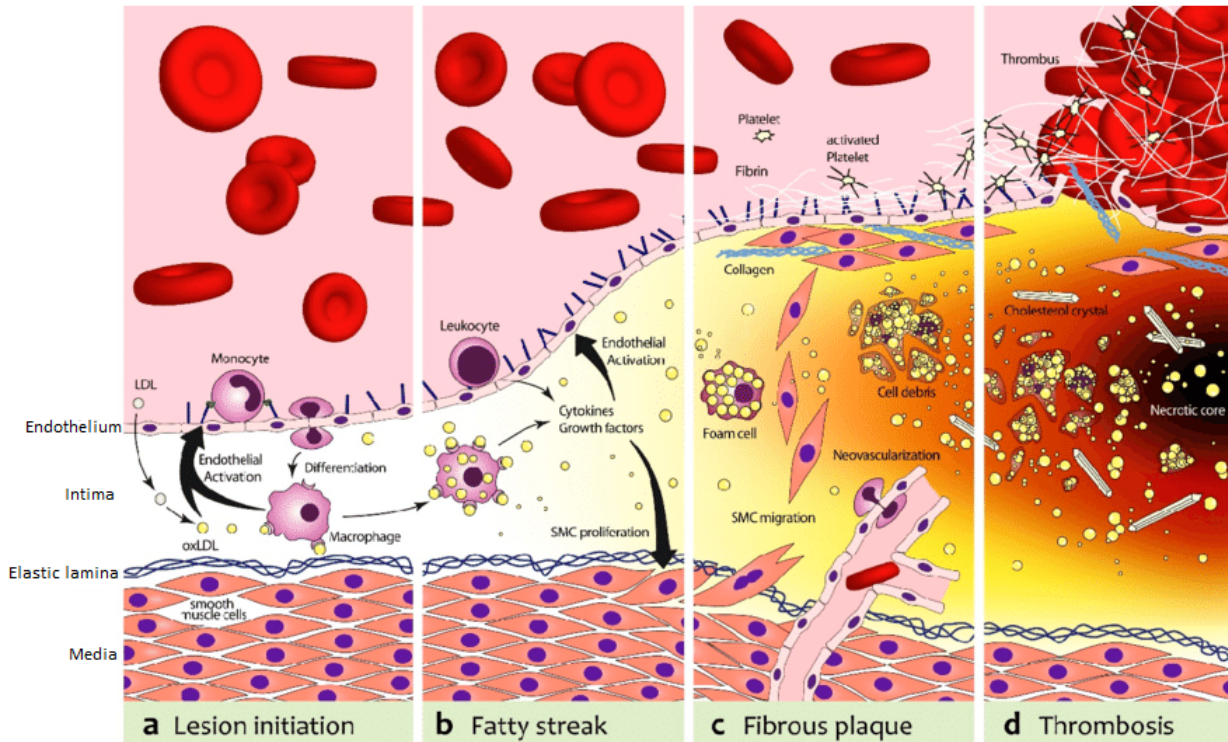


Figure 1: Steps in developing atherosclerotic plaque. Panel **a** shows the accumulation of LDL in the subendothelial space and the inflammatory response involving macrophages. Panel **b** shows the proliferation of SMC from the media to the subendothelial space and the accumulation of macrophages. Panel **c** shows the cell overturn of macrophages into fatty streaks and the formation of a fibrous cap and LRNC. Panel **d** shows the effect of plaque failure. Exposed lipid cells cause blood coagulation and lead to the development of thrombus. Image was retrieved from D. Steinel *et al.*, 2015 [12].

Although plaque morphology and composition are good indicators of vulnerability, studies have shown that local stress concentrations in the shoulder- and mid cap region have a high contribution to plaque rupture [13]. The rupture occurs when the stresses in the fibrous cap exceed its mechanical strength [14]. It has been shown that the main load bearing component in TCFA is the collagen matrix, therefore the rupture of the cap is associated with the failure of the collagenous structure [15]. The rupture causes the cap to open and expose the highly thrombogenic LRNC to the bloodstream. Therefore the study of vulnerable plaques from a mechanical point of view is crucial for the prevention of clinical events, but unfortunately, the scarcity of human unruptured vulnerable plaque tissues makes it difficult to make progress. For this reason, alternative methods are needed to study plaque rupture.

With the help of tissue-engineering it is possible to artificially create soft tissues with a controlled composition. This method can be used to create artificial structures with the composition similar to that of human TCFA. This would allow the study of plaque rupture in a controlled and reproducible environment. In a newly presented collaborated master project between the Erasmus MC, the Eindhoven University of Technology, and the Delft University of Technology S.M.Serra *et al.*, 2020 created tissue-engineered structures, which resemble the composition of a human TCFA [16]. Collagen type I and III mixed with fibrin forms the basis of the tissue sample. Half of the sample batch underwent the inclusion of a soft region to represent the lipid core under the fibrous cap. This soft lipid core inclusion is referred to as Soft

Inclusion (SI) throughout the rest of the study. The samples were then subjected to uniaxial tensile expansion to study their mechanical behaviour and the rupture. The strain and displacement field during the testing was captured with Digital Image Correlation technique (DIC) [16]. Figures 2 and 3 show the TCFA without SI (Figure 2/a) and with SI (2/b) as well as the setting for the uniaxial tensile test (Figure 3) respectively. A detailed explanation of the methodology of the study can be found in Appendix I.

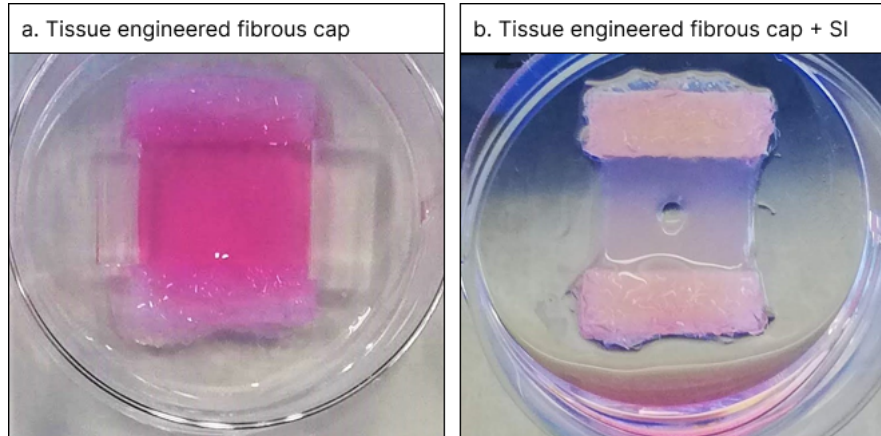


Figure 2: Tissue engineered fibrous cap (a) and fibrous cap + SI sample (b).

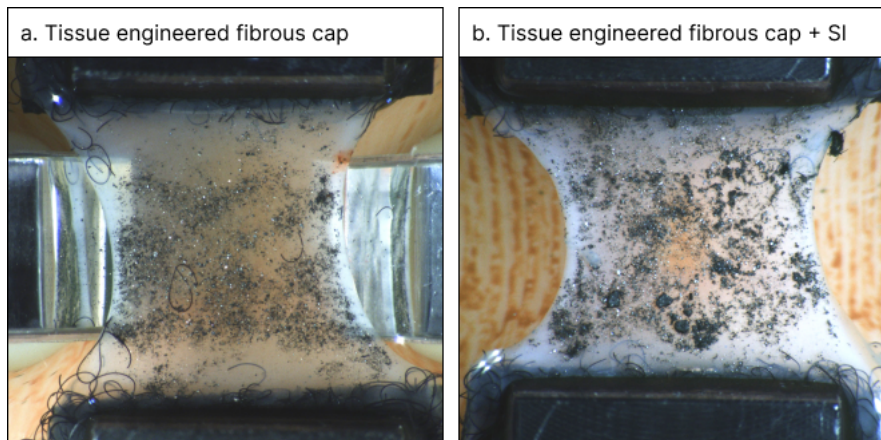


Figure 3: Samples clamped in for uniaxial tensile test, with speckle pattern applied to them for DIC. Images retrieved from S.M.Serra, 2020 [16].

## 1.1 Motivation of the study

The understanding of material properties of tissue-engineered fibrous cap structures contributes to the understanding of plaque rupture. In this study, a method is proposed to characterise the material properties of individual tissue-engineered TCFA samples and explore local heterogeneity at different positions of the samples.

The measured deformation is a suitable base for an inverse approach to find material parameters and inverse Finite Element Method (iFEM) has been successfully applied in previous studies to assess material properties of human plaque tissues [17, 18]. In iFEM, experimentally measured data gets compared to numerically generated data, using a computational model. The computational model is the implementation of

the physical experiment into a computational environment, with identical geometry and boundary conditions. The model contains an initial estimation of the material properties, to describe the global mechanical behaviour. The difference of the resulting displacement fields is represented by the objective function. The initially estimated parameters undergo an optimization procedure in order to reduce the difference between the measured and the computed data. After global assessment, sections with independent material properties were established to investigate local heterogeneity in the samples using the same procedure as before. Figure 4 outlines the main steps in iFEM applied in this study.

Two TCFA constructs were selected for this study based on high-quality DIC results. One sample contains a mix of collagen and fibrin. This sample will be referred to as fibrous cap construct. The other sample contains the soft lipid core inclusion, this sample will be referred to as fibrous cap + SI.

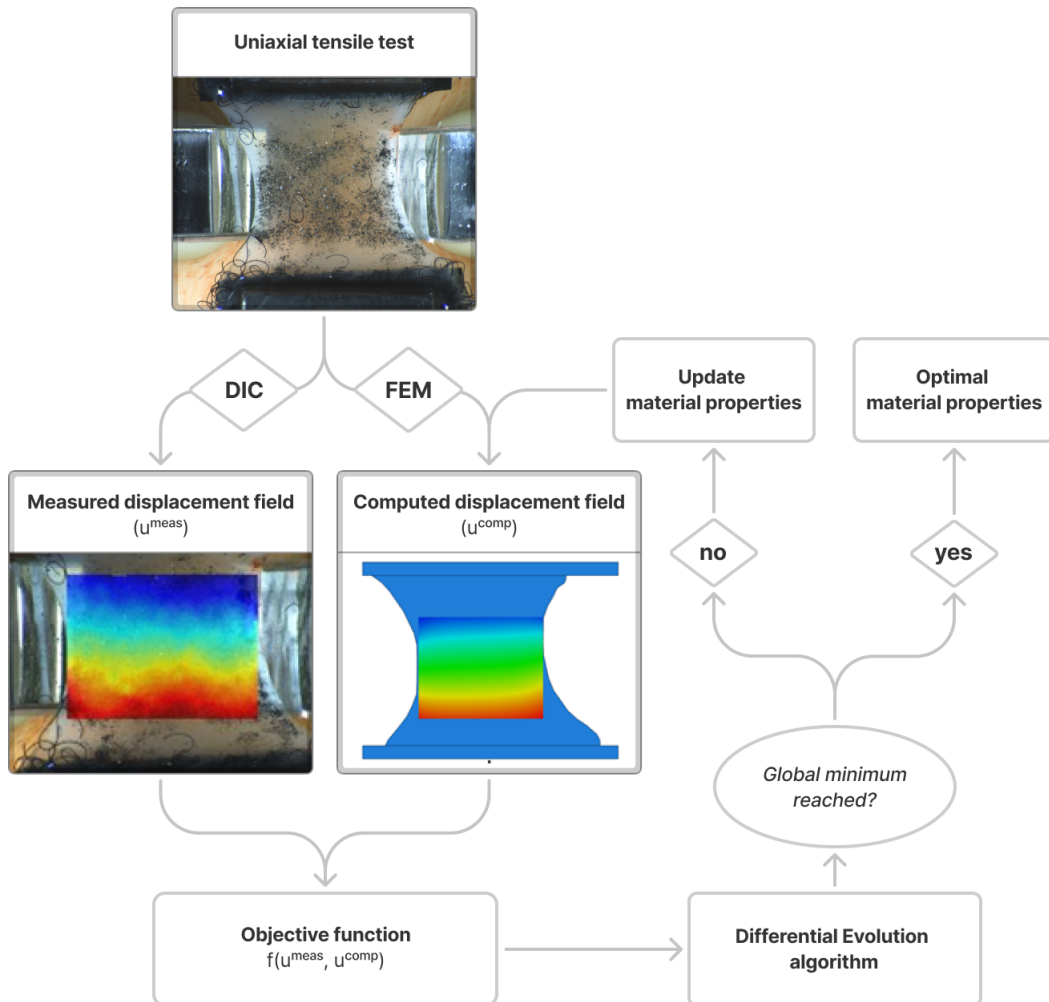


Figure 4: Flowchart of iFEM, visualising the main steps of the procedure. Measured and computed output fields are compared to each other in the objective function. The optimization algorithm changes the material properties in the numerical model until the minimum difference is reached.

## 1.2 Goals of the study

The underlying goal of this study is to set up an iFEM pipeline for material property characterisation of TCFA constructs, which enables the global and local assessment of mechanical behaviour. To guide the study the following goals were established:

- Create an inverse Finite Element Method pipeline for mechanical characterisation of tissue engineered TCFA structures, based on the DIC displacement field.
- Explore local heterogeneity of the samples, by determining mechanical behaviour at different regions of the samples, using independently variable parameters.
- Investigate the limits of the local material property estimation method by increasing the number of sections with independent material parameters used in the material model for characterisation.
- Investigate the effect of structural differences (presence of SI) on the local mechanical behaviour of the samples.

## 2 Methods

The methodologies for this study are subdivided into three parts. The first part contains the methodology for creating the Finite Element model for the study. It includes the methodology for the implementation of the geometry, the loading and boundary conditions, and an overview on the material model.

The second part contains the methods for local and global material property characterisation. In this part the method for comparing the experimental and computed data will be explained, including the determination of the objective function and a general overview on the optimization algorithm.

The third part focuses on synthetic data study to validate the methods. The methodology for investigating the effect of grid size, noise from the DIC, number of sections, and control parameters for optimization algorithm will be described.

### 2.1 Finite Element Method

For the creation of the mechanical model the Finite Element Method (FEM) implemented in ABAQUS version 2016 was used. The FEM is a numerical technique to solve problems described by partial differential equations. During the method the domain is subdivided into simple elements and the equations are linearised at the connection points (nodes) between neighbouring elements, in order to find approximate results of the equations.

The method is often applied in mechanics to calculate stresses and strains in structures with geometries, where there is no analytical solution for the governing equations. FEM can be implemented into a computational pipeline, which usually consists of the implementation of the structures geometry, the determination of the relevant loading and boundary conditions and the implementation of a material model.

A key step of FEM is the discretization of the domain into elements, and the size of the elements has an influence on the accuracy of the results. Smaller element size leads to more accurate approximations, but this is at the expense of higher computational effort. Therefore, it is important to carry out a mesh refinement analysis, to consider the computational effort and resulting accuracy. After running the FEM simulations the results always need to be interpreted and checked for correctness and, if necessary, the previous steps involving the determination of relevant loading and boundary conditions or the discretization have to be adjusted.

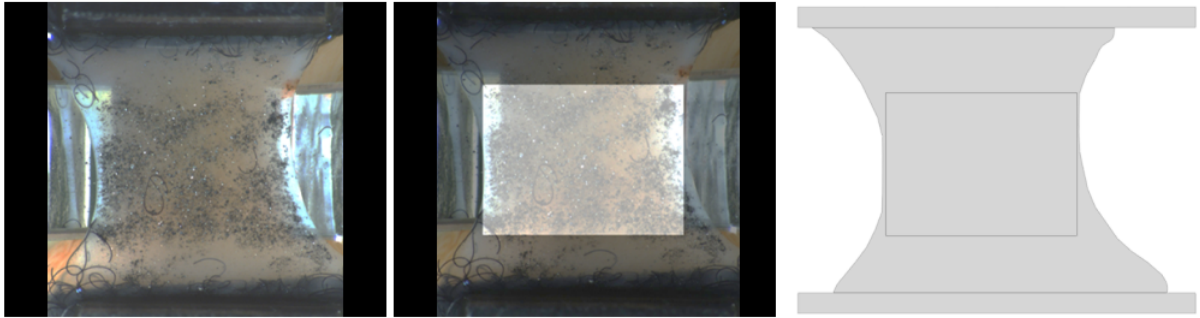
In the following sections, the implementation of the geometry, the loading and boundary conditions, the material model, and the methods for mesh refinement analysis are covered.

#### 2.1.1 Geometry

The recorded DIC frames were chosen as basis for the implementation of the geometry. The model includes three main sections; one section was created to represent the stiff clamps from the tensile experiment, the second section represents the TCFA construct between the clamps and is referred to as the tissue section, and lastly the Region of Interest (ROI) was defined as an independent section within the tissue section. The ROI was determined based on the DIC frame which highlights the position

of the ROI used for creating the experimental displacement field. The tissue section around the ROI was excluded from DIC due to unreliable results caused by velcro tapes near the clamp region. The ROI measures 9.3x6.9mm for the fibrous cap and 9x7.3 for the fibrous cap + SI models. The pre-stretched stress-free configuration, following the pre-conditioning cycle, was used as a reference image to outline the geometry of the structures. Figure 5 below shows the DIC frame with the stress-free geometry of TCFA constructs, the position of the ROI, and the implemented FEM models.

A



B

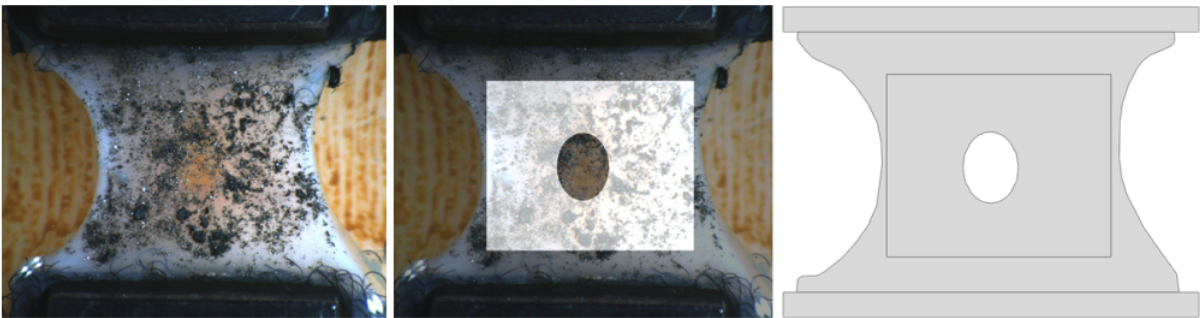


Figure 5: The geometries, positions of ROI, and the implemented geometries in ABAQUS. Panel A and B show the fibrous cap and fibrous cap + SI samples respectively. The images showing the TCFA constructs were retrieved from S.M. Serra, 2020, [16].

### 2.1.2 Loads & Boundary conditions

The loads and boundary conditions are representations of the external loads and movement restrictions that characterise the uniaxial tensile testing. Axial stress ( $\sigma$ ) was determined as the main loading condition during the experiment, therefore tension load was applied in the model. The tension load was calculated from the recorded actuator force ( $F_a$  in [mN]) and from the average cross sectional area ( $A$  in  $mm^2$ ) taken before the experiment. The displacements of the actuators ( $\Delta L$  in [mm]) were converted into stretches ( $\lambda_U$ ) in order to determine the stress-stretch curve of the tissue. The equations (eq. 1-2) to calculate the nominal axial stresses and stretches and the calculated stress-stretch curve (Figure 6 - 7) are shown below.

$$\sigma = \frac{F_a}{A} \quad (1)$$

$$\lambda_U = 1 + \frac{\Delta L}{L_0} \quad (2)$$

Due to the non-linear mechanical behaviour of the samples, which can be seen on the stress-stretch curves below, multiple loading steps were implemented in the mechanical model. Three different loading steps were defined so that they subdivide the curve into three sections, which cover the initial state, the middle, and the state before the rupture. Step 1 corresponds to 7.5 kPa, step 2 corresponds to 70.1 kPa, and step 3 to 190.6 kPa for the fibrous cap model and 7.7 kPa, 73.6 kPa, 194.4 kPa for the fibrous cap + SI model. These stress values were applied as pressure on the clamp region, with the assumption of pressure being homogeneously distributed along with the clamps. Figures 6 - 7 shows the stress-stretch curve for the fibrous cap and fibrous cap + SI respectively, the dashed lines indicate the implemented loading steps.

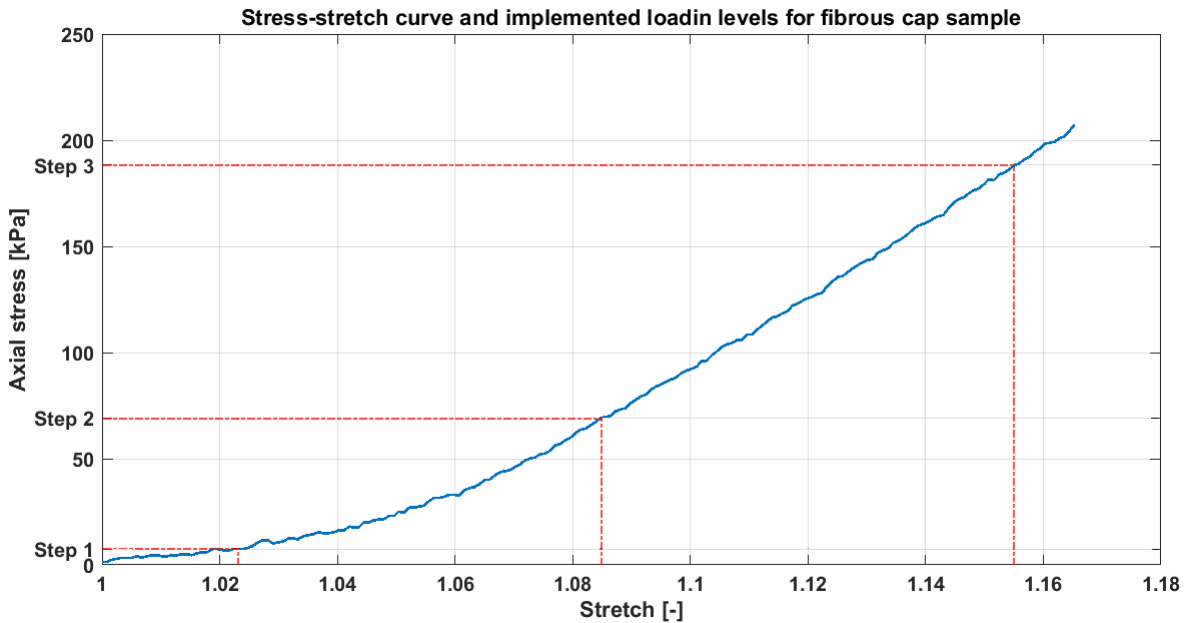


Figure 6: Axial Stress [kPa] and stretch [-] during the uniaxial tension test for the fibrous cap sample. The curve begins after the pre-conditioning cycle, and starts from the pre-stretched, stress-free configuration. The curve shows nonlinear mechanical behaviour, and strain stiffening behaviour as expected from tissue materials.

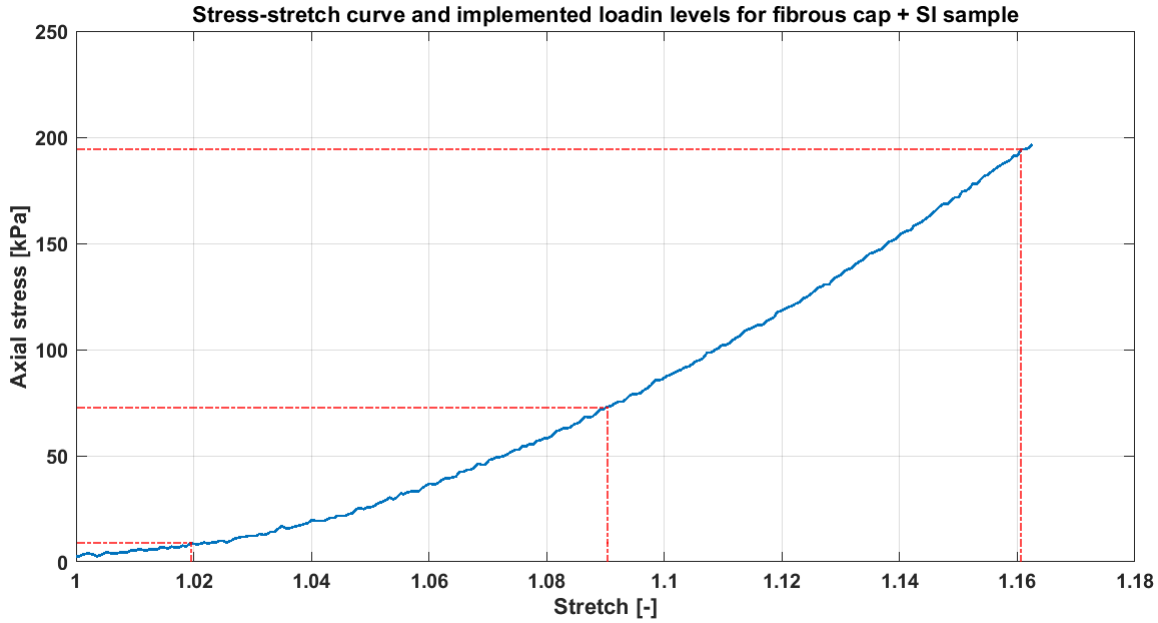


Figure 7: Axial Stress [kPa] and stretch [-] during the uniaxial tension test for the fibrous cap+SI sample. The curve beings after the pre-conditioning cycle, and starts from the pre-stretched, stress-free configuration. The curve shows nonlinear mechanical behaviour, and strain stiffening behaviour as expected from tissue materials.

Boundary conditions are constraints and initial values for problems where differential equations need to be solved. In the mechanical models used for this study, the boundary conditions represent restrictions of movements so, that they best characterise the movement restrictions from the experimental testing.

Two motion restrictions were applied in the mechanical model for two reasons: Firstly, to prevent rigid body motion of the structure for which a soft, compressible buffer region was created, and its edges were encastered. Secondly, the horizontal movement of the clamps was prevented by only allowing movement in the vertical direction. Figure 8 shows the axial stress applied along the clamp regions (Figure 8/A) and the implemented restrictions for rigid body motion and horizontal movement of the clamps (Figure 8/B) for the fibrous cap model. The same boundary and loading conditions were applied to the fibrous cap + SI model.

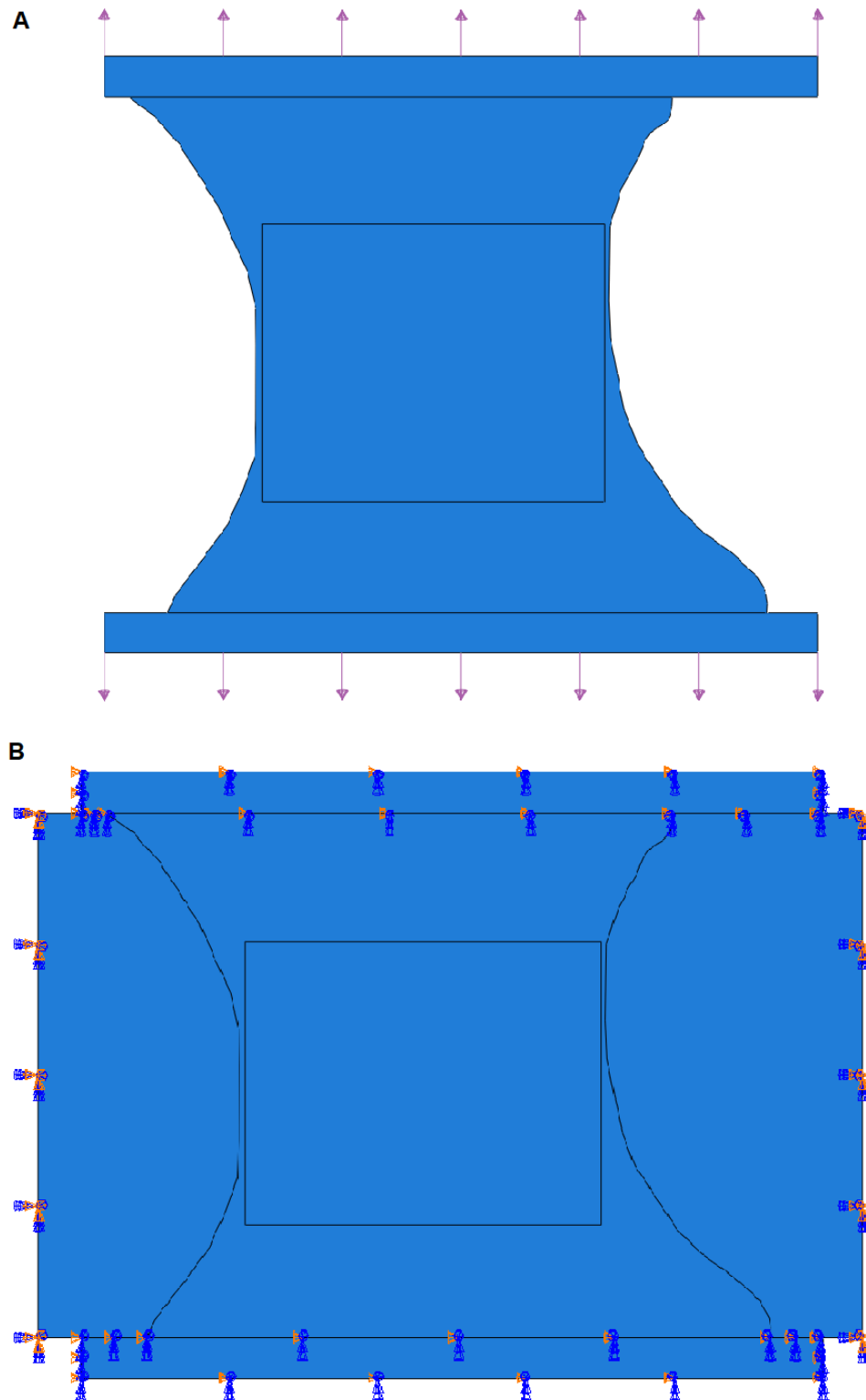


Figure 8: Panel A shows the axial stress along the clamp regions and panel B shows the restrictions for rigid body movements in the buffer regions and the restrictions for horizontal movement for the clamps.

### 2.1.3 Material Model

Soft tissues, including arteries, can undergo large deformations without significant, or close to negligible plastic deformation. In addition, arteries are considered to be incompressible and show strain stiffening behaviour. This type of behaviour is best characterised by hyperelastic material models. Due to the nonlinear behaviour of hyperelastic materials, the constitutive equations are best described by a strain-energy function ( $U$ ), rather than a linear coupling of stresses and strains [19].

The material model in this study has to fulfil the following criteria: It has to capture the non-linear behaviour of the tissue while using the least amount of independent material parameters. Hence a second-order reduced polynomial model was implemented in the mechanical model. The equation 3 shows the strain-energy function for a reduced polynomial hyperelastic material as it is implemented in ABAQUS [20].

$$U = \sum_{i=1}^N c_{i0} (\bar{I}_1 - 3)^i + \sum_{i=1}^N \frac{1}{D_i} (J^{el} - 1)^{2i} \quad (3)$$

The number of orders implemented in the function determines the number of parameters in the equation. When  $N=1$   $c_{10}$  and  $D_1$  represent the initial shear modulus ( $\mu_0 = 2c_{10}$ ) and initial bulk modulus ( $K_0 = \frac{2}{D_1}$ ) respectively. In higher orders the additional parameters are responsible to describe the non-linear behaviour of the material.  $\bar{I}_1$  is the first invariant of the deviatoric strain and it is the sum of squares of the principal stretches ( $\bar{\lambda}_1^2 + \bar{\lambda}_2^2 + \bar{\lambda}_3^2$ ) and  $J^{el}$  represents the elastic volume ratio.

An increased order of the function results in a better implementation of the non-linear behaviour of the model, but there are more parameters to characterise. The second order was chosen to keep the number of parameters low while sufficiently capturing the non-linear behaviour of the tissue.

Providing that there is uniaxial extension on a fully incompressible material ( $J^{el} = 1$ ) for  $N = 2$  the following equations 4 - 8 describe the strain-energy function, the principal stretches, the deviatoric strain and the coupling of stresses and stretches respectively. The parameters  $c_{10}$  and  $c_{20}$  from equation 8 are the parameters to be characterized in this study.

$$U = c_{10} (\bar{I}_1 - 3)^1 + c_{20} (\bar{I}_1 - 3)^2 \quad (4)$$

$$\bar{\lambda}_1 = \lambda_U, \quad (5)$$

$$\bar{\lambda}_2 = \bar{\lambda}_3 = \lambda_U^{-1/2} \quad (6)$$

$$\bar{I}_1 = \lambda_U^2 + 2\lambda_U^{-1} \quad (7)$$

$$\sigma = 2 \left( \lambda_U - \lambda_U^{-2} \right) \left[ c_{10} + 2 * c_{20} (\bar{I}_1 - 3) \right] \quad (8)$$

The initial estimate for the material property values was decided based on the results of the curve fitting procedure which was carried out using MATLAB, R2019b (Simulink). The result of the curve fitting procedure for the TCFA constructs is shown in Figures 9 - 10 below. The implemented stiffness and compression parameters for both models are listed in Table 2.

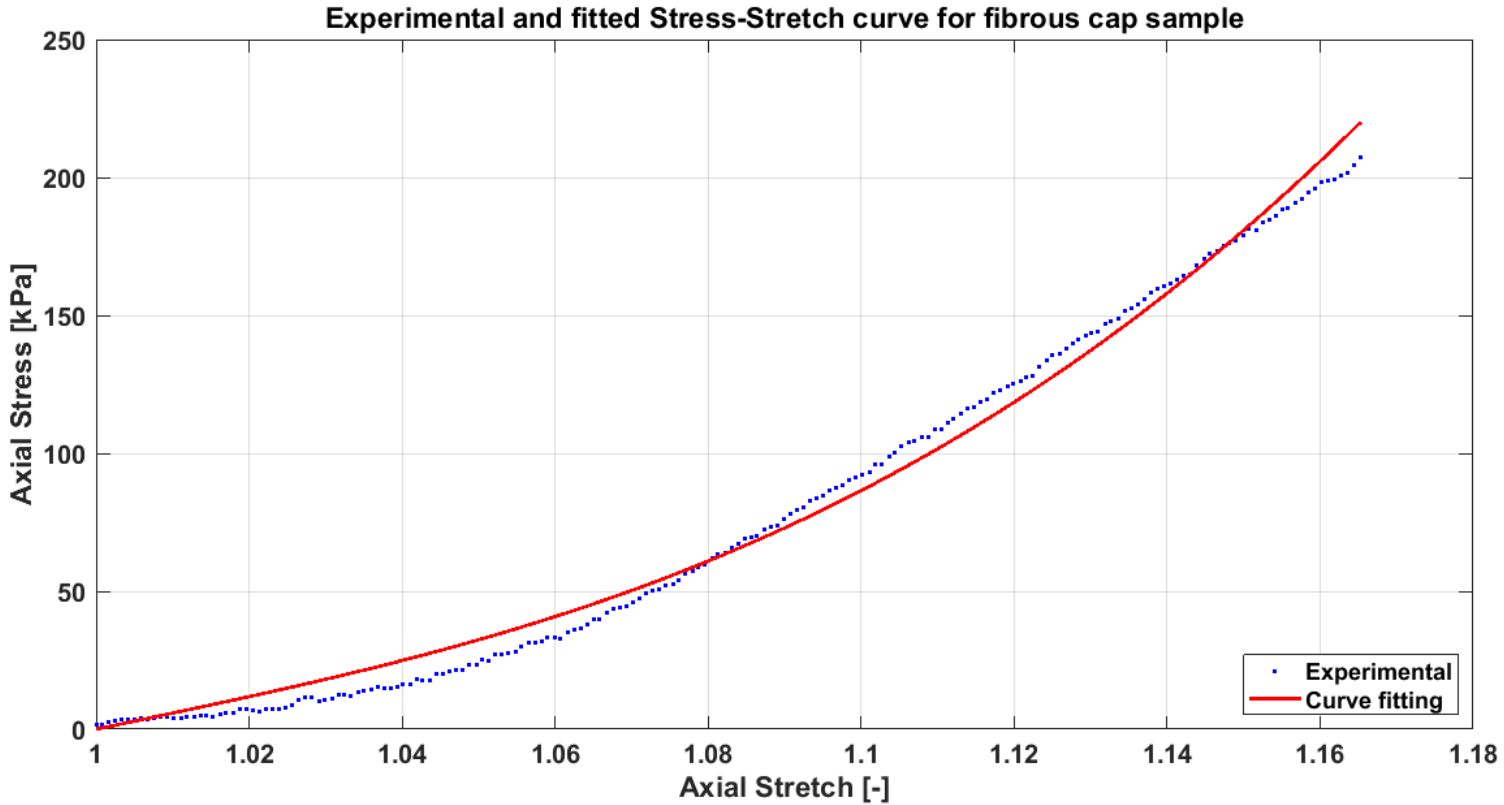


Figure 9: Results of the curve fitting procedure for fibrous cap sample. Blue dashed data represents the stress-stretch curve from the experiment, the red line represents the fitted curve. The material parameters were taken from equation nr. 8, when  $n = 2$ , the resulting  $c_{10}$  and  $c_{20}$  parameters were estimated as 97.86 kPa and 1069 kPa respectively, with 95% confidence bounds.

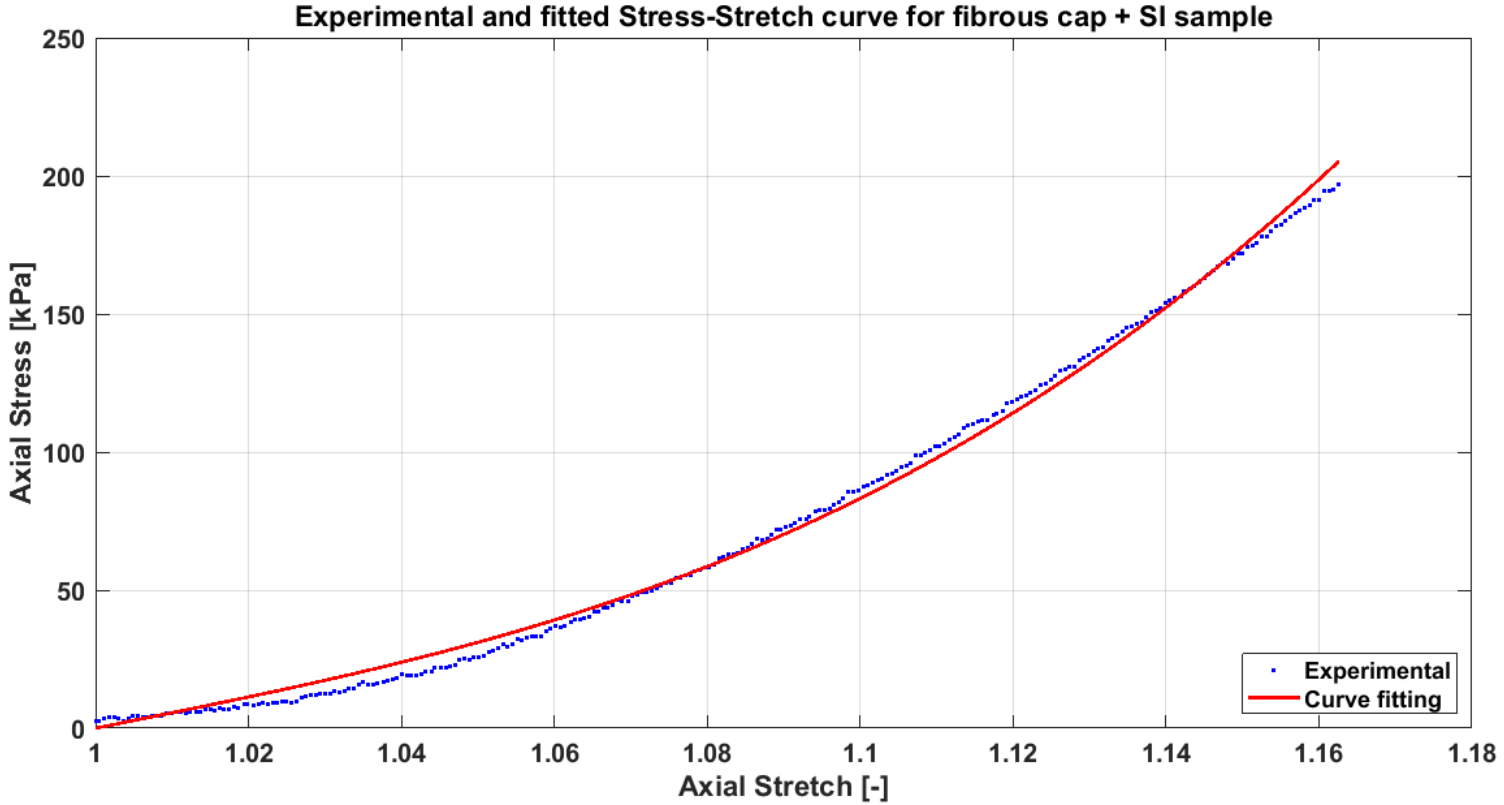


Figure 10: Results of the curve fitting procedure for fibrous cap + SI sample. Blue dashed data represents the stress-stretch curve from the experiment, the red line represents the fitted curve. The material parameters were taken from equation nr. 8, when  $n = 2$ , the resulting  $c_{10}$  and  $c_{20}$  parameters were estimated as 93.66 kPa and 1037 kPa respectively, with 95% confidence bounds.

Table 1: Material properties for fibrous cap and fibrous cap + SI models

Model Parameter	Fibrous cap				Fibrous cap + SI			
	$c_{10}$	$c_{20}$	D1	D2	$c_{10}$	$c_{20}$	D1	D2
Tissue	97.86	1069	1E-4	1E-4	93.66	1037	1E-4	1E-4
ROI	97.86	1069	1E-4	1E-4	93.66	1037	1E-4	1E-4
Buffer	1E-4	1E-4	1E5	1E5	1E-4	1E-4	1E5	1E5
Clamp	1E5	1E5	1E-4	1E-4	1E5	1E5	1E-4	1E-4

#### 2.1.4 Discretization and mesh refinement

The following element types were used for the computational model: CPE4RH (4-node, bilinear plane strain, quadrilateral, hybrid, reduced integration with hourglass control) and CPE3RH (3-node, bilinear plane strain, quadrilateral, hybrid, reduced integration with hourglass control).

Five different element sizes were investigated starting from 0.05mm to 0.8mm in equal intervals. An element size of 0.03mm is included to create a benchmark curve, as it represents the same number of data points as generated with the DIC field. For each interval the mesh was evaluated based on the resulting Y-displacement values along the upper edge of the ROI and on the resulting computational time to reach

results.

To compare the performance of the discretization, the distribution of the displacement values along the upper edge of ROI were plotted for the different models as well as the computational times corresponding to the different element sizes were visualised. Figure 11 and Figure 12 show the distribution of displacements and computational times for different element sizes respectively.

Figure 11 shows the asymmetrical distribution of the displacements. High displacement values occur on the left part of the curve which constantly decreases towards the right end of the curve. The curves show the decreasing difference between the distribution of the displacement values when going from coarse mesh (0.8mm) to fine mesh (0.05mm). The jump between curve blue and red (0.8mm - 0.4mm) is visibly higher than the jump between curve violet and green (0.1mm - 0.05mm), indicating that there is no significant improvement in the output field between these mesh sizes. As expected the computational time was highly influenced by the element size. Smaller element size results in a higher number of elements and nodes created during the discretization. The increase of computational time seems to increase exponentially with decreased element size. During the optimization procedure, FEM simulations will be carried out in the loop. The number of loops necessary can range from a couple of hundreds to thousands. For this reason, the computational time is a determining factor when deciding on element size in the FEM. The following hardware configuration was used for the estimation procedure; OP system: Microsoft Windows 10, 64 bit, CPU: Inter(R) Core(TM) i7-6700 @ 3.40 GHz, GPU: Intel(R) HD Graphics 530, RAM: 16 GB.

To preserve accuracy, whilst maintaining an optimal computational time, an element size of 0.2 mm element size was decided for the ROI, and an element size of 0.04mm was applied to the surrounding sections (clamp, buffer, tissue). The discretized fibrous cap model including the clamps and surrounding tissue is shown in Figure 13 below. The discretized fibrous cap + SI model can be found in the Appendix II.

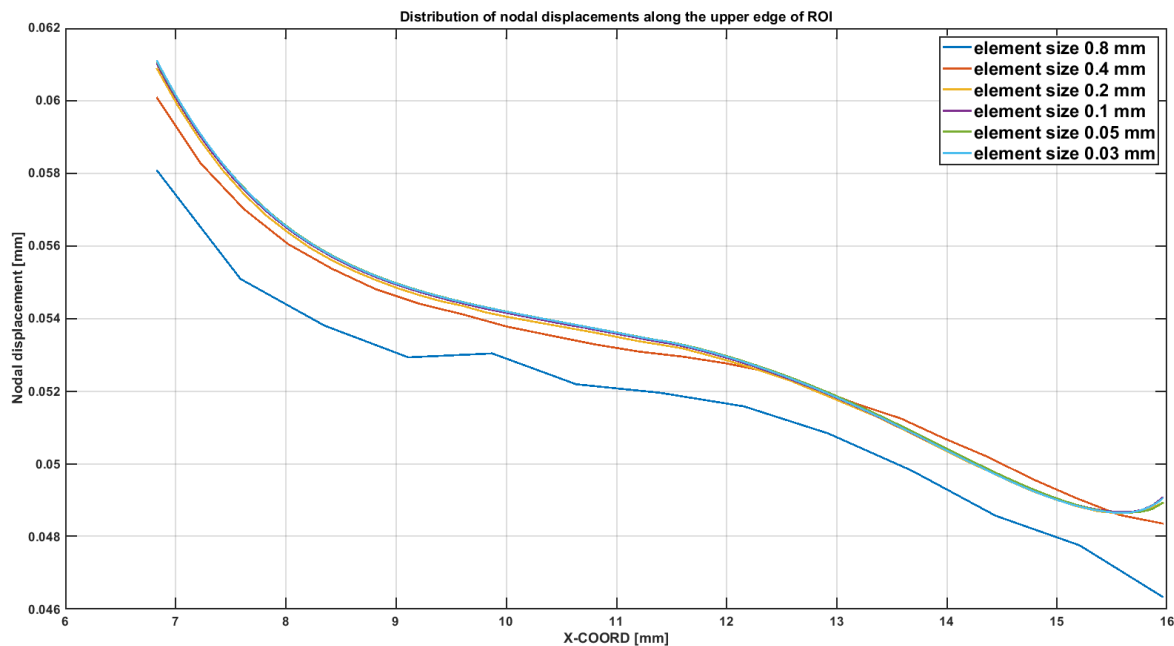


Figure 11: Result of mesh independency analysis. The X-axis shows the X-coordinates of the nodes along the upper edge of the ROI (in mm), and the Y-axis shows the corresponding displacement (in mm) at the corresponding node.

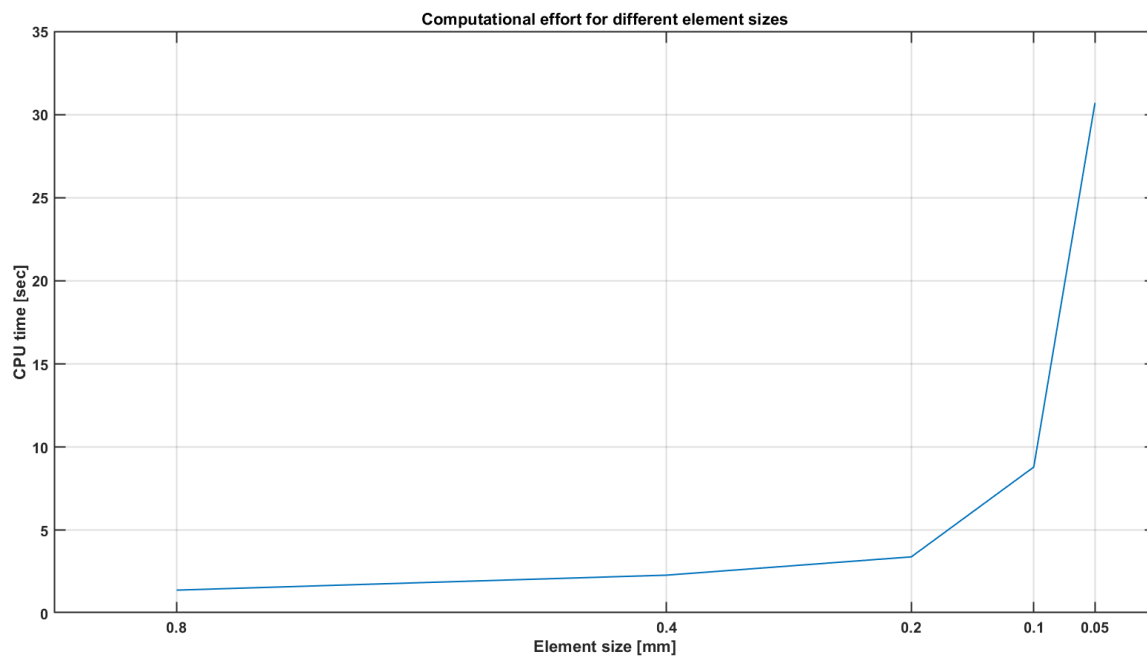


Figure 12: CPU time in sec for the models with different element sizes. X axis shows the element size in mm and Y axis shows the computational time in seconds, until compilation of the FEM.

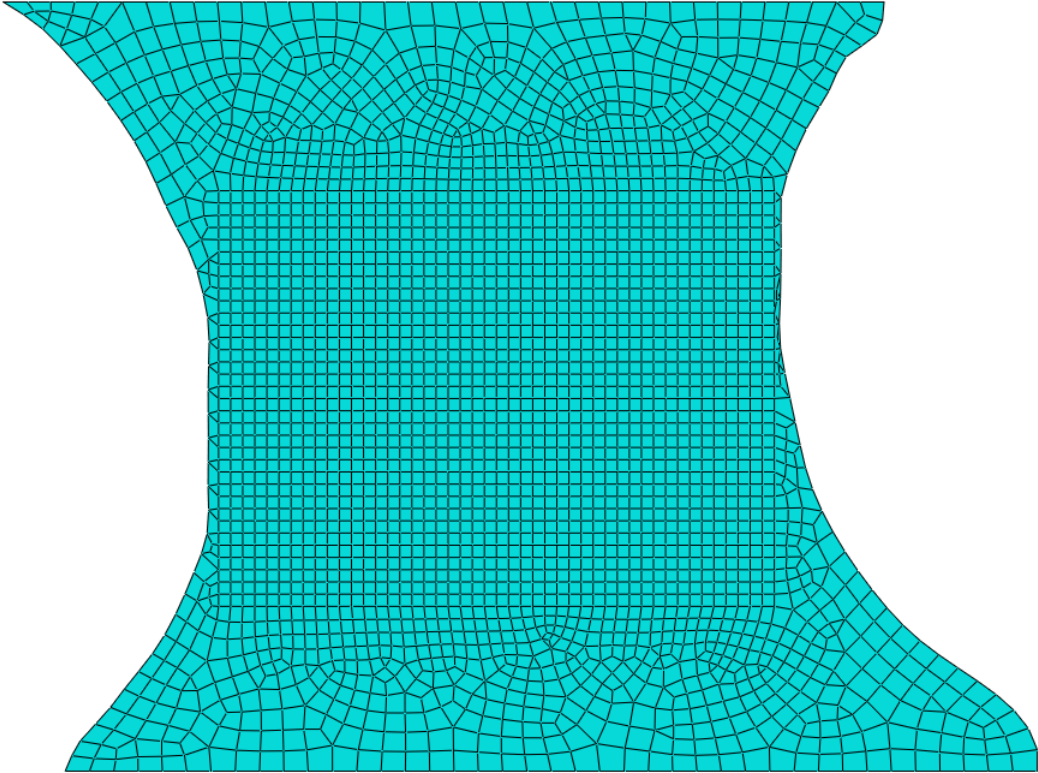


Figure 13: Discretized model for the fibrous cap model. ROI includes elements with 0.2mm size, the surrounding tissue contains elements with 0.4 mm.

## 2.2 Material property estimation

### 2.2.1 Grid and objective function

One of the challenges in iFEM is to map and compare the displacements, of the corresponding regions, between the measured and computed fields. A grid is often used in iFEM pipelines to map corresponding regions between the two data sets [17, 18]. The grid was applied so that it covers the same regions of the ROI in both the DIC and the computed model. To compare the measured and computed displacement fields the sum of average grid elements ( $u_i^{meas}, u_i^{comp}$ ) was calculated. The figure below shows an example of the grid applied to the ROI of the fibrous cap FEM model.

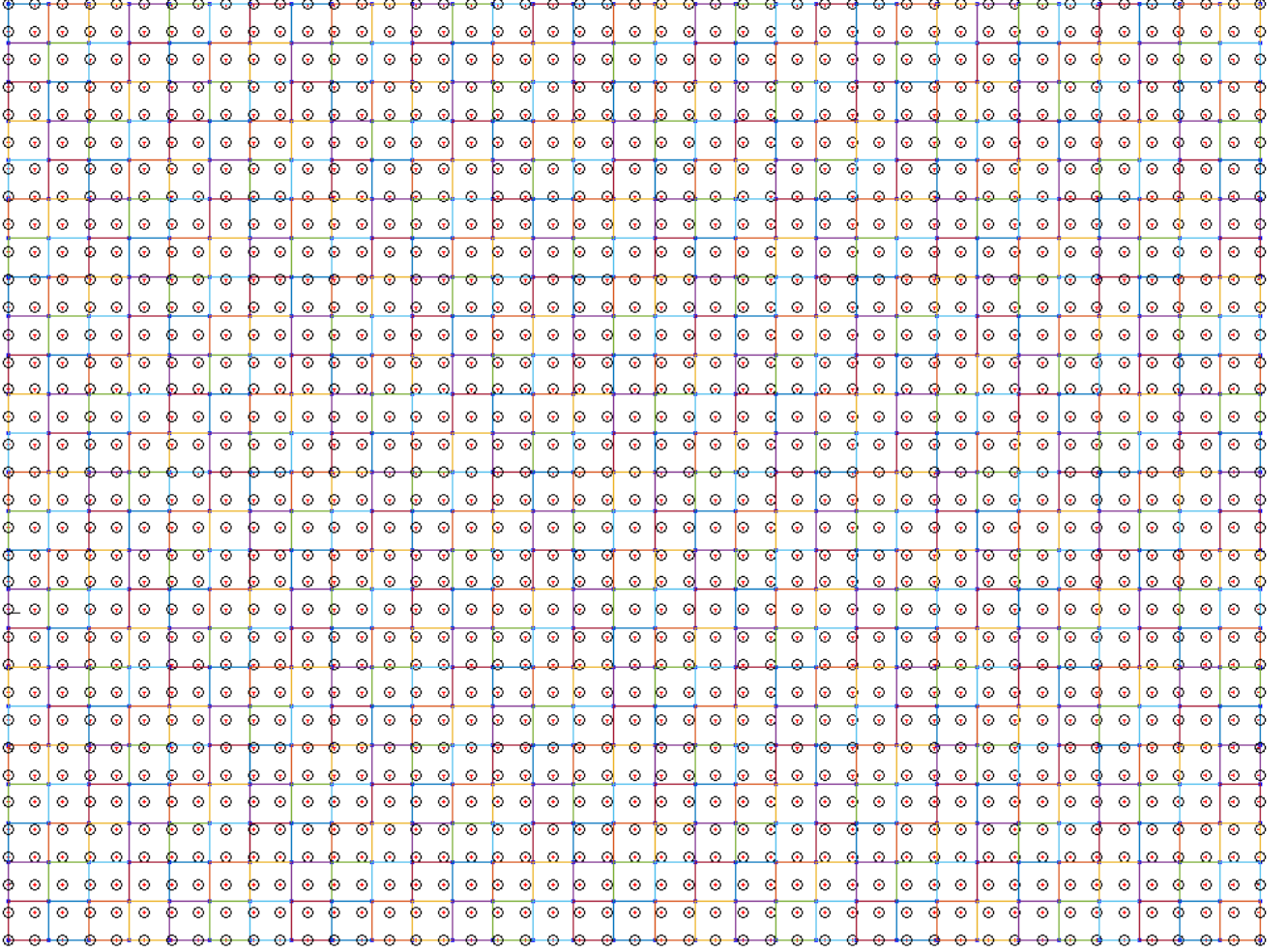


Figure 14: The grid applied to the ROI of the fibrous cap model. The dots represent the nodes from the Finite Element Model

The objective function represents the square root of the Normalised Mean Square Error (NRMSE) between the measured and the computed displacement in each grid, related to the mean of the measured displacements ( $\bar{u}^{meas}$ ) over all grid elements ( $n$ ) [21]. The equation 9 below was subjected to the minimization procedure. In a previous study the grid search method was applied successfully to characterise plaque material properties, this method however is time consuming and can be improved upon by implementing a machine learning algorithm to find the global minimum of the objective function [17]. In order to improve the estimation procedure Differential Evolution (DE) algorithm was implemented into the iFEM pipeline.

$$f(u_i^{comp}, u_i^{meas}) = \frac{\sqrt{\sum_{i=1}^n (u_i^{comp} - u_i^{meas})^2}}{\sqrt{\sum_{i=1}^n (u_i^{meas} - \bar{u}^{meas})^2}} \quad (9)$$

### 2.2.2 Differential evolution algorithm

Differential Evolution algorithm (DE) was proposed by Storn and Price to find a global optimum for non-linear, non-differentiable functions [22]. This function is referred to as the objective function. DE belongs to the group of evolutionary algorithms which share common attributes. The optimization is subdivided into generations, where each generation contains a number of members referred to as the population. Each population member represents a vector, which contains the input parameters that are used to calculate the value of the objective function [23]. The central method of evolutionary algorithms is the generation of variations within the population members by manipulating the input parameters of the objective function, and deciding whether the newly generated input parameters lead to more preferable results of the objective function.

The main steps in DE are summarised in the figure below. The parameters in the initial generation are randomly selected from the predefined search boundaries [ $X_{min}$  and  $X_{max}$ ]. Mutation and crossover are the subsequent methods to create variations within the generation. Finally, the parameters leading to the optimal solution within the generation are selected and propagated to the next generation where the procedure begins again with the mutation. The DE is explained using a working example in Appendix III.

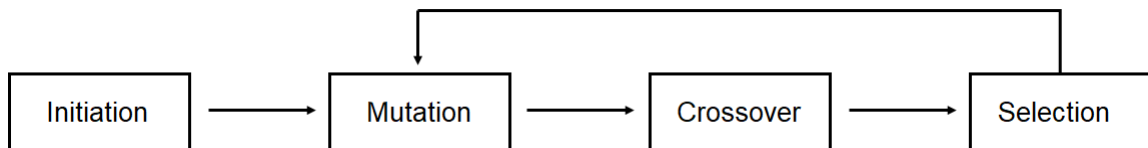


Figure 15: The main steps in DE. The procedure starts with the population initiation, followed by mutation and crossover, and finally the selection of the optimal parameters for the function. These parameters are propagated to the next generation where the procedure begins again.

The DE implemented into python as a SciPy algorithm was used for the purpose of the study, and the algorithm requires the specification of user defined parameters [24]. The specification of the user parameters for this study can be found in the methodologies of the synthetic data study (section 2.3) and the algorithm used for the study is included in the Appendix II.

### 2.2.3 Global and local material property estimation

For the global estimation, the resulting material properties from the curve fitting procedure were used as initial estimation. During the estimation procedure the same material property was assigned to both the ROI and the surrounding tissue area. However the basis of comparison remained the displacement field in the ROI.

To create a local material property estimation, the ROIs were subdivided into sections. The positions of the sections were determined based on the DIC displacement field. The ROIs were first subdivided into the left and right parts, and afterwards into top and bottom sections. Finally, the mid-sections were subdivided into two parts. During the local estimation, the surrounding tissue material properties were kept constant with the resulting values from the global estimation. In the case of the fibrous cap + SI model, the soft inclusion as well as the immediate surrounding area were excluded from the optimization. Seeing as it has previously been reported that peak deformations occur around the SI area [16]. Figure 16 shows the subdivided ROIs for the purpose of local estimation.

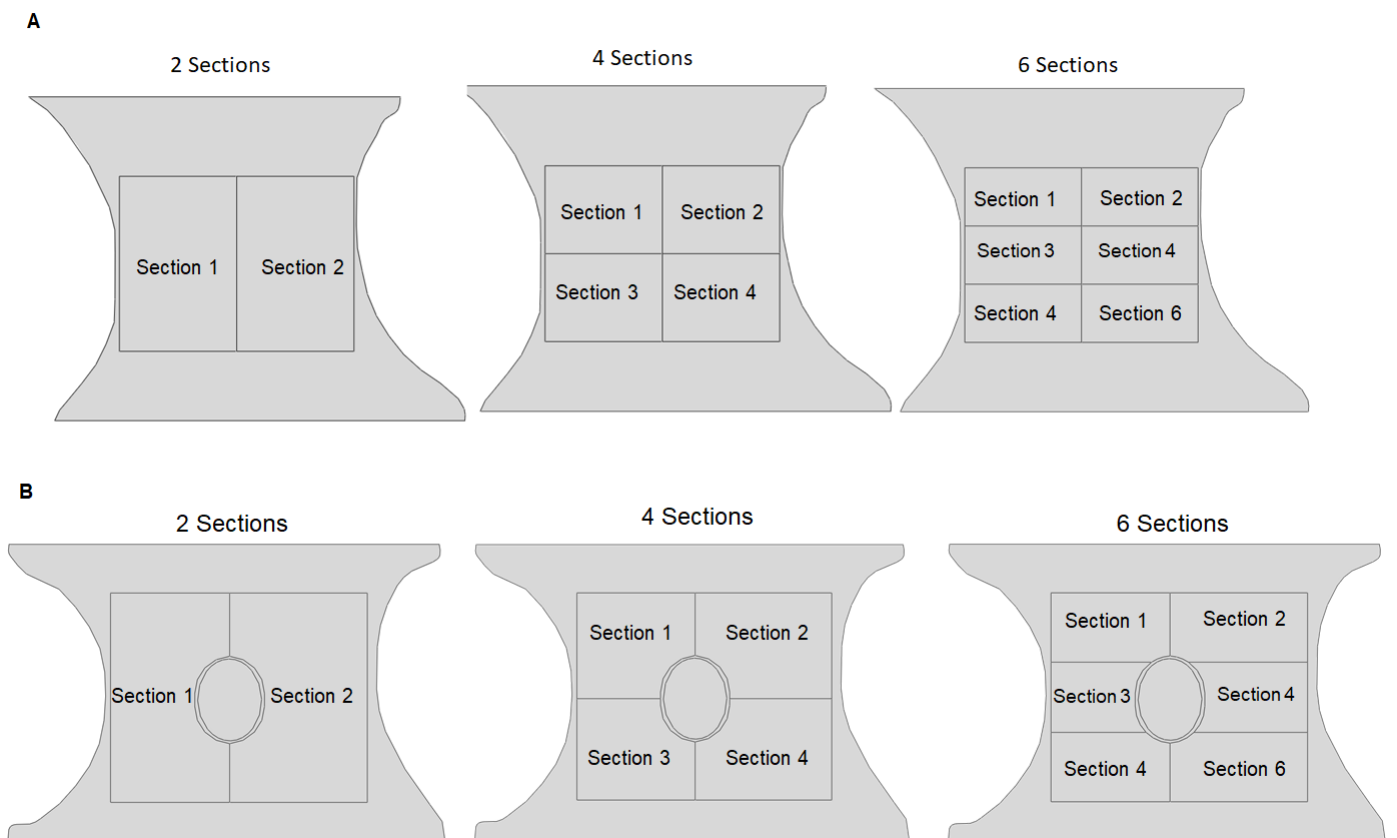


Figure 16: The sections for the local material property estimations. Four different subdivisions were tested for both models. The ROIs were subdivided into two four and six sections. Panel A and B show the sections for fibrous cap and fibrous cap + SI models respectively.

## 2.3 Methods for synthetic data study

The goal of the synthetic data study is to test the methodology of the material property characterisation. For this purpose, a synthetically generated displacement field was created using the FEM model, with its loading and boundary conditions, as described in the previous sections, with the element size that corresponds to the number of data points from the DIC (0.03mm), and with the initially estimated material properties from the curve fitting method. This synthetic displacement field will be referred to as the Ground Truth Data (GTD). The displacement field resulting from the model used for validation will be referred to as Computed Data (CD). The material properties of this model will be adjusted to the GTD during the iFEM. This allows for the comparison of the estimation procedures with different parameters and the adjustment of iFEM to the study. Within the framework of the synthetic data study, the effect of the grid size, the noise, the number of independent parameters, and DE control parameters were tested.

### 2.3.1 Effect of grid size

The first step in the iFEM pipeline is to determine on the grid size. Three different grid sizes were considered for the study: Grid 1 with 0.1x0.1 mm, grid 2 with 0.2x0.2 mm, and grid 3 with 0.3x0.3 mm. The different grid sizes require different amounts of rows and columns in order to cover the entire ROI. The different grid sizes applied on the GTD field are shown in the Appendix II. The following table summarises the grid sizes and the number of columns and rows Table 2.

Table 2: Number of columns and rows required to cover the ROI and the average number of data points in the grid elements in the GT displacement field.

Grid Size [mm]	Nr. columns	Nr. rows
0.1 x 0.1	93	70
0.2 x 0.2	47	36
0.3 x 0.3	31	24

### 2.3.2 Noise

The synthetic data study was based on the displacement field created with DIC. Performing and recording experiments involve the addition of noise which can come from a variety of sources and will lead to altered output data [25]. Studies that focus on the effect of noise on the accuracy of the displacement field using DIC implement artificial white Gaussian noise in their models [26]. For this reason, a random distribution of white Gaussian noise with zero mean was implemented in the GTD after the application of the grid. The amount of noise was determined based on the estimated noise from the experimental data. The Savitzky-Golay signal processing algorithm, which was implemented in MATLAB, was used to determine the amount of noise expected from the DIC recordings. The methods for noise estimation can be found in the Appendix II. To investigate the effect of noise expected from the experimental data the resulting values from the noise estimation, one and two percent zero-mean noise, were added to the average grid displacement value.

### 2.3.3 Number of sections

The number of sections determines the dimension of the objective function. Increased dimensionality in the objective function is one of the limitations of evolutionary algorithms, and it has been reported that such algorithms lose their effectiveness due to the increased search base and complexity [27]. Although differential evolution is known for its robustness, it also suffers from performance deterioration when the number of independent parameters in the objective function increases [28]. The mechanical behaviour of each section was defined with a material model including two parameters for the stiffness. Thus each additional section increases the dimension of the objective function by two. To incorporate heterogeneous distribution among the material parameters ten percent random zero-mean deviation was added to the  $c_{10}$  and  $c_{20}$  values which were established with the curve fitting procedure. The Table 3 shows the implemented material properties for the different sections.

Table 3: The material parameters implemented in different sections, in order to represent heterogeneity in the model

	c values [kPa]	ROI	2 Sections	4 Sections	6 Sections
Section 1	$c_{10}$	97.8	88.7	88.7	93.0
	$c_{20}$	1069	962.1	962.1	1016.6
Section 2	$c_{10}$	-	108.46	108.46	89.0
	$c_{20}$	-	1175.9	1175.9	1170.6
Section3	$c_{10}$	-	-	78.8	103.4
	$c_{20}$	-	-	855.2	1129.9
Section 4	$c_{10}$	-	-	118.3	91.4
	$c_{20}$	-	-	1282.8	999.5
Section 5	$c_{10}$	-	-	-	101.9
	$c_{20}$	-	-	-	1114.0
Section 6	$c_{10}$	-	-	-	90.4
	$c_{20}$	-	-	-	987.8

### 2.3.4 Differential evolution parameters

The SciPy algorithm requires the specification of the following parameters; the range of search boundaries, the number of populations, the maximum number of generations, the tolerance criteria for stopping the procedure, the mutation factor, the crossover probability as well as the selection of mutation strategies. In this section the meaning of the user parameters will be explained as well as the selected values for the parameters.

The search boundaries [ $X_{min}$ ,  $X_{max}$ ] determine the range of values which will be explored throughout the procedure. The boundaries for the  $c_{10}$  values were set so that they cover the physiological range of possible material parameters. The decision was based on previously reported stiffness values of plaque tissues with similar compositions [29]. No reported values regarding  $c_{20}$  were found for polynomial function, therefore the same boundaries were implemented for both parameters. The values were set to cover the range between [5 1500] kPa.

The population number determines the number of function evaluations in each generation, and can be set with  $pop$ , however the dimension of the objective function also affects the final size of the population by  $pop * dim$ . Therefore if the  $pop$  is set to 10 and the objective function value has a dimension of two, then the population size will be 20.

The general recommendation for the population size strongly depends on the purpose of the procedure. As a general rule it is recommended to use  $n = 10 * dim$ , however for low dimensionality ( $dim < 30$ ) other recommendations suggest to use  $n = 30 * dim$  [30,31]. Taking these recommendations into account for the global estimation ( $dim = 2$ ) a population number of 50 was chosen. It is also recommended to implement a linear increase of population with increased dimensionality [28]. Thus in the case of the local material property estimations, which require higher dimensions in the objective function, the following population sizes were implemented: 52 - 54 - 56 - 60 for the respective dimensions of 4 - 8 - 12 in the objective function.

The maximum number of iterations determines after how many generations the procedure should stop, this value is set by the user parameter  $maxiter$ . The total number of function evaluations ( $nfev$ ) throughout the procedure follows from the population number in each generation and from the dimension of the objective function:  $nfev = (maxiter + 1) * dim * pop$ . Where adding one represents the creation of the initial population. The maximum number of iterations, or  $maxiter$ , was set to 1000. Although there is no general recommendation regarding the maximum number of iterations, it was not expected that over 1000 generations would be required for the optimization procedure to find the optimal material parameters.

Another stopping criteria, besides the maximum number of function evaluations, is the tolerance criteria. The optimization procedure stops if the standard deviation of the objective function is within a certain range of the mean of the objective function. For this an absolute tolerance  $atol$ , or a relative tolerance  $tol$  can be determined. The standard setting for the tolerance criteria  $tol = 0.01$  was implemented in the algorithm and no absolute criteria was specified in the algorithm.

The previously described values were set constant throughout the synthetic and experimental data study. However, in order to find the optimal parameters, the mutation factor, the crossover probability, and the mutation strategy, underwent investigation regarding their effect on the optimization procedure.

The mutation factor (F) determines the weighting factor for creating the trial vector, for details see Appendix III, which can be defined either as a single value or as a range of values. Defining the mutation factor as a range is beneficial, because then for each evaluation the mutation factor gets updated based on the objective function value. Low F values are preferred when the objective function value is close to the global minimum and high values are preferred when the value is far from the minimum [24]. However, the large search radius slows down the procedure. For this reason, it is important to find the optimal range for F values. Two ranges were tested in the DE algorithm. There is no general recommendation on the value of the mutation factor, therefore two cases were investigated, one with a wide range between [0.2 1.5] and one with smaller range [0.5 1.25].

The other user parameter which was tested for this study is the mutation strategy. The mutation strategy determines the method of creating the first variation within the generation, which is the trial vector. For further details on the role of the trial vector in DE see equation 10 in the Appendix II. Different strategies for

the mutation procedure use different methods for creating the trial vector. Mutation strategies best2bin and rand1bin have been marked among the best performing strategies, according to G. Jeyacumar, *et al.*, 2011, therefore the estimation procedures using these two strategies were compared in the synthetic study [32]. The rand1bin method corresponds to the mutation strategy explained in equation 10, in which case the target vector is selected randomly. Best2bin uses the same equation, however the target vector in each case is the vector of parameters yielding the lowest objective function from the population.

The crossover factor reflects the probability in which the offspring vector inherits components from the trial vector (see equation 11 in Appendix III). A higher crossover value results in a higher probability to propagate toward the global minimum of the objective function instead of the local minimum [33, 34]. To investigate the effect of crossover probability, two values were tested. The first value 1 represents the case when in each generation the of offspring vector components are inherited from the trial vector. The second value 0.5 represents a 50 % chance that the offspring vector inherits components from the parent vector. It has been reported that the optimization procedure is more sensitive to the chosen mutation factor than to the crossover factor [35]. The following table summarises the settings for control parameters tested for this study, to decide for best fitting values.

Table 4: Investigated Differential evolution control parameters.

Sections	2 Sections					
DE Control parameter	Mutation factor F		Mutation strategy		Crossover probability P	
	[0.2 1.5]	[0.5 1.25]	best2bin	rand1bin	0.5	1

### 3 Results

In this section the results of the synthetic data study will be presented, followed by the results of the experimental data study. The main focus of the results of the synthetic data study are on the effect of the different settings on the resulting displacement field and on the accuracy of the procedure. The results of the experimental studies also include the evaluation of the estimation procedures, and the visualisation and comparison of the resulting displacement fields with the experimental displacement fields.

#### 3.1 Results of synthetic data study

##### 3.1.1 Grid size

The evaluation of the optimization procedures with different grid sizes was based on the number of generations, the evolution of material properties, the value of the objective function at the end, and the deviation between GTD and estimated material properties.

Table 5 summarises the results of the grid study. The number of generations needed for the procedure is the same for grid 2 and grid 3, and fewer generations were needed to reach an end for grid 1. The resulting objective functions do not seem to follow a pattern between the different grids. The lowest objective function results with the smallest grid size, followed by grid 3, and the highest objective function results with grid 2.

There is no consistent under or overestimation of the stiffness parameters between the different grids, and there is an increased error in the  $c_{20}$  compared to  $c_{10}$  in each case. The highest errors occur when using grid 2.

Table 5: The results if the grid study.

Section	ROI		
	Grid 0.1x0.1	Grid 0.2x0.2	Grid 0.3x0.3
Grid			
Duration [hrs]	7	8	8
Generations	23	27	27
Objective function	0.012	0.023	0.015
$c_{10}$ [kPa]	98.6	100.8	98.7
$c_{20}$ [kPa]	1094.9	1116.2	1084.4
$\Delta c_{10}$ [%]	0.04	2.19	0.14
$\Delta c_{20}$ [%]	2.4	4.44	1.44

The evolution of material properties and objective functions for different grids show similarities, therefore the results for grid 1 are representing the procedure. Figure 17 and Figure 18 show the evolution of material properties and the corresponding objective function values respectively, with the indication of resulting parameters

with red markers. For the estimation procedures belonging to grid 2 and 3 see Appendix IV Figure 45 - 48.

The evolution of  $c_{10}$  and  $c_{20}$  show similar distributions. For both, the distribution of material properties covers the range between the search boundaries until iteration number 600, although in the case of  $c_{10}$  the mean value appears to be closer to the resulting value than in the case of  $c_{20}$ . After that, the deviation of material parameters appears to be close to the resulting value, however, the deviation seems to be lower in the case of  $c_{10}$  than for  $c_{20}$ . This type of behaviour will be referred to as convergence of the material properties. Convergence behaviour can be observed for the objective function value can be observed starting from iteration number 600.

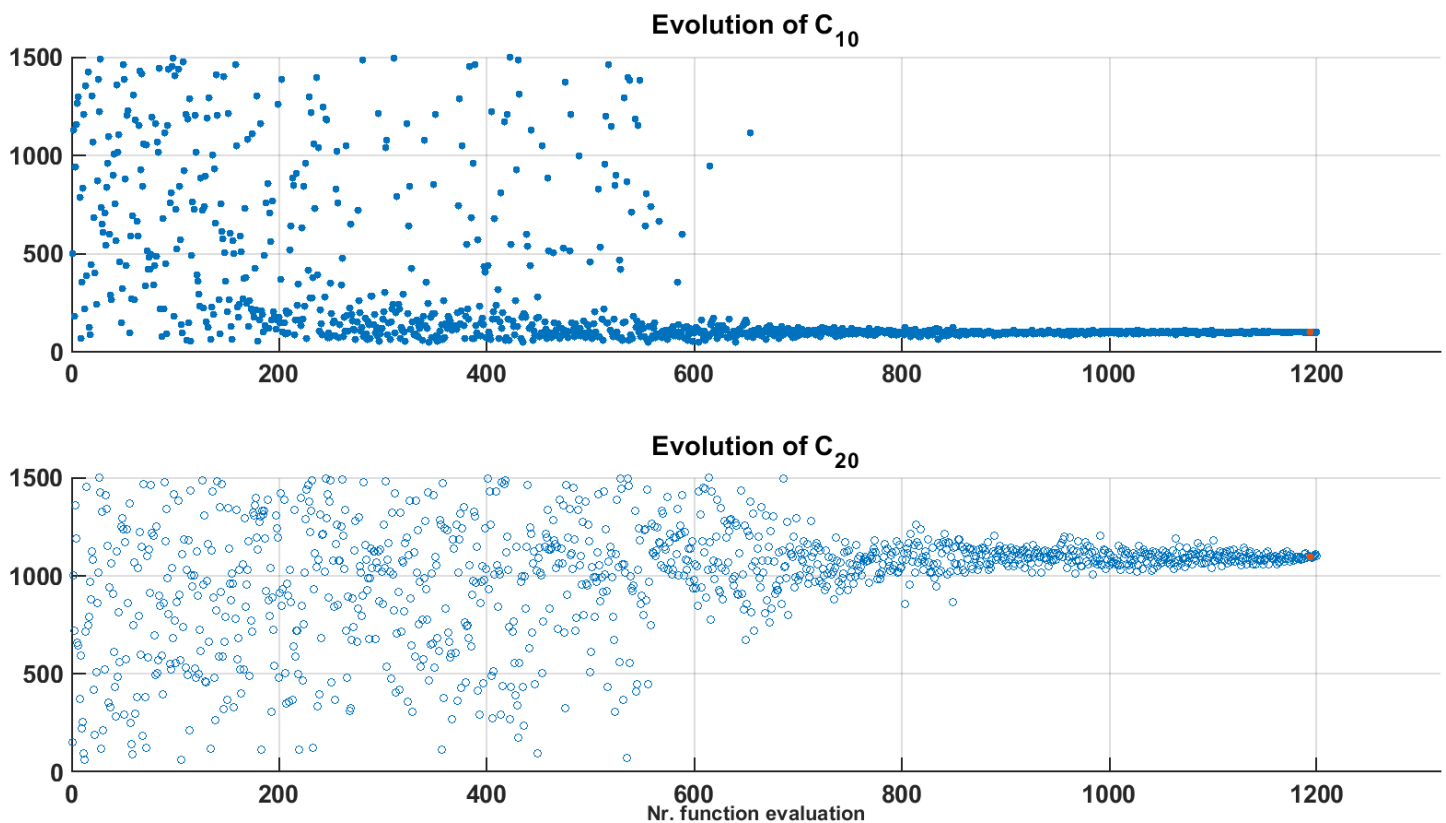


Figure 17: Evolution of material properties throughout the optimization procedure. Upper and lower panels show the evolution of  $c_{10}[kPa]$  and  $c_{20}[kPa]$  respectively. X axes show the iteration number and Y axes show the material parameters implemented in the FEA.

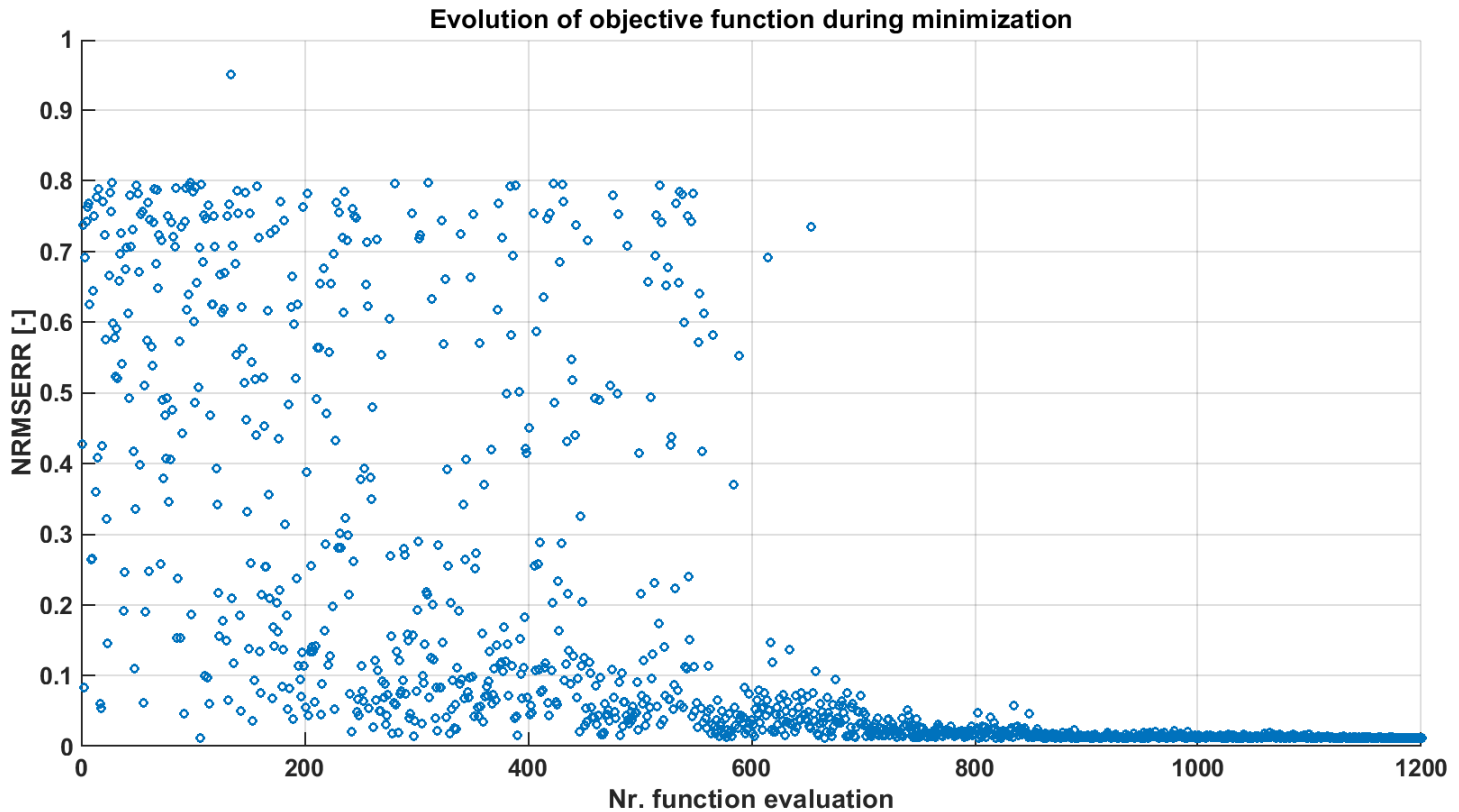


Figure 18: Evolution of objective function for grid 1 throughout the optimization procedure. X axis shows the iteration number and Y axis shows the resulting objective function (NRMSE [-]) to the corresponding set of material properties.

The resulting material properties were implemented into the FEM models and both the average grid values from the GTD and CD were visualised for comparison. Figure 19 shows the visualisation of the GTD (left) and CD (right) with the estimated material properties. The visual comparison of the results was based on the loading condition in step 1. The visual comparisons for loading steps 2 and 3 are included in the Appendix IV in Figures 49 and 51.

The size of the grid does not affect the visual comparisons of the displacement fields from the GTD, however, it has a great influence on the distribution of the CD. Due to the smaller number of nodes in the computational model, the finer grid of the CD results in multiple grid elements that do not contain any nodes. Grids that do not contain data from the GTD or the CD are excluded from the optimization procedure. Therefore the data is lost during the comparison if zero grids are present. The number of zero grids decreases when moving from  $0.1 \times 0.1 \text{ mm}$  (4865) to  $0.2 \times 0.2 \text{ mm}$  (47) and no zero grids are present with the grid size of  $0.3 \times 0.3 \text{ mm}$ .

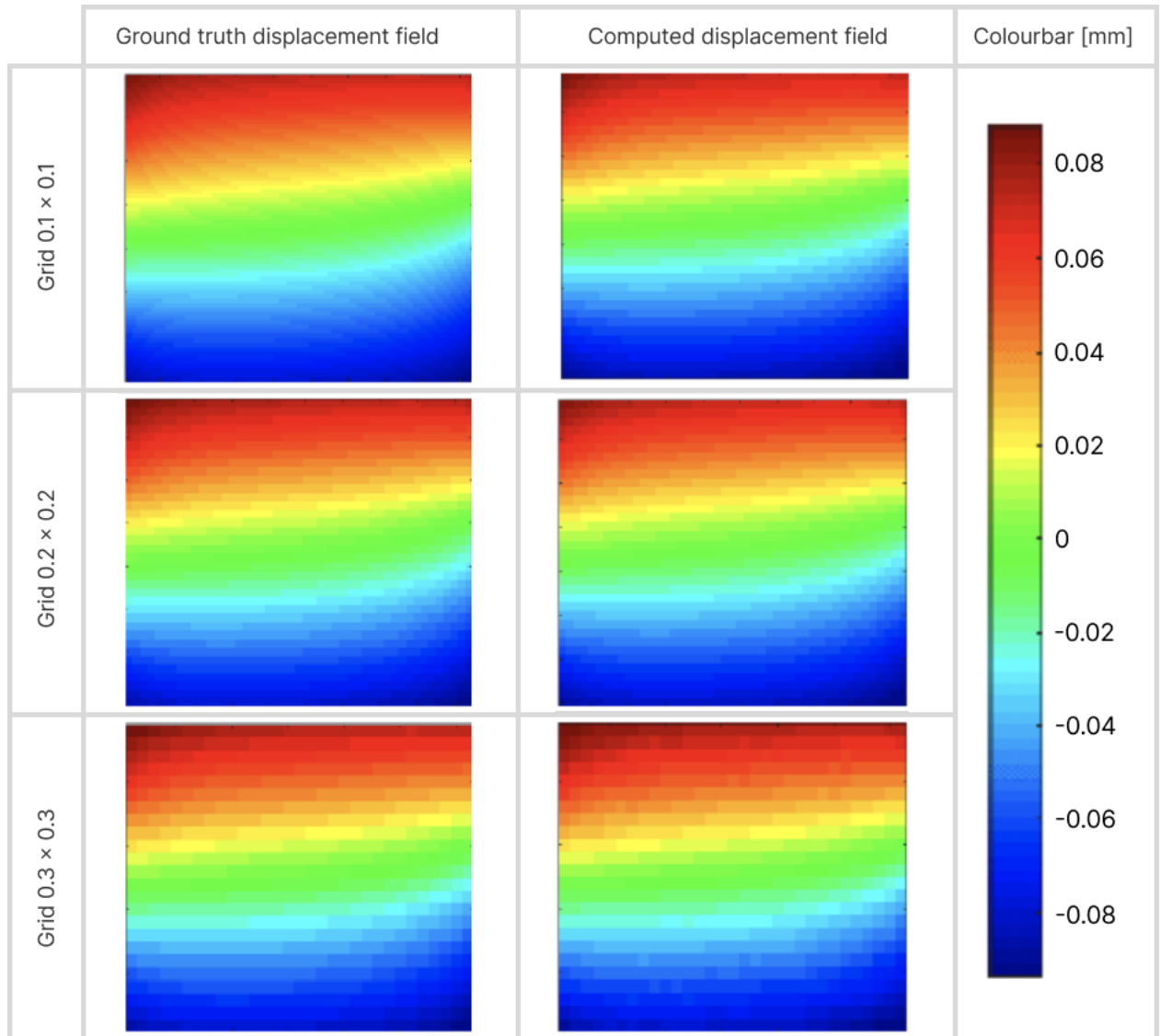


Figure 19: This figure shows the difference between the GTD (left) and CD (right) using different grid sizes. The results belong to the loading step 1.

In order to evaluate the difference between the resulting displacement fields the distribution of the displacement values along the upper edge of the ROIs for the different grid sizes were plotted. Figure 20 shows the distribution of displacements from GTD and CD with different grid sizes at loading step 1. The distribution of displacements for step 2 and step 3 are included in the Appendix IV in Figures 50 and 52. From the figure it can be seen that decreasing the resolution of the grid causes a change in the distribution of the displacement values. The average displacements decrease when increasing the grid size, due to larger area that is covered by the grid elements. The displacement values show a decrease when moving from the top towards the middle, hence the larger grid size results in a lower average displacement value per grid. It can also be seen that CD distributions are higher than the corresponding GTD distributions, the visual difference seems to be a manifestation of the objective function error. The difference between the curves belonging to grid 1 and 3 seem to be the of an equal amount, just like the objective function, and the difference between the curves from grid 2 appears to be the largest. Although grid 1 resulted with the same objective function value as grid 3 and performed bet-

ter than grid 2, in terms of resulting objective function an difference between GTD and estimated material properties, this grid size was excluded from further investigation due to the high amount of data loss caused by the low resolution of the grid size.

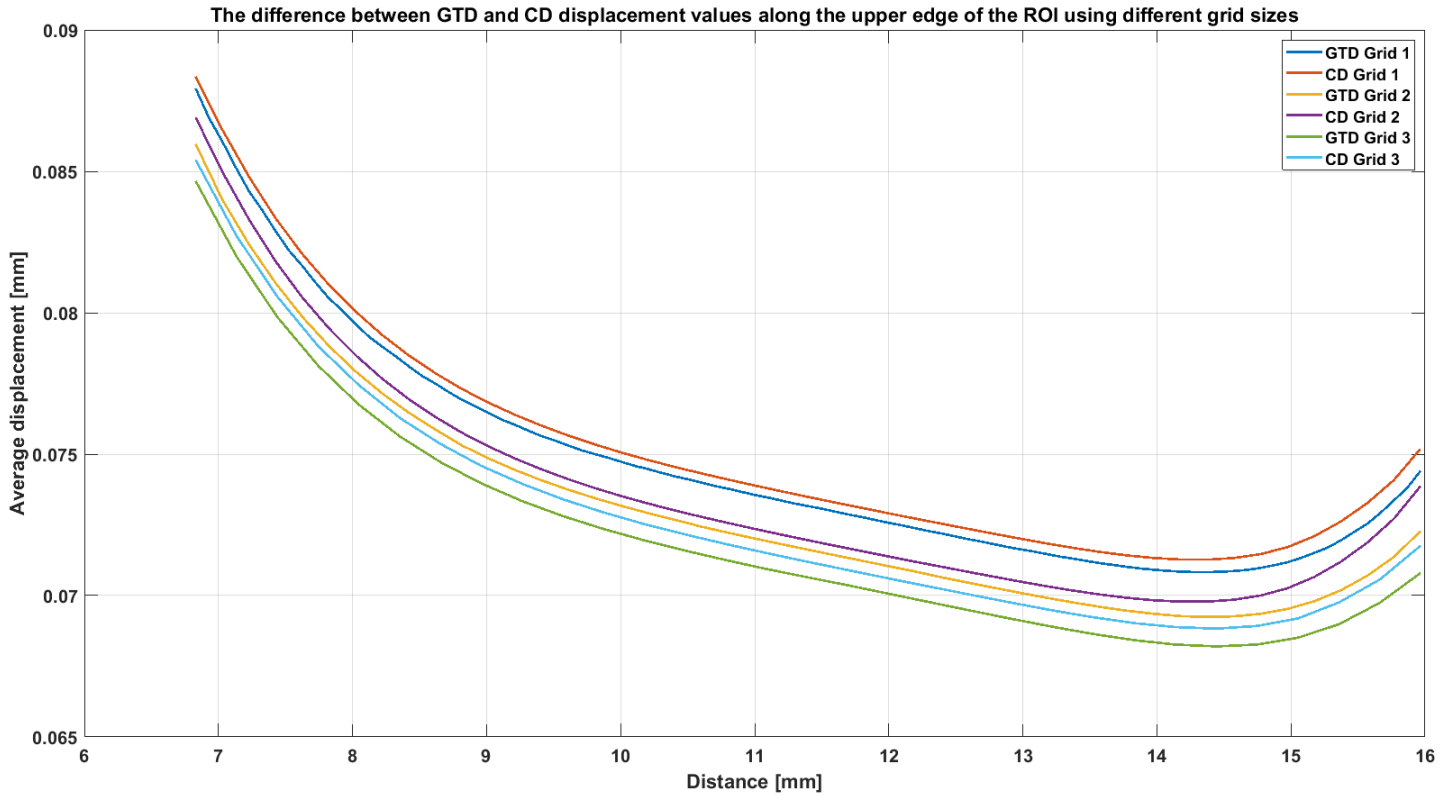


Figure 20: The average grid displacement along the upper edge of the ROI for different grid sizes. The curves show the distribution of displacements for the GTD data using different grid sizes and the resulting distribution from the computed displacement fields using the resulting material properties.

### 3.1.2 Effect of noise

The effect of noise was evaluated based on the same parameters as the effect of the grid size. The noise study was carried out using grid sizes  $0.2 \times 0.2$  and  $0.3 \times 0.3$  mm and the results are summarised in Table 6. The increased noise does lead to higher objective function values at the end of the optimization. This behaviour of the objective function concerning the noise was expected, due to the increased deviation from the GTD. There is no significant difference between the resulting material properties when noise is increased, which was expected based on the similar objective function values. Lastly, there is a continuous increase in the error of the second stiffness parameter in the case of grid 2. However, no such tendency can be observed in the case of grid 3.

Table 6: Summary of the results of the noise study. The section includes the ROI, zero percent noise was included as reference, duration, generations, resulting objective function and material properties as well as the error between GTD and estimated material properties.

Section	ROI					
	Grid 0.2x0.2			Grid 0.3x0.3		
Noise	0%	1%	2%	0%	1%	2%
Duration [hrs]	8	7	7	8	7	7
Generations	27	21	25	27	25	22
Objective function	0.023	0.024	0.026	0.015	0.016	0.019
$c_{10}$ [kPa]	100.8	100.3	100.6	98.7	99.2	99.3
$c_{20}$ [kPa]	1116.2	1118.9	1119.1	1084.4	1080.6	1080.0
$\Delta c_{10}$ [%]	2.19	1.7	2	0.14	0.6	0.7
$\Delta c_{20}$ [%]	4.44	4.67	4.68	1.44	1.09	1.03

The behaviour of the material properties and objective functions throughout the optimization procedure show great similarity to the results of the grid size study. The converging behaviour for the first material parameters occurs around the 650th iteration, and the convergence for the second parameter was pushed to iteration 800 when the noise was increased. The results are included in the Appendix IV in Figures 53 - 60.

The effect of the noise on the GTD was visualised using the distribution of the displacements along the upper edge of the ROI. The distribution of displacement values appears to be similar at high and low loading levels, therefore the distributions at loading step 1 are included here in Figure 21. The distributions at higher loading levels are included in the Appendix IV.

In Figure 22 the distribution of the computed grid displacements including 1 and 2 percent noise levels are compared to the GTD grid displacements. The average of one and two percent deviation from the GTD does not seem to have a visible effect on the distribution of displacement values along the ROI. The computed results with one percent noise appear to be close to the GTD values making them close to overlapping, while there is a visible difference for the values with two percent noise when compared to the GTD distribution.

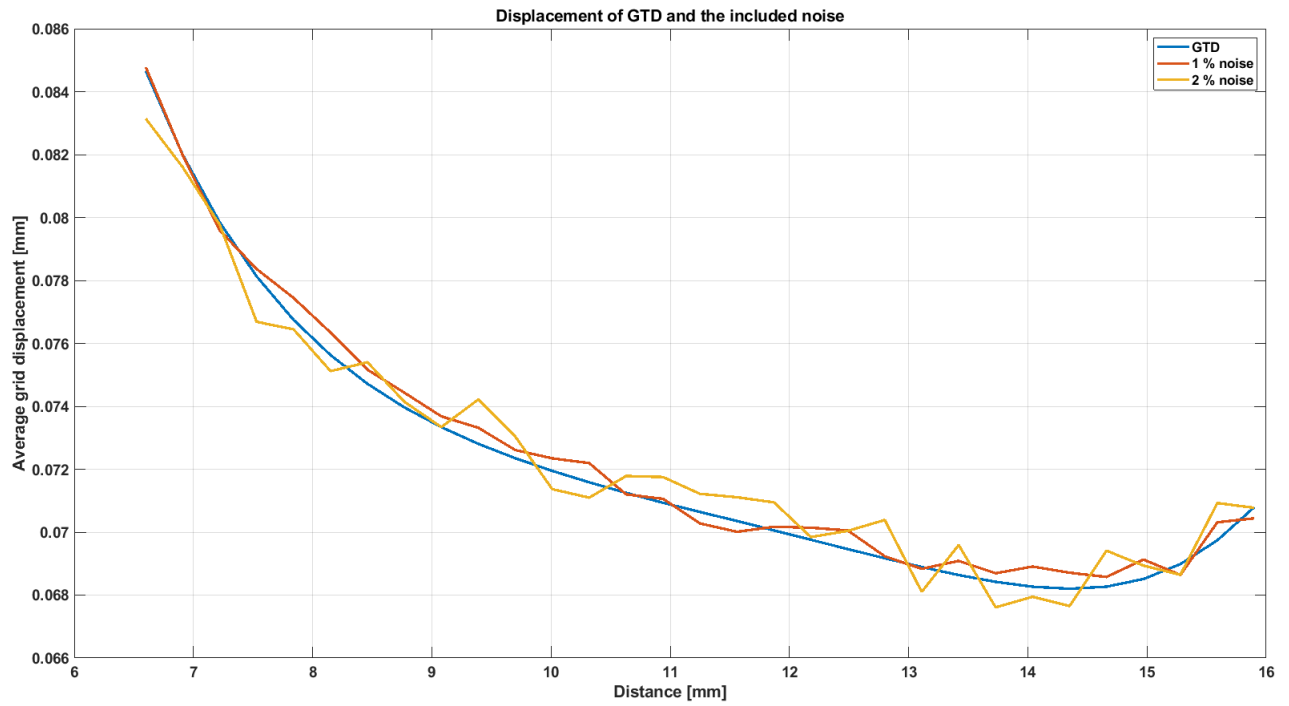


Figure 21: Distribution of displacement values along the upper edge of the ROI from the GTD (blue), and the altered GTD using 1 percent (red), and 2 percent (yellow) noise X axis shows the distance [mm] from the upper right corner of the ROI and y axis shows the average grid displacement values [mm].

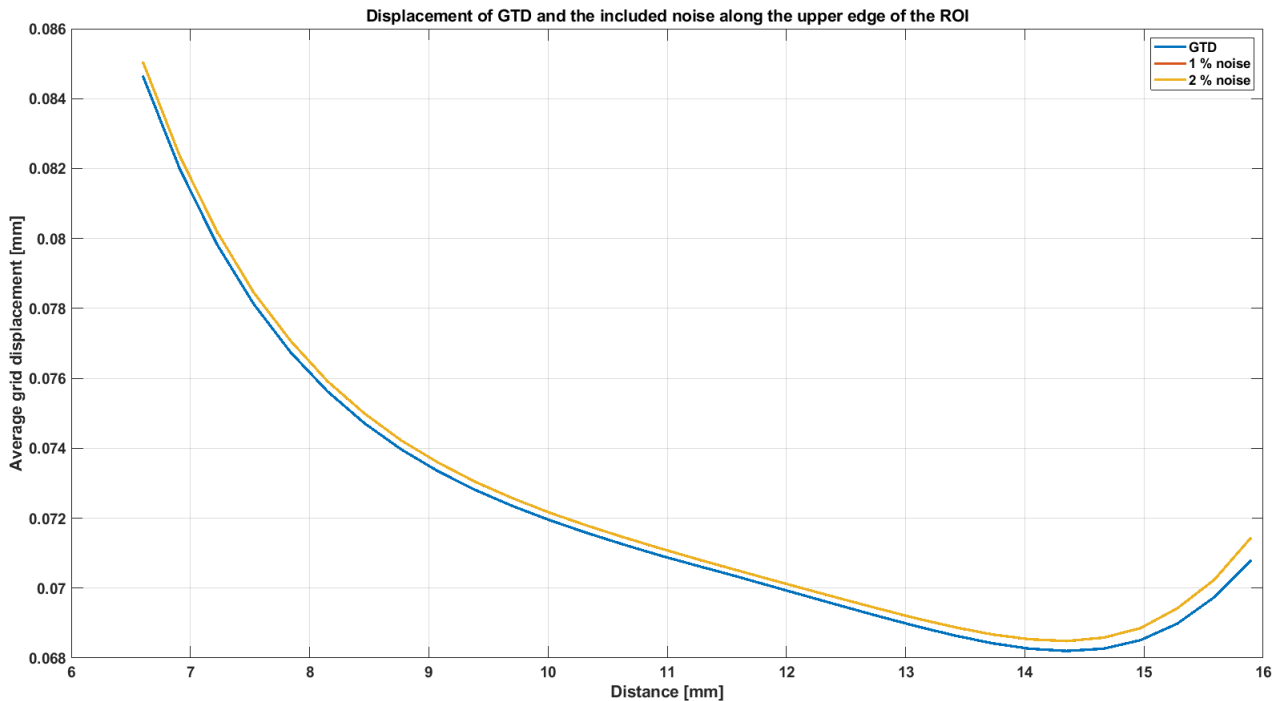


Figure 22: The difference between the grid displacement values for GTD and computed fields after estimation. Red and yellow curve belong to computed displacement using 1 and 2 percent noise respectively. The x axis shows the distance from the right upper corner of the ROI and the y axis shows the average grid displacement values [mm].

The noise does not seem to affect the estimation procedure and the results show little deviation from the GTD in the case of 1 percent noise. The implemented noise does not have different effects on the estimation procedure when using different grid sizes. For this reason, the section and the differential evolution control parameter study were carried out using 0.3x0.3mm grid and since the estimated noise from the experimental data did not exceed two percent noise, this level was implemented in the GTD for further investigations.

### 3.1.3 Number of sections

The effect of the dimensionality was evaluated based on the duration of the estimation procedure, the distribution of the objective function during the estimation, and the resulting objective function value. Table 7 summarises the results of the section study.

Table 7: Results of section study. The results of the ROI with grid 3 and two percent noise are included as a reference. The table compares the estimation procedures with an increased number of sections. The comparison includes the duration of the procedure, the number of generations, the resulting objective function and the resulting material properties.

Nr. Sections	ROI		2 Sections		4 Sections		6 Sections	
Duration [hrs]	7		17		48		96	
Generations	22		60		157		269	
Objective function	0.018		0.018		0.019		0.03	
Stiffness parameters	$c_{10}[kPa]$	$c_{20}[kPa]$	$c_{10}[kPa]$	$c_{20}[kPa]$	$c_{10}[kPa]$	$c_{20}[kPa]$	$c_{10}[kPa]$	$c_{20}[kPa]$
Section 1	99.3	1080.0	89.7	978.7	87.2	987.5	125.9	778.2
Section 2	-	-	106.3	1204.1	115.2	1127.9	117.2	922.8
Section 3	-	-	-	-	77.3	880.9	104.1	1036.6
Section 4	-	-	-	-	122.0	1324.0	80.1	1195.1
Section 5	-	-	-	-	-	-	126.1	960.5
Section 6	-	-	-	-	-	-	70.8	1127.0

The increase in computational time and objective function value was expected as it had also been observed in previous reports based on the effect of increased dimensionality [27, 28]. However, the resulting objective function values for one, two, and four sections do not seem to be different from each other. There is an increased objective function value in the case of six sections. Figure 23 shows the evolution of the objective function values throughout the procedure. In the case of one and two sections, high deviation occurs until mid and 2/3 into the optimization respectively. Afterwards, the objective function values appear to be distributed close to the resulting value. For the four-section, this behaviour is more difficult identify. Starting from iteration 5000 more values appear to be close to the resulting value, but the mean value appears to be higher than in previous sections. In the case of six sections, the mean of the objective values appear to decline until iteration number 6000, the deviation of values appears to cover the highest range among the procedures. One, two and four sections appear to have a lower limit which determines the minimum reachable difference between GTD and CD. This difference might be manifestation of error when using different element sizes. It can be seen in the mesh refinement study that although the difference is small, there is a deviation between the results of 0.03 mm mesh and 0.2 mm mesh. The 0.18 NRMSERR limit could occur due to this difference between the two models. No such lower limit can be seen in the case of six sections which might be due to the increased dimensionality of the objective function that resulted in a lower accuracy of the estimation procedure.

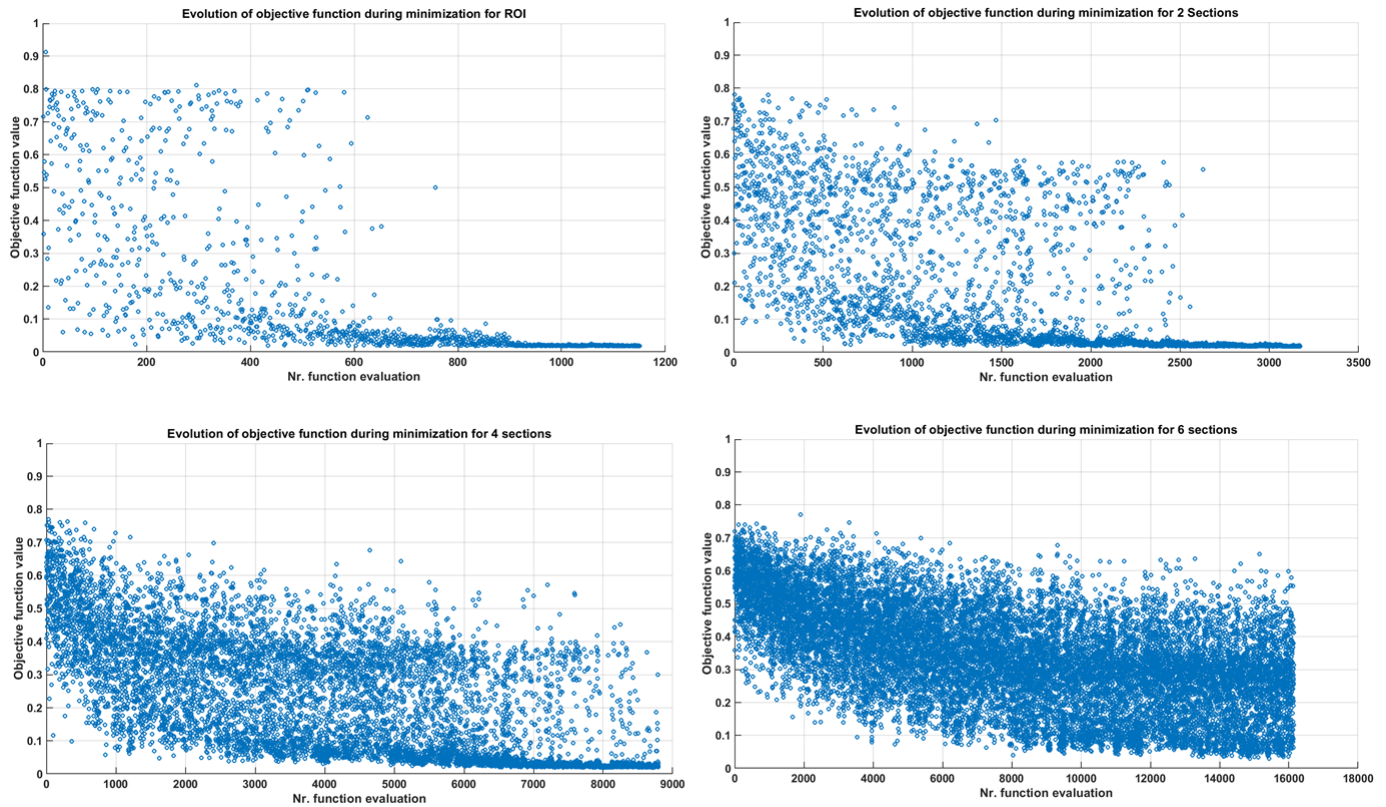


Figure 23: Objective function values throughout the optimization procedures for different sections. X axes show the iteration numbers and y axes show the objective function value corresponding to the iteration number.

### 3.1.4 Differential evolution control parameters

Table 8 below summarises the results of the DE control parameter study. It can be seen that the different settings for the DE control parameters affect the duration of the estimation procedure, but have little effect on the resulting objective function. The reference procedure when comparing the optimization procedures on the basis of the evolution of material properties and the evolution of the objective function belongs to the estimation procedure using  $F [0.5 \ 1.25]$ ,  $P=1$  and best2bin strategy. The Figures 85- 87 in the Appendix IV show the material properties and objective function values for the procedure.

Table 8: Results of DE control parameter study

Sections		2 Sections					
DE Control parameter		Mutation factor F		Mutation strategy		Crossover probability P	
		[0.2 1.5]	[0.5 1.25]	best2bin	rand1bin	0.5	1
Duration [hrs]		10	17	17	18	21	17
Generations		27	60	60	64	112	60
Objective function		0.018	0.018	0.018	0.018	0.018	0.018
Section1	$c_{10}$ [kPa]	87.8	89.7	89.7	89.5	86.8	89.7
	$c_{20}$ [kPa]	984.8	978.7	978.7	985.2	993.4	978.7
Section2	$c_{10}$ [kPa]	107.4	106.3	106.3	105.2	108.3	106.3
	$c_{20}$ [kPa]	1190.7	1204.1	1204.1	1204.9	1188.5	1204.1

### Mutation factor

Generally, the optimization procedure with F [0.2 1.5] required fewer generations than the procedure with [0.5 1.25]. This contradicts the expectation of the effect of the mutation factor. It was expected that a wider range for the mutation factor increases the number of generations. The distribution of material properties and the objective function are shown in Figures 112 and 113 in the Appendix IV.

There is similar narrowing behaviour of the parameters compared to what occurred in previous procedures. However, the converging behaviour occurs earlier in the procedure for F [0.2 1.5] than in the case of F [0.5 1.25]. The objective function follows the same behaviour as the material parameters. The optimization procedure resulted with the same objective function for both mutation factors. The increased range of mutation factors caused fewer iterations and faster occurring convergence of material property values.

### Mutation strategy

The mutation strategy affects the way in which the mutation procedure is carried out. Two strategies were investigated, rand1bin and best2bin. Figures 116 and 117 in Appendix IV show the distribution of material properties and the objective function for rand1bin.

Choosing random values for creating a target vector resulted in a longer estimation procedure, however, only four additional generations were required for the result. The estimated material properties and resulting objective function show little difference. The evolution of material properties seem to be affected in a way, that narrowing of the material properties occurred later in the procedure. The same can be said about the evolution of the objective function regarding the distribution of the values throughout the procedure. Choosing the best fitting value for creating offspring seems to require lower generation numbers.

### Crossover

The crossover probability affects the propagation of low objective function value into the next generations. Generally a higher  $P$  value results in a faster convergence around the global minimum. Therefore, it was expected that lowering the crossover probability will result in a longer estimation procedure.

Figures 114 and 115 in Appendix IV show the distribution of material properties and the objective function throughout the optimization belonging to the procedure using  $P = 0.5$ . The number of generations has doubled when using  $P = 0.5$  com-

pared to the  $P = 1$ . The narrowing of the material properties occurs at later stage of the procedure for  $P = 0.5$  than for  $P = 1$ .

The decreased crossover probability value seems to only affect the duration of the procedure. The objective function decreases throughout the procedure (Figure 115), with high values and deviation occurring at the beginning of the optimization and low values with smaller deviation from iteration 5000 onwards.

## 3.2 Results of experimental data study

### 3.2.1 Global material properties

Global material property estimation was carried out successfully to find an initial estimation of the material parameters. The optimization procedures stopped because the tolerance criteria were reached. This means that the objective function energies in the last generation were within 1 percent deviation from the mean energy [24]. This occurred after 13 generations for the fibrous cap and after 14 generations for the fibrous cap + SI models. The procedures took approximately 5 hours from start to end. The objective function value reached 0.25 NRMSE in the case of the fibrous cap and 0.27 for the fibrous cap+SI model. This error occurs when the displacement values resulting from three steps were implemented in the objective function during the optimization. The objective function value for each step, calculated with the resulting material properties shows a decreasing trend, with the highest occurring value at step one and the lowest at step three. Table 9 summarises the results of the global material property estimation.

Table 9: Summary of the results for global material property estimation.

Sections		Global material properties	
Sample		Fibrous cap	Fibrous cap + SI
Duration [hrs]		5	5
Generations		13	14
Estimated material properties [kPa]	$c_{10}$	462	447
	$c_{20}$	1498	1494
Objective function in step 1		0.72	0.70
Objective function in step 2		0.33	0.30
Objective function in step 3		0.21	0.20
Objective function total		0.25	0.27

The evolution of material properties and objective function for the two models can be found in Figures 130 - 133 in the Appendix V. The convergence in the  $c_{10}$  value appears to start around iteration number 300 and 375 for the fibrous cap and fibrous cap + SI sample respectively, however no convergence behaviour can be observed in the second material property ( $c_{20}$ ) for neither of the samples and they appear to be selected randomly. This might indicate that the second material property does not have a strong influence on the resulting displacement field. Figure 24 shows the boxplots of the  $c_{10}$  and  $c_{20}$  values during the estimation procedure for both of the samples. The whiskers are set to show the minimum and maximum values while the

top and bottom edges of the boxplot portray the 75th and 25th percentiles respectively. The red mark indicates the median of the values falling between the top and bottom percentile.

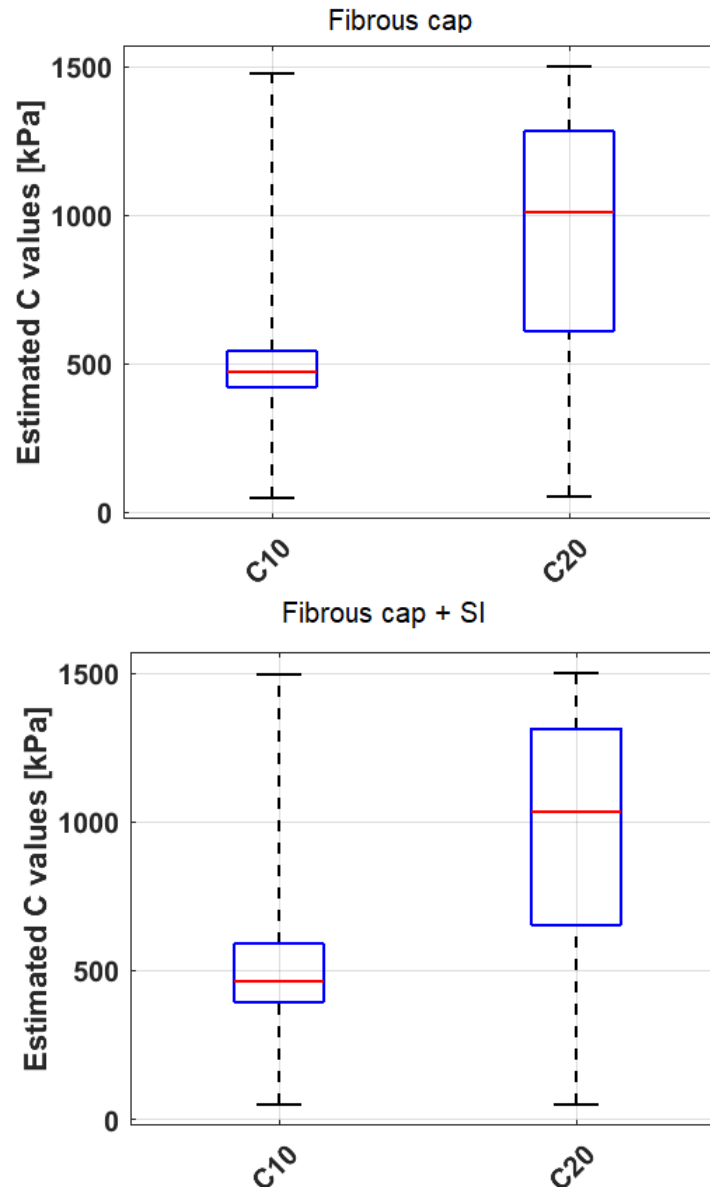


Figure 24: Boxplots for both material parameters throughout the procedure for fibrous cap (top) and fibrous cap + SI (bottom).

The distribution of the objective function shows converging behaviour towards a minimum value for both of the models. However, a higher limit to the objective function can be observed similar to the one reported in the synthetic data study. The higher limit can be caused by several factors. Firstly the accuracy of the mechanical model is a determining factor in reaching a minimum difference between experimental and computed data. Secondly the effect of the linearisation step in the FEM when calculating results for the nodes also has an influence on the minimum difference reachable between the two data sets.

The resulting material properties were implemented in the mechanical model and

the resulting displacement fields were generated. Afterwards, the average displacement values per grid were used for visual comparison. Figure 25 displays the average displacements per grid from the experimental data and the computed data for the fibrous cap and fibrous cap + SI models respectively. The figures visualise the displacements in the different loading steps.

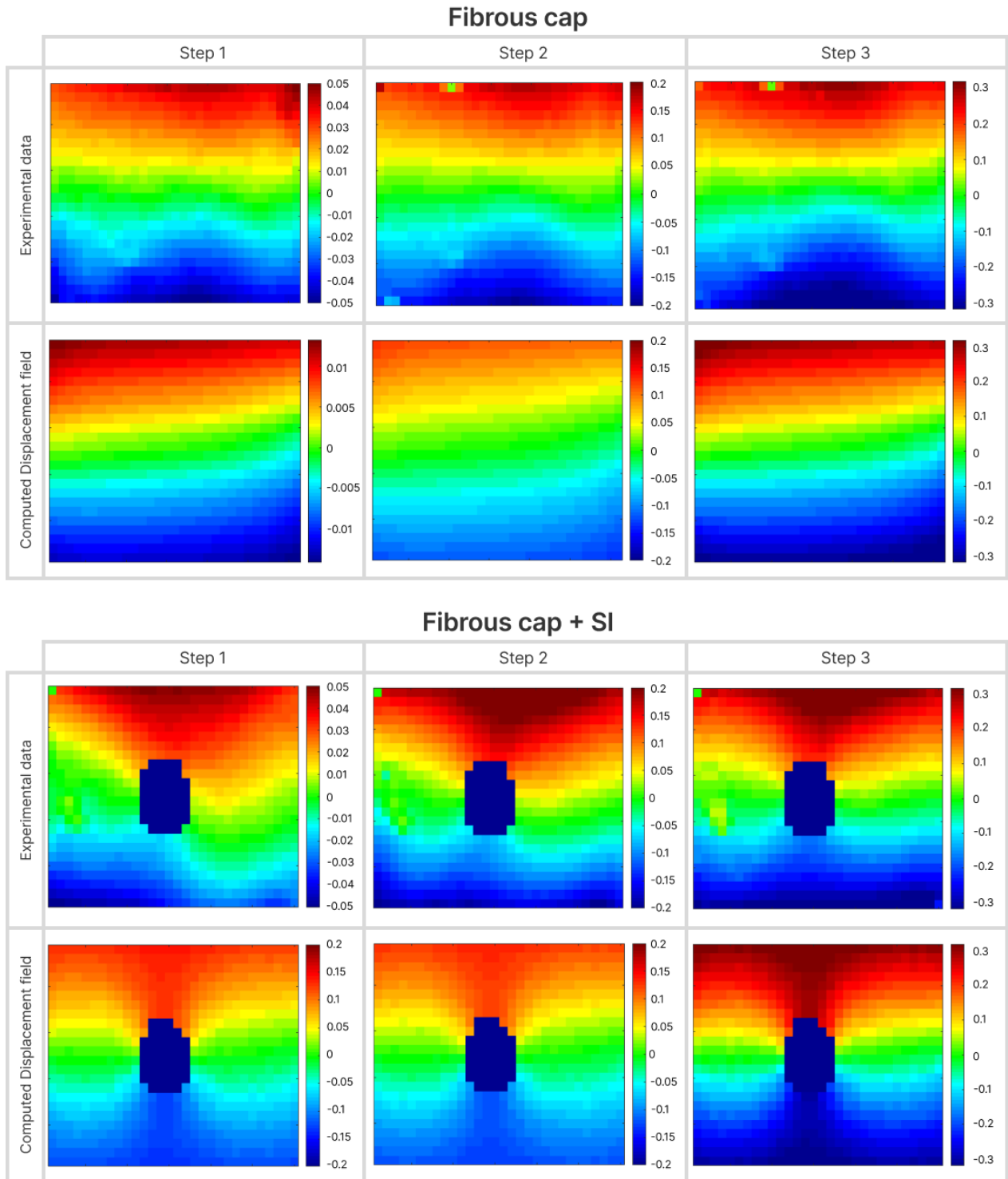


Figure 25: Visualisation of the experimental and computed displacement field in the ROI. The top row shows the distribution of the experimental data in each grid. The bottom row shows the computed displacements in each grid, using the resulting material properties at the end of the optimization. Different columns show the displacement fields at different loading levels. Due to the larger difference in the resulting displacement fields at step one, the colour bars show different scaling and range of values.

The experimental displacement field for the fibrous cap is characteristic for uniaxial tensile tests where both edges of the samples are displaced. The highest global

absolute values occur at the top and bottom edges of the sample. The middle part of the samples contains the neutral zone, where the lowest absolute values occur.

The displacement field shows several local minima and maxima in both the top and bottom sectors of the ROI. This wavy distribution is more prominent in the bottom section. Local minima and maxima might be caused by local heterogeneity in the sample. The transition between the neutral zone and the top seems to begin at the same distance from the horizontal axis. The position of the neutral zone appears to be constant in each loading step.

The computed displacement field of the model shows great similarity to the experimental field. Low and high absolutes on the top and bottom parts, however, no wave-like distribution can be detected in either of the sectors. The neutral zone is present in the middle, yet the transition to the top sector is shifted upwards. This distribution behaviour might be caused by asymmetrical geometry of the sample. The range of displacement values between experimental and computed fields corresponds the best at step 3, followed by step 2. In step 1 the maximum in the experiment field is six times the maximum from the computed field, however this is the step where the lowest displacement values occur in both experimental and computed data. The reason for the higher objective function value at step one can be related to the low displacement values at the loading step. It might be that due to the linearisation method that, the approximated results from the FEM reach their limit at lower loading steps to create a better match between experimental and computed displacements.

The fibrous cap + SI model shows similar displacement distributions in the experimental displacement field to the other sample. With high global absolute values on the top and bottom sectors and a neutral zone in the middle. There appears to be a local minimum in the high absolute zones, which are located above the SI. The location of the minima above the SI seems to be shifted to the right side. The neutral zone seems to be shifted upwards on both sides of the SI compared to the experimental results. This might be due to the presence of the softer region, or due to the asymmetrical geometry of the model. The transition from the neutral zone to the top zone appears to be shifted up as well.

The computed displacement field appears to be more symmetrical than the experimental displacement field. The width of the neutral zone seems to be of the same size on both sides of the SI. Both local minima in the high absolute zones were captured, however, they appear to be located above and below the SI. Generally, we can see that the displacement values in step 1 cover different ranges between the experimental and computed fields. This trend can be seen in both models.

In order to quantify the differences between the computed and experimental displacement fields, the absolute differences were plotted along the second row of the ROIs. This position was chosen because the experimental displacement fields contain values along the top edge which do not fall in line with the rest of the values. These values were marked as green, and they appear due to missing values from the DIC recordings. Figure 26 and 27 show the distribution of the differences for fibrous cap and fibrous cap + SI respectively. The absolute difference between experimental and calculated displacement values for step 1 varies between 0.019 and 0.039 mm for both models. The low absolute differences in this step might be the reason for the high normalised error during the optimization. The distribution of the difference for step 2 shows a decreasing tendency when moving along the horizontal line towards

the middle. The difference increases in the middle of the section, resulting in a local maxima, after which the difference decreases again. After a local minima the difference increases again. The difference in step 3 shows one global maxima in the middle of the selected line. The absolute difference for the fibrous cap model seems to be lower than the one belonging to the fibrous cap + SI model.

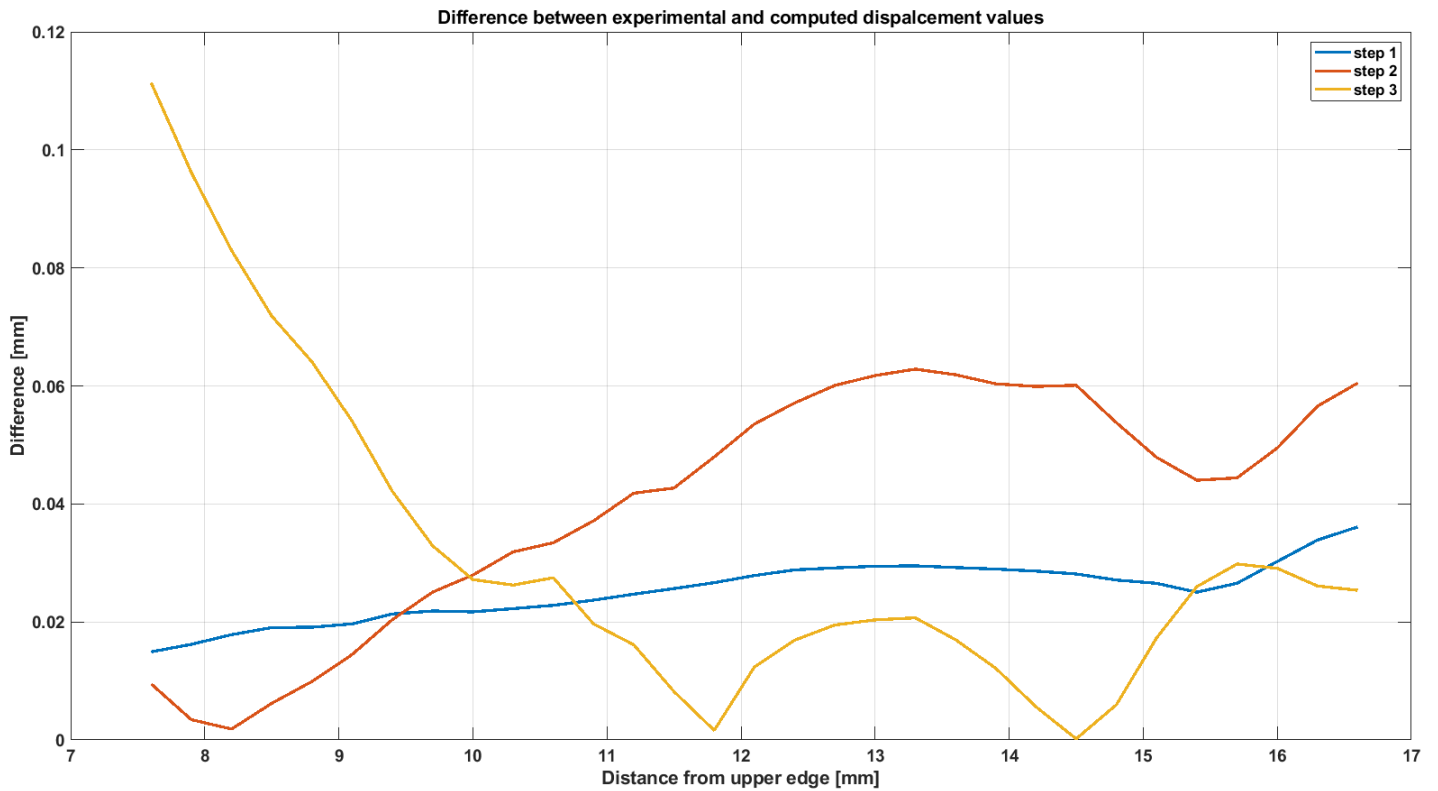


Figure 26: The distribution of absolute difference in mm along the selected line from the ROI for the fibrous cap model. Blue represents step 1 red and yellow represent step 2 and step 3 respectively. The X-axis shows the distance in mm along the second row in the ROI. The Y-axis shows the difference between the grid values from the experimental and computed fields.

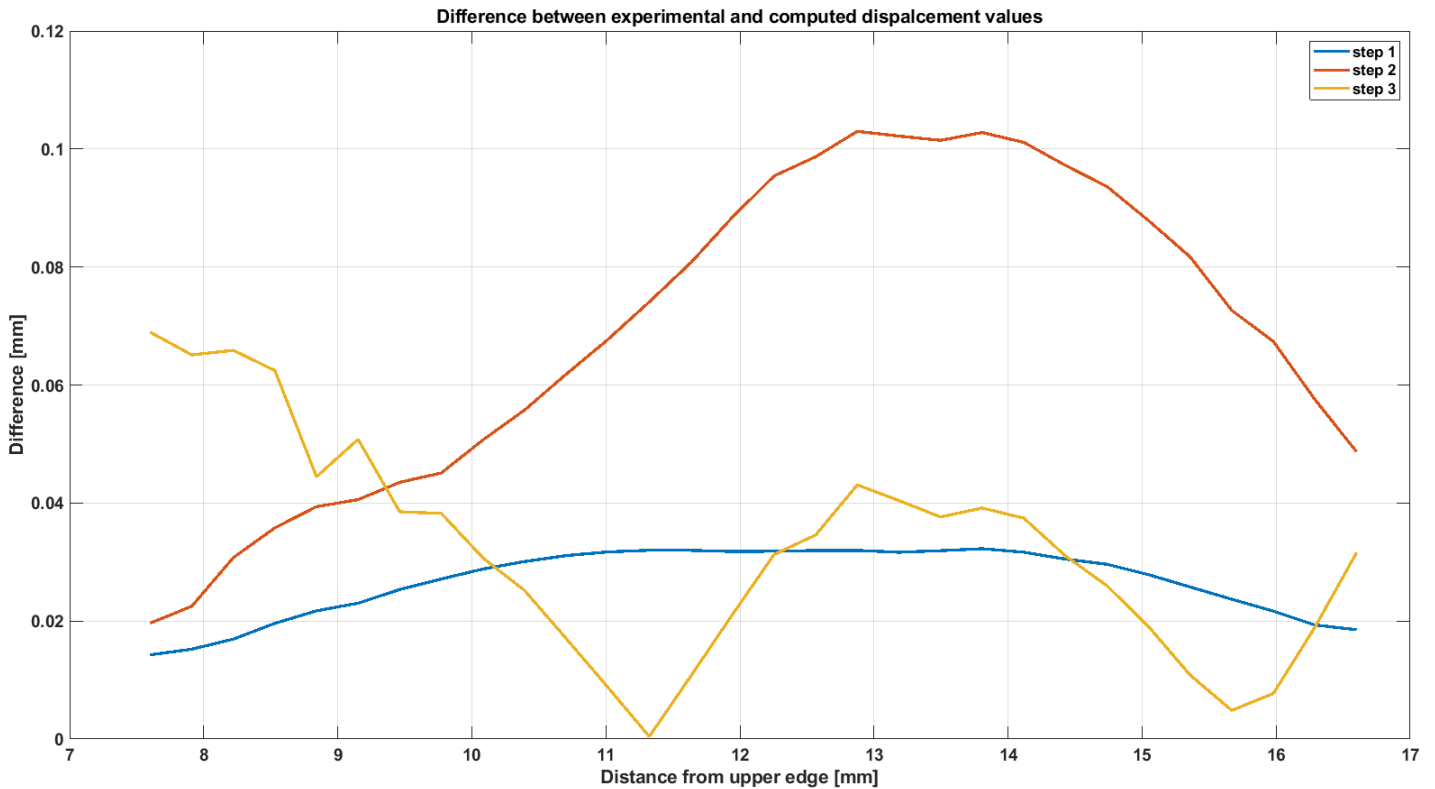


Figure 27: The distribution of absolute difference in mm along the selected line for the fibrous cap + SI model. Blue represents step 1 red and yellow represent step 2 and step 3 respectively. The X-axis shows the distance in mm along the second row in the ROI The Y-axis shows the difference between the grid values from the experimental and computed fields.

The computational models appear to capture the global distribution of the displacement field. The iFEM converged for the first material parameter ( $c_{10}$ ), but no convergence was reached for the second material parameter ( $c_{20}$ ). The implemented parameters in the computational models lead to global mechanical behaviour similar to the experimental displacement field, but, local differences were not captured with this procedure.

### 3.2.2 Local material property estimation

Local heterogeneity within the models was explored by applying the different number of sections. This part contains the summary of the estimation procedures for both samples, followed by the visual comparison of the resulting  $c_{10}$  stiffness values. After that, the visual comparison of the displacement and the quantitative evaluation of the resulting displacement fields are portrayed.

The results of the local material property estimation are summarised in Table 10. The duration of the estimation procedures increased with an increasing number of parameters. The optimizations for the fibrous cap model with two and four sections stopped after the tolerance criteria was reached. In the case of six sections, the optimization was aborted manually. Seeing as the optimization failed to converge to a minimum value after multiple restarts, no further attempts were made and the material parameters resulting with the lowest objective function were selected to represent the results. All estimation procedures for the fibrous cap + SI model terminated successfully when the tolerance criteria was reached. In both models step three was estimated with the lowest objective function value, followed by step two and then step one. The evolution of material properties and the objective function during the procedure are included in Appendix V in Figures 134 - 163.

Table 10: Summary of the results of local parameter estimation for both samples. The material properties marked with \* belong to manually terminated procedure.

	2 Sections		4 Sections		6 Sections		
	Fibrous cap	Fibrous cap + SI	Fibrous cap	Fibrous cap + SI	Fibrous cap	Fibrous cap + SI	
Duration [hrs]	6	6.5	15	13	72	83	
Generations	15	17	47	42	118	99	
Objective function in step 1	0.72	0.52	0.72	0.51	0.66	0.52	
Objective function in step 2	0.34	0.32	0.33	0.29	0.29	0.30	
Objective function in step 3	0.20	0.17	0.20	0.17	0.20	0.17	
Objective function total	0.26	0.25	0.25	0.23	0.24	0.23	
Section 1	$c_{10}$	585	864	513	885	918 *	585
	$c_{20}$	1470	1443	1330	1304	1231 *	1230
Section 2	$c_{10}$	379	178	429	319	942 *	323
	$c_{20}$	1440	1496	974	1094	225 *	147
Section 3	$c_{10}$	-	-	712	777	151 *	1055
	$c_{20}$	-	-	1425	1449	1398 *	1425
Section 4	$c_{10}$	-	-	320	102	60 *	314
	$c_{20}$	-	-	1097	1458	1418 *	1580
Section 5	$c_{10}$	-	-	-	-	1288 *	612
	$c_{20}$	-	-	-	-	801 *	500
Section 6	$c_{10}$	-	-	-	-	766 *	85
	$c_{20}$	-	-	-	-	909 *	1484

The  $c_{10}$  parameters appear to show convergence behaviour for two and four sections, for both of the models, however no convergence can be observed in the case of six sections. The  $c_{20}$  parameter did not converge in any of the cases. For this reason, and because the first parameter is the determining factor describing the stiffness of the model, the visualisation of the distribution of the local material parameters will only be based on the first parameter only. The figure 28 shows the estimated  $c_{10}$  values in kPa.

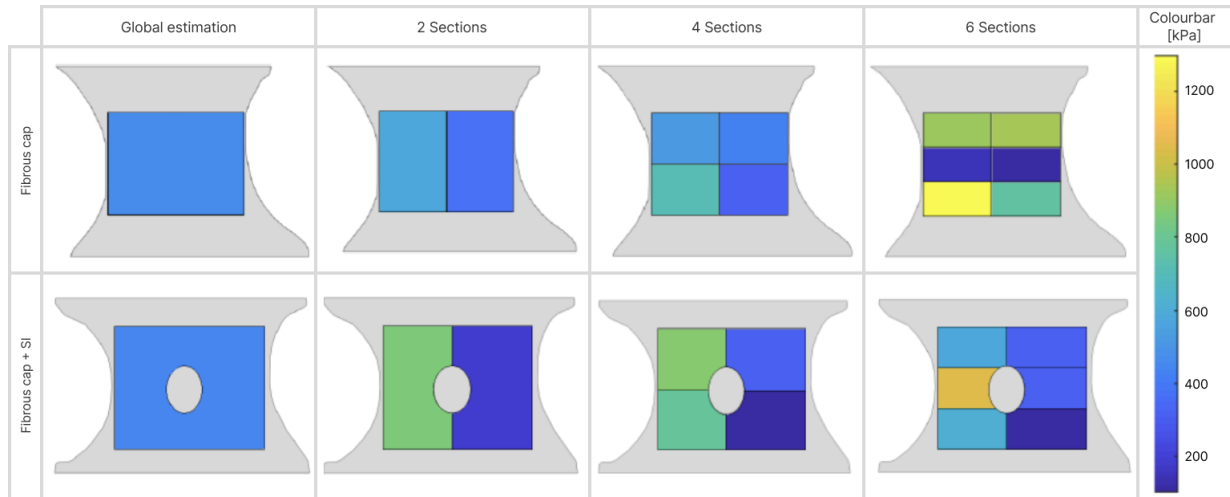


Figure 28: Visual representation of the resulting  $c_{10}$  values for each sections. The upper row shows the fibrous cap structure, the lower includes the sample with SI. Stiffness values are represented in kPa.

The estimated parameter on the left side of the model appears to be higher than on the right side. This tendency can be seen for both samples in the case of two and four sections. The left side of the fibrous cap model appears to be softer than the left side of the fibrous cap + SI model. The right side of the fibrous cap model however seems to be estimated to be stiffer than the same side on the fibrous cap + SI model. The model with four sections reveal differences between the local material properties from the top and bottom of the samples. The bottom-left section (Section 3) was estimated with the highest stiffness from the fibrous cap model, and the top left (Section 1) was the stiffest for the fibrous cap + SI model.

In the case of the fibrous cap model with six sections, the local estimation reveals a soft middle section at the region at the region of the displacement field where the lowest displacement values occur. As well as relatively stiffer top and bottom sections, with the stiffer region located on the bottom left side of the model. Six sections for the fibrous cap + SI model reveal a stiff mid-region on the left side and a soft region on the right corner of the model. The visualisation of the resulting displacement fields is portrayed in Figure 29. The comparison contains the experimental displacement field and the results of the global estimations in the first and second row. Below that the results for two, four, and six sections are shown. Loading step 3 was selected for the visual representation of the displacement fields. The displacement fields belonging to step 1 and step 2 are included in the Appendix V in Figures 164 and 167.

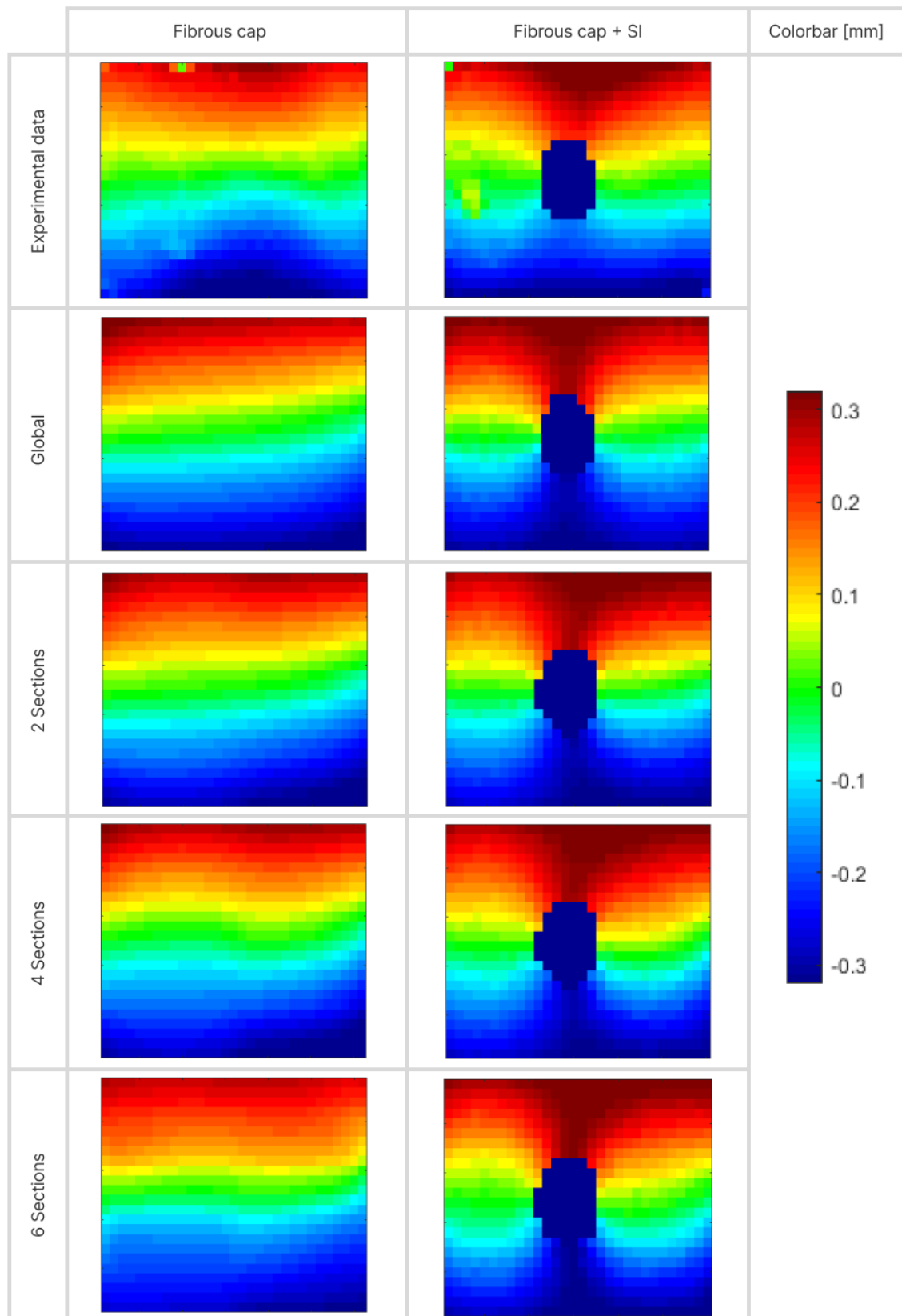


Figure 29: Visual comparisons of the resulting displacement fields with different sections. The top figure shows the experimental displacement field. Below that the figure shows the results for global, two, four, and six sections models. The range of displacement values agree the most at loading level three, therefore the visual comparison was based on this level. The colour bar on the right shows the range of values in mm.

The displacement fields appear to show little difference from the global estimation in the case of two sections for both of the models. For the fibrous cap model, the neutral zone appears to be shifted higher upwards, compared to the displacement field after global estimation. This might be the effect of the asymmetrical shape and the softer  $c_{10}$  values on the right side.

The neutral zone in the fibrous cap + SI model with 2 Sections appears to have different widths on the left and right sides. Additionally the transition zones cover different ranges of displacement values on the different sides.

In the case of 4 Sections, the fibrous cap model appears to be able to capture the wave pattern of the neutral zone. Local maxima and minima seem to be present in the transition zones.

The 4 Section fibrous cap + SI model shows a similar distribution, however, the neutral zone appears to point upwards on the right side, while on the left side it remains more horizontal. This might be due to the stiffer top on the right side of the model.

The resulting displacement field for the fibrous cap model with 6 sections also captures the wavy pattern caused by local maxima and minima, however the effect is less prominent than in models with fewer sections.

For the fibrous cap + SI model the position and distribution of the zones appear to align between the experimental and the 6 Sections model. There is a wider neutral zone on the left side, with localised minima and maxima in the transitions. The neutral zone on the right side slants upward and appears to be wider than of the 4 Sections model.

In order to evaluate the differences between the displacement fields from the experimental data and the model with different sections, the distribution was plotted along the second row from the top to the top edge. Figure 30 shows the comparison of the distributions of the displacement fields belonging to loading step 3. The distributions from step 1 and step 2 are included in the Appendix V in Figures 165 - 166 and Figures 168 - 169.

Figure 30/A shows the distribution of displacements from the fibrous cap model, and the distributions in Figure 30/B belong to the fibrous cap + SI model. The displacement values for both fibrous cap and fibrous cap + SI models cover the same range of values as the experimental values. The experimental displacement values of the fibrous cap sample show a global maximum around the middle section of the sample, however, the computed displacements show different distribution. The distribution after the global estimation (red) shows the smallest agreement with the experimental distribution. This was expected because the experimental displacement fields suggest heterogeneous distribution of material properties, but during the global estimation the model was assumed to be homogeneous. Introducing sections with independent material properties increases the accuracy of the distributions. The model with 2 Sections introduces local minima and maxima and the agreement between computed and measured displacement seems increase with increased number of independent sections. The highest deviation from the experimental displacements are found on the left side of the computed distribution. The position of the local maxima from the computed distributions after the saddle point are close to the global experimental maxima.

The distribution of displacement values from the fibrous cap + SI models seems to be closer to the experimental distribution than those of the fibrous cap model.

Both experimental and computed displacement fields have a global maximum in the middle of the investigated area. Differences occur at the edges of the curves, the middle section appears to agree between the experimental and computed data. The globally estimated distribution (red) is lower than the displacements belonging to the local estimations. Introducing additional sections in the model seems to increase the accuracy of the estimation procedure.

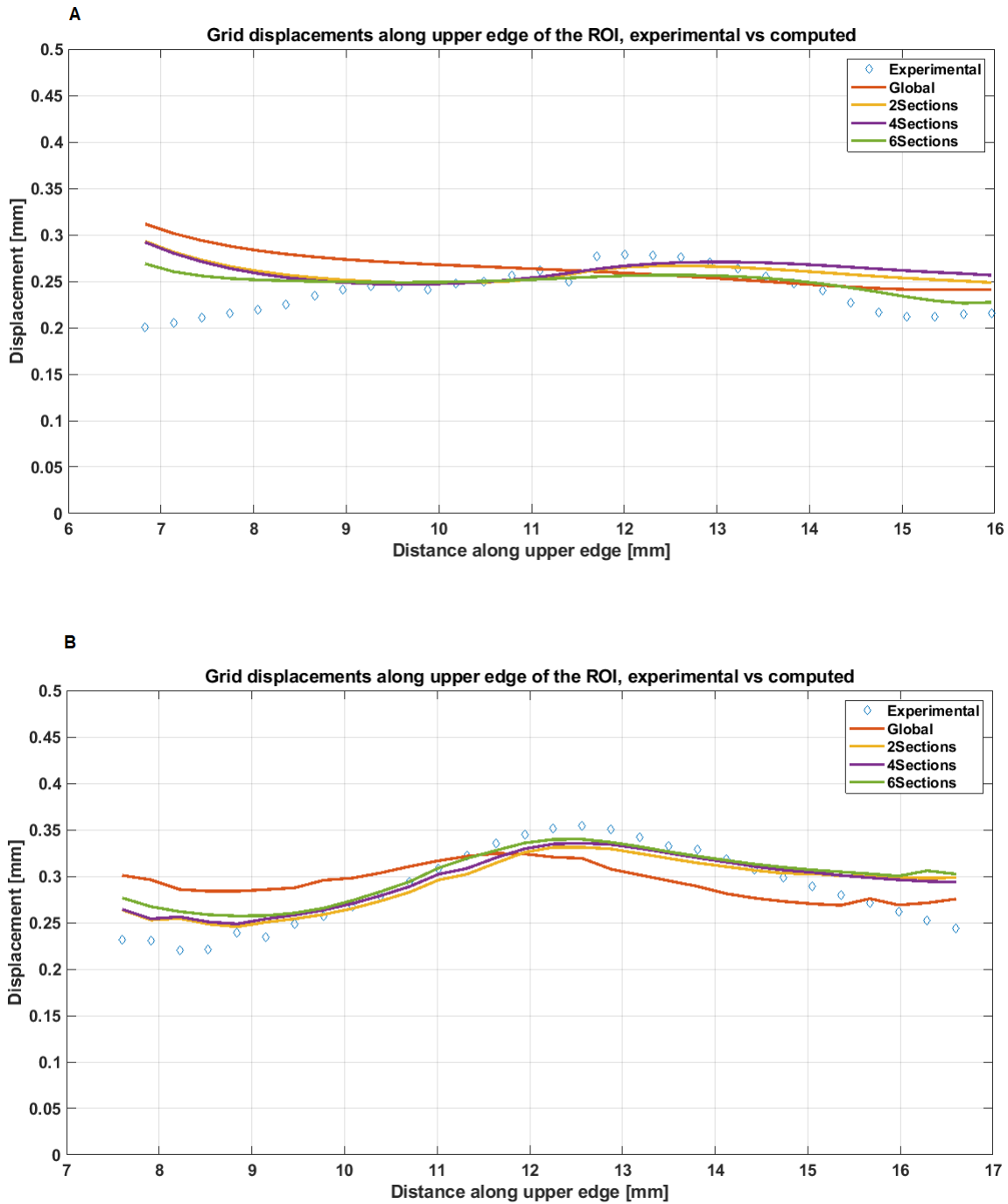


Figure 30: The distribution of displacement values along the selected line from the experimental (blue), the globally estimated displacements (red), the locally estimated models (yellow, purple green), for two, four, and six sections. The top panel shows the distributions belonging to fibrous cap model, the bottom panel shows the distribution belonging to fibrous cap + SI model. The X-axis shows the position along the selected row along the ROI and Y axis show the average grid displacement [mm].

## 4 Discussion

The main goal of the study was to create a pipeline for mechanical characterisation of tissue-engineered fibrous cap structures with different structural components. In addition to examining the global mechanical characteristics, the study investigated local heterogeneity by performing local characterisation of mechanical properties. This novel method for investigating material properties combines the measured displacement field with DIC during uniaxial tensile test, FEM modelling, and the use of Differential Evolution algorithm. Prior to the usage of experimental data, the pipeline was tested using synthetically generated data, to find optimal settings for control parameters.

### 4.1 Synthetic data study

The synthetic data study aimed to determine the effect of grid size, the amount of noise from the DIC, the number of independent characterised sections, and the DE control parameter settings. In this section, the results of the grid, noise, sections, and DE control parameter studies are discussed respectively.

#### 4.1.1 Grid study

There were no recommendations found regarding the size of the grid in iFEM pipelines, therefore it was important to investigate the effect of grid size on the estimation procedure, in order to find the optimal parameter for this study.

The effect of grid size on the estimation procedure can be explained when looking into the ratio between the data points from the GTD and the CD.

With the 0.1x0.1mm grid size, the grid elements from the GTD contained on average 16 data points. The grid elements from the CD contained one data point per grid. Due to the high resolution of the grid, the majority of CD grid elements did not contain entrees, therefore more than half of the displacement values were excluded from the comparison.

In the case of Grid 0.2x0.2, the resolution of the grid lead to the same amount of data points as using the finer grid, but with a lower ratio between the displacement values. Due to the lower resolution of the grid the ratio was reduced to 49 to 1 between GTD and CD. The objective function yielded the highest value when using this grid, which indicates that the ratio between the data points is the influencing factor on the resulting objective function.

Using the Grid 0.3x0.3, the average data point ratio between GTD and CD was 25 to 1, which is closer to the ratio of using Grid 0.1x0.1mm. However, unlike the Grid 1 there were no zero grid elements created in the Grid 0.3x0.3mm. Interestingly the objective function yielded the same value with the finest as with the coarsest mesh, which indicates that the size of the data that gets compared is less of a determining factor in the procedure.

Considering the results of the optimization procedures with different grid sizes it can be said that the low data ratio negatively affects the optimization procedure, therefore it is recommended to consider the number of data points per grid when applying this method in followup studies. For this study Grid size 0.3x0.3mm was

implemented into the iFEM pipeline.

#### 4.1.2 Noise study

Evolutionary algorithms such as DE are proven to be robust enough not to be highly influenced by the presence of noise [36]. In addition to that, it also has been reported that a larger population size decreases the effect of noise [37].

A. Acciaoli *et al.*, 2018 investigated the effect of noise from DIC measurement on the estimated Young's modulus and Poisson's ratio [38]. The error between GTD and DIC based calculated material properties were in the order of magnitude of 1.8 % - 3.3%. In this study the reported errors between GTD and CD material properties were between 0.14 % - 4.68 % which is in the same order of magnitude as the values in the aforementioned study. Therefore it can be said that the noise is not a determining factor in the accuracy of the estimated material properties.

#### 4.1.3 Section study

The difference in performances of the procedures with an increased number of sections is related to the increased dimensionality of the objective function. The increased dimensionality affects the computational effort in terms of increased number of generations until convergence and the decreased accuracy of the estimated material properties.

It has been reported that a linear increase in dimensionality leads to a super linear increase in computational effort, in terms of generations needed for convergence [28]. In this study, the dimensionality was increased from two for to four, to eight, and then twelve as the ROI got subdivided into more sections. The increase in computational time, in terms of generations until convergence changed from 22 to 60, to 157 and to 269, which falls in line with the reported connection between dimensionality and computational effort.

Higher dimensionality negatively affects the accuracy of the procedure, but the effect can be minimised with the careful selection of the number of populations in each generation. As a general rule it is recommended to use  $n = 10 * dim$ , however for low dimensionality ( $dim < 30$ ) other recommendations suggest to use  $n = 30 * dim$  [30, 31]. It has also been reported that an increased population number can increase the performance of the procedure, but additional increase of the population number will negatively affect the computational time. A population number that is too high can also lead to poor performance of the procedure, due to an inadequate coverage of search base [28].

When looking into the deviations between GTD and the estimated material properties (see Table 11 below), it can be seen that for up to 4 Sections the error does not exceed 6.2 %. Taking the constant objective function value for 1-2-4 Sections into consideration, this might suggest that the applied DE parameter setting can accurately find material properties when the dimension of the objective function does not exceed 8. However, it is important to note that in the case of 6 Sections ( $dim = 12$ ), the deviations increase to up to 35.4 % and the objective function value also increases. With an exception for Section 3, which shows relatively low deviations compared to the other sections. Unfortunately, there is no explanation for this

phenomena and further investigation is needed to explore this finding.

Table 11: The deviations in percentage between GTD and estimated material properties for different sections.

Number of Sections	1 Section		2 Sections		4 Sections		6 Sections	
Deviation from GTD [%]	$c_{10}$	$c_{20}$	$c_{10}$	$c_{20}$	$c_{10}$	$c_{20}$	$c_{10}$	$c_{20}$
Section 1	1.5	1.0	1.1	1.7	1.7	2.7	35.4	23.5
Section 2	-	-	2.0	2.4	6.2	4.1	31.6	21.2
Section 3	-	-	-	-	2.0	3.0	0.7	8.2
Section 4	-	-	-	-	3.1	3.2	12.4	19.6
Section 5	-	-	-	-	-	-	23.7	13.8
Section 6	-	-	-	-	-	-	21.7	14.1

The higher deviations of 6 Sections could potentially be resolved with fine-tuning of the number of populations. It has been reported that in the case of higher dimensionality, a decrease in population number leads to better performance of DE [28], however this theory was not tested in this study. Therefore it is recommended to look into the performance of the optimization procedure with 6 sections using a smaller population number. This might result in a higher computational effort but in an increased accuracy. As an alternative, it also has been suggested to use a gradient-based optimization procedure for problems with higher dimensions, such as the Bayesian type optimization procedure [39].

#### 4.1.4 DE control parameters

There is a wide range of possible values for the control parameters and only a small segment of those was investigated. The value of the crossover probability had the highest impact on the estimation procedure, however, the effect only manifested in the number of generations. This was expected because the crossover probability of one results in an immediate acceptance of the mutated parameters. This combined with the best2bin strategy, which takes the best-fitting parameter as the target vector leads to the constant refinement of the best parameter throughout the procedure. The mutation strategy was investigated using the crossover probability of 1, therefore it can be stated that using different mutation strategies alone improves optimization only by a small reduction in the number of generations.

The increased radius for the mutation factor did not affect the value of the objective function, but it did affect the number of generations needed for convergence. The wider radius led to an increased number of variations to be explored, therefore it led to a higher probability of creating mutations which lead to better fitting material properties. There is little difference between the accuracy of the resulting material properties, and the different radii of the mutation factors led to the same objective function. The smaller radius resulted in more generations needed for convergence. For this method wider mutation radius is suggested.

## 4.2 Experimental data study

The discussion of the results of the experimental data is subdivided into four parts. First, the results of the global material property estimation will be elaborated, then the focus shifts to the results of the local estimation. Finally, the section contains limitations associated with the study and concludes ends with future recommendations.

### 4.2.1 Discussion global material properties

Two material parameters were characterised for each model in order to describe their global mechanical behaviour. The estimated parameters were based on a second-order reduced polynomial function and their values were  $c_{10} = 462$  kPa,  $c_{20} = 1498$  kPa for the fibrous cap sample and  $c_{10} = 447$  kPa,  $c_{20} = 1494$  kPa for the fibrous cap + SI sample. Unfortunately, it is not easy to assign physical meaning to the estimated parameters, however, it can be said that the  $c_{10}$  parameter is connected to the initial shear modulus and therefore to the Young's modulus of the structure through the following connection  $E = 6 * c_{10}$  [17].

T.B. Wissing *et al.*, 2021 reported estimated material properties of the fibrous cap + SI model, based on linear coupling of local strain and measured stress, at different strain levels. At two, five and 10 percent strain the average of the estimated stiffness of the fibrous cap + SI model were  $400 \pm 200$  kPa,  $1200 \pm 400$  kPa and  $2200 \pm 900$  kPa respectively [40]. Maher *et al.*, 2009 estimated material properties of carotid plaque after endarterectomy, using second order isotropic polynomial function with five parameters ( $c_{10}$ ,  $c_{01}$ ,  $c_{20}$ ,  $c_{11}$ ,  $c_{02}$ ) and reported mean values of  $23.4 \pm 33.9$  kPa and  $817 \pm 2441$  kPa for  $c_{10}$  and  $c_{20}$  respectively [41]. Based on the previously reported stiffness values from other studies, it can be stated that the global estimation resulted in stiffness values that fall within the range of reported stiffness values of fibrous intima tissue [29].

It is important to discuss the non-converging behaviour of the second parameter. Similar behaviour was reported by S. G. Torun *et al.*, 2022, when they used a three-parameter Yeoh model to characterise the material properties of fibrous intima and arterial wall [18]. The parameters in that model play a similar role to the parameters used in this study, in which  $c_1$  value is connected to the stiffness of the structure, and additional parameters are responsible for describing the non-linearity of the stress-stretch curve [42]. The deviation of the  $c_1$  parameter was the lowest among the material parameters followed by  $c_2$  and the  $c_3$  parameter showed the highest deviation. However, the reason behind such behaviour was not discussed. It might be that the value of the  $c_{20}$  parameter in the FEM model has a limited effect on the resulting displacement field therefore its value has a lower contribution to the objective function than the  $c_{10}$  value.

To test the hypothesis two results were selected with similar  $c_{10}$  values but differing  $c_{20}$  values and their corresponding displacement distributions were compared, at step 3 along the upper edge of the ROIs. The fibrous cap +SI model was used for this exploration. Figure 31 below shows the comparison of the displacement distributions using the different  $c_{20}$  values and Figure 32 shows the distribution when using different  $c_{10}$  values.

Displacement field one (blue) was created using material parameters  $c_{10} = 447.1$  kPa,

$c_{20} = 157.4kPa$ , with a corresponding objective function value of  $f = 0.37$  and displacement field two (red) was created with  $c_{10} = 447.2$ ,  $c_{20} = 1494.0kPa$ , with a corresponding objective function value of 0.27. The latter is the resulting set of material parameters at the end of the optimization procedure.

Interestingly the higher  $c_{20}$  value led to an overall decrease in the displacement values along the investigated line, and one order of magnitude higher  $c_{20}$  value manifested itself in around a  $60 \mu m$  decrease between the two curves.

In Figure 32, the  $c_{20}$  values were kept constant and the Displacement fields were created using different  $c_{10}$  values. Displacement field 1 (blue) was created using  $c_{10} = 187.5kPa$  and  $c_{20} = 1440kPa$ , and Displacement field 2 (red) belongs to the parameter pair of  $c_{10} = 1161kPa$  and  $c_{20} = 1437kPa$ . The one order of magnitude higher  $c_{10}$  value resulted in a  $400 \mu m$  increase between the displacement fields. The figures demonstrate that the  $c_{10}$  value has a far higher influence on the resulting displacement field, and this might be the reason for the seemingly random selection of  $c_{20}$  values throughout the optimization procedure. For this reason when discussing the local mechanical behaviour of the samples only the distribution of the  $c_{10}$  parameter will be taken into consideration.

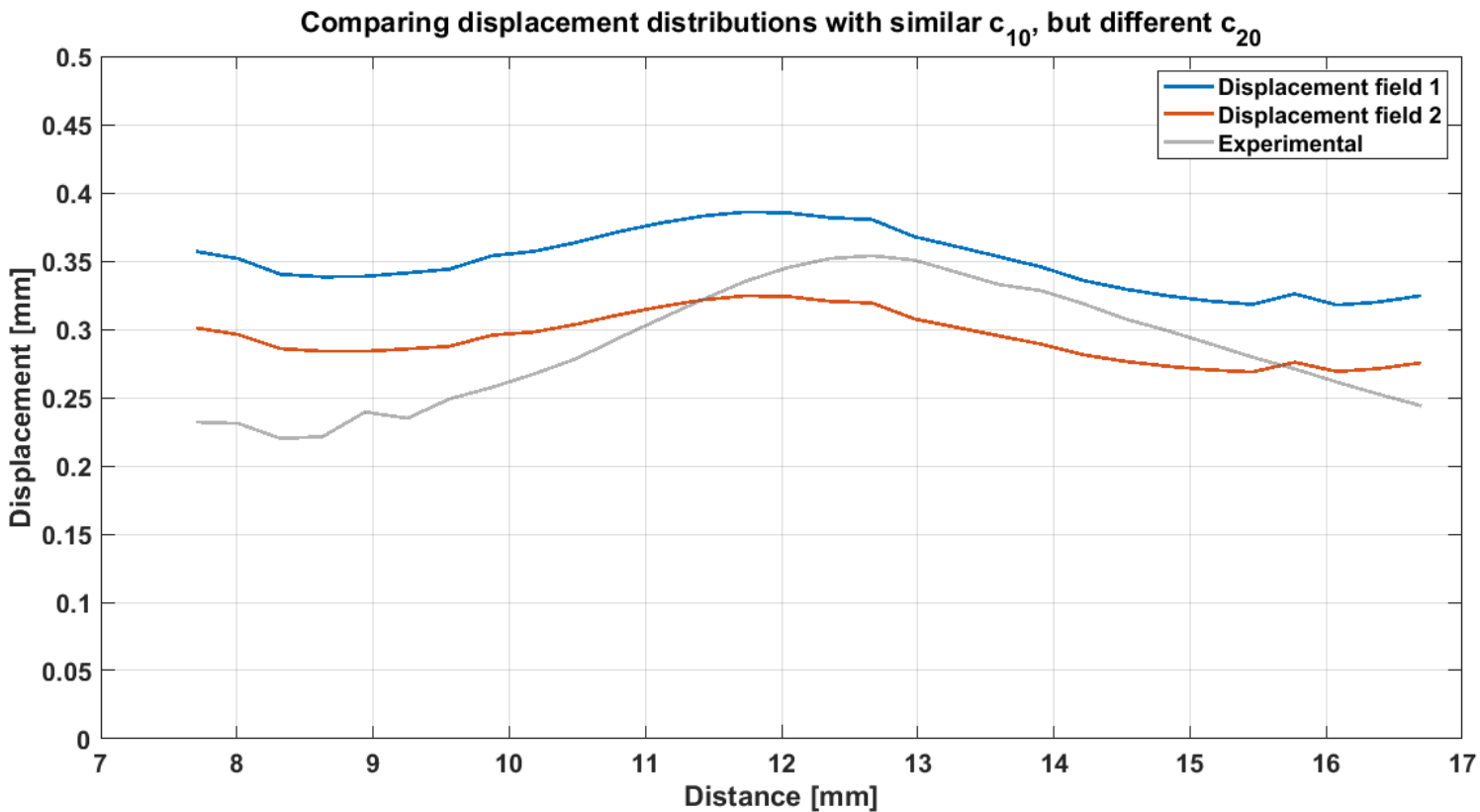


Figure 31: The difference between the distributions when using different  $c_{20}$  values.

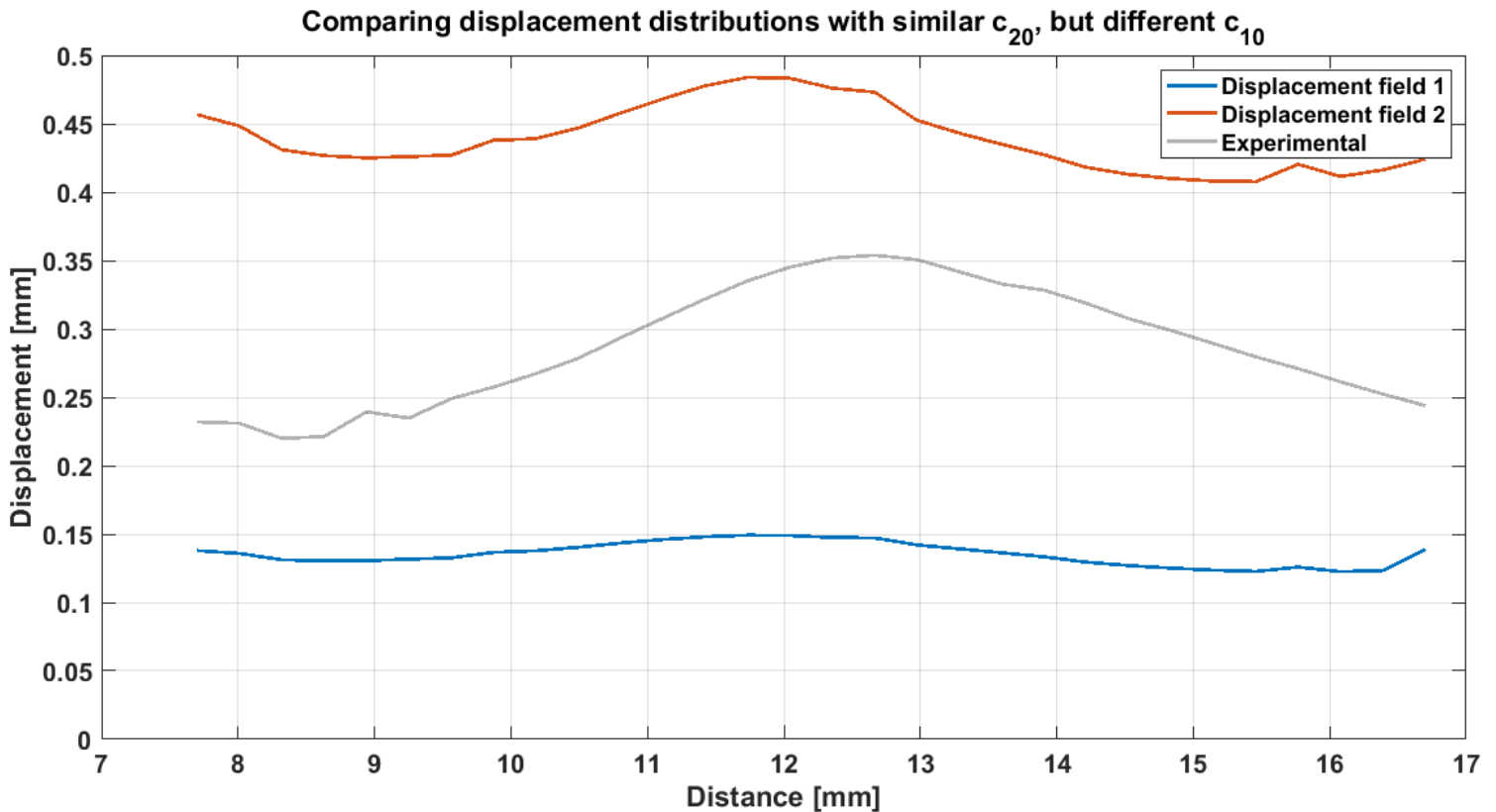


Figure 32: The difference between the distributions when using different  $c_{10}$  values.

#### 4.2.2 Discussion local material properties

The local material property estimation revealed local differences in the mechanical behaviour of the samples. There is a general enhancement of the material property assessment when using local characterisation, and the method revealed local inhomogeneities within the samples, which are not capturable when using global estimation. The estimated stiffness values fall in line with the values from global estimation, and the results remained consistent when the resolution was increased by subdividing the ROI in up to six sections with twelve independent material properties. This method is an improvement towards more localised assessment of material properties compared to previously reported studies which used two independent sections to characterise local material parameters of fibrous plaque tissue [17, 18].

The local estimation revealed differences in the material properties compared to the global estimation. For the fibrous cap model, the percentile difference between the global estimation and the mean of the  $c_{10}$  values from models with a different number of sections is +4.3 %, +6.8 %, and +46.9 % for 2 - 4 - 6 Sections respectively. There is a general growth of the differences between globally estimated  $c_{10}$  and the mean of the locally estimated parameters with the increased number of sections. The difference for the  $c_{20}$  values changes from -2.9 % to -19.5 % and to -33.4 % for the subsequent sections. There is a similar tendency regarding the growth of differences between global  $c_{20}$  and the mean of local estimations. The first parameter showed a general increase in the mean value compared to the global value, the second parameter showed a decrease in the mean value.

For the fibrous cap + SI model, the differences for the  $c_{10}$  value are the same for

2 and 4 Sections and the deviation of the mean values is +16.5 % from the global value. In the case of 6 Sections there is a +10.9 % increase in the mean values compared to the global material property. Other than continuous growth of the mean values for a different section, no constant increase can be seen, as in the case of the fibrous cap model. For the  $c_{20}$  parameter the percentage difference for different sections are -1.6 %, -11.2 % and -29.0 % for subsequent sections. The difference of the second parameter shows similar behaviour to the ones from the fibrous cap model.

It can be seen that the locally estimated parameters are in close range of the globally estimated parameters, but there is noticeable deviation with increased number of sections. Yet the estimated local parameters also fall within the reported range of material properties for plaques with similar compositions [29].

Corresponding sections between the models show different mechanical behaviour. Stiff regions from the fibrous cap sample occur at the top and bottom regions, and the estimation revealed soft regions in the middle of the sample. Whilst from the fibrous cap + SI sample the stiffest region occurred in the middle and the softest region in the bottom section. These local variations might be caused by the presence of the SI, but also could be linked to the differences in the underlying composition, such as the orientation of the load bearing fibres or the amount of cross-linking between the fibres, but based on only two samples and not accounting for anisotropic behaviour in the material model, such statements are highly speculative. Regardless of that it can be said that the pipeline can be used to effectively characterise differences between samples with varying structural components and explore the effect of such components on the local mechanical behaviour.

However it is important to point out that the method has its limitations connected to the number of independent sections, it can be seen, that under the experimental conditions used in this study, that six sections, 12 independent material parameters approaches the boundary of the method.

Based on the results of this study it can be concluded that the method reliably characterises local mechanical behaviour and the pipeline can be applied to investigate heterogeneous distribution of mechanical properties at different locations within TE fibrous cap structures.

### 4.3 Limitations

The main bottlenecks in the iFEM pipeline is the accuracy of the mechanical model. In ABAQUS, hyperelastic materials are assumed to be isotropic, however, it was reported that the samples displayed highly anisotropic behaviour at different locations [40]. Therefore it is recommended to use a material model implementing anisotropic behaviour in follow-up studies. However anisotropic hyperelastic material models in ABAQUS require the definition of 21 material parameters for Fung-Anisotropic, 9 parameters for Fung-Orthotropic, and 4 parameter to describe GOH-Anisotropic behaviour, therefore the local optimization procedure would be highly affected by the dimensionality of the objective function.

Plane strain elements were used to create the resulting displacement field, which elements implement the assumption of in-plane deformation. Although the samples show low thickness-to-width ratio, out-of-plane deformations are expected during

the experiment.

Furthermore during the implementation of the geometry stress-free configuration was assumed, however, pre-stresses might occur due to pre-loading of the sample.

In order to fully characterise hyperelastic behaviour, at least three experiments under different modes of deformations need to be carried out. Besides a tensile test, it is recommended to carry out a biaxial and an out of plane (shear) experiment, to fully define anisotropic hyperelastic behaviour.

Finally, the chosen optimization algorithm has proven to be efficient to characterise material properties, but with a limited amount of independent material parameters. Other non-evolutionary algorithms have proven to not be limited by the dimensionality of the objective function. Such algorithms fall under the category of Bayesian algorithms.

#### **4.4 Future recommendations**

It is recommended to increase the number of samples and apply the established pipeline to investigate local material properties and carry out a statistical analysis.

It also recommended to take the distribution of collagen structure into account when determining the location of the sections. In order to capture anisotropic behaviour of the samples, it is recommended to implement an orthotropic anisotropic material model, which is able to capture different material properties in different directions.

## 5 Conclusion

In the framework of this study, an inverse Finite Element pipeline was created to characterise global and local mechanical parameters of tissue-engineered fibrous cap structures. Using the methodology global material properties of two different tissue-engineered fibrous cap structures were characterised. The material parameters responsible for describing the stiffness of the structures fell in line with previously reported stiffness values of tissues with similar composition.

Local stiffness parameters were successfully characterised for 4 sections in the case of fibrous cap structure and 6 sections in the case of the fibrous cap + SI construct. The results of the local estimation procedure revealed differences in the local mechanical behaviour between the samples with and without SI.

Based on the presented results, the method can be successfully implemented to characterise global material properties of tissue engineered fibrous cap structures and in addition to that it successfully enables the exploration of local heterogeneities within the samples.

## References

- [1] “Cardiovascular disease in Europe 2016: an epidemiological update,” *European Heart Journal*, vol. 37, no. 42, pp. 3182–3183, 11 2016. [Online]. Available: <https://doi.org/10.1093/eurheartj/ehw468>
- [2] E. Wilkins, L. Wilson, K. Wickramasinghe, P. Bhatnagar, J. Leal, R. Luengo-Fernandez, R. Burns, M. Rayner, and N. Townsend, *European Cardiovascular Disease Statistics 2017*. Belgium: European Heart Network, Feb. 2017.
- [3] P. A. VanderLaan, C. A. Reardon, and G. S. Getz, “Site specificity of atherosclerosis,” *Arteriosclerosis, Thrombosis, and Vascular Biology*, vol. 24, no. 1, pp. 12–22, 2004.
- [4] A. J. Lusis, “Atherosclerosis,” *Nature*, vol. 407, 6801, pp. 233 – 241, 2000.
- [5] J. W. Insull, “The pathology of atherosclerosis: Plaque development and plaque responses to medical treatment,” *American Journal of Medicine*, vol. 122 (1 SUPPL.), pp. S3–S14, 2009.
- [6] P. Libby, J. Buring, L. Badimon, G. Hansson, J. Deanfield, M. Bittencourt, L. Tokgözoğlu, and E. Lewis, “Atherosclerosis,” *Nature Reviews Disease Primers*, vol. 5, 12 2019.
- [7] L. Badimon and G. Vilahur, “Thrombosis formation on atherosclerotic lesions and plaque rupture,” *Journal of Internal Medicine*, vol. 276, no. 6, pp. 618–632, 2014. [Online]. Available: <https://onlinelibrary.wiley.com/doi/abs/10.1111/joim.12296>
- [8] A. Hafiane, “Vulnerable plaque, characteristics, detection, and potential therapies,” *Journal of Cardiovascular Development and Disease*, vol. 6, p. 26, 07 2019.
- [9] A. Lafont, “Basic aspects of plaque vulnerability,” *Heart*, vol. 89, no. 10, pp. 1262–1267, 2003. [Online]. Available: <https://heart.bmj.com/content/89/10/1262>
- [10] K. Sakakura, M. Nakano, F. Otsuka, E. Ladich, F. D. Kolodgie, and R. Virmani, “Pathophysiology of atherosclerosis plaque progression,” *Heart, Lung and Circulation*, vol. 22, no. 6, pp. 399–411, 2013. [Online]. Available: <https://www.sciencedirect.com/science/article/pii/S1443950613000711>
- [11] J. Schaar, J. Muller, E. Falk, R. Virmani, V. Fuster, P. Serruys, A. Colombo, C. Stefanadis, S. Casscells, P. Moreno, A. Maseri, and A. van der Steen, “Terminology for high-risk and vulnerable coronary artery plaques report of a meeting on the vulnerable plaque, june 17 and 18, 2003, santorini, greece,” *European heart journal*, vol. 25, pp. 1077–82, 07 2004.
- [12] D. Steinl and B. Kaufmann, “Ultrasound imaging for risk assessment in atherosclerosis,” *International Journal of Molecular Sciences*, vol. 16, pp. 9749–9769, 05 2015.

- [13] Z.-Y. Li, S. Howarth, R. A. Trivedi, J. M. U-King-Im, M. J. Graves, A. Brown, L. Wang, and J. H. Gillard, "Stress analysis of carotid plaque rupture based on in vivo high resolution mri," *Journal of Biomechanics*, vol. 39, no. 14, pp. 2611–2622, 2006. [Online]. Available: <https://www.sciencedirect.com/science/article/pii/S0021929005003994>
- [14] G. Holzapfel, T. Gasser, and R. Ogden, "A new constitutive framework for arterial wall mechanics and a comparative study of material models," *Journal of Elasticity*, vol. 61, pp. 1–48, 04 2012.
- [15] G. Holzapfel, "Collagen in arterial walls: Biomechanical aspects," *Collagen Structures and Mechanics*, 01 2008.
- [16] S. M. Serra, "Mechanical characterization of tissue engineered fibrous cap constructs: Towards the development of an in vitro atherosclerotic disease model," MSc Thesis, Dep. BioMedical Engineering, Delft University of Technology, The Netherlands, Delft, 2628 CD, Mekelweg 5, 2020. [Online]. Available: <https://repository.tudelft.nl/islandora/object/uuid:7e9040d6-5b38-4918-9dc4-41d422afa3dd?collection=education>
- [17] A. C. Akyildiz, H. H. G. Hansen, H. A. Nieuwstadt, L. Spleeman, C. L. De Korte, A. F. van der Steen, and F. J. H. Gijsen, "A framework for local mechanical characterization of atherosclerotic plaques: Combination of ultrarounds displacement imaging and inverse finite element analysis," *Annals of Biomedical Engineering*, vol. 44, p. 968–979, 2016.
- [18] S. Guvenir Torun, H. Torun, H. Hansen, G. Gandini, I. Berselli, V. Codazzi, C. de Korte, A. van der Steen, F. Migliavacca, C. Chiastra, and A. Akyildiz, "Multicomponent mechanical characterization of atherosclerotic human coronary arteries: An experimental and computational hybrid approach," *Frontiers in Physiology*, vol. 12, 2021.
- [19] G. A. Holzapfel, R. Eberlein, P. Wriggers, and H. W. Weizsäcker, "Large strain analysis of soft biological membranes: Formulation and finite element analysis," *Computer Methods in Applied Mechanics and Engineering*, vol. 132, no. 1, pp. 45–61, 1996. [Online]. Available: <https://www.sciencedirect.com/science/article/pii/0045782596009991>
- [20] M. Smith, *ABAQUS/Standard User's Manual, Version 6.9*. United States: Dassault Systèmes Simulia Corp, 2009.
- [21] H. M. Torun and M. Swaminathan, "High-dimensional global optimization method for high-frequency electronic design," *IEEE Transactions on Microwave Theory and Techniques*, vol. 67, no. 6, pp. 2128–2142, 2019.
- [22] R. Storn and K. V. Price, "Differential evolution – a simple and efficient heuristic for global optimization over continuous spaces," *Journal of Global Optimization*, vol. 11, pp. 341–359, 1997.
- [23] S. Das, S. S. Mullick, and P. Suganthan, "Recent advances in differential evolution – an updated survey," *Swarm and Evolutionary Computation*,

- vol. 27, pp. 1–30, 2016. [Online]. Available: <https://www.sciencedirect.com/science/article/pii/S2210650216000146>
- [24] “scipy.optimize.differential evolution - scipy v1.6.2 reference guide.” [Online]. Available: [https://docs.scipy.org/doc/scipy/reference/generated/scipy.optimize.differential\\_evolution.html](https://docs.scipy.org/doc/scipy/reference/generated/scipy.optimize.differential_evolution.html)
- [25] Z. Gao, X. Xu, Y. Su, and Q. Zhang, “Experimental analysis of image noise and interpolation bias in digital image correlation,” *Optics and Lasers in Engineering*, vol. 81, pp. 46–53, 2016. [Online]. Available: <https://www.sciencedirect.com/science/article/pii/S0143816616000063>
- [26] P. Lava, S. Cooreman, S. Coppieters, M. De Strycker, and D. Debruyne, “Assessment of measuring errors in dic using deformation fields generated by plastic fea,” *Optics and Lasers in Engineering*, vol. 47, no. 7, pp. 747–753, 2009. [Online]. Available: <https://www.sciencedirect.com/science/article/pii/S0143816609000451>
- [27] H. Wang, Z. Wu, and S. Rahnamayan, “Enhanced opposition-based differential evolution for solving high-dimensional continuous optimization problems,” *Soft Computing*, vol. 15, no. 11, pp. 2127–2140, 2011. [Online]. Available: <https://link.springer.com/article/10.1007/s00500-010-0642-7>
- [28] S. Chen, J. Montgomery, and A. Bolufé-Röhler, “Measuring the curse of dimensionality and its effects on particle swarm optimization and differential evolution,” *Applied Intelligence*, vol. 42, no. 3, pp. 514–526, 2015.
- [29] A. C. Akyildiz, L. Speelman, and F. J. Gijzen, “Mechanical properties of human atherosclerotic intima tissue,” *Journal of biomechanics*, vol. 47, no. 4, pp. 773–783, 2014.
- [30] R. Storn, “On the usage of differential evolution for function optimization,” in *Proceedings of north american fuzzy information processing*. Ieee, 1996, pp. 519–523.
- [31] A. P. Piotrowski, “Review of differential evolution population size,” *Swarm and Evolutionary Computation*, vol. 32, pp. 1–24, 2017.
- [32] G. Jeyakumar and C. Shanmugavelayutham, “Convergence analysis of differential evolution variants on unconstrained global optimization functions,” *International Journal of Artificial Intelligence Applications*, vol. 2, no. 2, p. 116–127, Apr 2011. [Online]. Available: <http://dx.doi.org/10.5121/ijaiia.2011.2209>
- [33] F. Peñuñuri, C. Cab, O. Carvente, M. Zambrano-Arjona, and J. Tapia, “A study of the classical differential evolution control parameters,” *Swarm and Evolutionary Computation*, vol. 26, pp. 86–96, 2016. [Online]. Available: <https://www.sciencedirect.com/science/article/pii/S221065021500067X>
- [34] M. Centeno-Telleria, E. Zulueta, U. Fernandez-Gamiz, D. Teso-Fz-Betoño, and A. Teso-Fz-Betoño, “Differential evolution optimal parameters tuning with artificial neural network,” *Mathematics*, vol. 9, no. 4, p. 427, 2021.

- [35] J. Brest, S. Greiner, B. Boskovic, M. Mernik, and V. Zumer, “Self-adapting control parameters in differential evolution: A comparative study on numerical benchmark problems,” *IEEE Transactions on Evolutionary Computation*, vol. 10, no. 6, pp. 646–657, 2006.
- [36] D. Rullière, A. Faleh, F. Planchet, and W. Youssef, “Exploring or reducing noise?: A global optimization algorithm in the presence of noise,” *Structural and Multidisciplinary Optimization*, vol. 47, 06 2013.
- [37] J. M. Fitzpatrick and J. J. Grefenstette, “Genetic algorithms in noisy environments,” *Machine learning*, vol. 3, no. 2, pp. 101–120, 1988.
- [38] A. Acciaioli, G. Lionello, and M. Baleani, “Experimentally achievable accuracy using a digital image correlation technique in measuring small-magnitude ( $\epsilon < 0.12018$ ). [Online]. Available: <https://www.mdpi.com/1996-1944/11/5/751>
- [39] W. Chu, X. Gao, and S. Sorooshian, “A new evolutionary search strategy for global optimization of high-dimensional problems,” *Information Sciences*, vol. 181, no. 22, pp. 4909–4927, 2011.
- [40] T. Wissing, K. Van der Heiden, S. Serra, A. Smits, C. Bouten, and F. Gijzen, “Tissue-engineered collagenous fibrous cap models to systematically elucidate atherosclerotic plaque rupture,” *bioRxiv*, 2021. [Online]. Available: <https://www.biorxiv.org/content/early/2021/07/20/2021.07.20.451997>
- [41] E. Maher, A. Creane, P. S. Sultan, N. Hynes, C. Lally, and D. Kelly, “Tensile and compressive properties of fresh human carotid atherosclerotic plaques,” *Journal of biomechanics*, vol. 42, pp. 2760–7, 09 2009.
- [42] O. H. Yeoh, “Some forms of the strain energy function for rubber,” *Rubber Chemistry and Technology*, vol. 66, pp. 754–771, 1993.
- [43] D. Zaharie, “Influence of crossover on the behavior of differential evolution algorithms,” *Applied Soft Computing*, vol. 9, no. 3, pp. 1126–1138, 2009. [Online]. Available: <https://www.sciencedirect.com/science/article/pii/S1568494609000325>

# Appendix I - Information on creating the TCFA

## A Cell culturing

The tissue-engineered constructs were created by adding a fibrin-based matrix to collagen cell culture, which was created by using myofibroblasts from human vena saphena magna.

The cells were seeded between two 15x5 mm Velcro stripes which were 10 mm apart from each other. The geometry of the cell culturing mold including the Velcro strips is shown in the Figure 33 below.

After 7 days of culturing a soft inclusion (SI) was introduced in the cellular structure by punching a 2 mm centered hole. The same fibrin gel was used to fill the SI, excluding the collagen structure driven from the vena saphena magna.

After that further culturing followed for 14 days. Two cell-culturing methods were used for the study. 4 samples underwent static cell straining while 4 samples underwent static + intermittent straining. Since the conclusion of the study more samples were created by using continuous straining. The different straining protocols are shown in the Figure 34 below. The straining protocol includes 4% strain on 0.5Hz for the duration of 1 hour followed by 0% strain for for 3 hours, in case of intermittent straining. Continuous straining protocol includes the same strain percentage and uninterrupted duration.

After straining the tissue-engineered structures underwent uniaxial testing method on the 21st day.

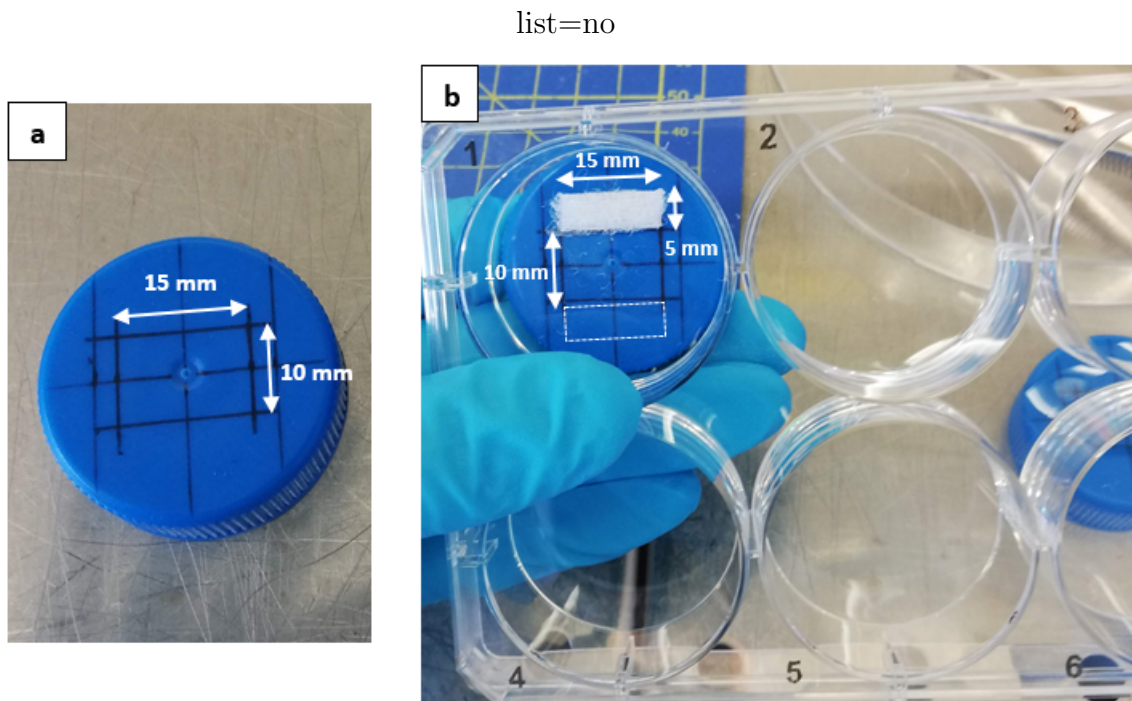


Figure 33: Position and dimension of Velcro tapes. Image was retrieved from S.M.Serra, 2020.

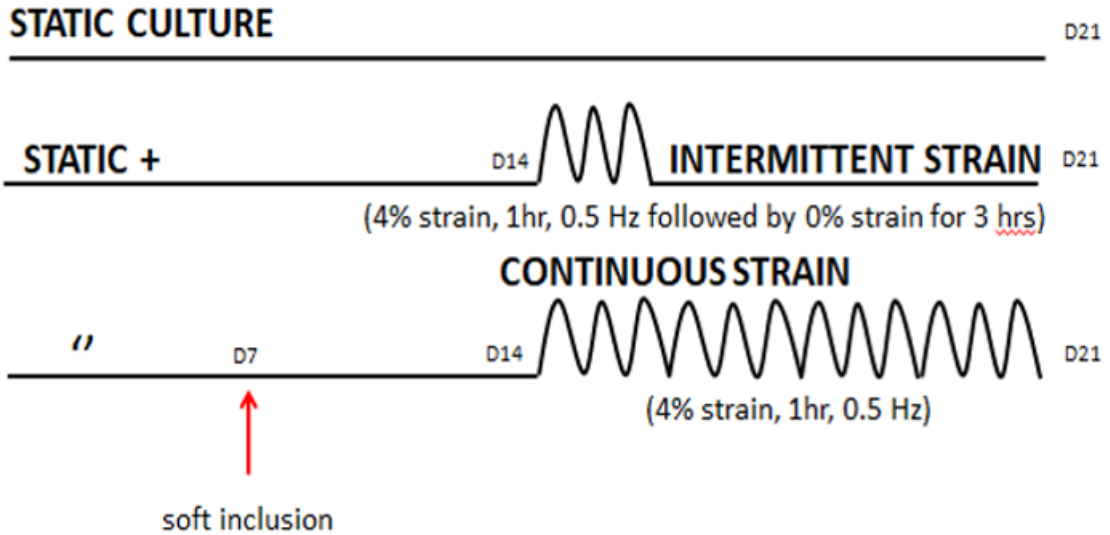


Figure 34: Schematic representation of straining protocols applied on the samples. Static culture (top), static+intermittent strain (middle) and continuous straining (bottom). Red marking indicates the day when the soft inclusion was introduced

## B Uniaxial tensile test

The uniaxial tensile test was performed using a commercial biaxial tester equipped with two 5N load cells. The samples were lowered into 37 °C PBS solution. A high-resolution camera was used for the DIC analysis using 15Hz sampling rate. The Figure 35 below shows the experimental setup used for the mechanical testing.

The tensile test was carried out at a strain rate of 100% min<sup>-1</sup>, until failure. Prior to the test, the samples were preconditioned at 10% strain rate for 10 cycles in order to create reproducible results. During the test, two-dimensional DIC was performed using an open-source software.

NCorr, implemented in MATLAB. Images were recorded after the preconditioning and ended before the rupture of the samples. The first image served as the reference image and the strain and X,-and Y-displacement field was mapped over that image. The Region of Interest (ROI) was chosen so that it excludes the clamp region. This decision was made because the Velcro stripes around the clamp region make the interpretation of the structure's mechanical behavior difficult.



Figure 35: Uniaxial mechanical testing setup with components pointed out [Biomaterial Testing, Waterloo, Canada].

## C Results of the study

The global mechanical behavior showed no difference between the samples created using different straining protocols. However the alignment of matrix elements due to fibre alignment towards loading direction should have an effect on the local mechanical behaviour. We intend to investigate the effect of different straining protocols near the soft inclusion and in the mid-cap region of the ROI, where high extensive strains are reported in loading direction.

SI represents a disruption of homogeneous material properties therefore, as expected, extreme compaction and extension strains occur at the edge of SI. High extensive stresses occur in the loading direction, on left and right side of the SI, while high

compacting stresses occur in the perpendicular direction of loading, on the top and bottom interface between tissue and SI.

## Appendix II - Supplementary information to the methods

### D FEM of the fibrous cap + SI

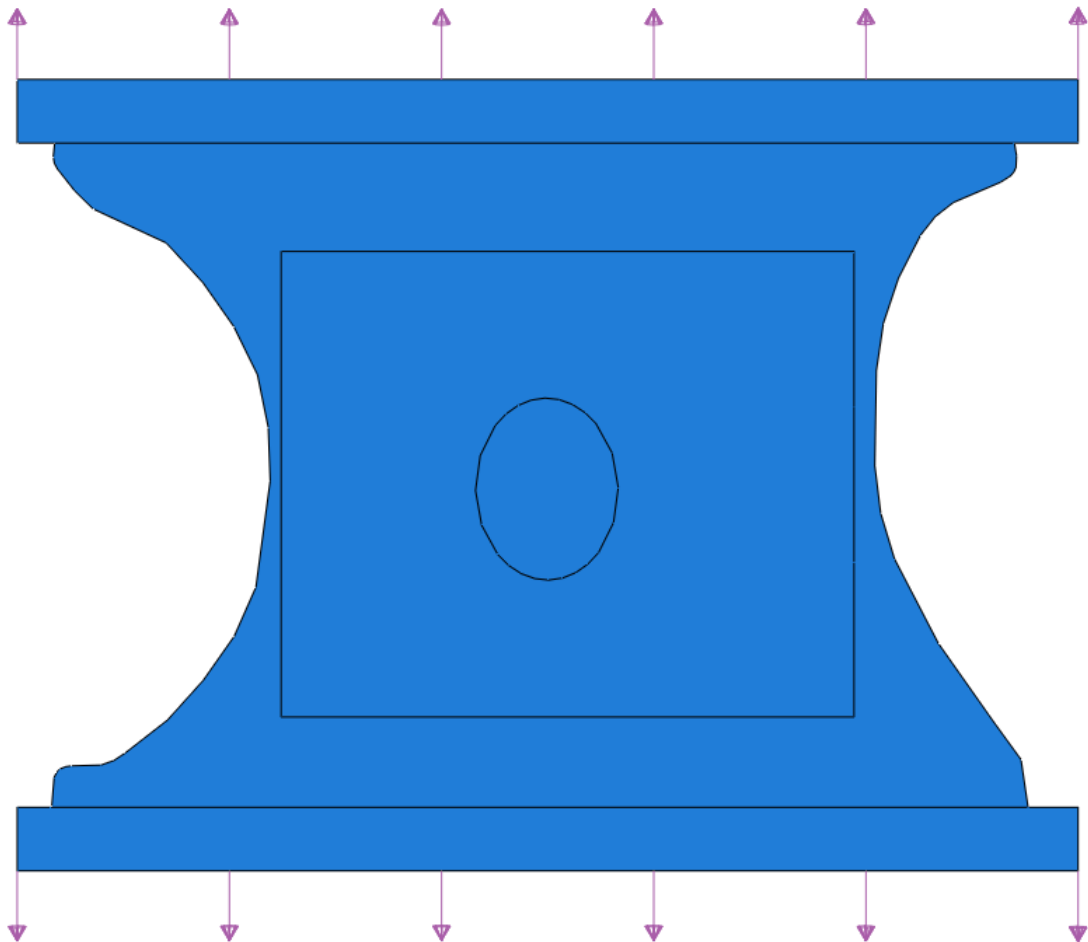


Figure 36: The loading applied on the clam as uniformly distributed pressure, for the fibrous cap+SI model.

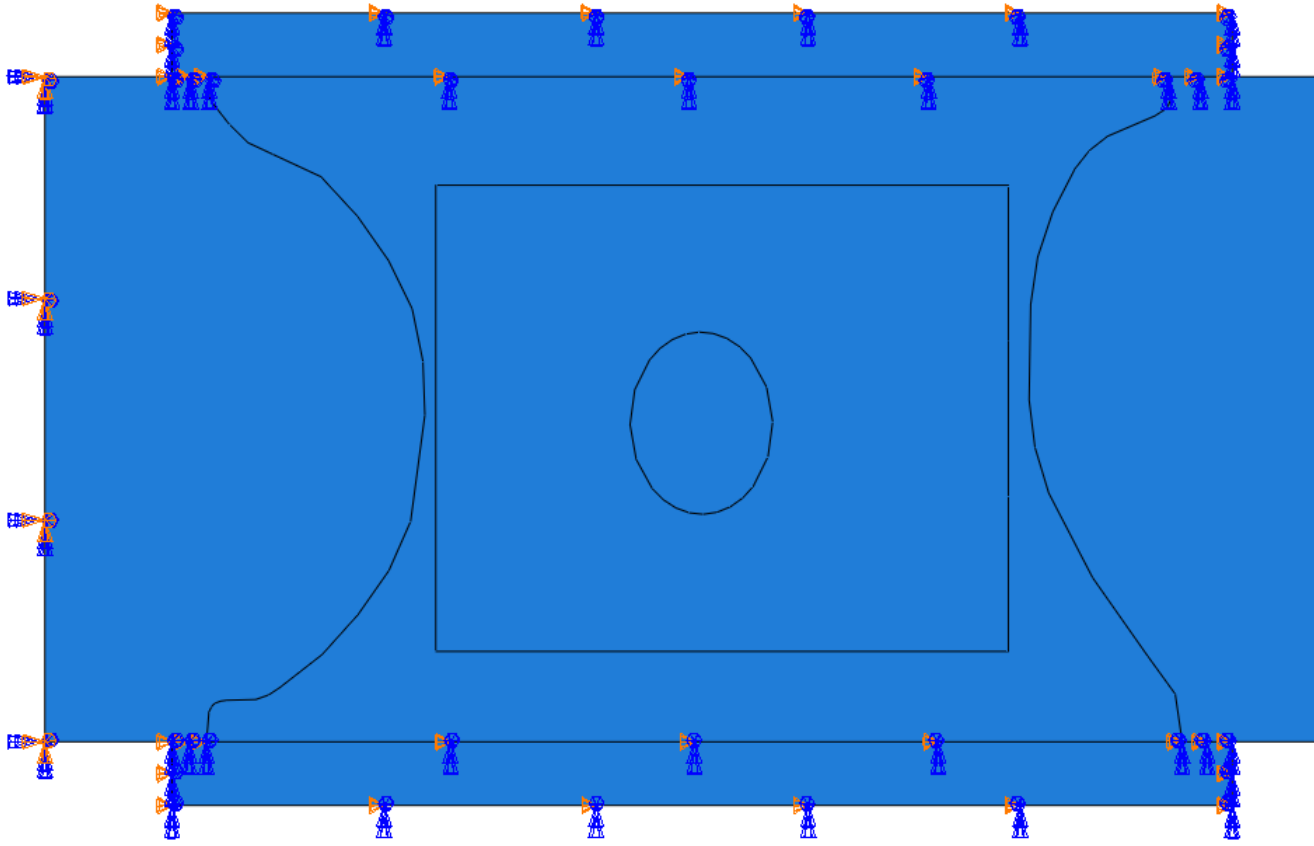


Figure 37: The boundary conditions applied to the fibrous cap + SI model

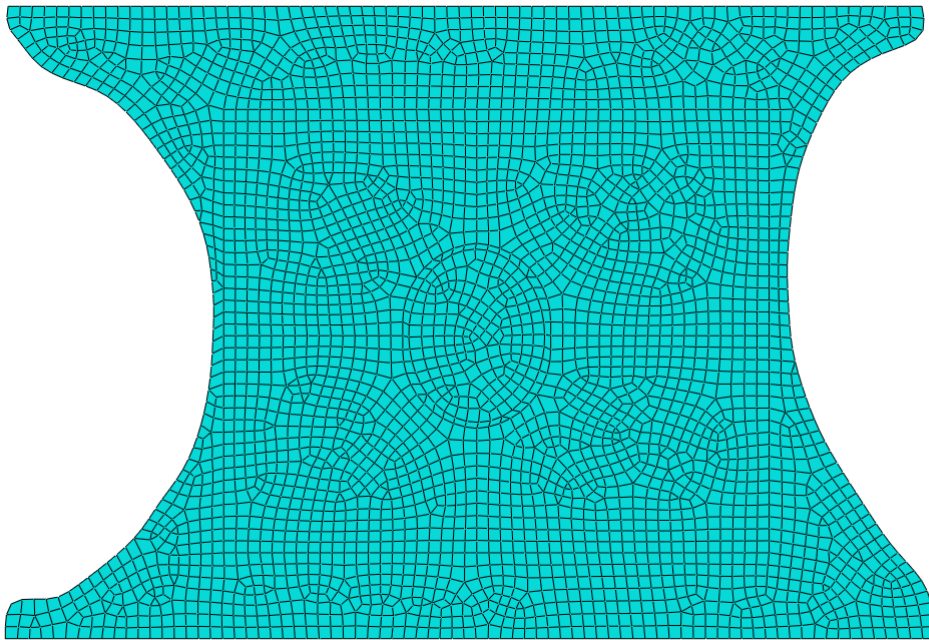


Figure 38: The discretized geometry of the fibrous cap + SI model. Element size 0.2mm was used for the ROI and 0.4mm for the surrounding tissue.

## **E Different grid sizes applied to the computed displacement fields**

### **E.1 Fibrous cap model**

The Figures 39 - 41 show the different grid sizes applied on the computed displacement fields from the fibrous cap model. Figures 39, 40, 41 show the grid sizes  $0.1 \times 0.1$ ,  $0.2 \times 0.2$  and  $0.3 \times 0.3$  respectively.

### Grid 0.1x0.1 applied on the fibrous cap model



Figure 39: Grid size 0.1x0.1 mm applied to the computed displacement field from the fibrous cap model.

**Grid 0.2x0.2 applied on the fibrous cap model**



Figure 40: Grid size 0.2x0.2 mm applied to the computed displacement field from the fibrous cap model.

### Grid 0.3x0.3 applied on the fibrous cap model

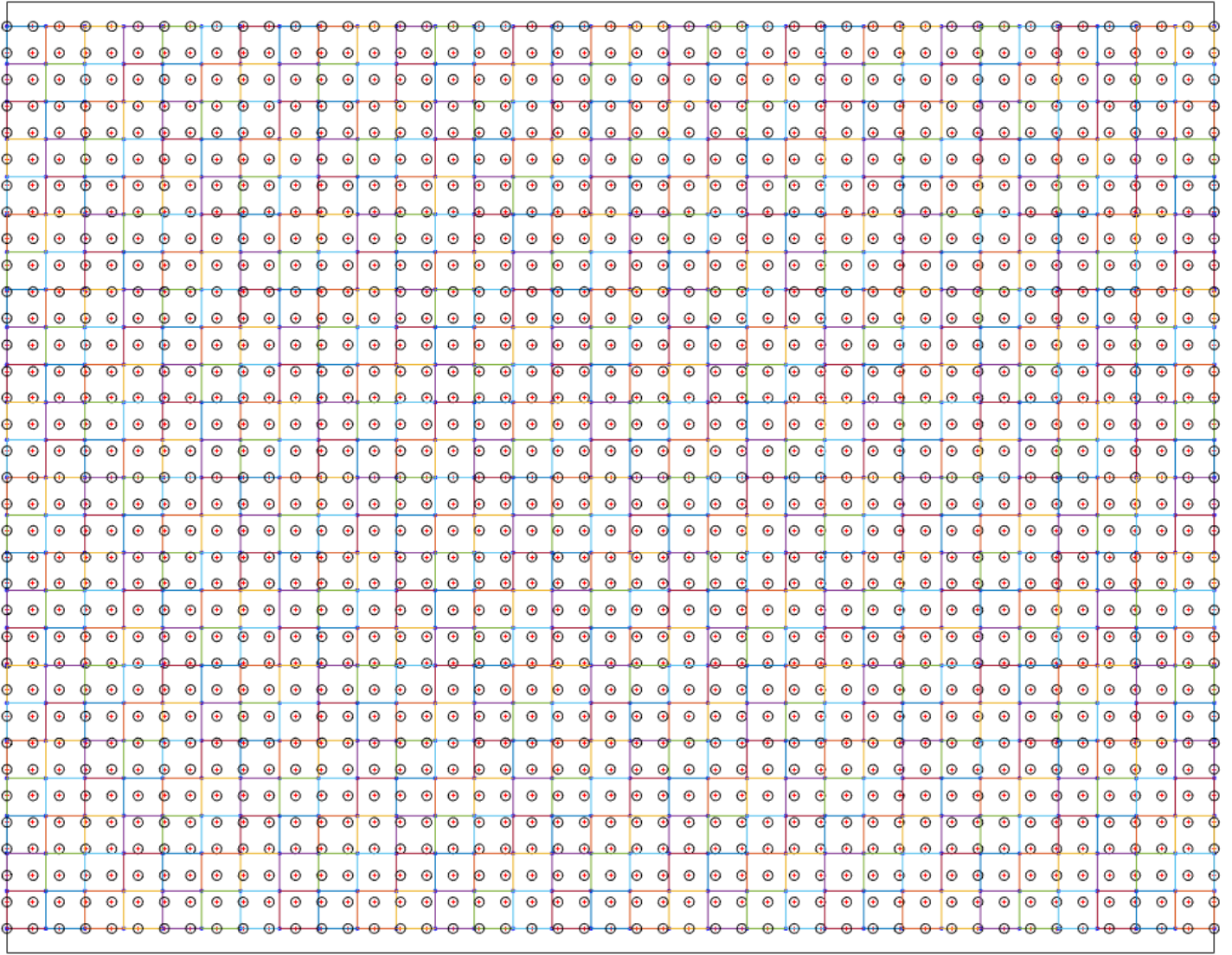


Figure 41: Grid size 0.3x0.3 mm applied to the computed displacement field from the fibrous cap model.

## E.2 Fibrous cap + SI model

The material properties from the fibrous cap + SI model were investigated using 0.3x0.3mm grid. Figure 42 shows the grid applied on the model.

**Grid 0.3x0.3 applied on the fibrous cap + SI model**

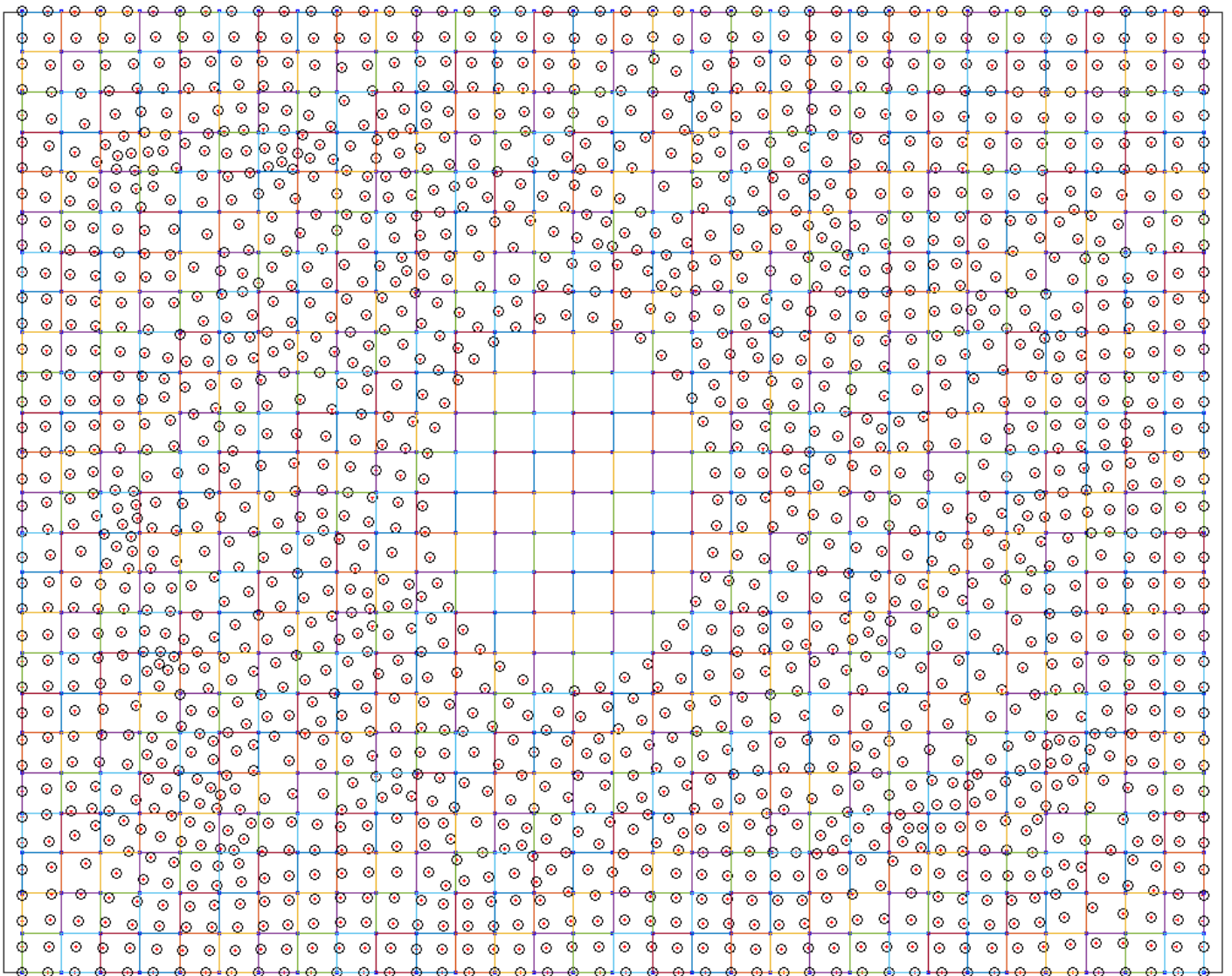


Figure 42: Grid size 0.3x0.3 mm applied to the computed displacement field from the fibrous cap + SI model.

## F Noise estimation

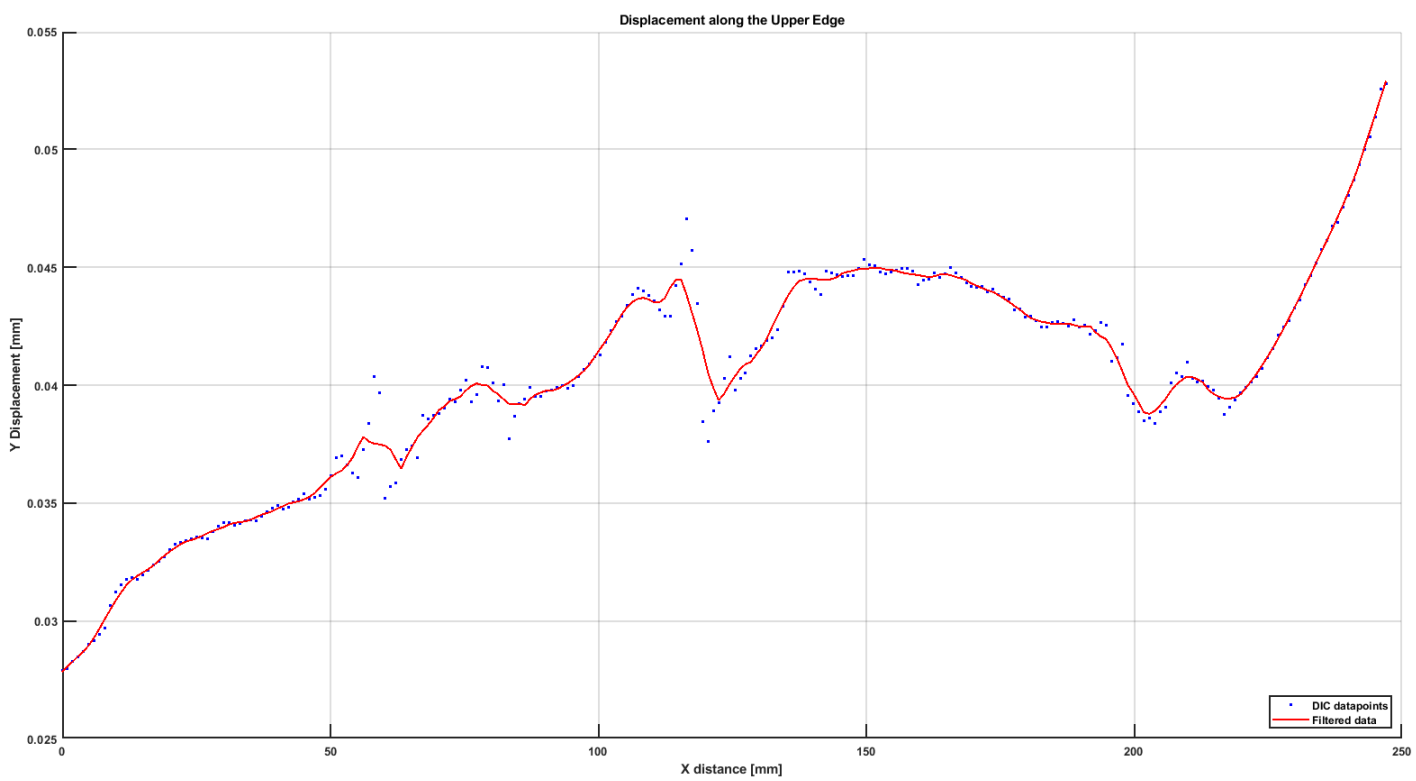


Figure 43: The noise estimation for fibrous cap sample.

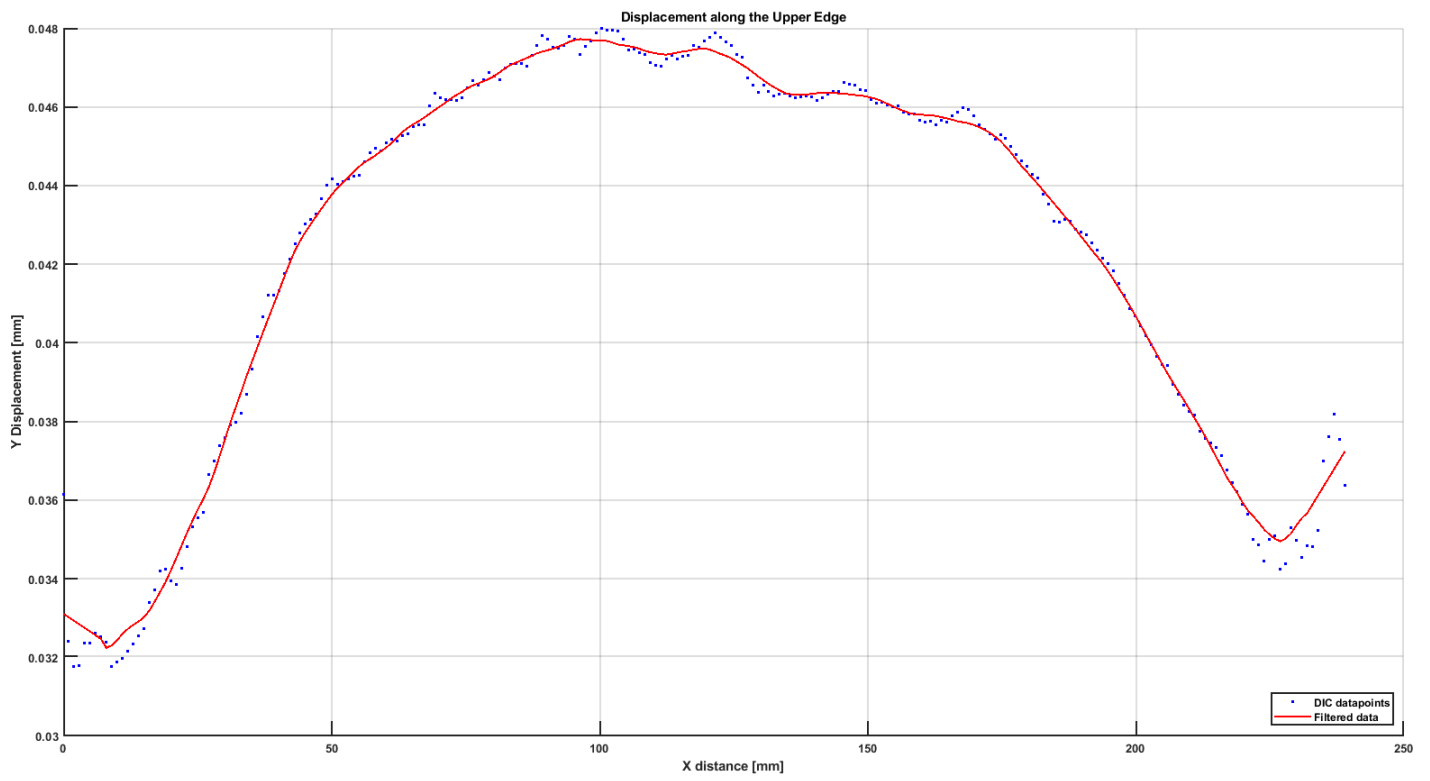


Figure 44: The noise estimation for fibrous cap + SI sample.

# Appendix III - Supplementary information on Differential evolution algorithm

## G Working example of differential evolution

In this part DE procedure will be explained using a working example. The example is based on a population of five ( $N_p = 5$ ). In the initiation step, five solutions of the function will be generated so that the selected parameters cover the search boundaries evenly. The function evaluations  $x_i(p_i, k_i)$  and the solutions  $a_i$  will be denoted as shown below.

- $x_1(p_1, k_1) = a_1$
- $x_2(p_2, k_2) = a_2$
- $x_3(p_3, k_3) = a_3$
- $x_4(p_4, k_4) = a_4$
- $x_5(p_5, k_5) = a_5$

In order to carry out mutation and crossover, four parameter pairs will be selected randomly. The parameter pairs will be referred to as vector since they contain the  $p_i, k_i$ . First, a parent vector is selected from the population. To each parent vector belong a target vector ( $x_i$ ) and two more randomly selected vectors ( $x_{r1}, x_{r2}$ ). For this purpose  $x_1$  will be selected as parent,  $x_2, x_3$ , and  $x_4$  will be random vector 1 and 2 and the target vector respectively. In the mutation step a trial vector  $v_{i,j}$  is generated using equation 10. In this equation the trial vector is generated by adding the weighted difference of the randomly selected vectors to the target vector. The weighting factor is often referred to as mutation factor or scaling factor.

$$v_{11} = p_4 + F(p_2 - p_3), v_{12} = k_4 + F(k_2 - k_3) \quad (10)$$

It is important to check if the newly created parameters are within the searching boundaries or not. If they are, the values will be adjusted to the closest boundary value ( $X_{min}$  or  $X_{max}$ ). After creating the trial vector, the next operation is the crossover. During crossover, an offspring vector is generated by recombination of the parent and the target vectors. The main goal of the crossover operation is to decide whether the the newly generated offspring leads to lower objective function than the parent vector. The offspring vector will be denoted as  $u_{1,j}$  and it is generated by following the principle in equation 11 below.

$$u_{1,j} = \begin{cases} v_{1,j} & \text{if } r \leq CR \text{ OR } j = k \\ x_{1,j} & \text{if } r > CR \text{ AND } j \neq k \end{cases} \quad (11)$$

In the equation above  $j$  stands for the respective component of the offspring vector. In this case  $u$  has two component, therefore if  $j = 1$ , the  $u_{11}$  component is under

creation, if  $j = 2$  the  $u_{12}$  is under creation. The number 'r' represents a randomly created value between  $[0, 1]$  and separate  $r$  is created for each  $j$ -th component of the offspring. The crossover probability CR is a user-defined parameter from  $[0, 1]$ . The value of  $k$  is a randomly selected number from  $[0, 1, \dots \text{dimension}]$ . The meaning of the equation 11 is the following: the  $j$ -th component of the offspring vector  $u$  inherits the  $j$ -th component from the target vector if the first criteria is met, namely, if the randomly created number  $r$  is lower or equal to the user defined CR value, or if the randomly created value  $k$  equals the  $j$ -th component of the vector that is currently investigated. Otherwise, if the second criteria is met, the  $j$ -th component of the offspring inherits the  $j$ -th component from the parent vector [43].

For this example, let CR be 0.7. For the first component of the offspring vector ( $j = 1$ ), let the randomly created number  $r = 0.5$  and the random indices  $k = 2$ . Since  $r \leq CR$  was fulfilled by  $r < CR$ , the first parameter for the offspring ( $v_{11}$ ) was taken from the trial vector ( $u_{11}$ ). Let  $r$  be higher than CR for the second component ( $j = 2$ ), and  $k$  be one. In this case the second criteria is met and the  $j = 2$  component of the Offspring is the second component from the parent ( $x_1(12) = k_1$ ). The created Offspring vector therefore has the form  $u(v_{11}, k_1)$ . In the selection step the objective function value using the parameters from the Offspring gets compared to the objective function value of the parent vector. If the Offspring vector leads to lower objective function, then it gets propagated to the next generation. The procedure is repeated until every member from the initial population has served as parent vector. In the next part the implementation of DE into a SciPy algorithm will be explained

## H Differential Evolution Algorithm

The following Python script was created by Ali. C. Akyildiz maintained by Su Guvenir Torun

```

1  # -*- coding: utf-8 -*-
2  """
3  @Created by Ali Akyildiz (acakyildiz@gmail.com) - 2016
4  @Modified and maintained by Giulia Gandini - March 21, 2019
5  @Modified and maintained by Su Guvenir (s.guvenir@erasmusmc.nl) -
6  December 19, 2019
7  """
8  #-----Only Modify Here
9  -----
10 directory = 'C:/Users/daniel/Desktop/
11           ForDaniel_Inverse_FEM_06_02_2020 '
12 JobName = '10_80mmHg_step1 '
13 PressureSteps = [80, 100,120]
14 NoPressSteps=len(PressureSteps)
15 abaqusSection1Name= "Section1"
16 abaqusSection2Name= "Section2"
17 abaqusSection3Name= "Section3"
18 abaqusSection4Name= "Section4"
19 abaqusTissueName = 'Tissue '
20 CreateReportFileName = "CreateReportFileFromOdb_multistep.py"
21 Material_Model= "Polynomial" #Type either Neo-Hookean or Yeoh (Note
22 that other than the buffer, all layers are incompressible!)

```

```

19 i=0 #this corresponds to the pressure step 0-->80, 1--->100,
    2---->120mmHg.
20 sheet=1 #chose the index of the excel sheet depending on the
    pressure step you are interested in. 10->0, 80->1, 100->2,
    120->3
21
22
23 dummyFileName = 'Yeoh_Model_Multistep.txt'
24 dummyFileName_short = 'Yeoh_Model_Multistep_short.txt'
25 dummy2_Name = 'Materials_and_energies.txt'
26 dummy3_Name = 'Computed displacements.txt'
27 #
    -----
28
29 ## -----To create a dummy text file that will contain necessary
    info-----
30 NotesFile = open(str(directory) + '\BookKeeping.txt','w+')
31 NotesFile.write(directory+'\n')
32 NotesFile.write(JobName+'\n')
33 NotesFile.close()
34
35 ## Import Libraries
    -----
36
37 #import sys
38 import os
39 import numpy
40 from numpy import *
41 #from numpy import matrix
42 from numpy import array
43 from xlrd import open_workbook
44 #import time
45 import scipy
46 from scipy import io
47 from scipy import optimize
48 import time
49 import timeit
50 import h5py
51 #import sympy
52 #from sympy import *
53
54 os.chdir(directory)
55
56 ##
    -----
57
58 def iteration(MatProps):
59
60
61     global iterNo
62     iterNo = iterNo+1
63     print (iterNo)
64
65 ## -----To edit ABAQUS input file
    -----

```

```

66     ##Neo-Hookean
-----
67     if Material_Model == "Neo-Hookean":
68         ROIC10=MatProps[0]
69         #WallC10=MatProps[1] #Neo-Hookean Wall C1
70
71         print('ROIC10 = ' + str(ROIC10) + '\n') #Neo-Hookean Intima
72         C1 print
73         #print('WallC10 = ' + str(WallC10)) #Neo-Hookean Wall C1
74         print
75         inp=str(JobName) + '.inp'
76         inputFile=open(inp,'r')
77
78         temp=str(directory) + '\\ ' + str(JobName) + '.txt'
79         tempFile=open(temp,'w')
80         lines=inputFile.read().splitlines()
81         line_2 = ('*Material, name=' + str(abaqusSection1Name)) #
82         line_1 = "*Material, name=FibrInt"
83         line_3 = ('*Material, name=' + str(abaqusTissueName)) #
84         line_3 = "*Material, name=Wall"
85
86         for counter1 in range(len(lines)):
87             if lines [counter1-2]==line_2:
88                 lines[counter1]=(str(ROIC10) + ', 0.0001') #for
89                 Neo_Hookean Model here you could change D value + ', 0.' - to D
90                 value
91             if lines [counter1-2]==line_3:
92                 lines[counter1]=(str(ROIC10) + ', 0.0001') #for
93                 Neo_Hookean Material Model
94
95             tempFile.write(lines[counter1]+'\\n')
96
97         inputFile.close()
98         os.remove(inp)
99         tempFile.close()
100         os.rename(temp,inp)
101     ##Mooney-Rivlin
-----
102     elif Material_Model == "Mooney":
103         Section1C10=MatProps[0]
104         Section1C01=MatProps[1]
105         Section2C10=MatProps[2]
106         Section2C01=MatProps[3]
107         Section3C10=MatProps[4]
108         Section3C01=MatProps[5]
109         Section4C10=MatProps[6]
110         Section4C01=MatProps[7]
111
112         print('Section1C10= ' + str(Section1C10) + '; Section1C01 =
113         ' + str(Section1C01) + '\\n')
114         print('Section2C10= ' + str(Section2C10) + '; Section2C01 =
115         ' + str(Section2C01) + '\\n')
116         print('Section3C10= ' + str(Section3C10) + '; Section3C01 =
117         ' + str(Section3C01) + '\\n')

```

```

111     print('Section4C10= ' + str(Section4C10) + '; Section4C01 =
      ' + str(Section4C01) + '\n')
112
113
114
115     inp=str(directory) + '\\\' + str(JobName) + '.inp'
116     inputFile=open(inp,'r')
117
118     temp=str(directory) + '\\\' + str(JobName) + '.txt'
119     tempFile=open(temp,'w')
120     lines=inputFile.read().splitlines()
121     line_1 = ('*Material, name=' + str(abaqusSection1Name)) #
122     line_1 = "*Material, name=FibrInt"
123     line_2 = ('*Material, name=' + str(abaqusSection2Name)) #
124     line_3 = "*Material, name=Wall"
125     line_3 = ('*Material, name=' + str(abaqusSection3Name)) #
126     line_1 = "*Material, name=FibrInt"
127     line_4 = ('*Material, name=' + str(abaqusSection4Name)) #
128     line_3 = "*Material, name=Wall"
129     # line_5 = ('*Material, name=' + str(abaqusTissueName)) #
130     line_3 = "*Material, name=Wall"
131
132     for counter1 in range(len(lines)):
133         if lines [counter1-2]==line_1:
134             lines[counter1]=(str(Section1C10) + ', ' + str(
135 Section1C01) + ', 0.0001') #for Yeoh Material Model
136         if lines [counter1-2]==line_2:
137             lines[counter1]=(str(Section2C10) + ', ' + str(
138 Section2C01) + ', 0.0001') #for Yeoh Material Model
139         if lines [counter1-2]==line_3:
140             lines[counter1]=(str(Section3C10) + ', ' + str(
141 Section3C01) + ', 0.0001') #for Yeoh Material Model
142         if lines [counter1-2]==line_4:
143             lines[counter1]=(str(Section4C10) + ', ' + str(
144 Section4C01) + ', 0.0001') #for Yeoh Material Model
145         # if lines [counter1-2]==line_5:
146         #     lines[counter1]=(str(Section1C10) + ', ' + str(
147 Section1C01) + ', 0.0001') #for Yeoh Material Model
148
149         tempFile.write(lines[counter1]+'\\n')
150
151     inputFile.close()
152     os.remove(inp)
153     tempFile.close()
154     os.rename(temp,inp)
155
156     ##Polynomial Nonlinear Model
-----
157     elif Material_Model == "Polynomial":
158         TissueC10=MatProps [0]
159         TissueC20=MatProps [1]
160         # Section1C10=MatProps [0]
161         # Section1C20=MatProps [1]
162         # Section2C10=MatProps [2]
163         # Section2C20=MatProps [3]

```

```

157     # Section3C10=MatProps [4]
158     # Section3C20=MatProps [5]
159     # Section4C10=MatProps [6]
160     # Section4C20=MatProps [7]
161
162
163     # print('Section1C10= ' + str(Section1C10) + '; Section1C20
= ' + str(Section1C20) + '\n')
164     # print('Section2C10= ' + str(Section2C10) + '; Section2C20
= ' + str(Section2C20) + '\n')
165     # print('Section3C10= ' + str(Section3C10) + '; Section3C20
= ' + str(Section3C20) + '\n')
166     # print('Section4C10= ' + str(Section4C10) + '; Section4C20
= ' + str(Section4C20) + '\n')
167     print('TissueC10= ' + str(TissueC10) + '; TissueC20 = ' +
str(TissueC20) + '\n')
168
169
170
171     inp=str(directory) + '\\\' + str(JobName) + '.inp'
172     inputFile=open(inp,'r')
173
174     temp=str(directory) + '\\\' + str(JobName) + '.txt'
175     tempFile=open(temp,'w')
176     lines=inputFile.read().splitlines()
177     line_1 = ('*Material, name=' + str(abaqusSection1Name)) #
line_1 = "*Material, name=FibrInt"
178     line_2 = ('*Material, name=' + str(abaqusSection2Name)) #
line_3 = "*Material, name=Wall"
179     line_3 = ('*Material, name=' + str(abaqusSection3Name)) #
line_1 = "*Material, name=FibrInt"
180     line_4 = ('*Material, name=' + str(abaqusSection4Name)) #
line_3 = "*Material, name=Wall"
181     line_5 = ('*Material, name=' + str(abaqusTissueName)) #
line_3 = "*Material, name=Wall"
182
183
184
185     for counter1 in range(len(lines)):
186         if lines [counter1-2]==line_1:
187             lines[counter1]=(str(TissueC10) + ', ' + str(
TissueC20) + ', 0.0001' + ', 0.0001') #for Yeoh Material Model
188         if lines [counter1-2]==line_2:
189             lines[counter1]=(str(TissueC10) + ', ' + str(
TissueC20) + ', 0.0001' + ', 0.0001') #for Yeoh Material Model
190         if lines [counter1-2]==line_3:
191             lines[counter1]=(str(TissueC10) + ', ' + str(
TissueC20) + ', 0.0001' + ', 0.0001') #for Yeoh Material Model
192         if lines [counter1-2]==line_4:
193             lines[counter1]=(str(TissueC10) + ', ' + str(
TissueC20) + ', 0.0001' + ', 0.0001') #for Yeoh Material Model
194         if lines [counter1-2]==line_5:
195             lines[counter1]=(str(TissueC10) + ', ' + str(
TissueC20) + ', 0.0001' + ', 0.0001') #for Yeoh Material Model
196
197
198     tempFile.write(lines[counter1]+'\\n')
199

```

```

200     inputFile.close()
201     os.remove(inp)
202     tempFile.close()
203     os.rename(temp,inp)
204
205     else:
206         print ("Choose either the Neo-Hookean or Yeoh Material
207 Model by changing the Material_Model variable")
208     #
209     ##-----To remove lck file if something goes wrong
210     -----
211     FileToRemove = ".lck"
212     try:
213         os.remove(directory + "\\\" + JobName + FileToRemove)
214     except OSError:
215         pass
216     ## -----To run ABAQUS simulation & generate report file
217     -----
218     time.sleep(10)
219     os.system('abq2016 job=' + JobName + ' interactive') #+ "pause"
220     os.system('abq2016 cae noGUI=' + str(CreateReportFileName))
221
222     ##-----To relocate the odb file
223     -----
224     if not os.path.exists(JobName):
225         os.makedirs(JobName)
226
227     FileTypes = [".odb", ".dat", ".msg", ".prt", ".sim", ".sta", ".
228 com", ".lck"]
229
230     for counter in range(len(FileTypes)):
231
232         try:
233             os.remove(directory + '\\\' + JobName + "\\\" + JobName +
234 FileTypes[counter])
235         except OSError:
236             pass
237
238         try:
239             os.rename(directory + '\\\' + JobName + FileTypes[
240 counter], directory + '\\\' + JobName + "\\\" + JobName +
241 FileTypes[counter])
242         except OSError:
243             pass
244
245         try:
246             os.remove(directory + '\\dummyMatEstimation.txt')
247         except OSError:
248             pass
249
250         try:
251             os.rename(directory + '\\dummyMatEstimation.txt',
252 directory + '\\\' + JobName + '\\dummyMatEstimation.txt')

```

```

247     except OSError:
248         pass
249
250
251     try:
252         os.remove(directory + '\\dummyMatEstimation_short.txt')
253     except OSError:
254         pass
255
256     try:
257         os.rename(directory + '\\dummyMatEstimation_short.txt',
258                 directory + '\\ ' + JobName + '\\dummyMatEstimation_short.txt')
259     except OSError:
260         pass
261
262     #
263     ##-----To average the computational results in FE grid
264     regions -----
265     MeanSimResults=[]
266
267     for i in range(NoPressSteps):
268         try:
269             reportFile = open(str(directory)+'\\'+ 'report'+str(i
270 +1)+'.rpt','r')
271         except:
272             nan_array = numpy.full((NoGridSegments), numpy.nan).
273             tolist()
274             MeanSimResults.extend(nan_array)
275             continue
276
277         ini=[]
278         end=[]
279
280         line_1 = '
281
282         line_2 = ""
283         rptLines = reportFile.read().splitlines()
284
285         for counter2 in range(len(rptLines)):
286             if rptLines [counter2] == line_1:
287                 ini.append(counter2)
288                 for counter22 in range(len(rptLines)-counter2):
289                     if rptLines [counter2+counter22] == line_2:
290                         end.append(counter2+counter22-1)
291                         break
292
293         NodeNumbers=[]
294         y_displacements=[]
295         for counter31 in range(len(ini)):
296             for counter3 in range (len(rptLines)):
297                 if counter3 > ini[counter31] and counter3 <= (end[
298 counter31]):
299                     [a,b,c,d,e]=rptLines[counter3].split() #the rpt
300 file has 5 lines: nodes, x-coord, y-coord, y-displ, x-displ
301                     NodeNumbers.append(int(a))

```

```

295         y_displacements.append(float(e))
296
297     NodeNumbers2=[0]*len(NodeNumbers)
298     Strain_yy=numpy.zeros(len(NodeNumbers))
299
300     for counter55 in range(len(NodeNumbers)):
301         dummy=NodeNumbers[counter55]
302         NodeNumbers2[dummy-1]=dummy
303         Strain_yy[dummy-1]=y_displacements[counter55]
304
305     Result=Strain_yy
306
307     for counter100 in range(NoGridSegments): #NoGridSegments
comes from the xls, calculated in StrainFromExcel function.
308         RegionNodes=[]
309
310         RegionNodes=Nodes_Global[counter100] #for each line,
Nodes_Global has all the nodes belonging to a specific region
311         a=[]
312         for counter101 in range(len(RegionNodes)):
313             m=int(RegionNodes[counter101]) #int() is necessary
otherwise this is considered
314             #as a "single cell array" that cannot be used as index. A
index is needed
315             #for the following step.
316             a.append(Result[m-1]) #a is a vector where all the
displacements of a single region are stored
317
318             Mean=numpy.mean(a) #mean of all the elements of a, i.e.
you get the mean computed displacement for each region
319             MeanSimResults.append(Mean)
320
321     reportFile.close()
322     return MeanSimResults
323
324     #d is a vector where all the displacements of a single region
are stored
325
326
327 ## -----To get the measured strain from xls-file
-----
328
329 def StrainFromExcel():
330     y=[]
331     #wb = open_workbook('MeasuredDispYY'+str(Pressure)+'.xls')
332     wb = open_workbook('MeasuredDispYY.xls') #Change file name
333     #wb_x = open_workbook('MeasuredDispXX.xls') #Change file name
334     for sheet in range(NoPressSteps):
335         deformed_sheet = sheet+1
336         sh_y = wb.sheet_by_index(deformed_sheet) #here I choose the
Excel sheet I want to consider, different index depending on the
pressure level
337         #sh_x = wb_x.sheet_by_index(0)
338
339         col_y = sh_y.col_values(0)
340         row_y = sh_y.row_values(0)
341         a = len(col_y)
342         b = len(row_y)

```

```

343 NoGridElements = int(a*b)
344 #col_x = sh_x.col_values(0)
345 #row_x = sh_x.row_values(0)
346 for counter102 in range(len(row_y)):
347     for counter101 in range(len(col_y)):
348         cell_y = sh_y.cell(counter101, counter102)
349         #cell_x = sh_x.cell(counter101, counter102)
350         if cell_y.value == '':
351             y.append(0)
352         else:
353             y.append(cell_y.value)
354 #     y.extend([Measured_RF]*874)           #x.append(cell_x.
value)
355 return y, NoGridElements #,x # y will be called
MeasuredDeformation_Global in main code, NoGridElements will be
NoGridSegments in main code!
356 ##----- To include measured force from actuator
357
358 ## -----To get the node numbers from the .mat files
-----
359
360 def NodeNoFromMatFiles():
361     file = h5py.File('Regions.mat', 'r')
362     row = len(file['Region']['Nodes'][0]) #a matrix is an array of
arrays
363     col = len(file['Region']['Nodes'])
364     print(row, col)
365
366     nodes_vector = [] #vector that will include, in each line, a
vector of nodes corresponding to each region
367     for c in range(col):
368         for r in range(row):
369             # The following lines help in reading the Matlab struct
370             ref = file['Region']['Nodes'][c][r]
371             name = h5py.h5r.get_name(ref, file.id)
372             data = file[name].value
373
374             toRemove = array([1, 0])
375             if data.all() == toRemove.all(): #when the is [], data
becomes [1 0] for unknown reasons. This way, an empty
376                 #array is reported instead, as it should be
according to the "Region.mat"
377                 nodes_vector.append([])
378             else:
379                 nodes_vector.append(data)
380     return nodes_vector # Will be named as Node_Global in main.
381
382 ## -----To get the node numbers from the .mat files
-----
383
384 # def NodeNoFromMatFiles_RF(): #this is not part of Function 2 WHY?
385 #     file_RF = h5py.File('Regions_RF.mat', 'r')
386 #     row_RF = len(file_RF['Region_RF']['Nodes_RF'][0]) #a matrix
is an array of arrays
387 #     col_RF = len(file_RF['Region_RF']['Nodes_RF'])
388 #     print(row_RF, col_RF)
389

```

```

390 #     nodes_vector_RF = [] #vector that will include, in each line,
      a vector of nodes corresponding to each region
391 #     for c in range(col_RF):
392 #         for r in range(row_RF):
393 #             # The following lines help in reading the Matlab struct
394 #                 ref_RF = file_RF['Region_RF']['Nodes_RF'][c][r]
395 #                 name_RF = h5py.h5r.get_name(ref_RF, file_RF.id)
396 #                 data_RF = file_RF[name_RF].value
397
398 #                 toRemove = array([1, 0])
399 #                 if data_RF.all() == toRemove.all(): #when the is [],
      data becomes [1 0] for unknown reasons. This way, an empty
400 #                     #array is reported instead, as it should be
      according to the "Region.mat"
401 #                         nodes_vector_RF.append([])
402 #                     else:
403 #                         nodes_vector_RF.append(data_RF)
404 #     return nodes_vector_RF # This is Node_Global_RF in main code!
405
406 ## -----Function to evaluate the residuals
      -----
407
408 def residuals(MatProps, iteration, MeasuredDeformation_Global):
409
410     global old_err
411
412     ComputedDeformation = iteration(MatProps)
413     for ii in range(NoPressSteps):
414         try:
415             reportFile = open(str(directory)+'\\'+ 'report'+str(ii
+1)+'.rpt', 'r')
416             reportFile.close()
417         except:
418             return numpy.nan
419
420     index_to_remove = []
421     US_measurements=[0]*NoGridSegments*3
422     FEM_measurements=[0]*NoGridSegments*3
423
424
425 #     US_Force=[0]*NoGridSegments
426 #     FEM_Force=[0]*NoGridSegments
427
428
429
430     # referenceUS = [MeasuredDeformation_Global[
reference_grid_element_number],
431 #                 MeasuredDeformation_Global[
reference_grid_element_number + NoGridSegments],
432 #                 MeasuredDeformation_Global[
reference_grid_element_number + 2*NoGridSegments]]
433     # referenceFEM = [ComputedDeformation[
reference_grid_element_number], ComputedDeformation[
reference_grid_element_number+ NoGridSegments],
434 #                 ComputedDeformation[
reference_grid_element_number + 2*NoGridSegments]]
435
436     #for i in range(NoGridSegments):

```

```

437 #     if (MeasuredDeformation_Global[i]==0 or
ComputedDeformation[i]==0 or numpy.isnan(ComputedDeformation[i])
):
438     #         index_to_remove.append(i)
439
440 #for u in range(NoGridSegments):
441 #     US_measurements[u] = array(MeasuredDeformation_Global[u])
442 #     FEM_measurements[u] = array(ComputedDeformation[u])
443
444
445 #referenceUS = MeasuredDeformation_Global[
reference_grid_element_number]
446 #referenceFEM = ComputedDeformation[
reference_grid_element_number]
447
448 for i in range(NoGridSegments*3):
449     if (MeasuredDeformation_Global[i]==0 or ComputedDeformation
[i]==0 or numpy.isnan(ComputedDeformation[i])):
450         index_to_remove.append(i)
451
452 for u in range(NoGridSegments*3):
453     US_measurements[u] = array(MeasuredDeformation_Global[u])#
- array(referenceUS)
454     FEM_measurements[u] = array(ComputedDeformation[u])# -
array(referenceFEM)
455
456 US_measurements[0:NoGridSegments] = array(
MeasuredDeformation_Global[0:NoGridSegments])
457 US_measurements[NoGridSegments:2*NoGridSegments] = array(
MeasuredDeformation_Global[NoGridSegments:2*NoGridSegments])
458 US_measurements[2*NoGridSegments:3*NoGridSegments] = array(
MeasuredDeformation_Global[2*NoGridSegments:3*NoGridSegments])
459
460 FEM_measurements[0:NoGridSegments] = array(ComputedDeformation
[0:NoGridSegments])
461 FEM_measurements[NoGridSegments:2*NoGridSegments] = array(
ComputedDeformation[NoGridSegments:2*NoGridSegments])
462 FEM_measurements[2*NoGridSegments:3*NoGridSegments] = array(
ComputedDeformation[2*NoGridSegments:3*NoGridSegments])
463
464 realResults = []
465 FE_results = []
466
467
468 realResults = numpy.delete(US_measurements, index_to_remove)
469 FE_results = numpy.delete(FEM_measurements, index_to_remove)
470
471
472 #NRMSE Definition
473 # meanref = realResults.mean()
474 #err2=array(FE_results)-array(realResults)
475 err1 = numpy.sqrt(((FE_results-realResults)**2).sum()) #
squared 2-norm of err vector
476 meanref = realResults.mean()
477 normalizing = numpy.sqrt(((realResults-meanref)**2).sum()) #
squared 2-norm of reference vector
478
479 err_HMT = err1/normalizing

```

```

480
481
482 #Two Seperate Dummy Files
483 dummyFile=open(str(directory) + dummyFileName, 'a+')
484 dummyFile_short=open(str(directory) + dummyFileName_short, 'a+')
485
486 dummyFile.write('** iteration #' + str(iterNo)+' **\n\n')
487 dummyFile.write('Material constants = ' + str(MatProps)+'\n\n')
488 # dummyFile.write('Measured Result:'+str(realResults)+'\n\n')
489 # dummyFile.write('Computed Result:'+str(FE_results)+'\n\n')
490 # dummyFile.write('Error:'+str(err3)+'\n\n')
491 dummyFile.write('NRMSE:'+str(err_HMT)+'\n\n')
492 dummyFile.write('
-----\n\n')
493 dummyFile.close()
494
495 dummyFile_short.write('** iteration #' + str(iterNo)+' **\n\n')
496 dummyFile_short.write('Material constants = ' + str(MatProps)+'
\n')
497 dummyFile_short.write('NRMSE = ' + str(err_HMT)+'\n\n')
498 dummyFile_short.write('
-----\n\n')
499 dummyFile_short.close()
500
501 time.sleep(5)
502 print('iteration #' + str(iterNo))
503 print('Mat Constants = ' + str(MatProps))
504 print('NRMSEerr = ' + str(err_HMT) + '\n\n')
505 print('-----\n')
506
507 #Txt file that contains the material properties and cost function
value at each iteration (Materials & Energies txt file)
508 dummy2 = open(dummy2_Name, 'a+')
509 dummy2.write('** iteration #' + str(iterNo) + ' **\n\n')
510 dummy2.write('TissueC10 = ' + str(MatProps[0]) + '\n')
511 dummy2.write('TissueC20 = ' + str(MatProps[1]) + '\n')
512 # dummy2.write('Section2C10 = ' + str(MatProps[2]) + '\n')
513 # dummy2.write('Section2C20 = ' + str(MatProps[3]) + '\n')
514 # dummy2.write('Section3C10 = ' + str(MatProps[4]) + '\n')
515 # dummy2.write('Section3C01 = ' + str(MatProps[5]) + '\n')
516 # dummy2.write('Section4C10 = ' + str(MatProps[6]) + '\n')
517 # dummy2.write('Section4C01 = ' + str(MatProps[7]) + '\n')
518
519 dummy2.write('Cost function value = ' + str(err_HMT) + '\n')
520 #dummy2.write('Force Difference = ' + str(err_HMT_f)) + '\n'
521 #dummy2.write('Displacement Difference = ' + str(err_HMT_u) +
'\n')
522 dummy2.write('\n
-----\n\n')
523 dummy2.close()
524
525 #Txt file that contains the computed displacements at each
iteration (Computed displacements txt file)
526 dummy3 = open(str(directory) + dummy3_Name, 'a+')
527 dummy3.write('** iteration #' + str(iterNo)+' **\n\n')
528 dummy3.write('Computed Result:'+str(ComputedDeformation)+'\n')
529 dummy3.write('-----\n\
n')

```

```

530 dummy3.close()
531
532     return err_HMT
533 ## -----Main body of the script
534     -----
535 MeasuredDeformation_Global, NoGridSegments = StrainFromExcel()
536
537 # Nodes_Global_RF = NodeNoFromMatFiles_RF()
538 Nodes_Global = NodeNoFromMatFiles()
539
540
541 #print (MeasuredDeformation_Global, NoGridSegments)
542 print (NoGridSegments)
543
544
545 old_deformation = []
546 iterNo=0
547 ##-----Bayesian Optimization
548     -----
549 #matproperties_all = io.loadmat('C:\\Users\\SuGuvenir\\Desktop\\
    Paper_2_Coronary_iFEM_OCT_SuGuvenir\\9
    _Documents_For_First_Run_Coronary\\1
    _FirstRun_Sample_FEM_S10_138_US_148_4_su_coronary\\Matlab\\
    matproperties_to_python_temp.mat')
550 #matproperties_all = io.loadmat('C:\\Users\\SuGuvenir\\Desktop\\
    Case_11_12_17_Right\\7_InverseFiniteElement\\Matlab\\
    matproperties_to_python_temp.mat')
551 #matproperties = matproperties_all['matProperties'][0]
552 #NRMSE = residuals(matproperties, iteration,
    MeasuredDeformation_Global)
553 #io.savemat('C:\\Users\\SuGuvenir\\Desktop\\
    Paper_2_Coronary_iFEM_OCT_SuGuvenir\\9
    _Documents_For_First_Run_Coronary\\1
    _FirstRun_Sample_FEM_S10_138_US_148_4_su_coronary\\Matlab\\
    from_python_Abaqus_NRMSE_temp.mat', {'NRMSE':NRMSE})
554 #try:
555     #os.remove(directory + '\\report1.rpt')
556 #except OSError:
557     #pass
558 #try:
559     #os.remove(directory + '\\report2.rpt')
560 #except OSError:
561     #pass
562 #try:
563     #os.remove(directory + '\\report3.rpt')
564 #except OSError:
565     #pass
566 #io.savemat('C:\\Users\\SuGuvenir\\Desktop\\Case_11_12_17_Right\\7
    _InverseFiniteElement\\Matlab\\from_python_Abaqus_NRMSE_temp.mat
    ', {'NRMSE':NRMSE})
567
568 #
569     #-----

```

```

570 #-----Differential Evolution
571 -----
572 Bounds = [(50, 1500), (50, 1500)]
573
574 def additional_stopping_criterion(current_guess, convergence):
575     current_energy = residuals(current_guess, iteration,
576                               MeasuredDeformation_Global)
577     if current_energy < 0.01:
578         return True
579
580 sol = scipy.optimize.differential_evolution(residuals, Bounds, args
581                                             =(iteration, MeasuredDeformation_Global), strategy='best2bin',
582                                             maxiter=1000,
583                                             popsize=25, tol=0.01,
584                                             mutation=(0.5, 1.25), recombination=1.0,
585                                             seed=None, callback=
586                                             None, disp=True, polish=False, init='latinhypercube')
587 print(sol)
588
589
590 data_report = open(str(directory) + '\
591                   Diff_Evolution_NH_80mmHg_5cols.txt', 'a+')
592 data_report.write('Function Evaluations = ' + str(sol['nfev']) + '\n')
593 data_report.write('Generations (iterations) = ' + str(sol['nit']) + '\
594                   n')
595 data_report.write('Function best value = ' + str(sol['fun']) + '\n')
596 data_report.write('Results = ' + str(sol['x']) + '\n')
597 data_report.write('Reason for termination = ' + str(sol['message']) +
598                   '\n')
599 data_report.write('Optimality = ' + str(sol['success']) + '\n')
600 data_report.write('\n
601                   -----\n\n')
602 data_report.close()
603
604
605 time.sleep(5)
606
607 try:
608     os.rename(directory + '\\dummyMatEstimation.txt', directory + '
609               \\ ' + JobName + '\\dummyMatEstimation.txt')
610 except OSError:
611     pass
612
613 try:
614     os.remove(directory + '\\dummyMatEstimation.txt')
615 except OSError:
616     pass
617
618 try:
619     os.rename(directory + '\\dummyMatEstimation_short.txt',
620               directory + '\\ ' + JobName + '\\dummyMatEstimation_short.txt')
621 except OSError:
622     pass
623
624 try:
625     os.remove(directory + '\\dummyMatEstimation_short.txt')

```

```
616 except OSError:  
617     pass
```

```
[language=Python]
```

# Appendix IV -Supplementary results to the synthetic data study

Supplementary results from synthetic data study.

## I Grid study

### I.1 Estimation procedure

Grid 0.2x0.2 mm

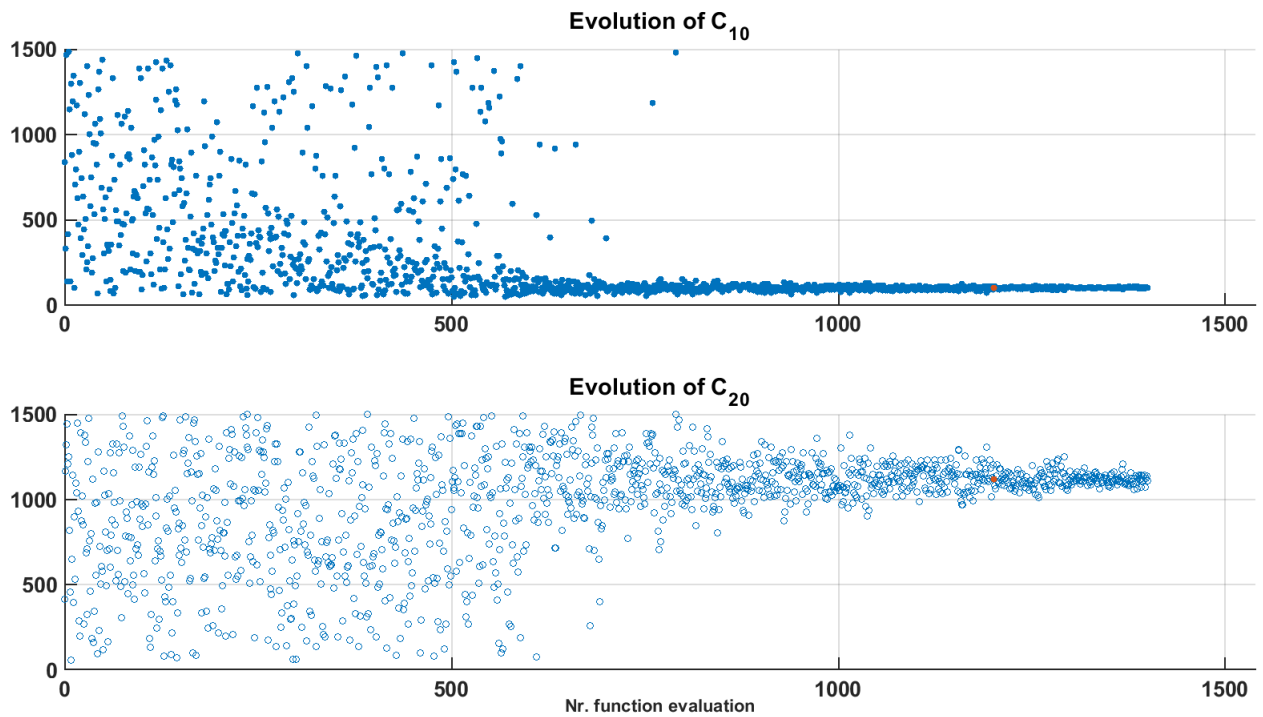


Figure 45: Evolution of material properties using grid 0.2x0.2.

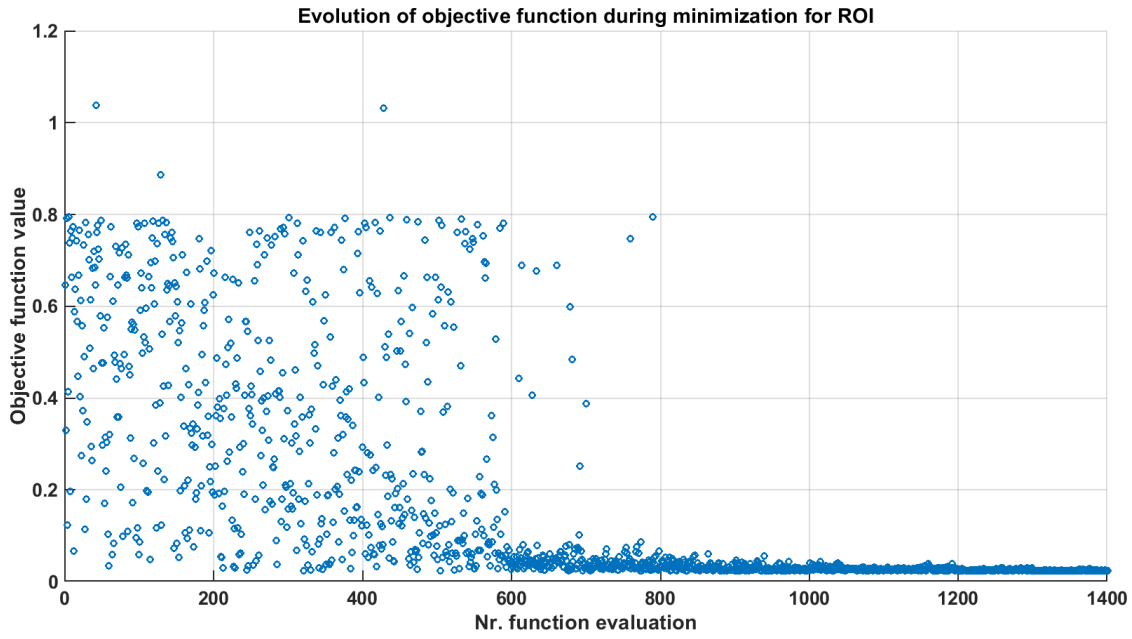


Figure 46: Evolution of the objective function for the estimation procedure belonging to grid 0.2x0.2.

### Grid 0.3x0.3 mm

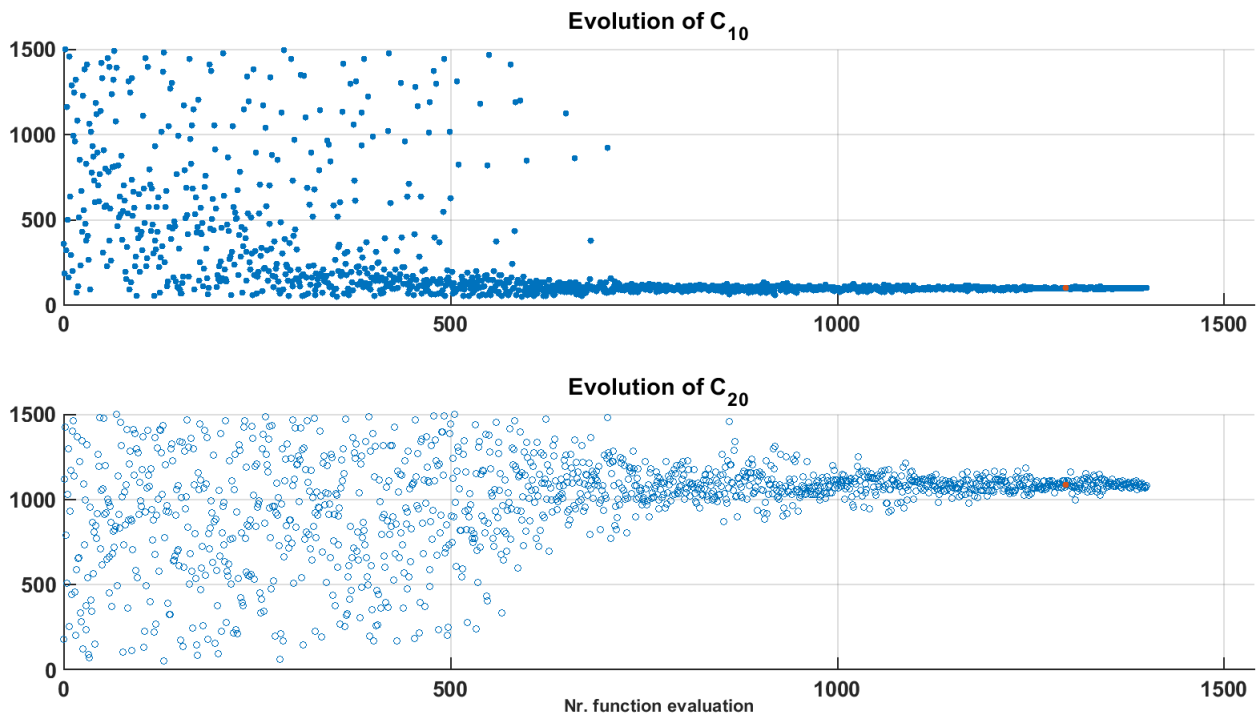


Figure 47: Evolution of material properties using grid 0.3x0.3.

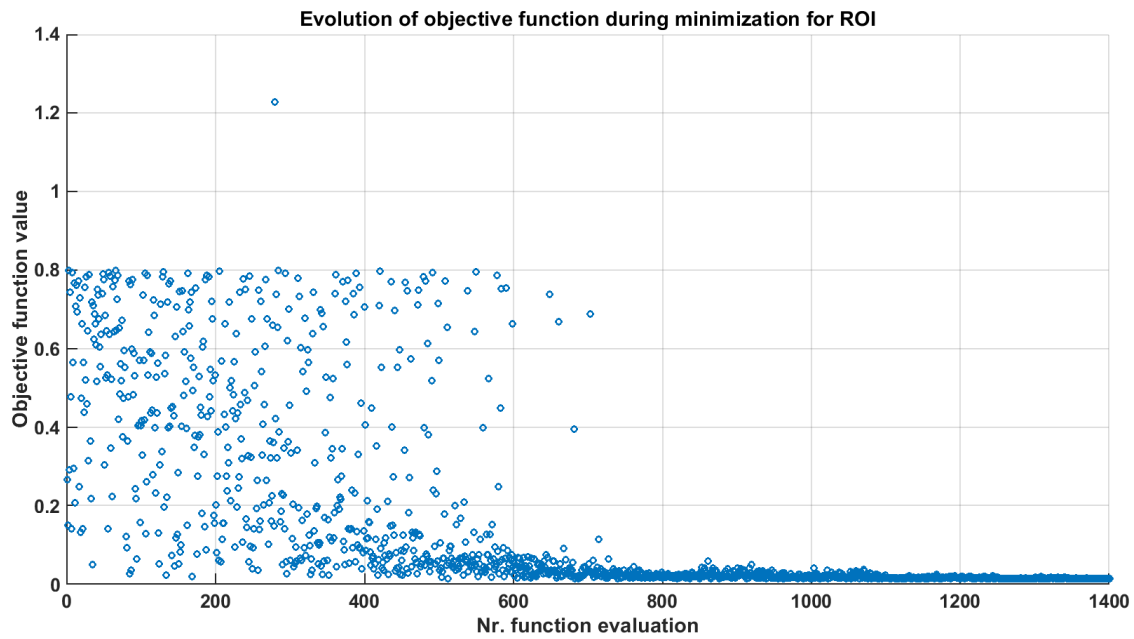


Figure 48: Evolution of the objective function for the estimation procedure belonging to grid 0.3x0.3.

## I.2 Resulting displacement fields

### Step 2

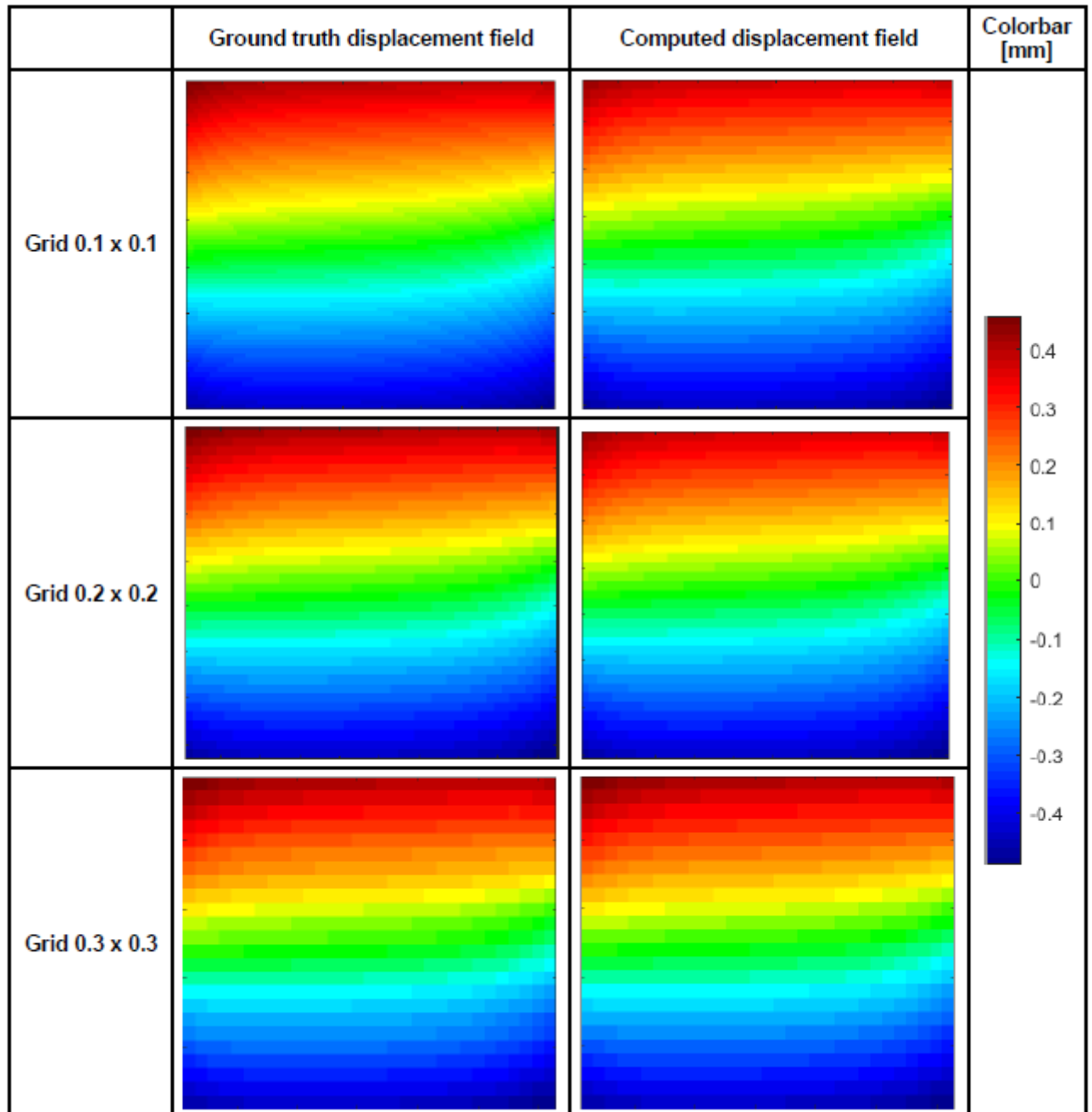


Figure 49: Comparison between the GTD and CD displacement field using different grid sizes. Left side shows the grid applied on the GTD and right side shows the grid applied on the CD. Grid 1, Grid 2 and Grid 3 are shown from top moving towards the bottom. The displacement fields belong to step 2.

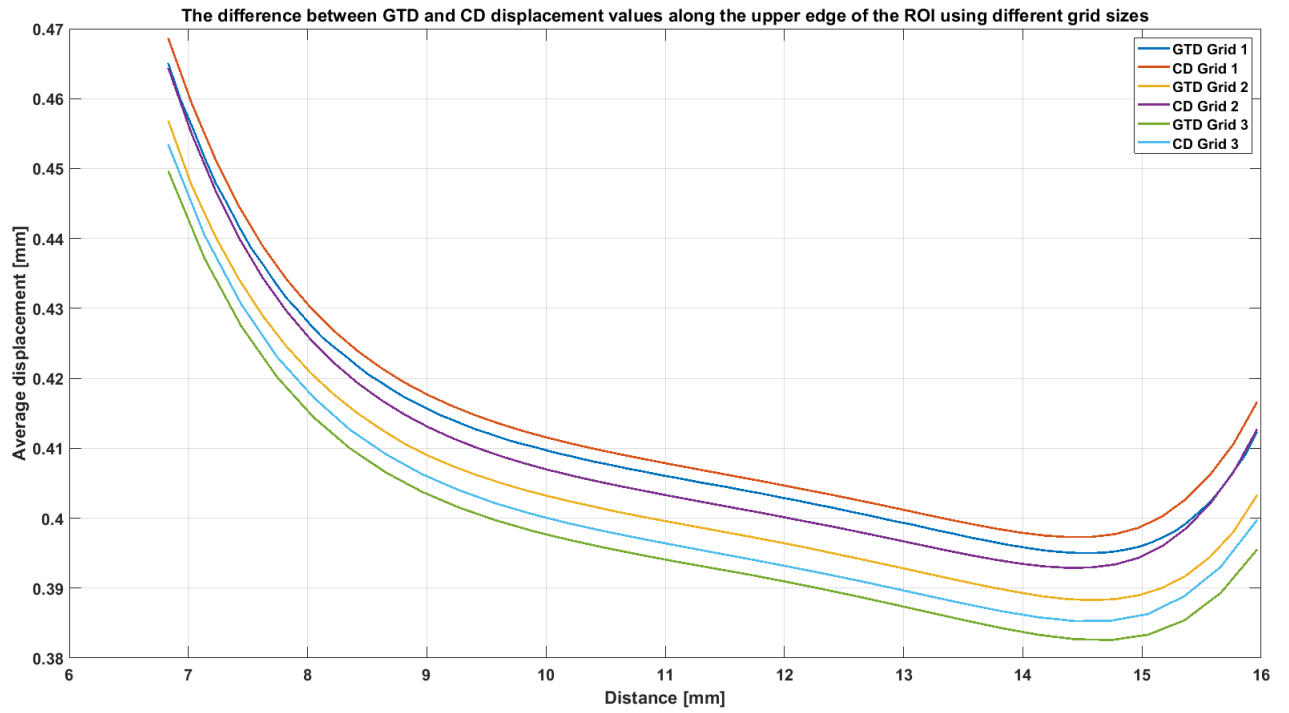


Figure 50: The Distribution of displacement values from different grid sizes. The figure contains the distributions from the GTD and from the CD. The distribution belongs to loading step 2.

step 3

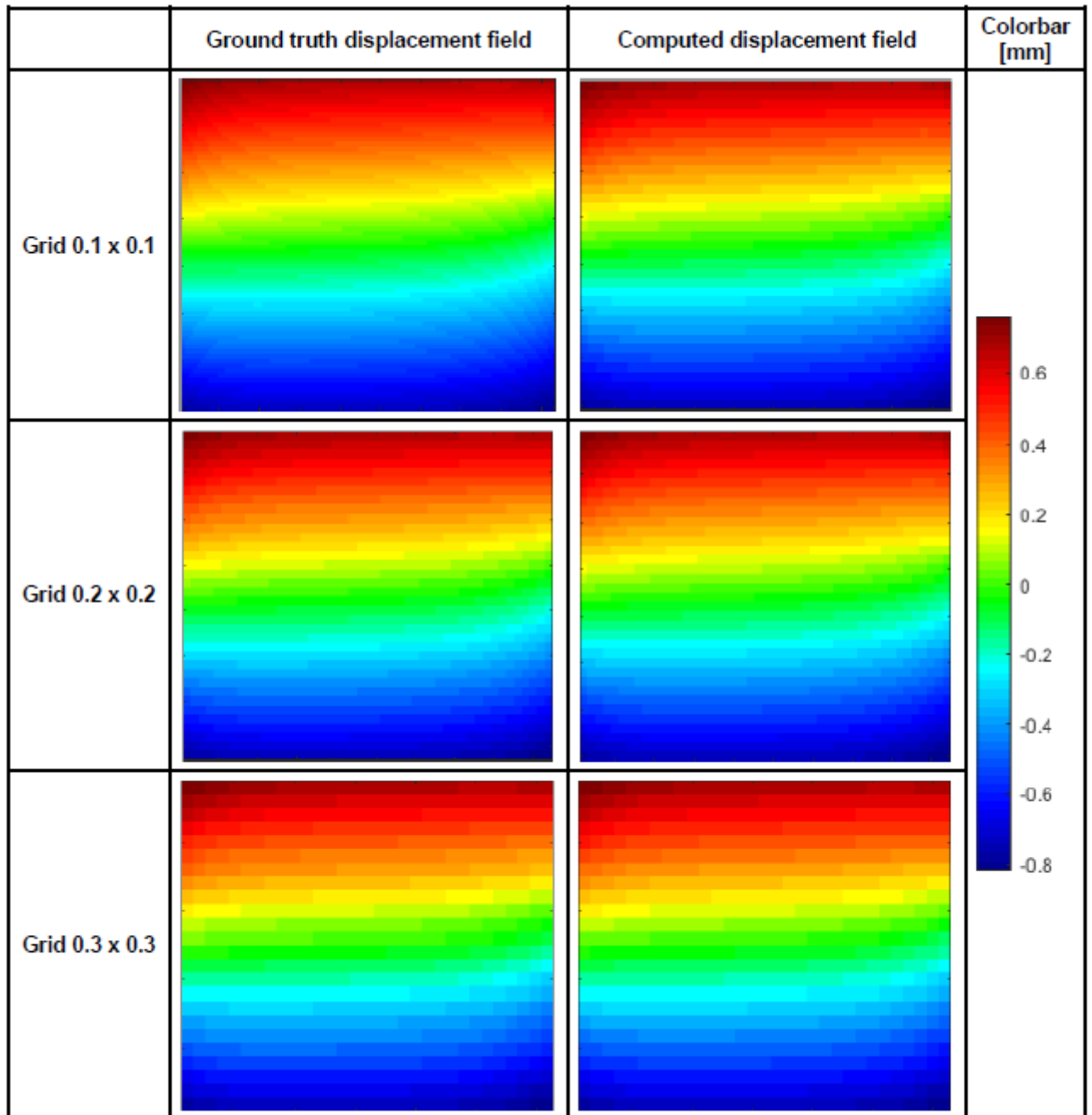


Figure 51: Comparison between the GTD and CD displacement field using different grid sizes. Left side shows the grid applied on the GTD and right side shows the grid applied on the CD. Grid 1, Grid 2 and Grid 3 are shown from top moving towards the bottom. The displacement fields belong to step 3.

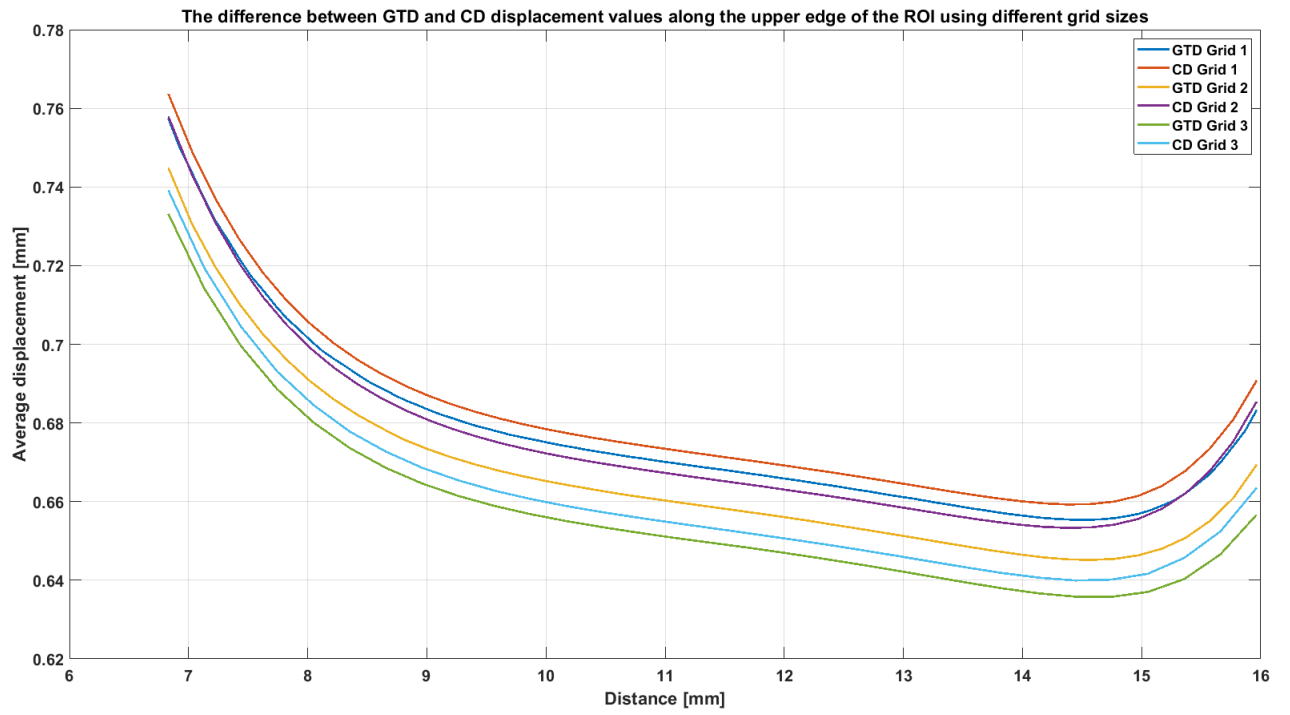


Figure 52: The Distribution of displacement values from different grid sizes. The figure contains the distributions from the GTD and from the CD. The distribution belongs to loading step 3.

## J Noise study

### J.1 Estimation procedure

Grid 0.2x0.2, Noise 1 %

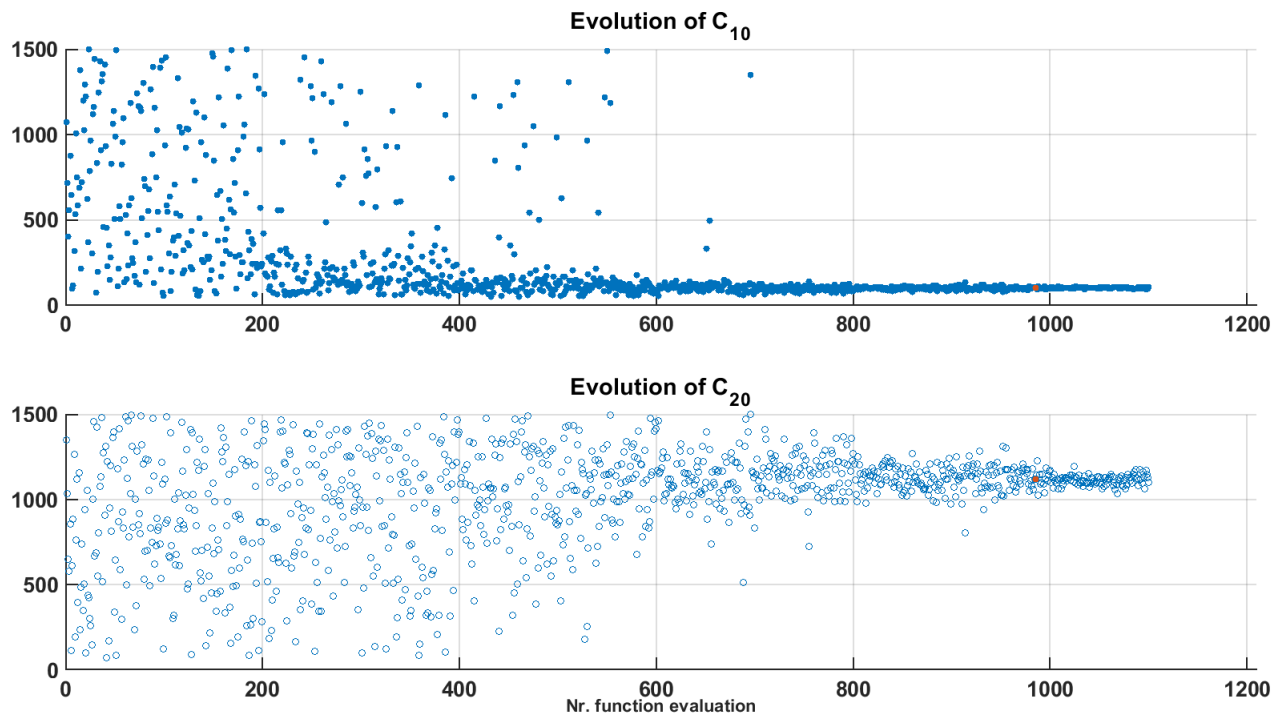


Figure 53: Evolution of material properties using grid 0.2x0.2 and implementing 1 % noise in the GTD

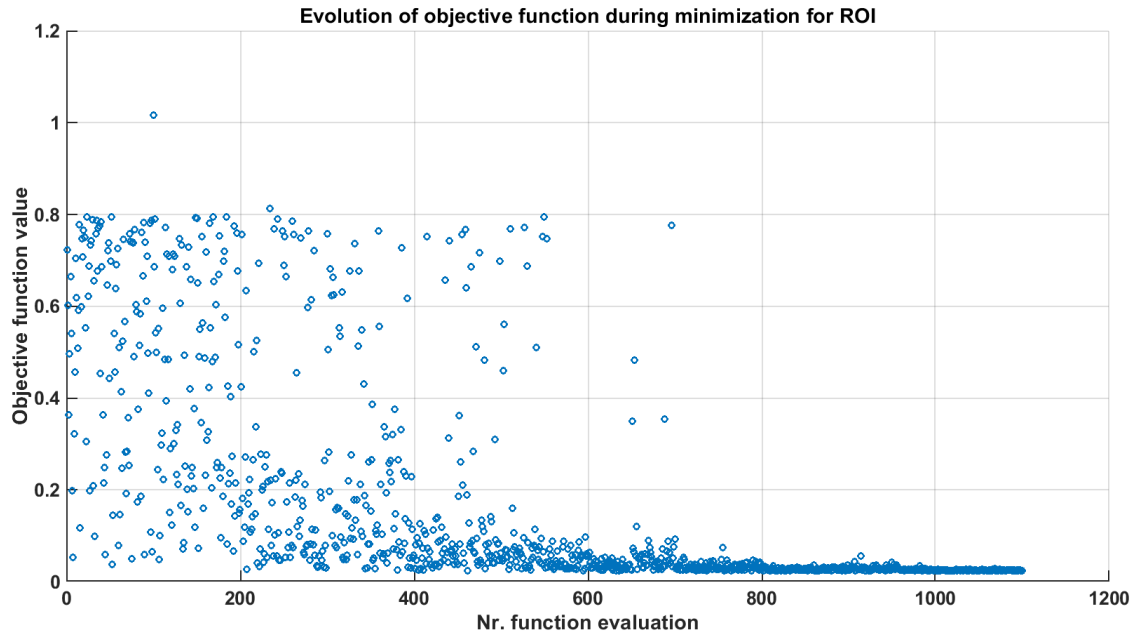


Figure 54: Evolution of the objective function for the estimation procedure belonging to grid 0.2x0.2 and 1 % noise in the GTD

Grid 0.2x0.2, Noise 2 %

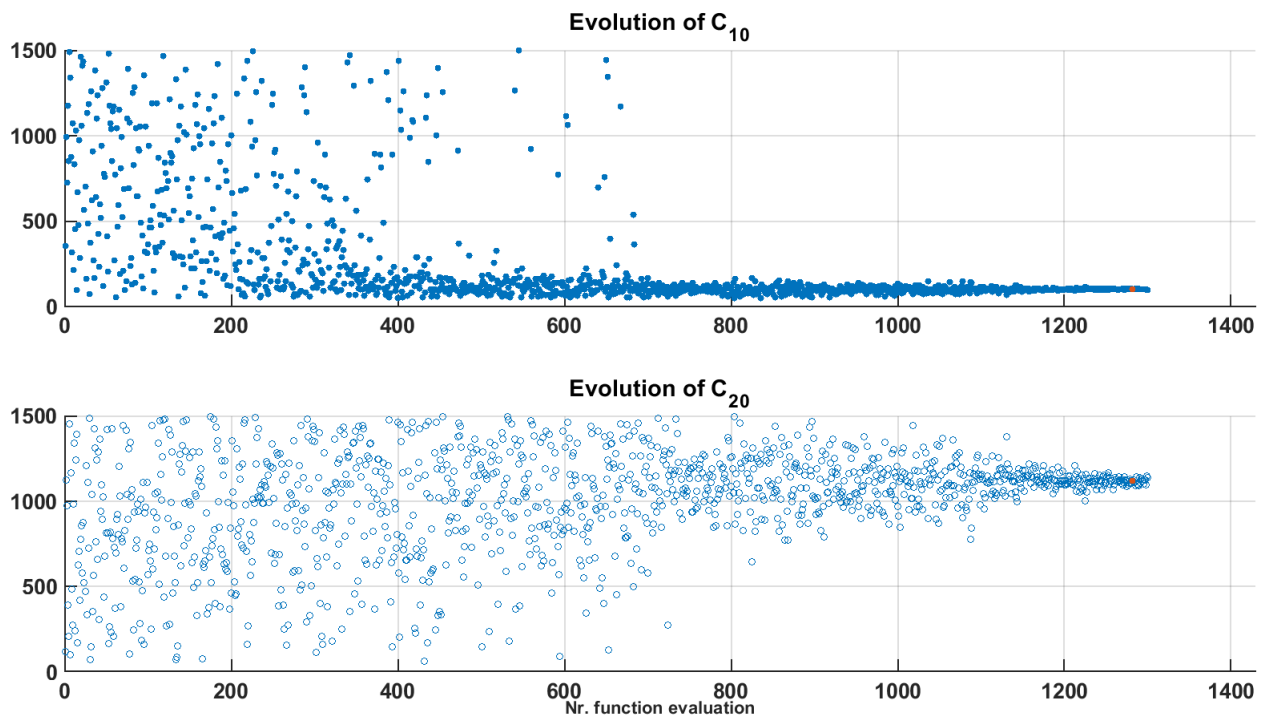


Figure 55: Evolution of material properties using grid 0.2x0.2 and implementing 2 % noise in the GTD

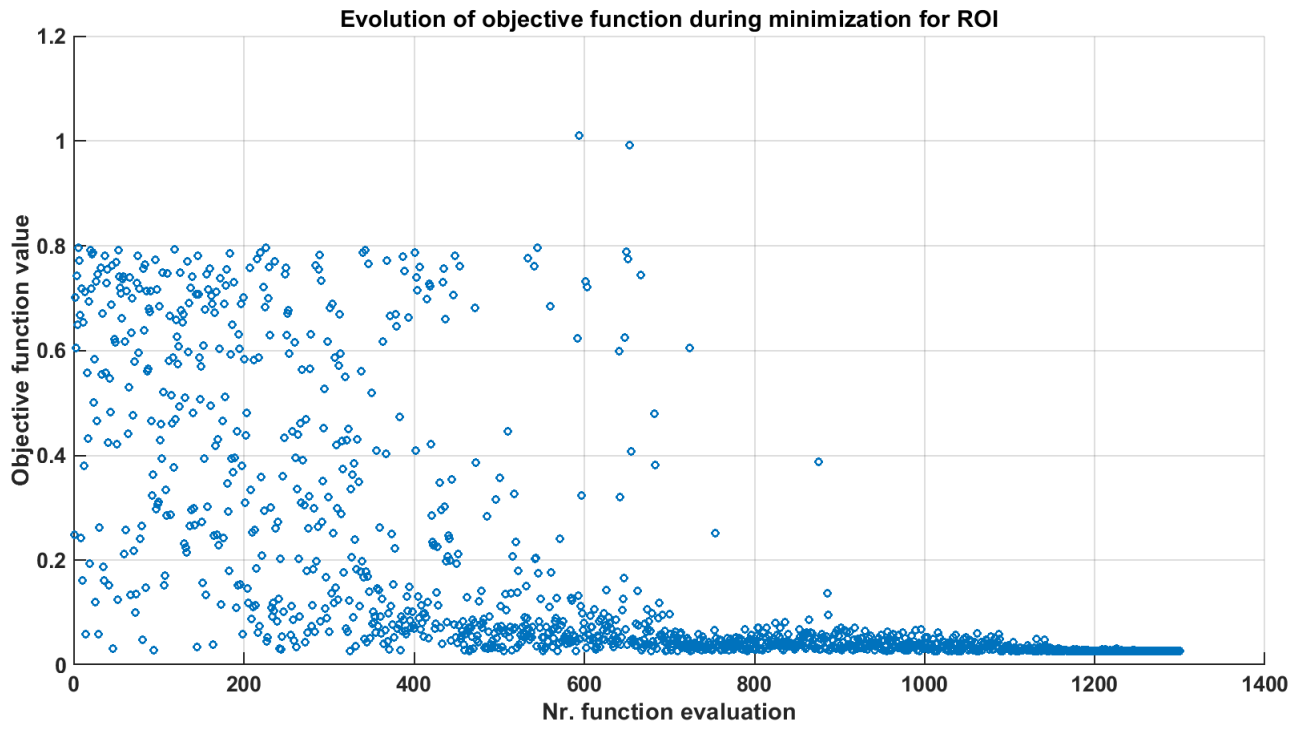


Figure 56: Evolution of the objective function for the estimation procedure belonging to grid  $0.2 \times 0.2$  and 2 % noise in the GTD

Grid 0.3x0.3, Noise 1 %

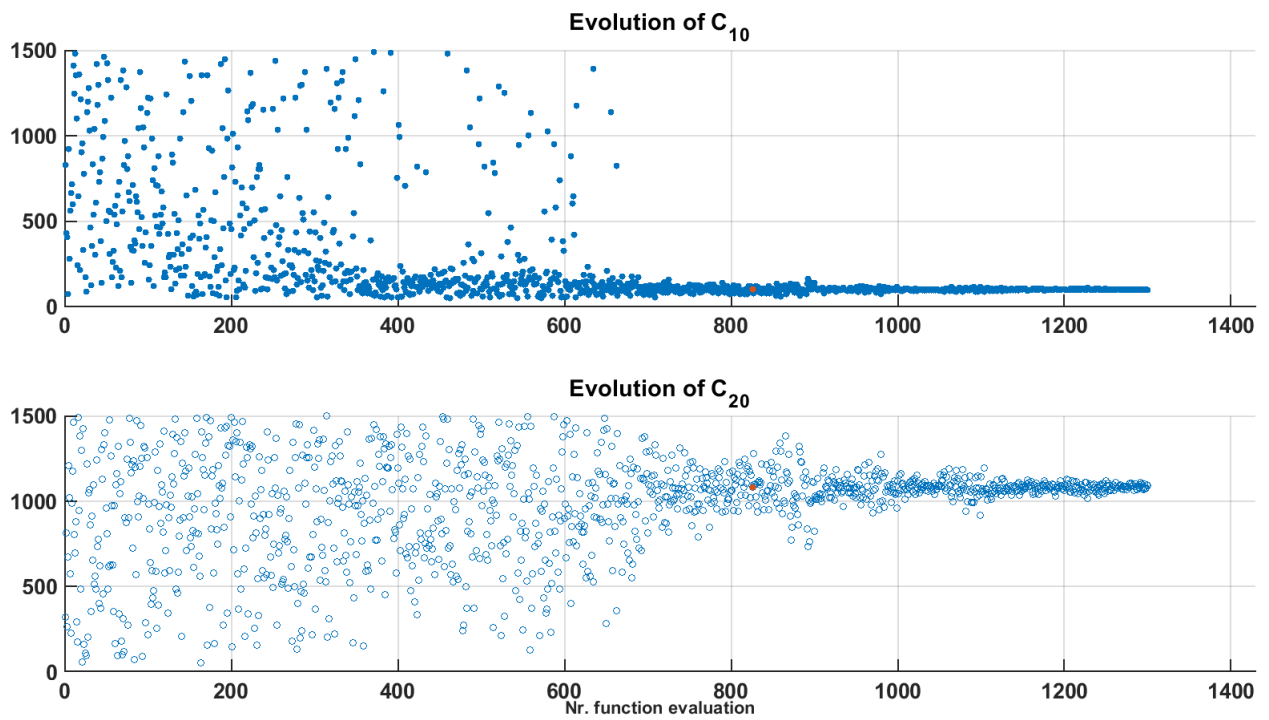


Figure 57: Evolution of material properties using grid 0.3x0.3 and implementing 1 % noise in the GTD

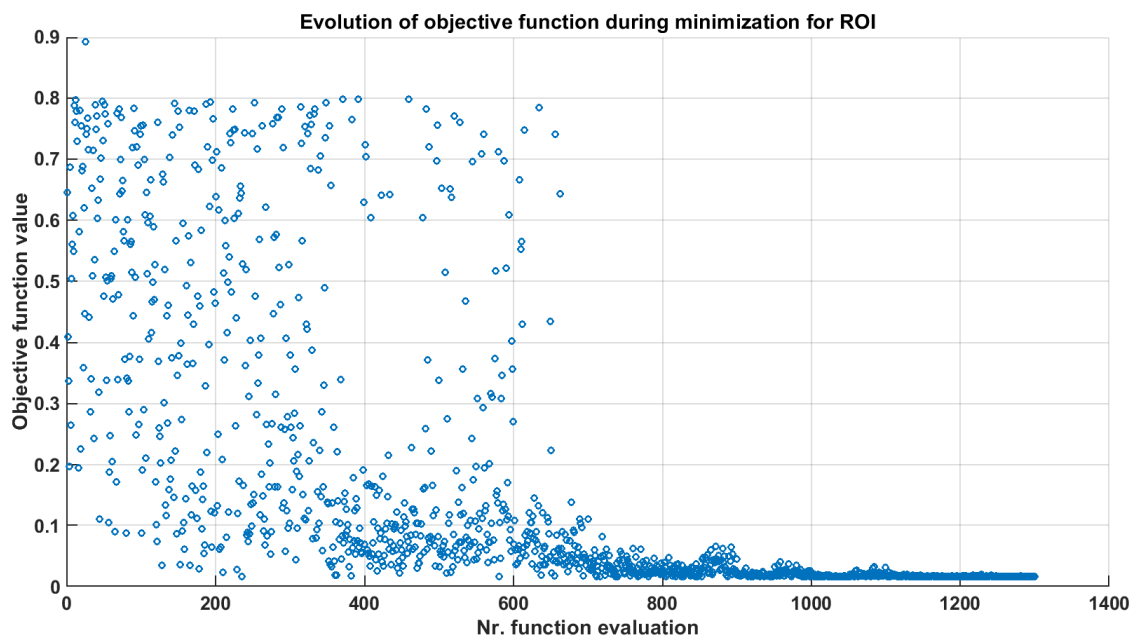


Figure 58: Evolution of the objective function for the estimation procedure belonging to grid 0.3x0.3 and 1 % noise in the GTD

Grid 0.3x0.3, Noise 2 %

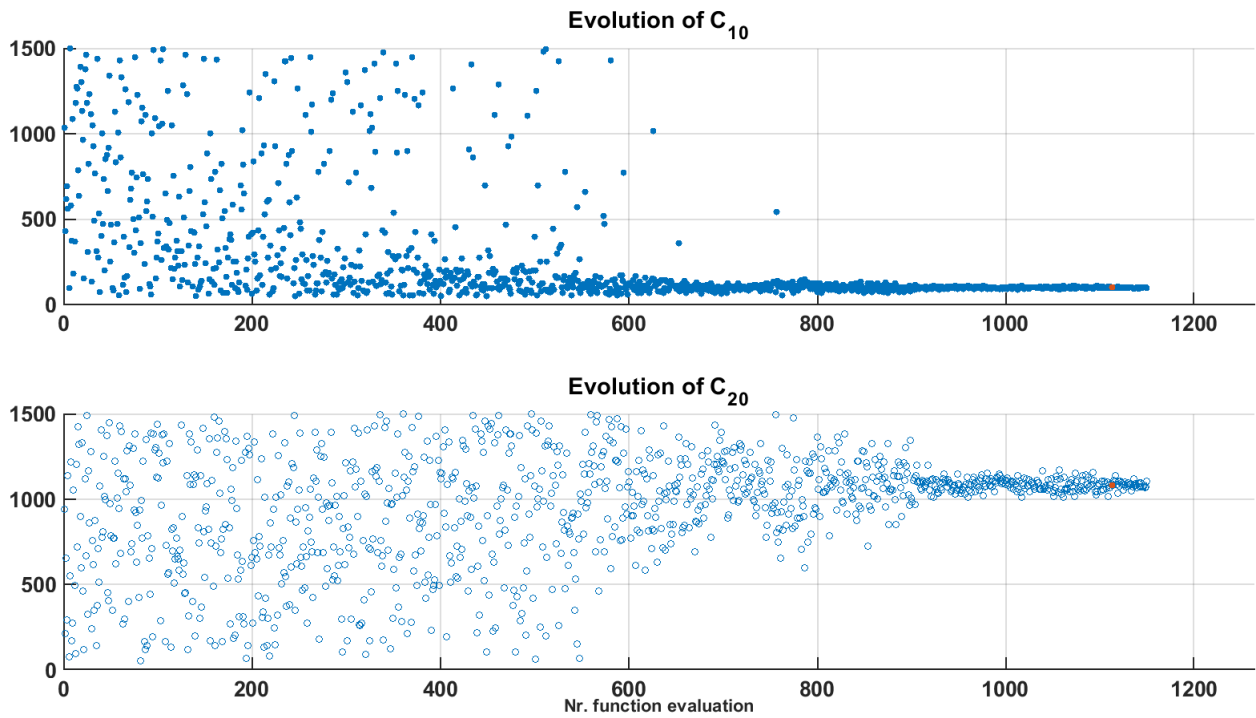


Figure 59: Evolution of material properties using grid 0.3x0.3 and implementing 2 % noise in the GTD

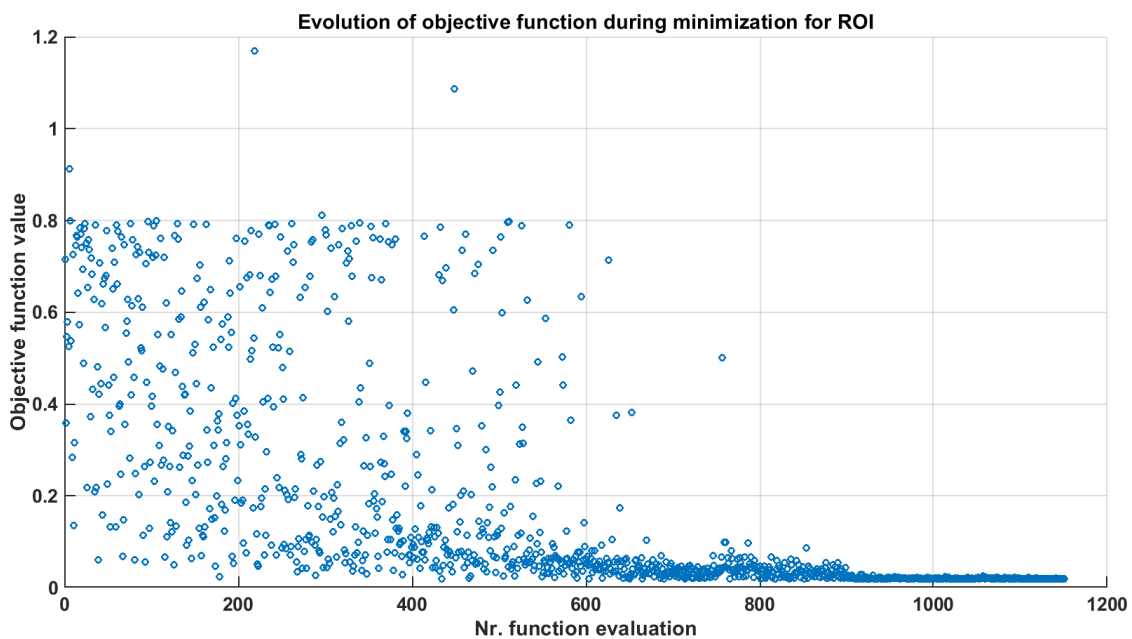


Figure 60: Evolution of the objective function for the estimation procedure belonging to grid 0.3x0.3 and 2 % noise in the GTD

## J.2 Resulting displacement fields

### Grid 2 - step 1

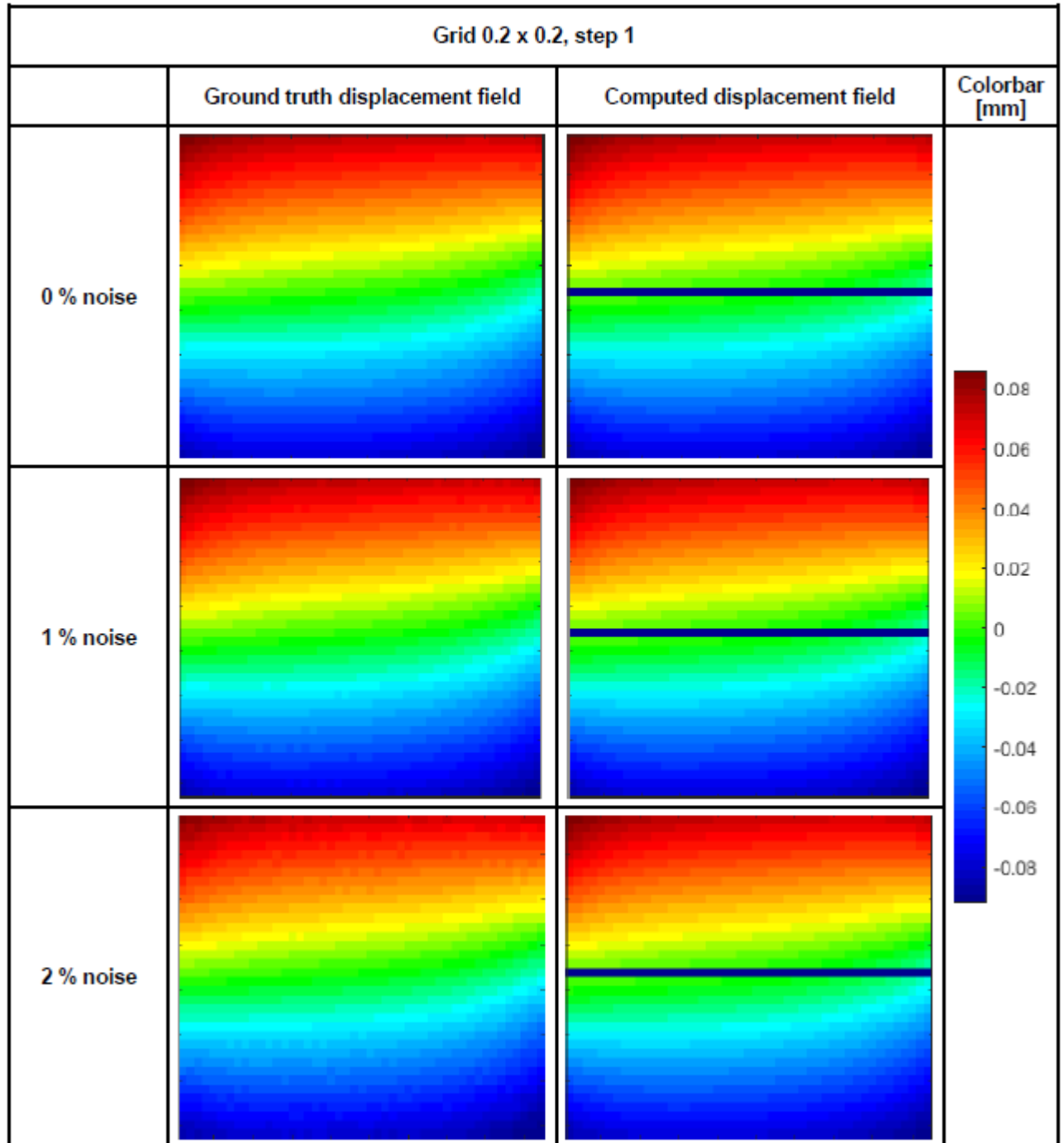


Figure 61: Comparison between GTD and CD displacement fields with increased noise. The displacement fields belong to grid 0.2x0.2 at step 1.

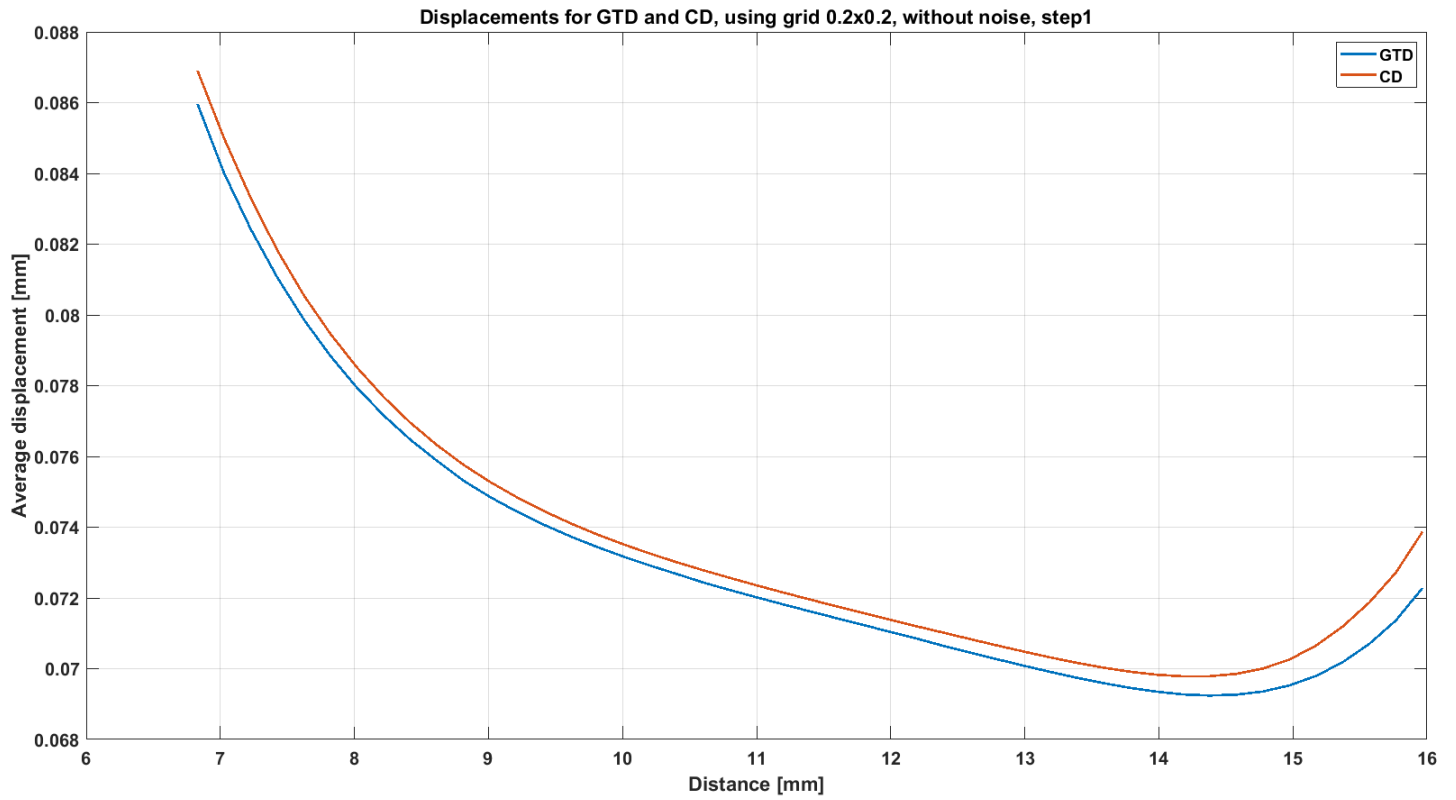


Figure 62: The Distribution of displacement values using grid 0.2x0.2 and implementing no noise. The figure contains the distributions from the GTD and from the CD. The distribution belongs to loading step 1.

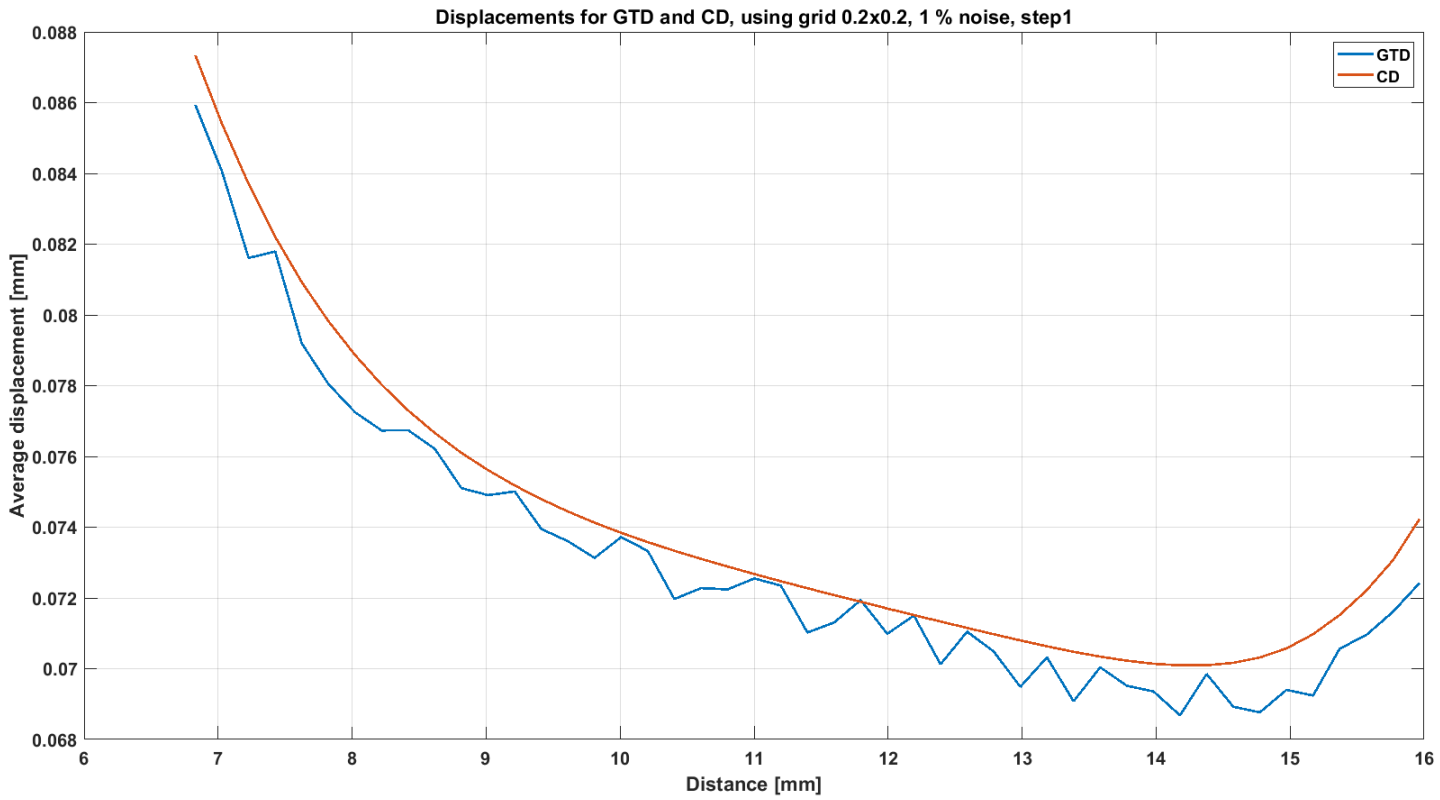


Figure 63: The Distribution of displacement values using grid 0.2x0.2 and implementing 1% noise. The figure contains the distributions from the GTD and from the CD. The distribution belongs to loading step 1.

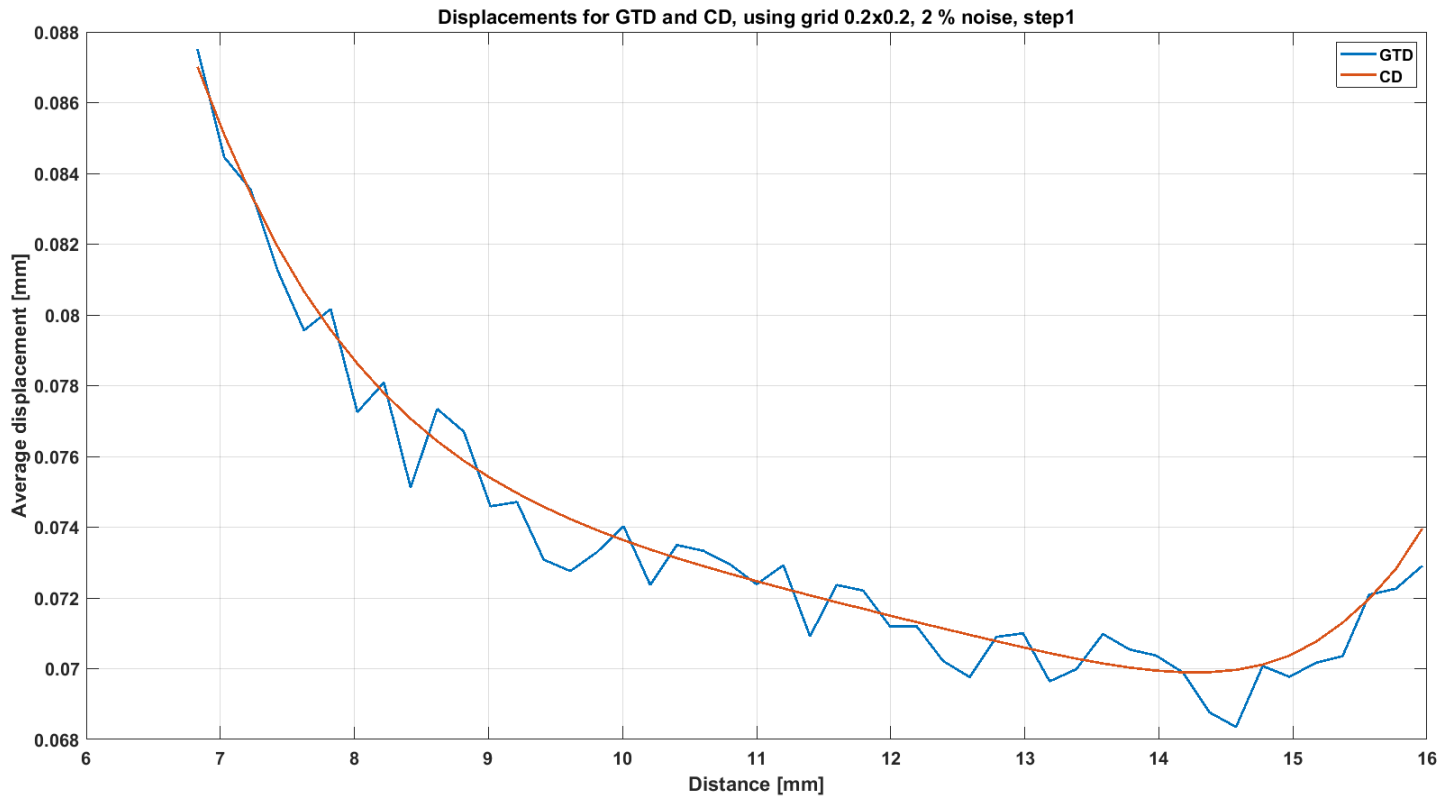


Figure 64: The Distribution of displacement values using grid 0.2x0.2 and implementing 2% noise. The figure contains the distributions from the GTD and from the CD. The distribution belongs to loading step 1.

Grid 2 - step 2

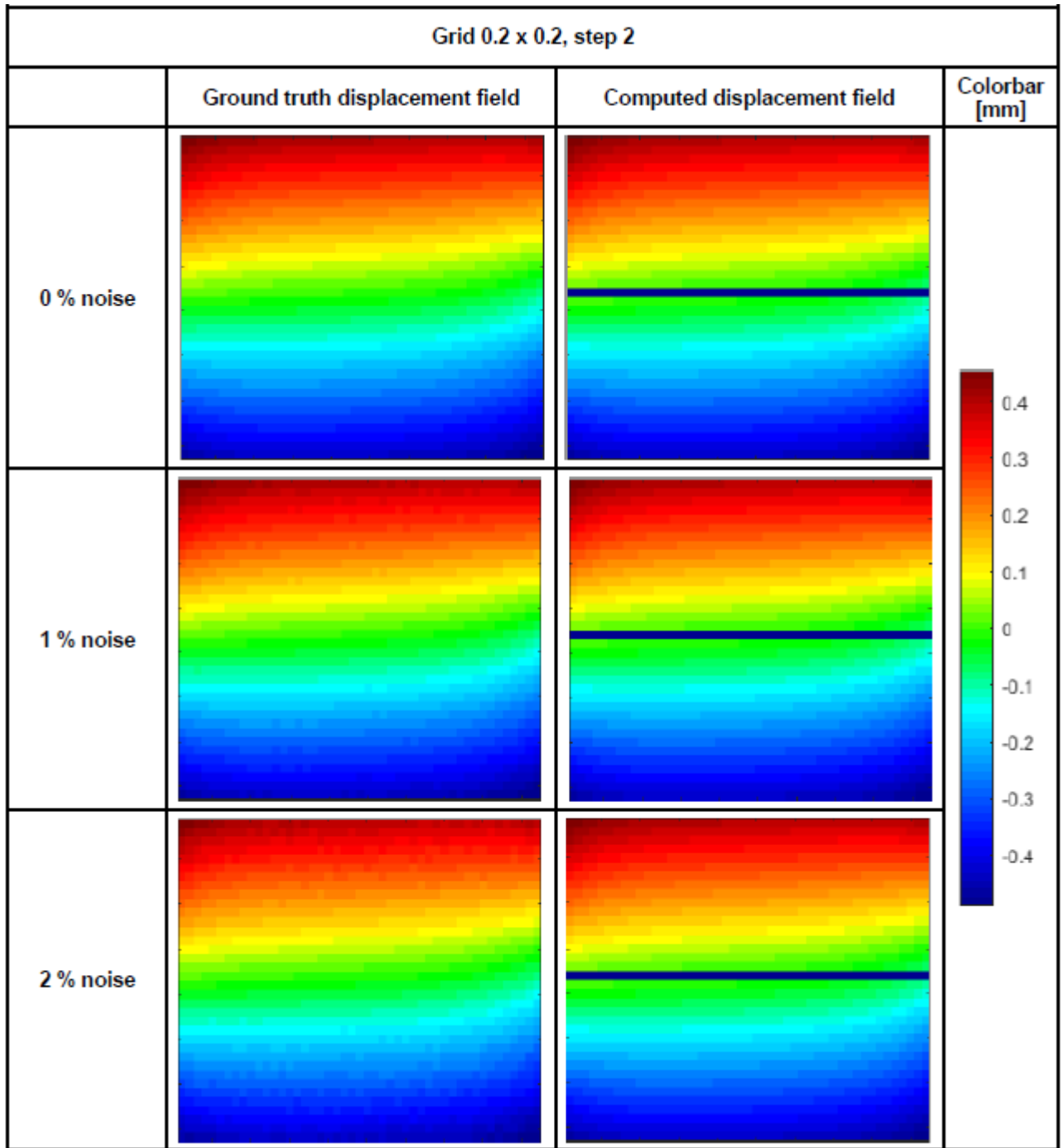


Figure 65: Comparison between GTD and CD displacement fields with increased noise. The displacement fields belong to grid 0.2x0.2 at step 2.

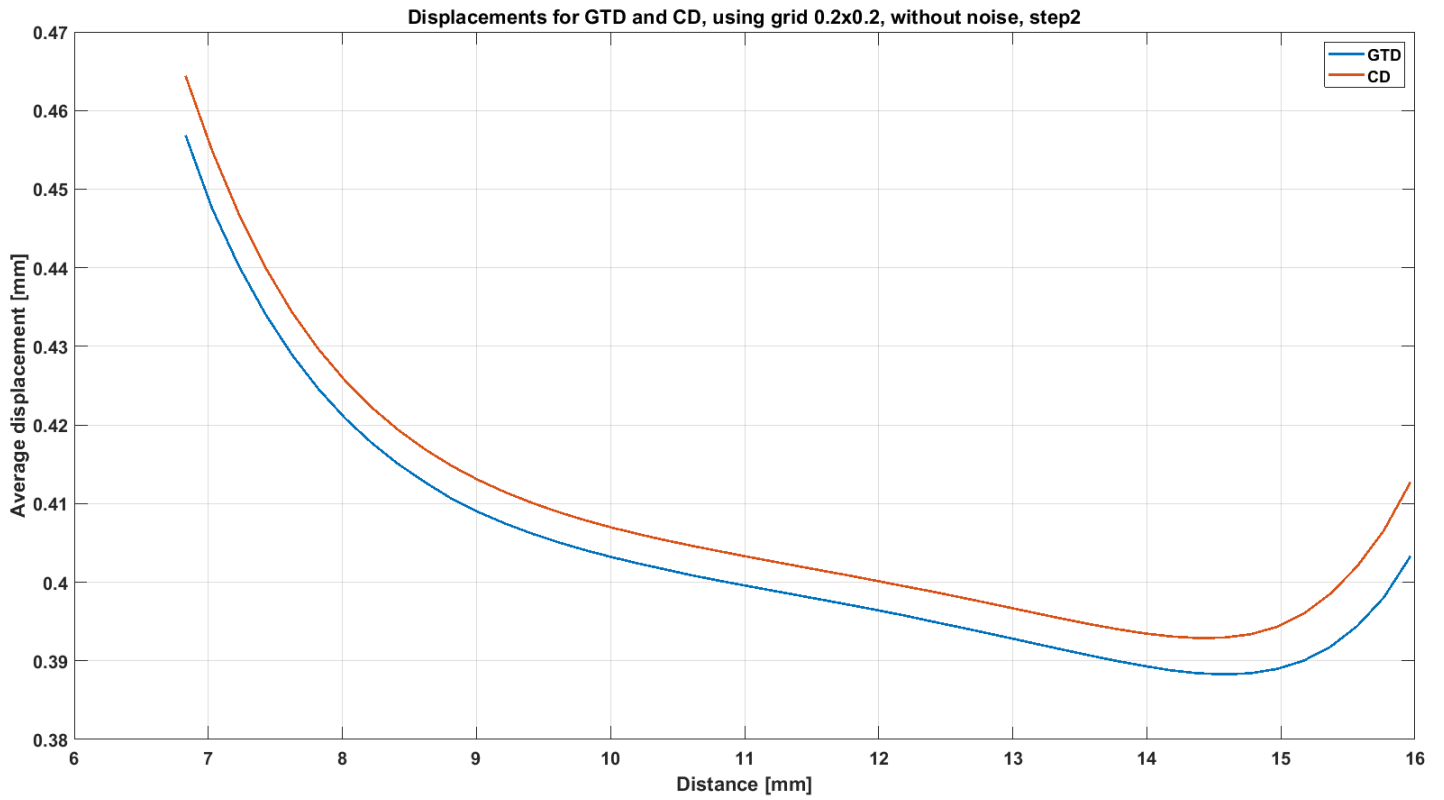


Figure 66: The Distribution of displacement values using grid 0.2x0.2 and implementing no noise. The figure contains the distributions from the GTD and from the CD. The distribution belongs to loading step 2.

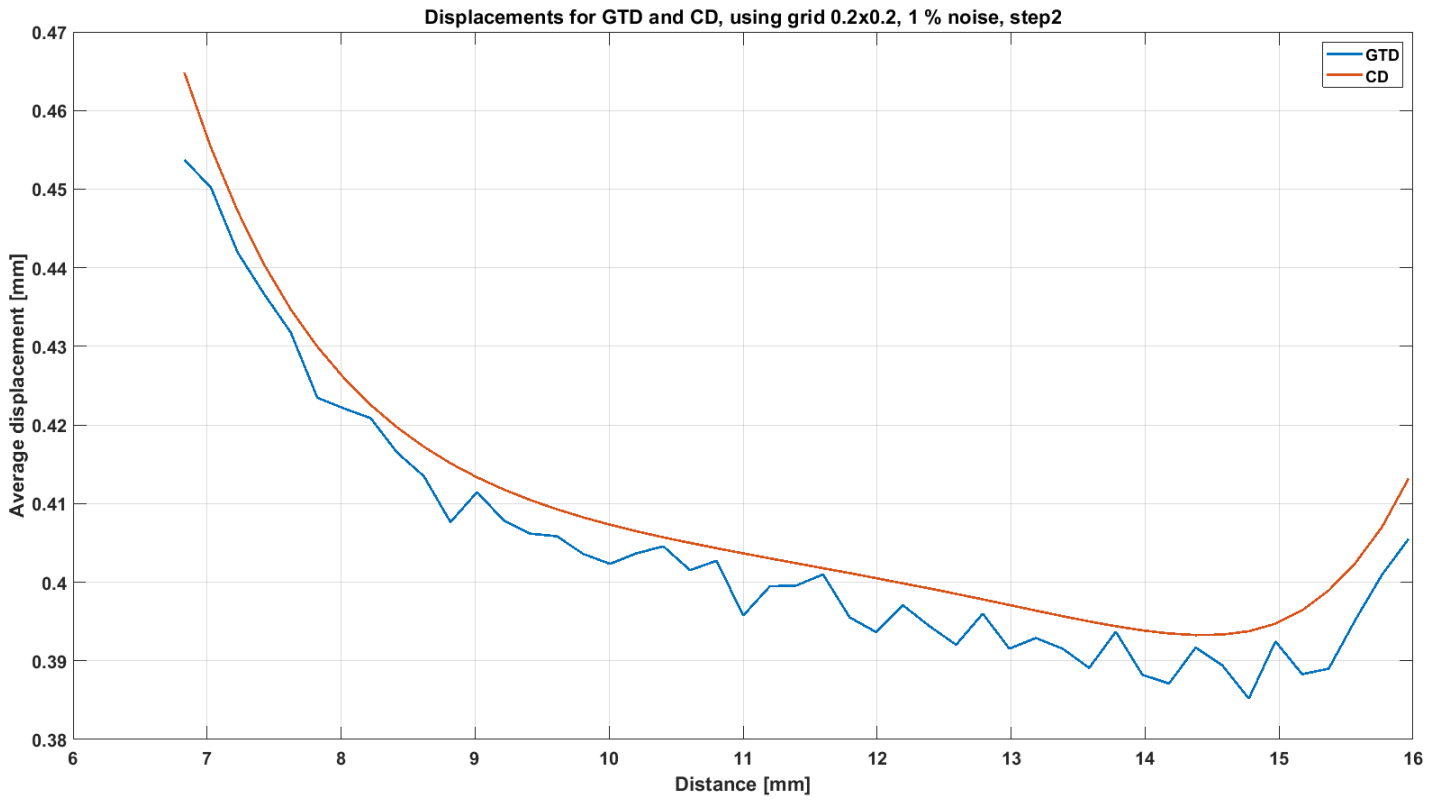


Figure 67: The Distribution of displacement values using grid 0.2x0.2 and implementing 1% noise. The figure contains the distributions from the GTD and from the CD. The distribution belongs to loading step 2.

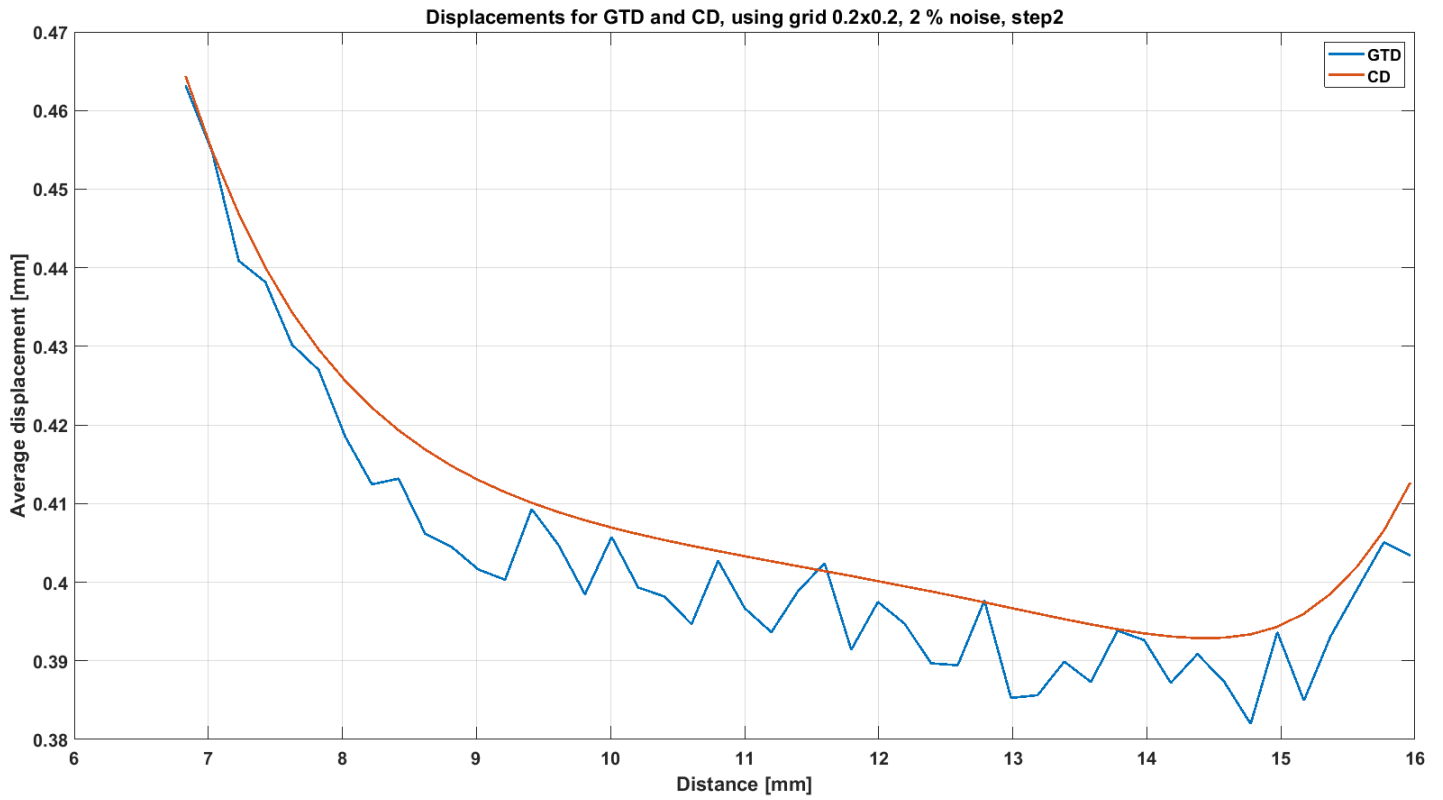


Figure 68: The Distribution of displacement values using grid 0.2x0.2 and implementing 2% noise. The figure contains the distributions from the GTD and from the CD. The distribution belongs to loading step 2.

Grid 2 - step 3

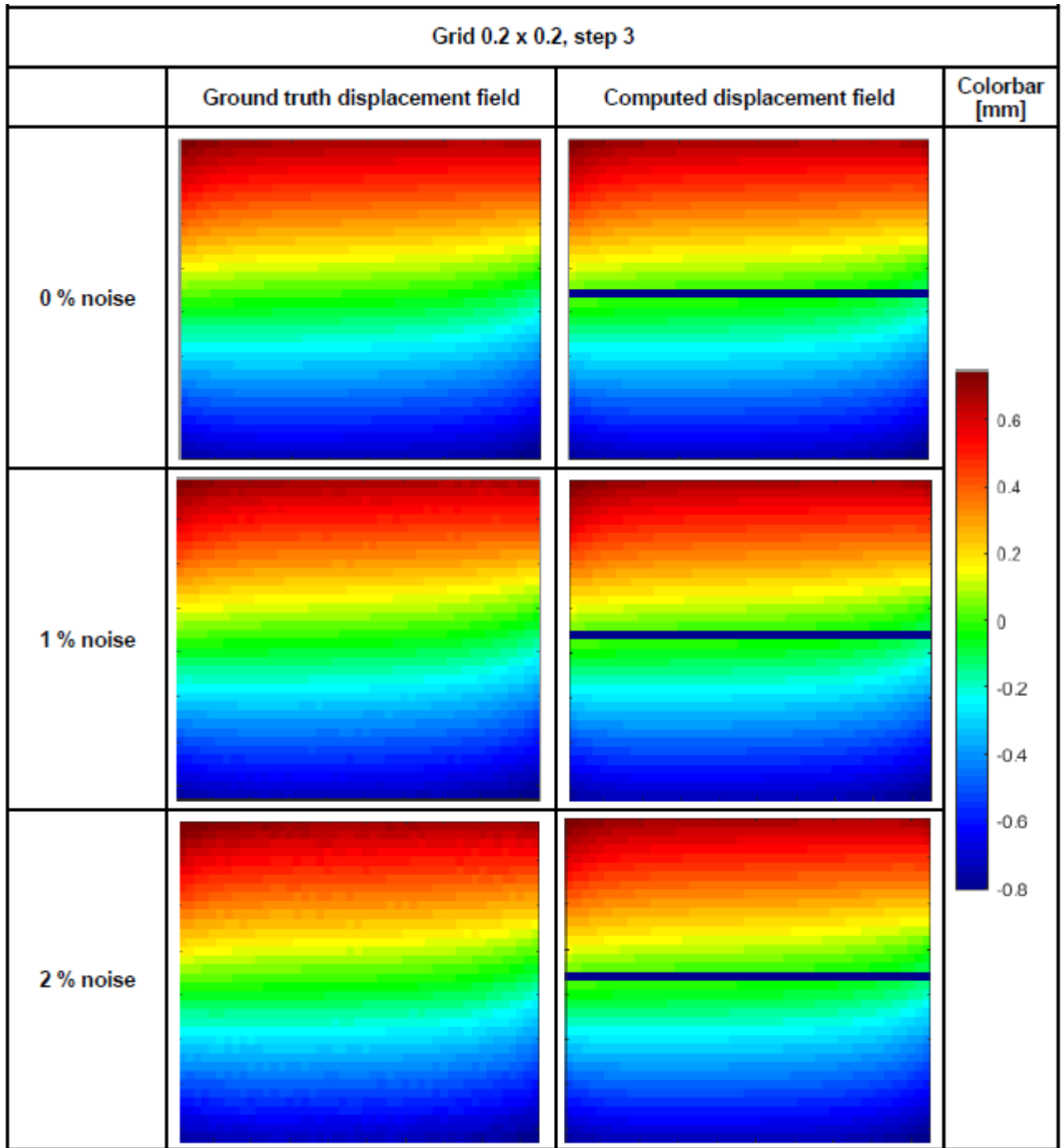


Figure 69: Comparison between GTD and CD displacement fields with increased noise. The displacement fields belong to grid 0.2x0.2 at step 3.

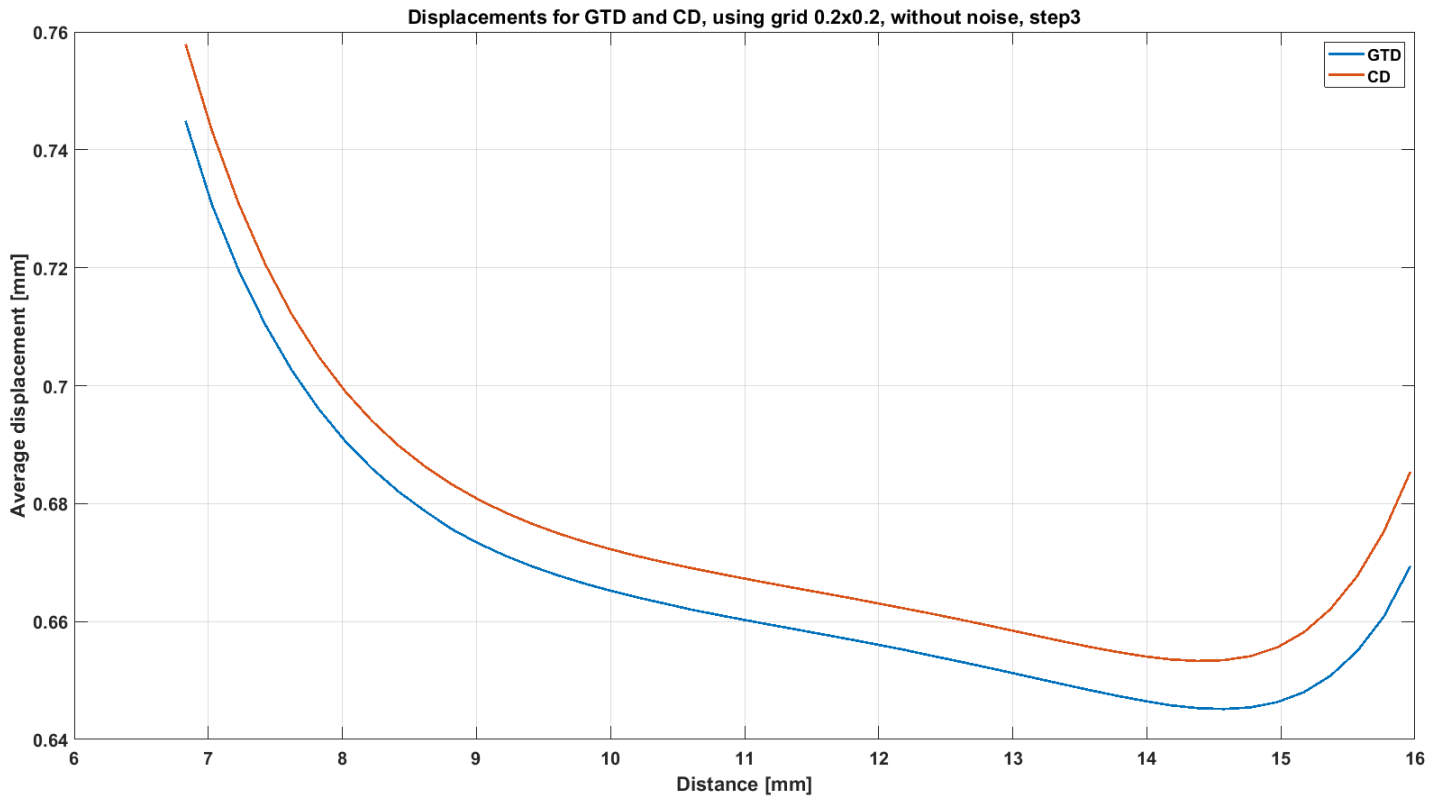


Figure 70: The Distribution of displacement values using grid 0.2x0.2 and implementing no noise. The figure contains the distributions from the GTD and from the CD. The distribution belongs to loading step 3.

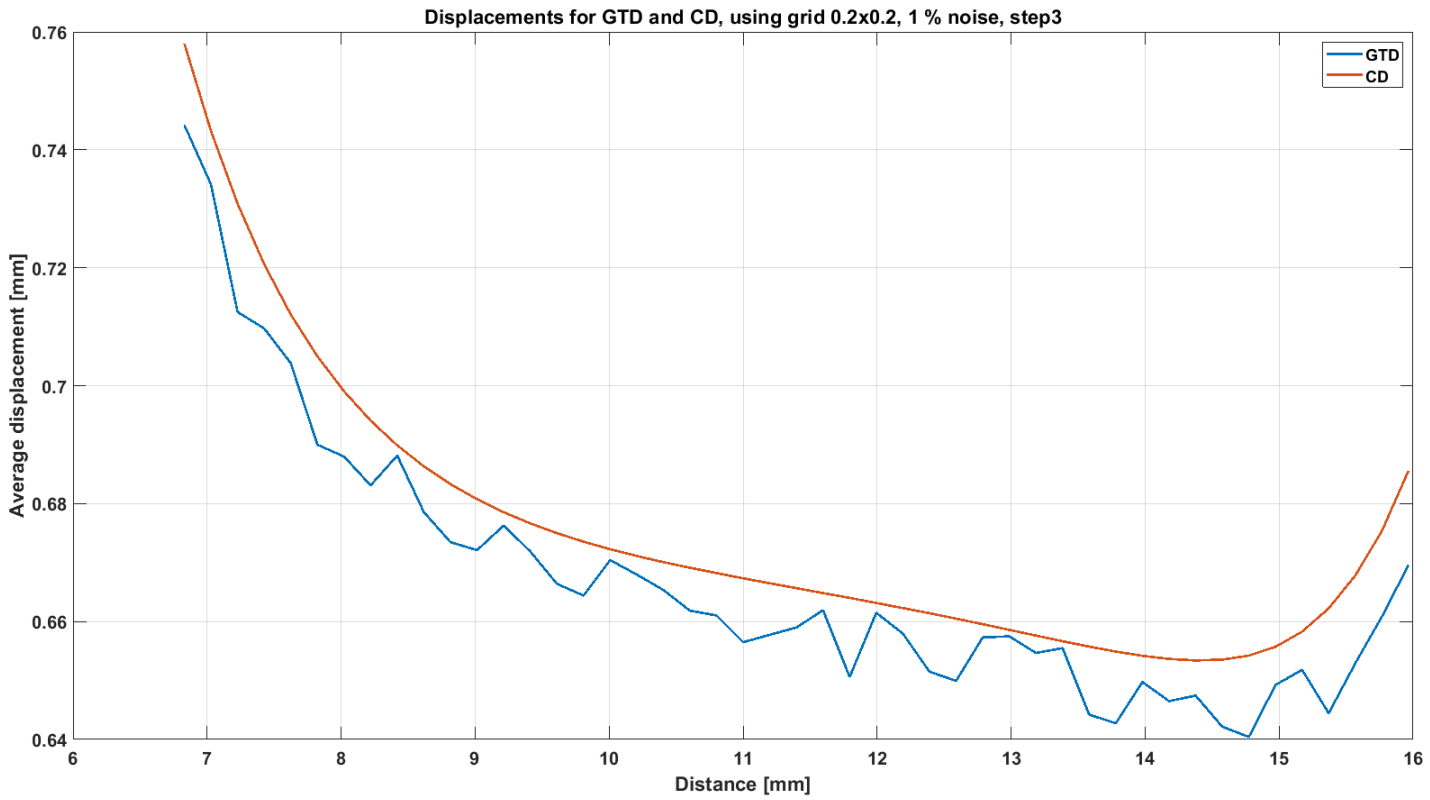


Figure 71: The Distribution of displacement values using grid 0.2x0.2 and implementing 1% noise. The figure contains the distributions from the GTD and from the CD. The distribution belongs to loading step 3.

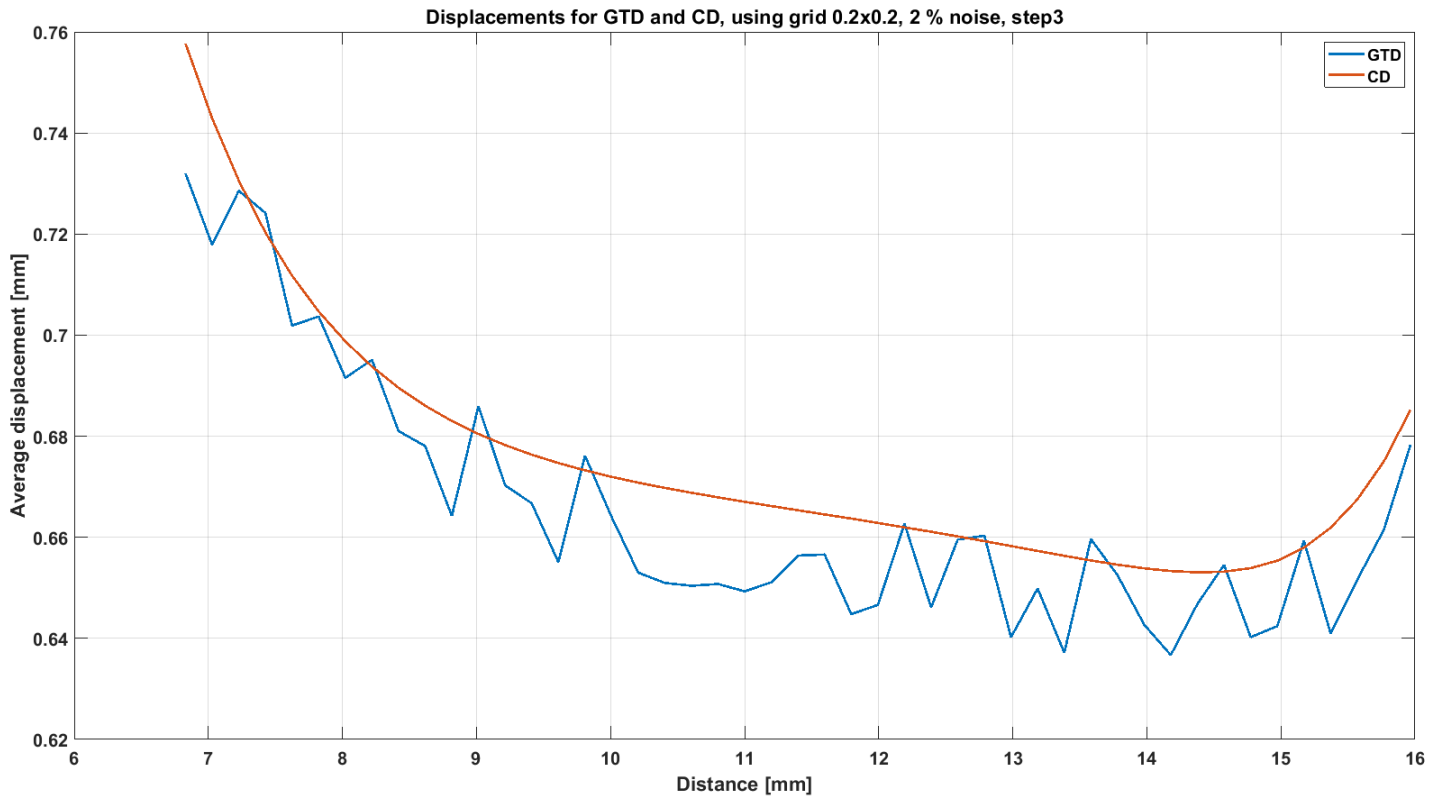


Figure 72: The Distribution of displacement values using grid 0.2x0.2 and implementing 2% noise. The figure contains the distributions from the GTD and from the CD. The distribution belongs to loading step 3.

Grid 3 - step 1

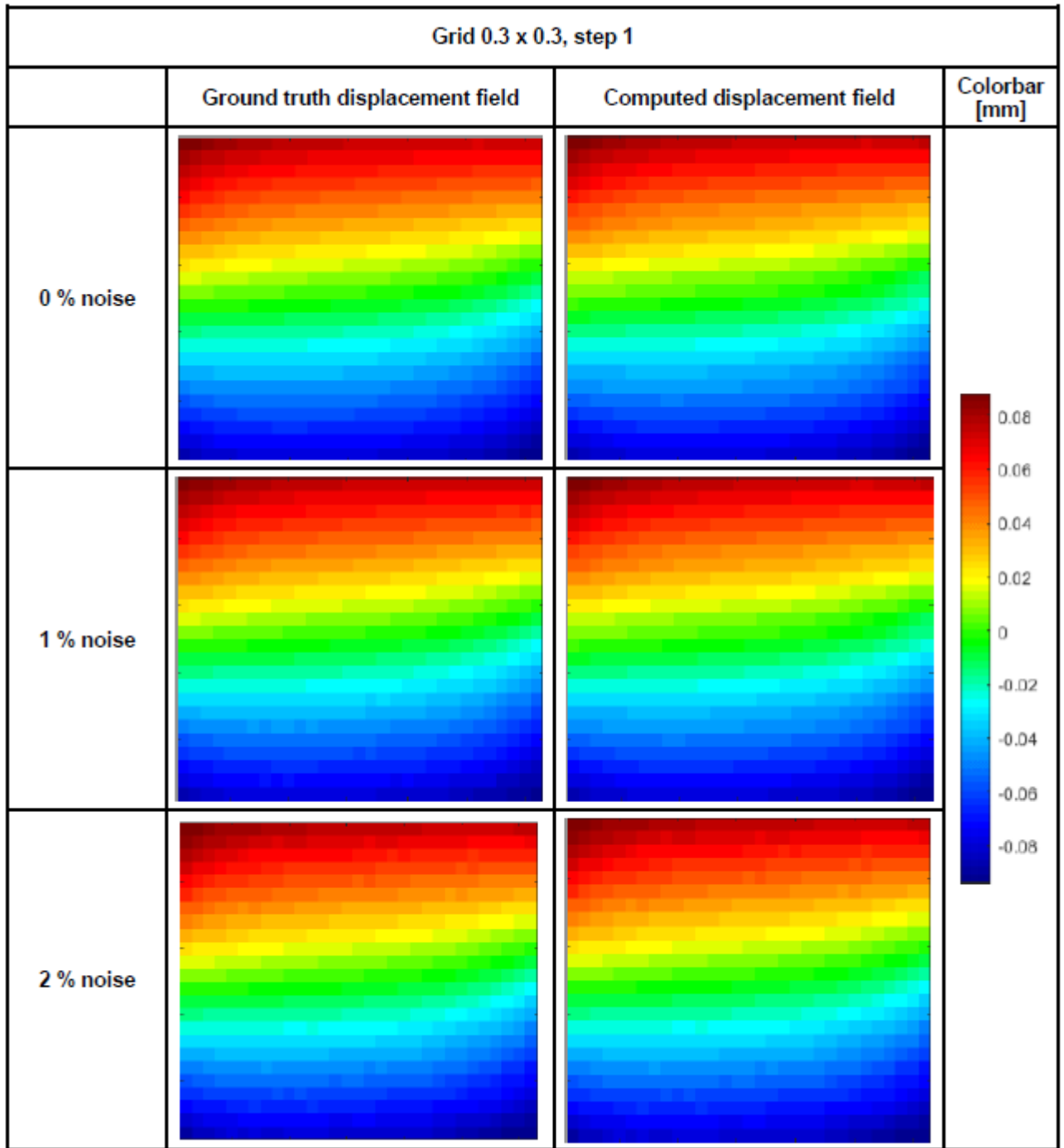


Figure 73: Comparison between GTD and CD displacement fields with increased noise. The displacement fields belong to grid 0.3x0.3 at step 1.

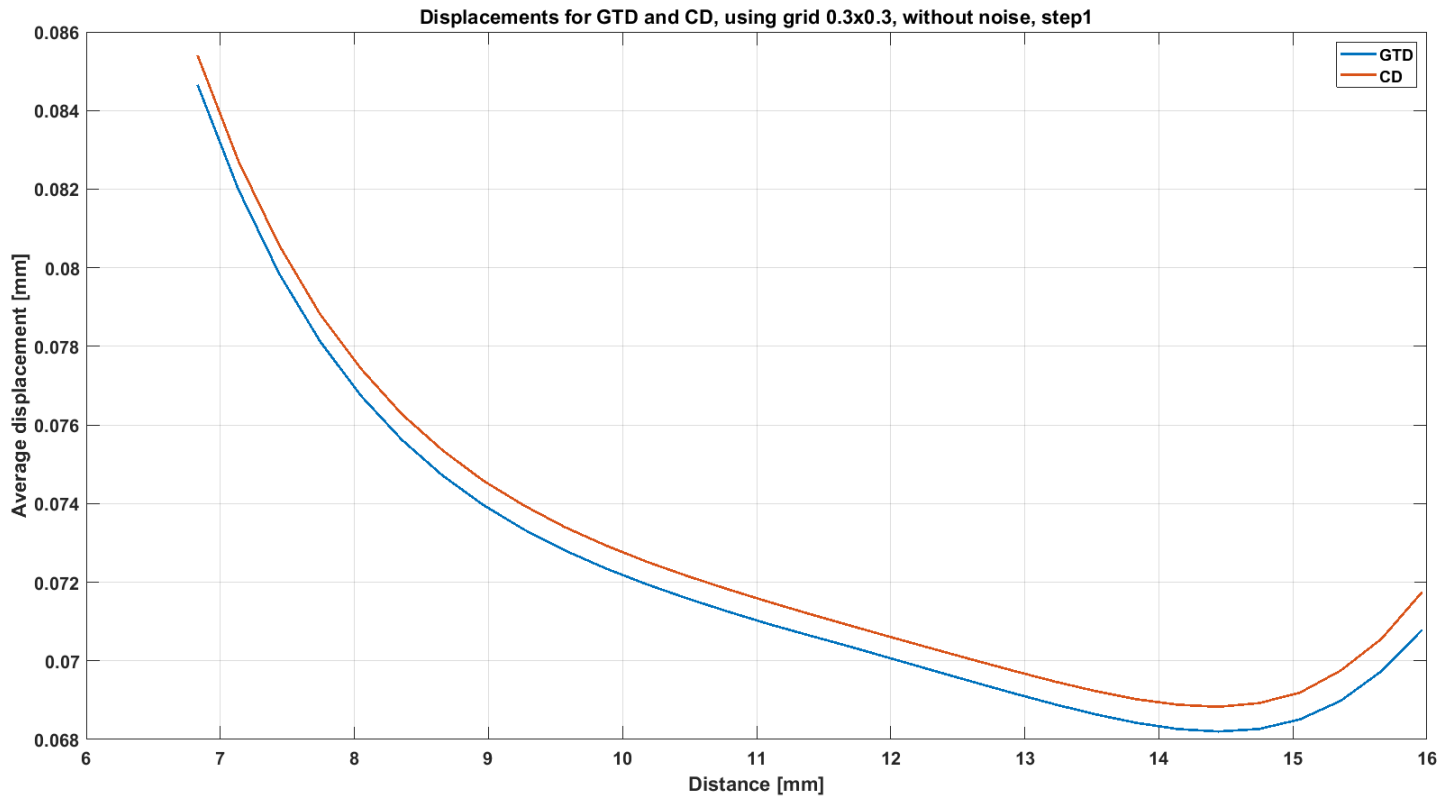


Figure 74: The Distribution of displacement values using grid 0.2x0.2. The figure contains the distributions from the GTD and from the CD. The distribution belongs to loading step 1.

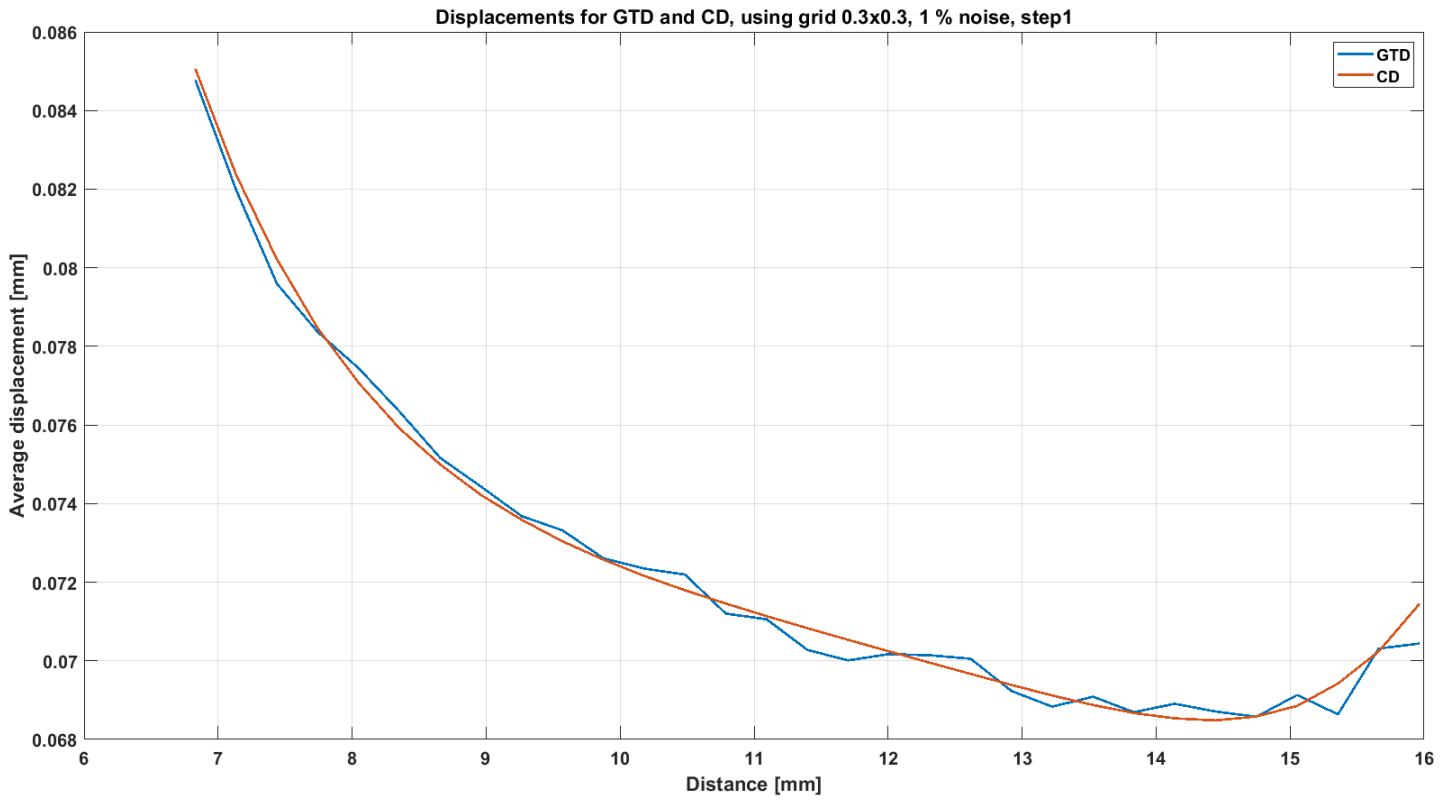


Figure 75: The Distribution of displacement values using grid 0.2x0.2 and implementing 1% noise. The figure contains the distributions from the GTD and from the CD. The distribution belongs to loading step 1.

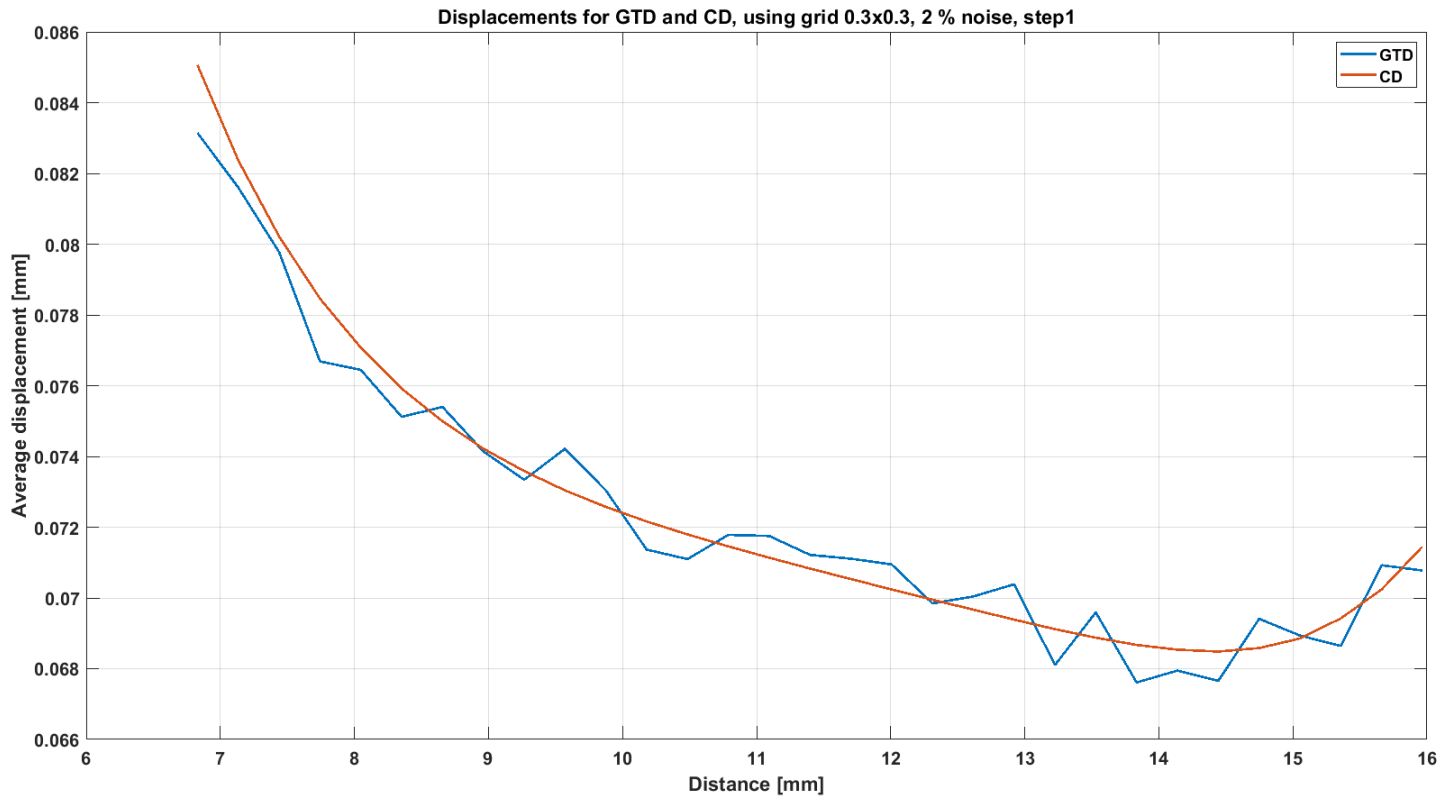


Figure 76: The Distribution of displacement values using grid 0.2x0.2 and implementing 2% noise. The figure contains the distributions from the GTD and from the CD. The distribution belongs to loading step 1.

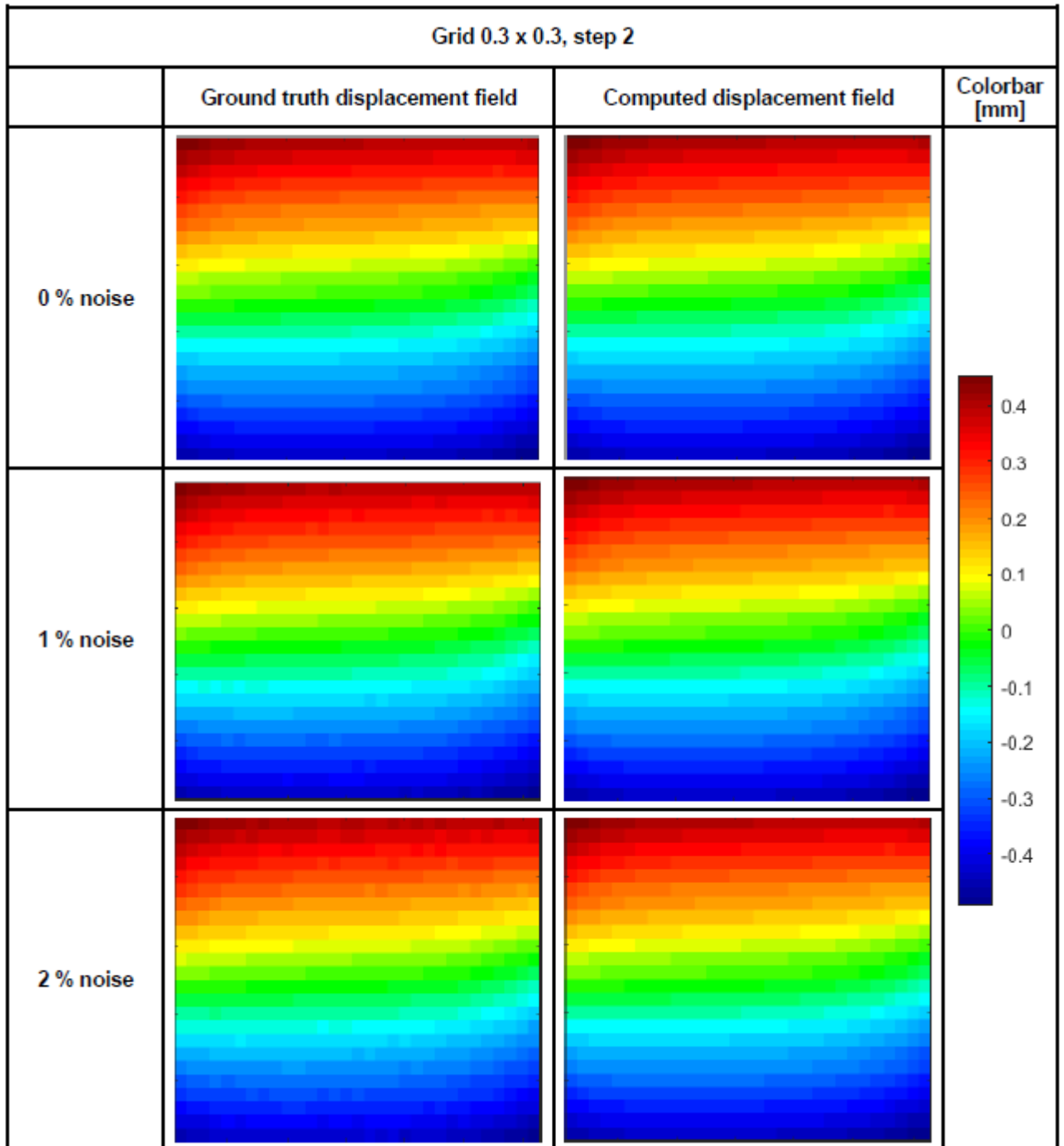


Figure 77: Comparison between GTD and CD displacement fields with increased noise. The displacement fields belong to grid 0.3x0.3 at step 2.

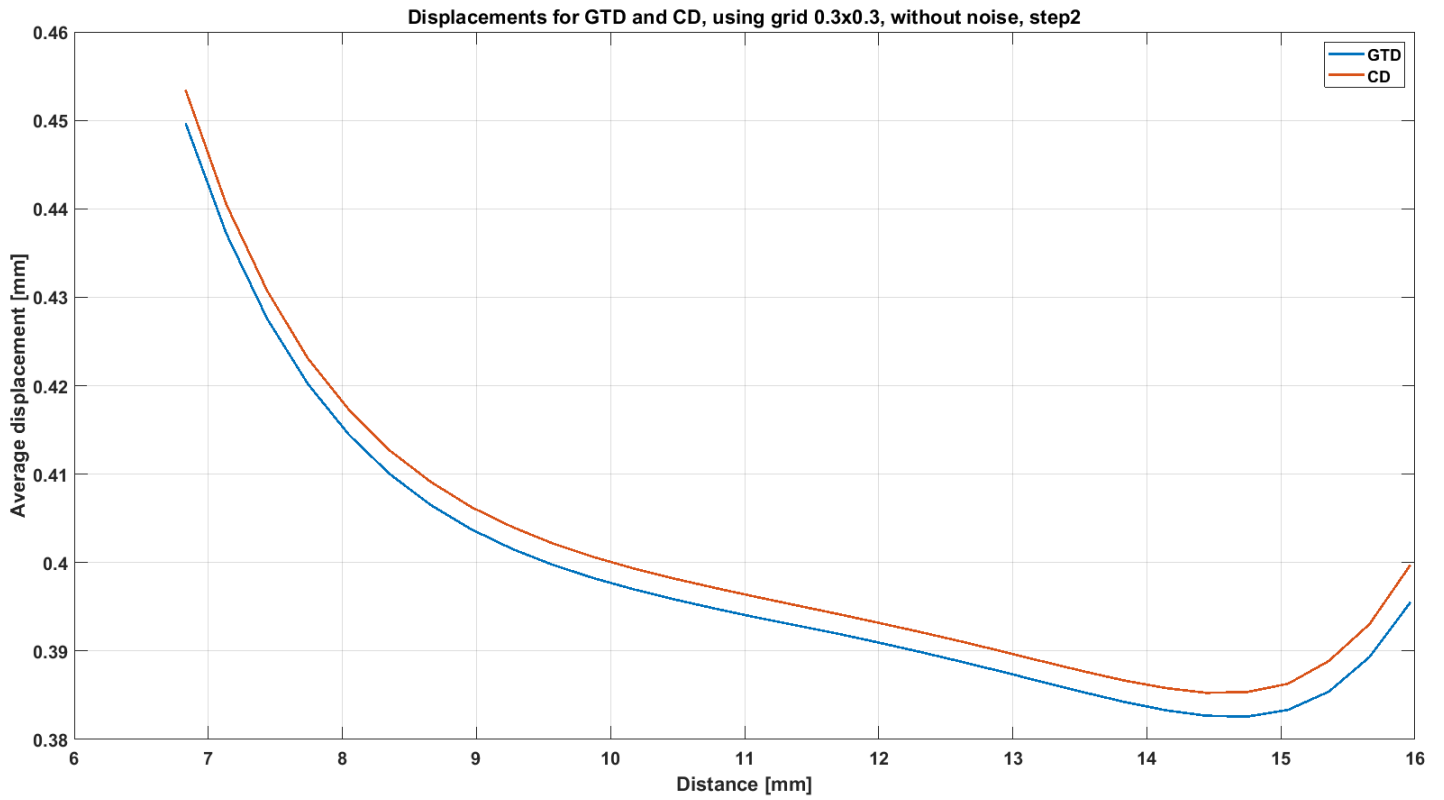


Figure 78: The Distribution of displacement values using grid 0.2x0.2. The figure contains the distributions from the GTD and from the CD. The distribution belongs to loading step 2.

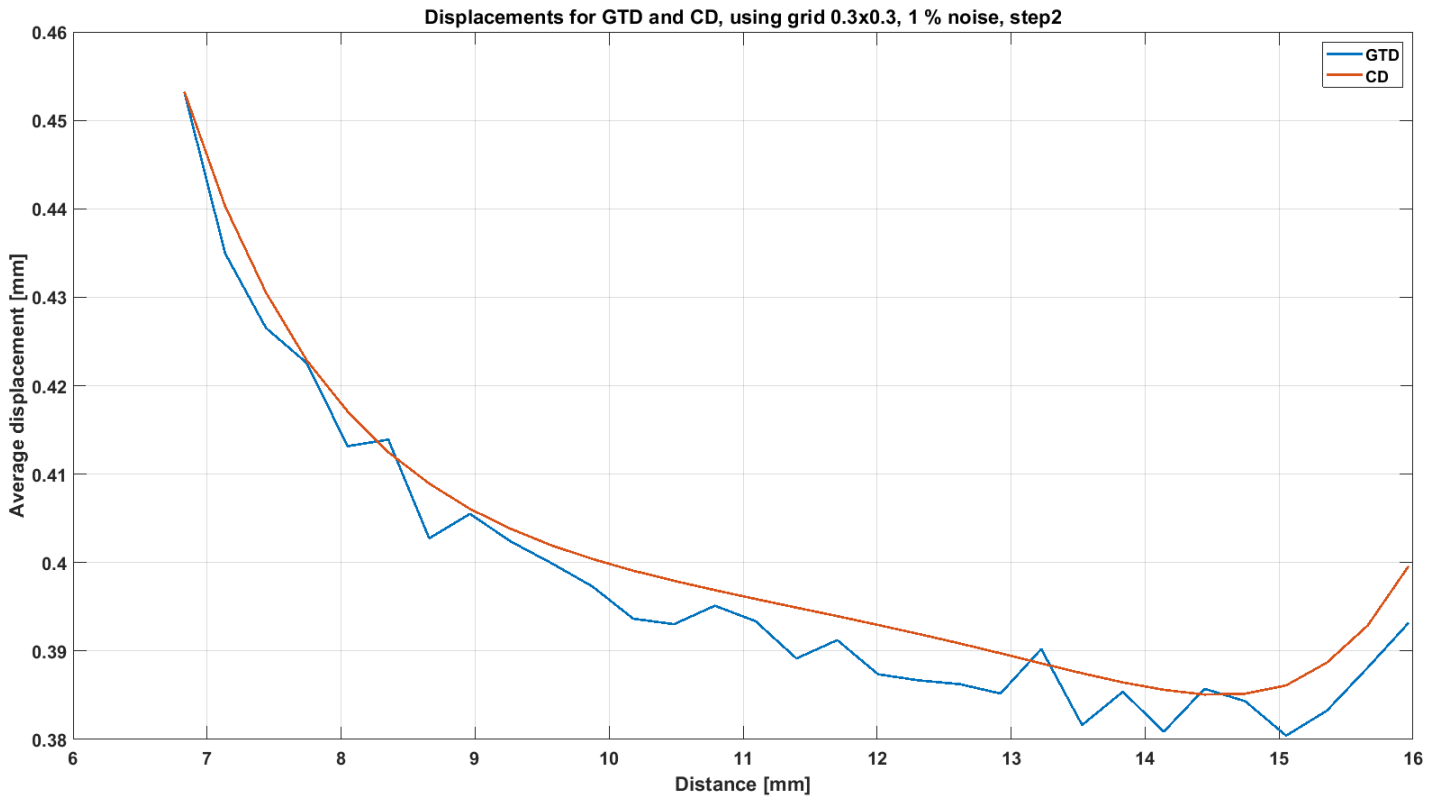


Figure 79: The Distribution of displacement values using grid 0.2x0.2 and implementing 1% noise. The figure contains the distributions from the GTD and from the CD. The distribution belongs to loading step 2.

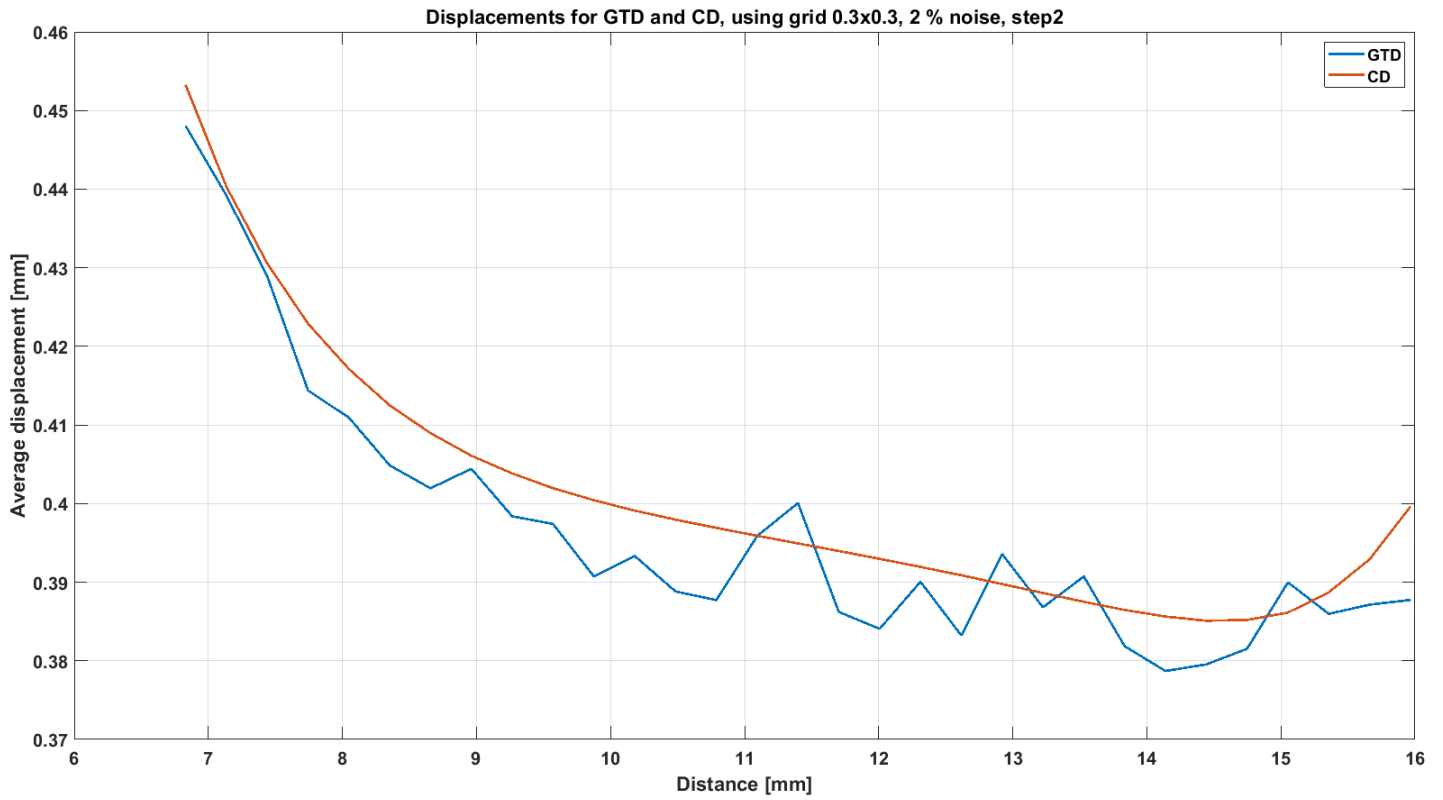


Figure 80: The Distribution of displacement values using grid 0.2x0.2 and implementing 2% noise. The figure contains the distributions from the GTD and from the CD. The distribution belongs to loading step 2.

Grid 3 - step 1

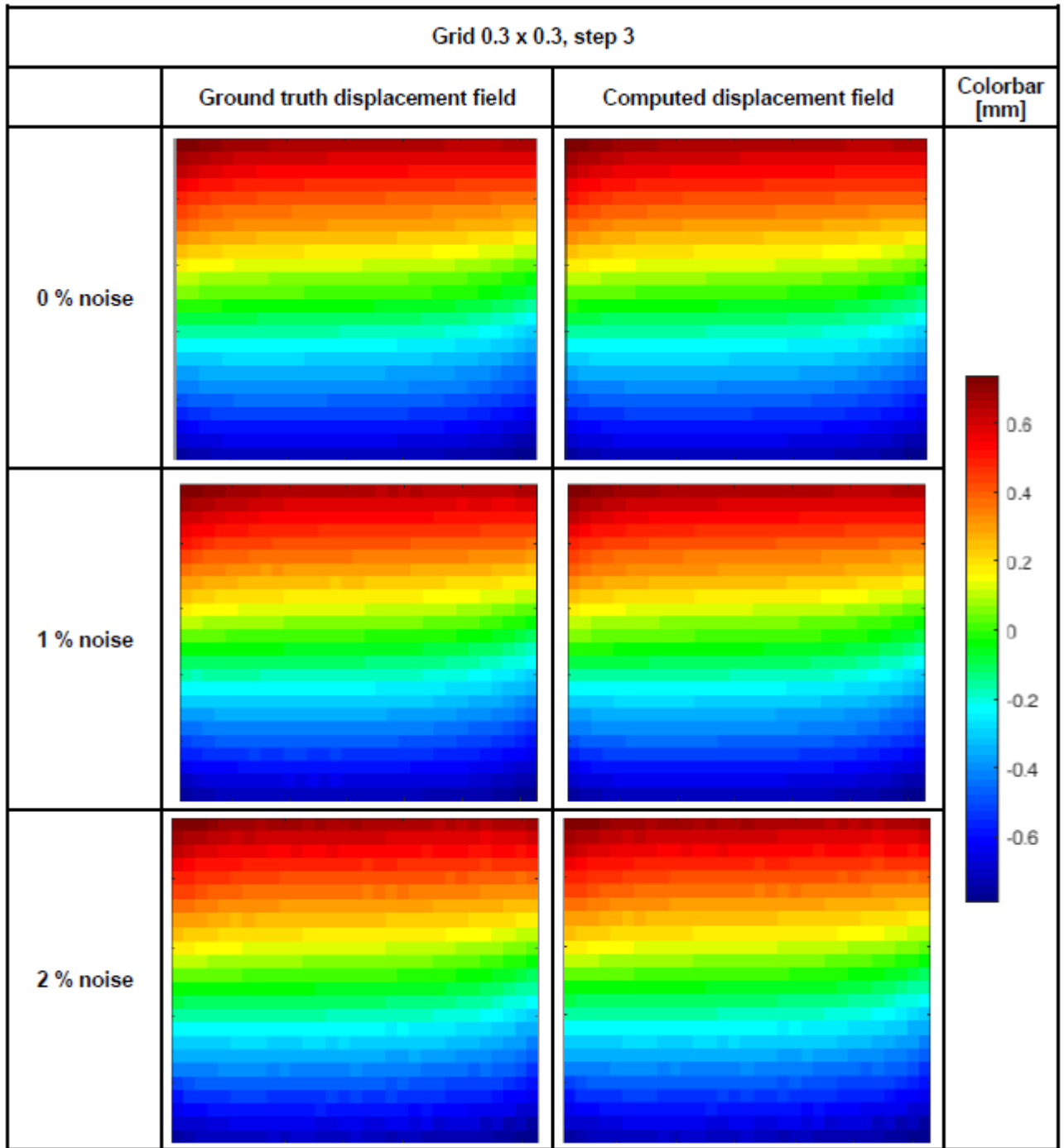


Figure 81: Comparison between GTD and CD displacement fields with increased noise. The displacement fields belong to grid 0.3x0.3 at step 3.

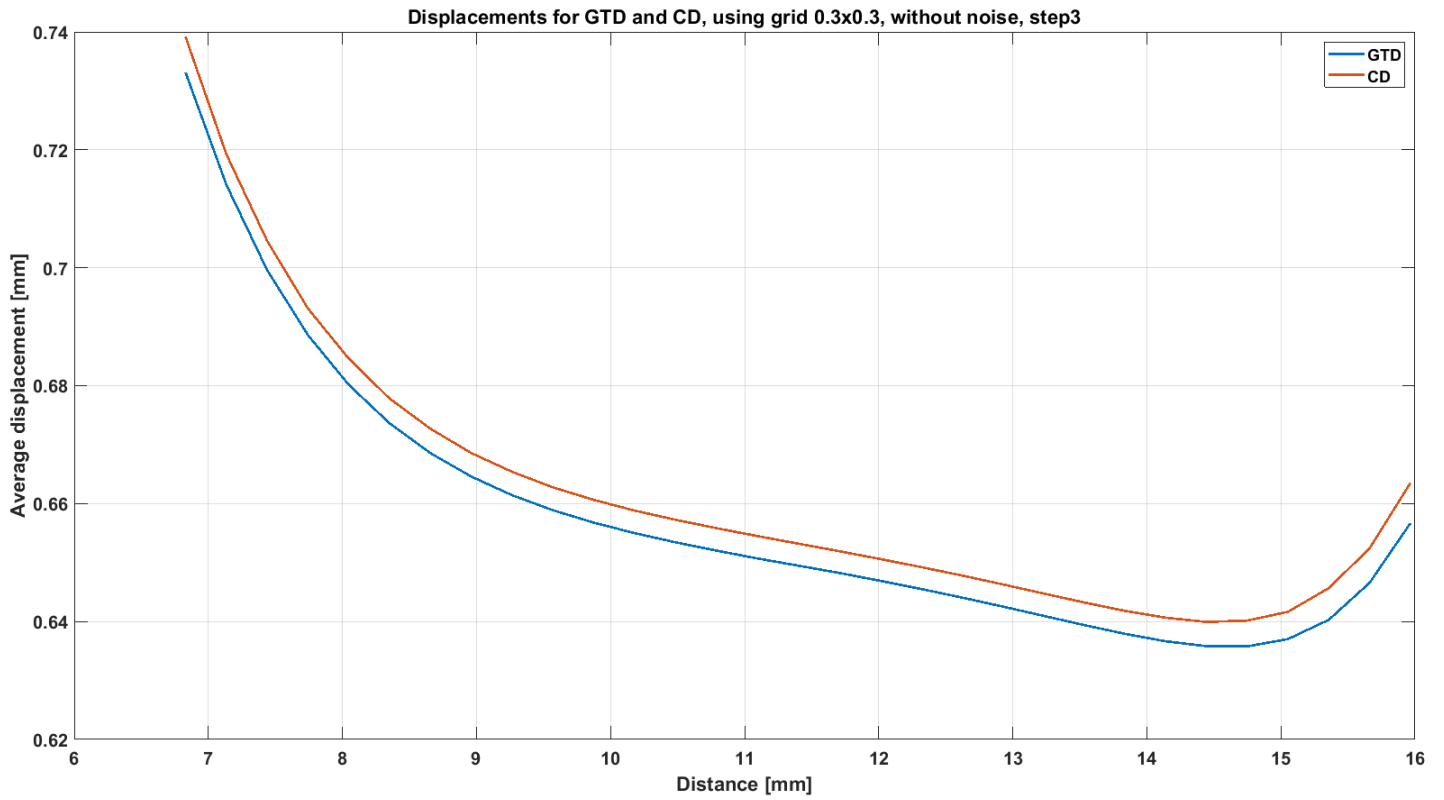


Figure 82: The Distribution of displacement values using grid 0.2x0.2. The figure contains the distributions from the GTD and from the CD. The distribution belongs to loading step 3.

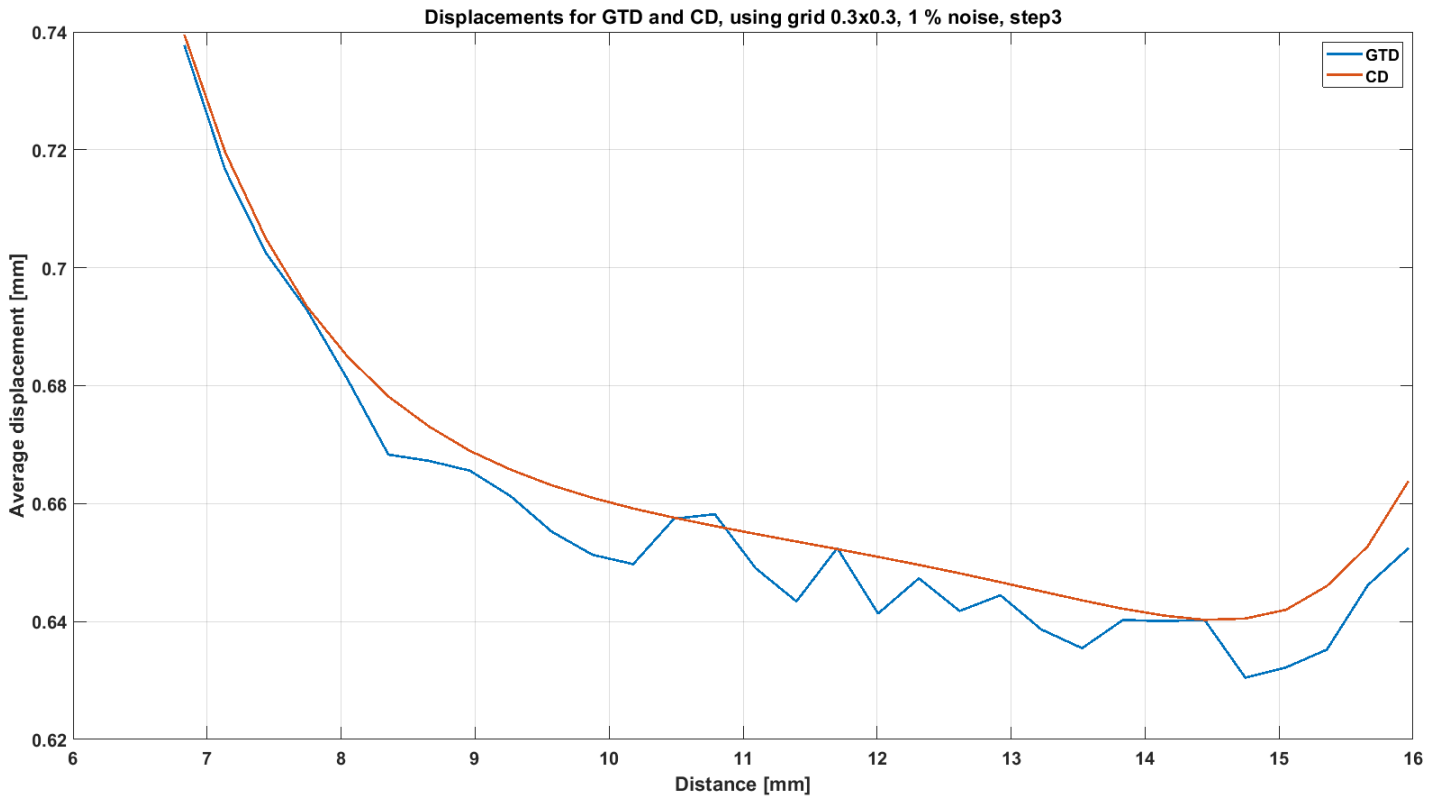


Figure 83: The Distribution of displacement values using grid 0.2x0.2 and implementing 1% noise. The figure contains the distributions from the GTD and from the CD. The distribution belongs to loading step 3.

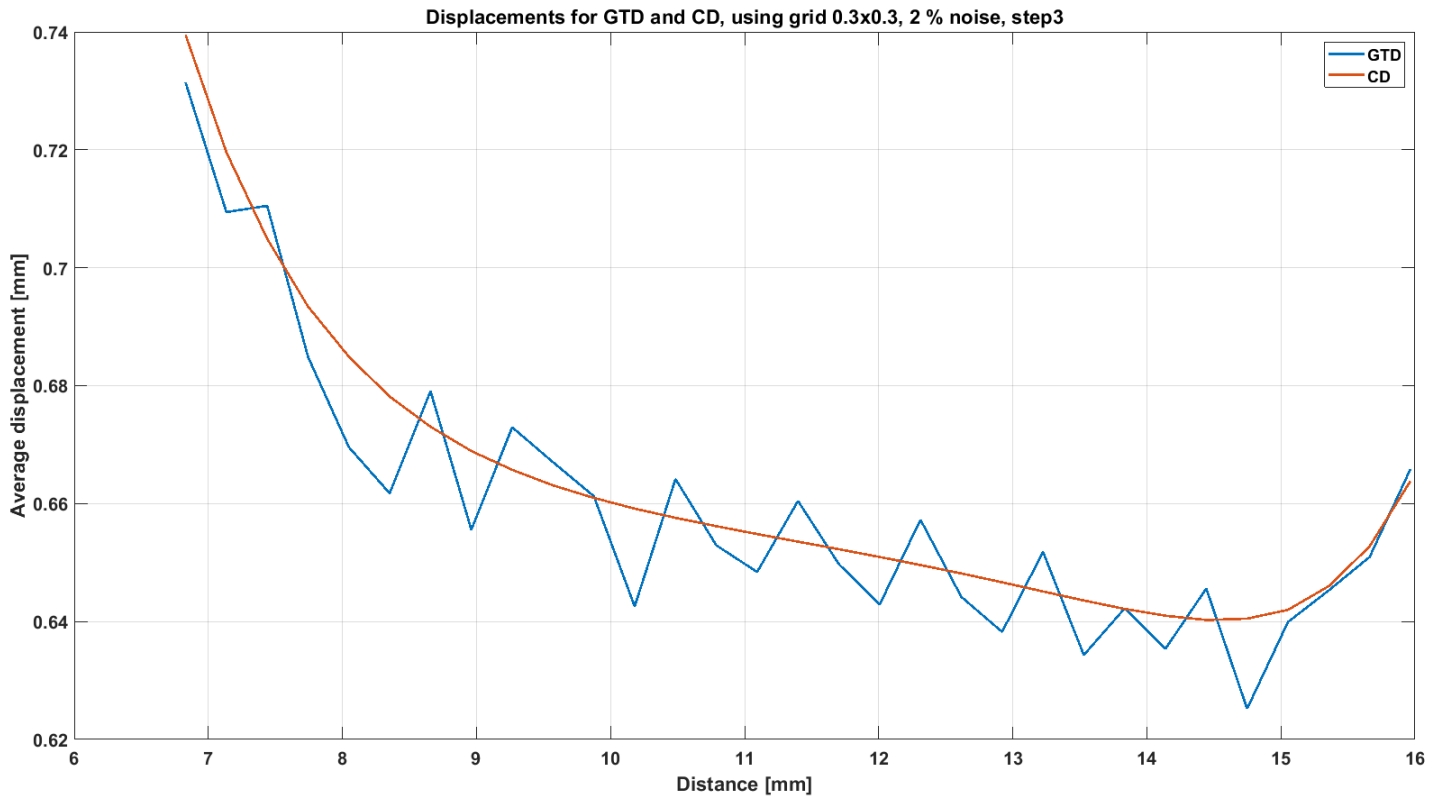


Figure 84: The Distribution of displacement values using grid 0.2x0.2 and implementing 2% noise. The figure contains the distributions from the GTD and from the CD. The distribution belongs to loading step 3.

## K Section Study

### K.1 Estimation procedure

#### 2Sections

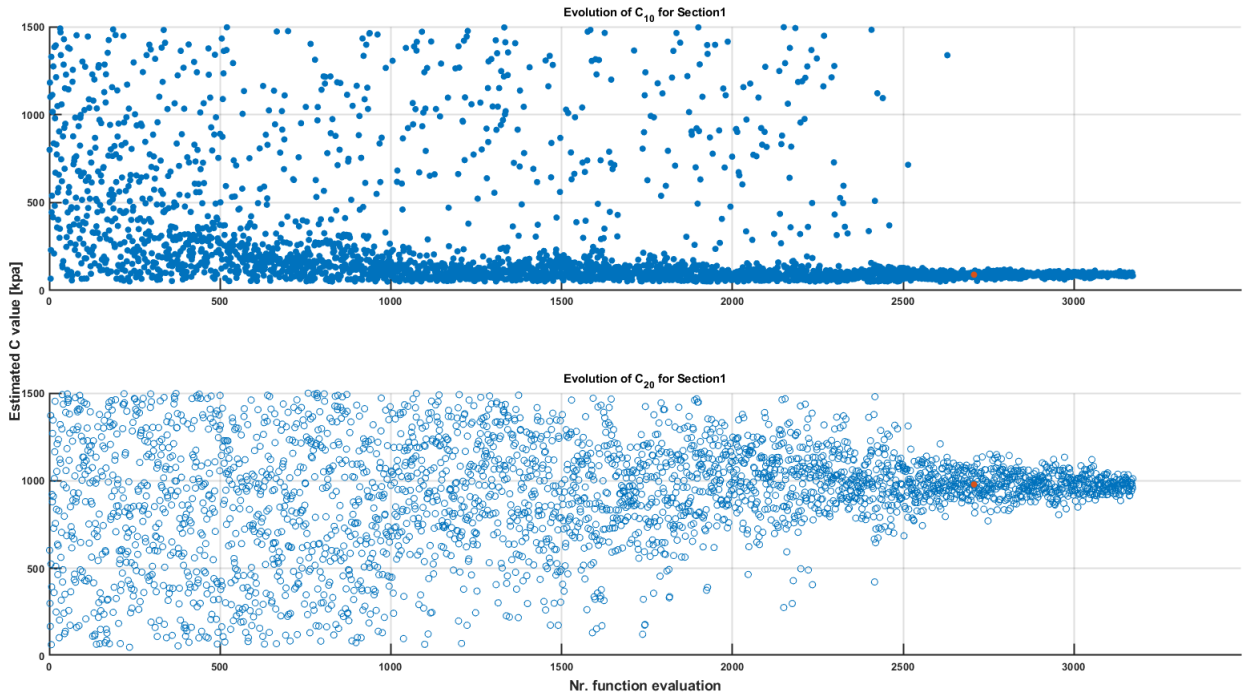


Figure 85: Evolution of material properties during the section study using 2 Sections. Material properties belong to Section 1.

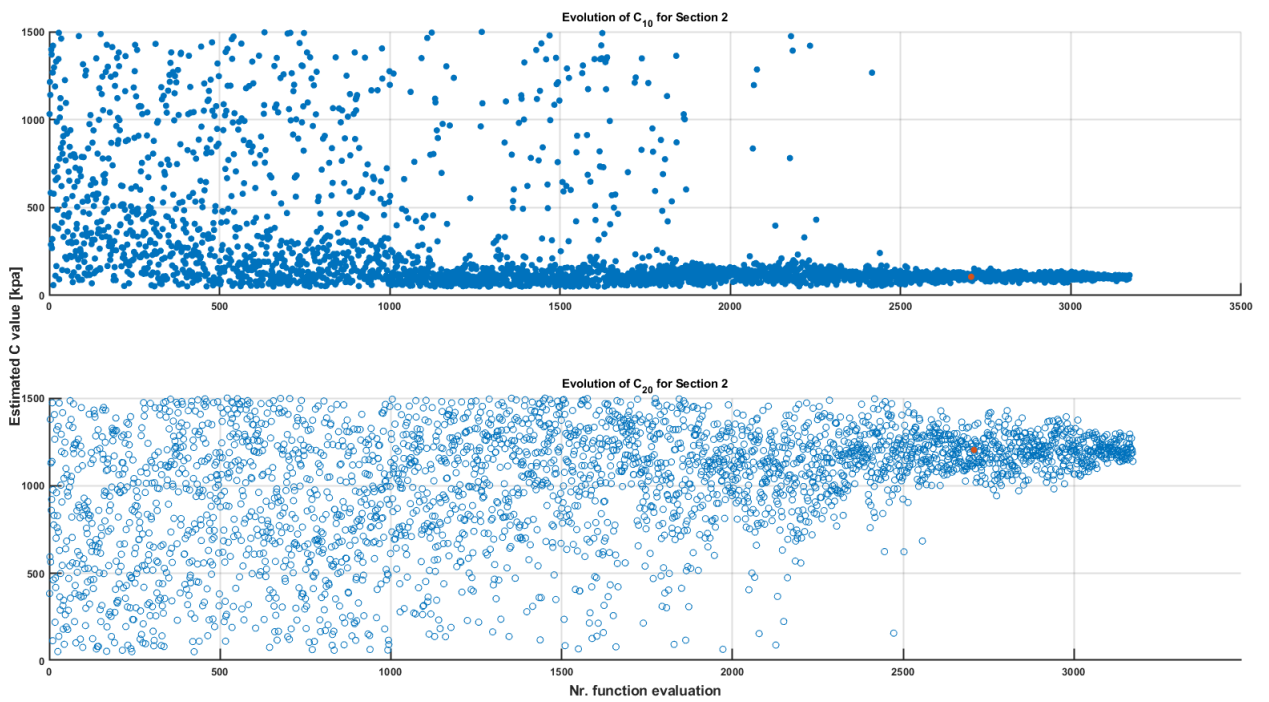


Figure 86: Evolution of material properties during the section study using 2 Sections. Material properties belong to Section 2.

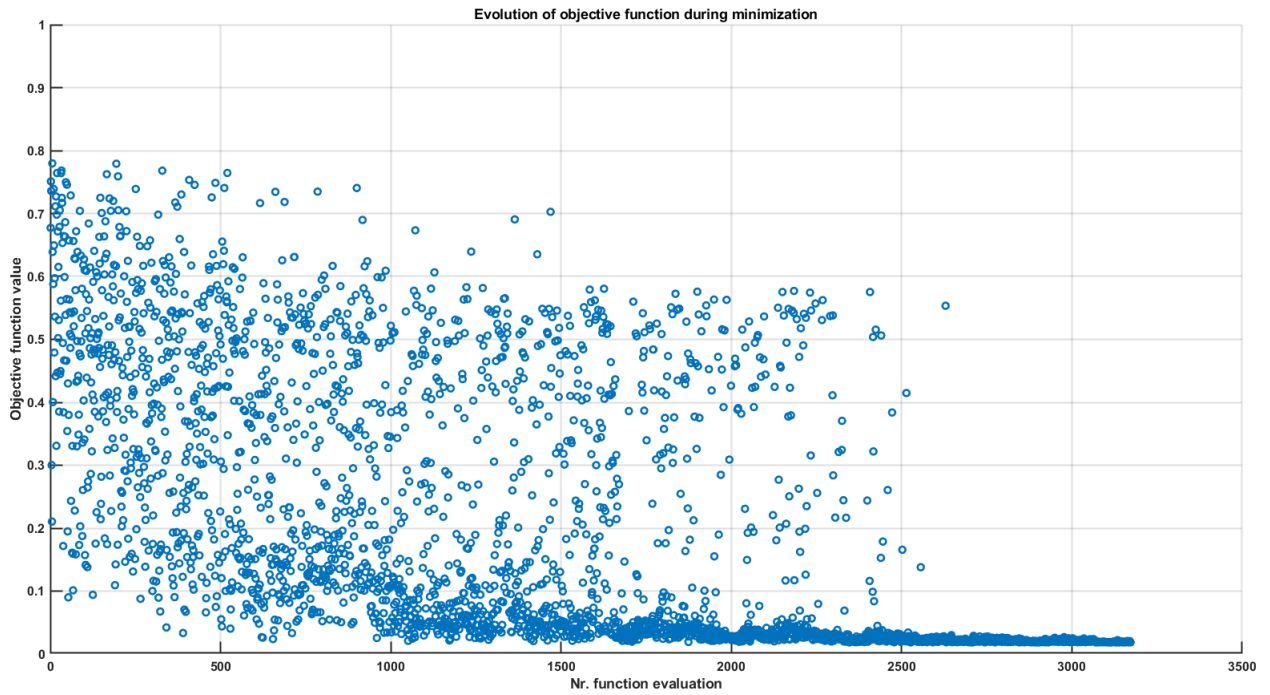


Figure 87: Evolution of the objective function during the section study using 2 Sections.

#### 4 Sections

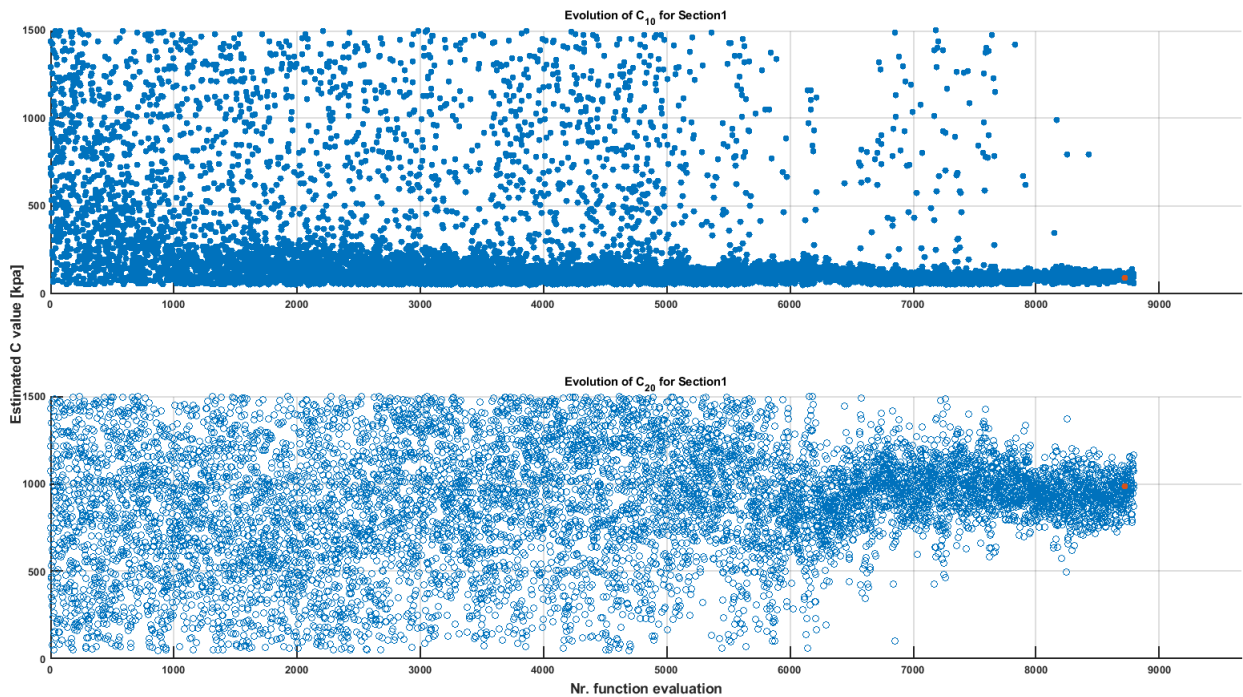


Figure 88: Evolution of material properties during the section study using 4 Sections. Material properties belong to Section 1.

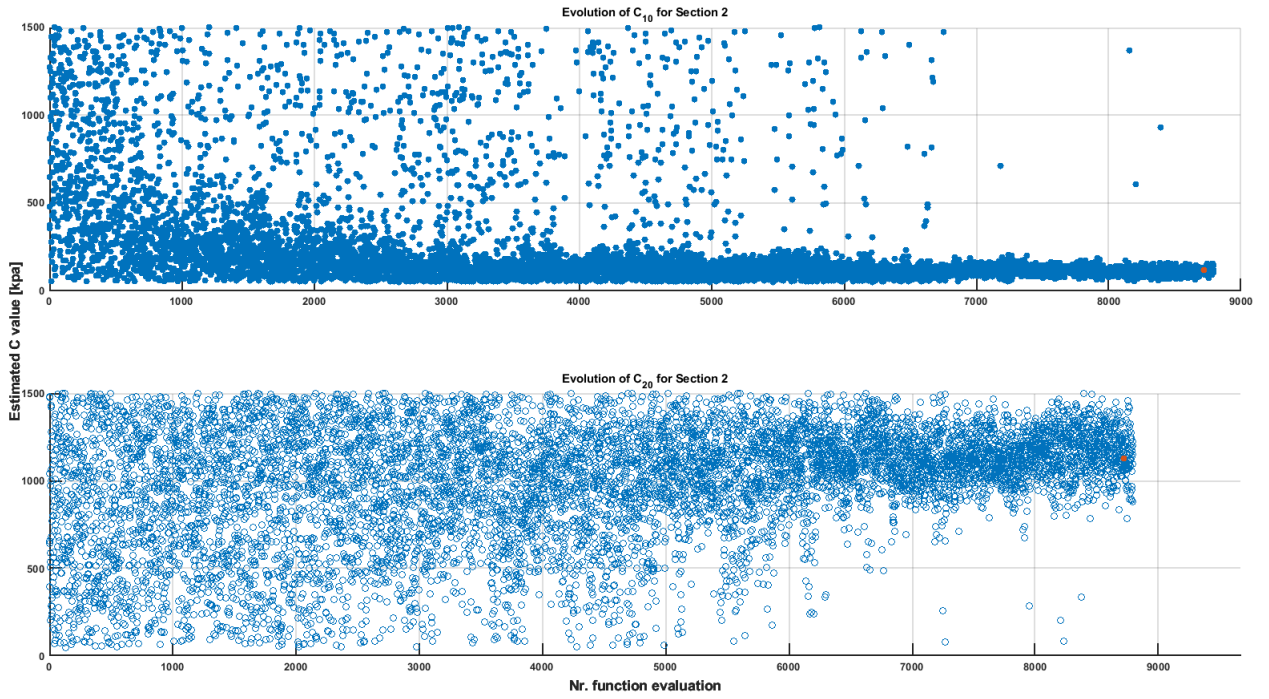


Figure 89: Evolution of material properties during the section study using 4 Sections. Material properties belong to Section 2.

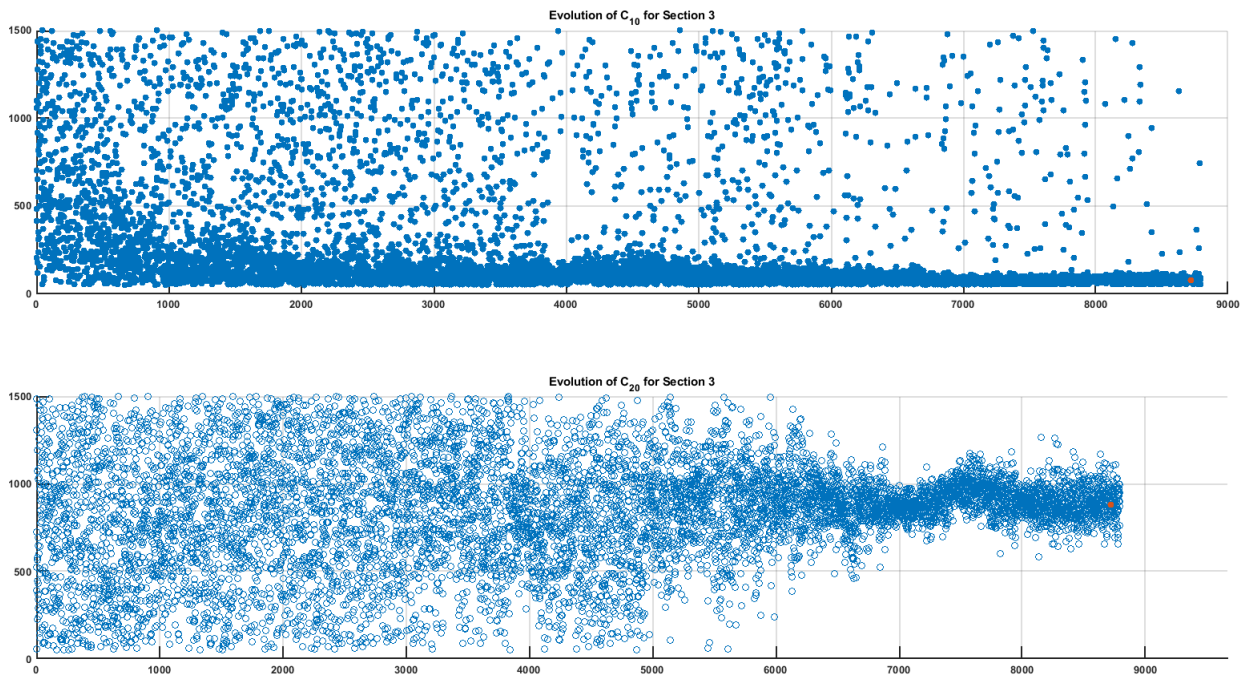


Figure 90: Evolution of material properties during the section study using 4 Sections. Material properties belong to Section 3.

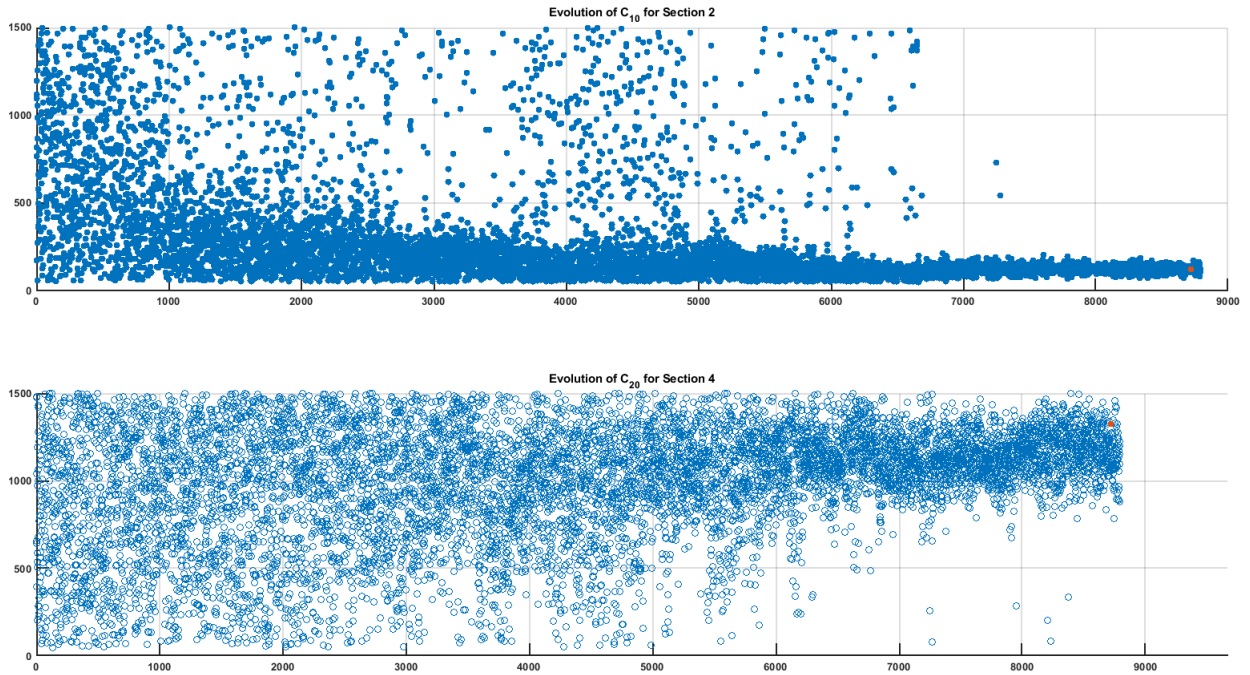


Figure 91: Evolution of material properties during the section study using 4 Sections. Material properties belong to Section 4.

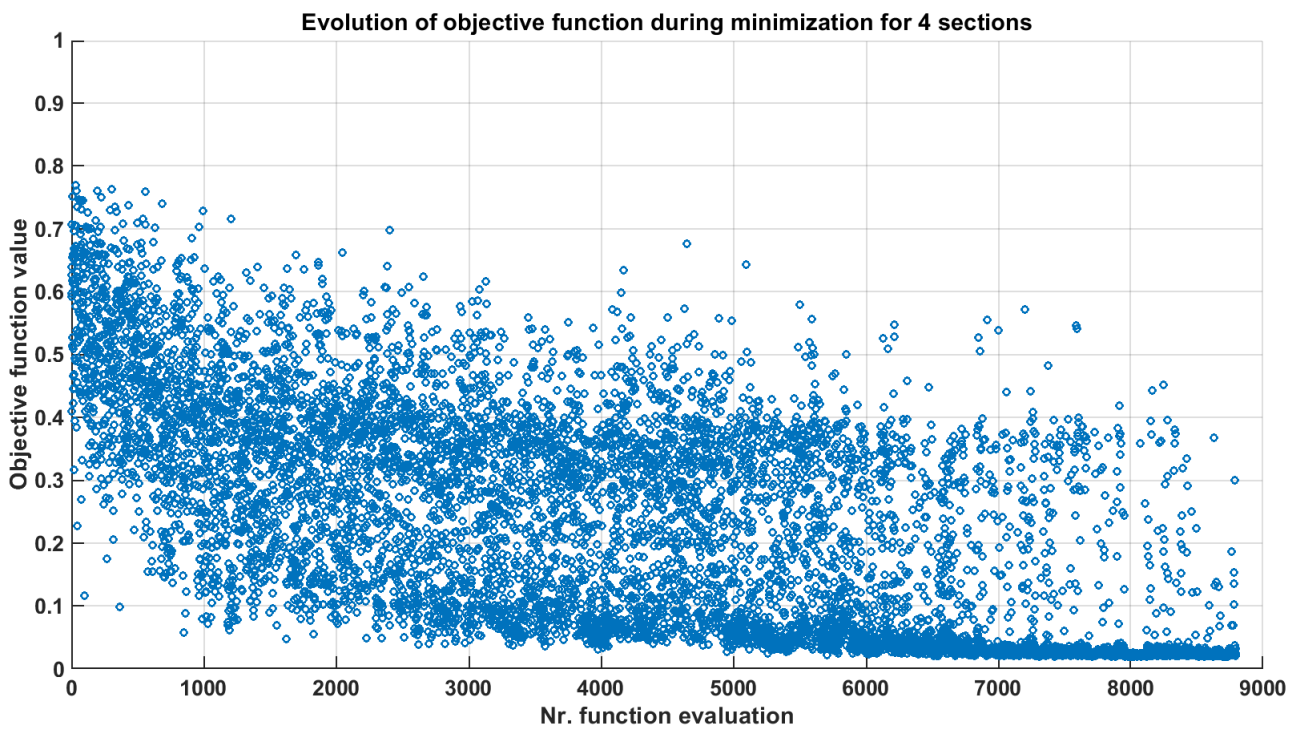


Figure 92: Evolution of the objective function during the section study using 4 Sections.

6 Sections

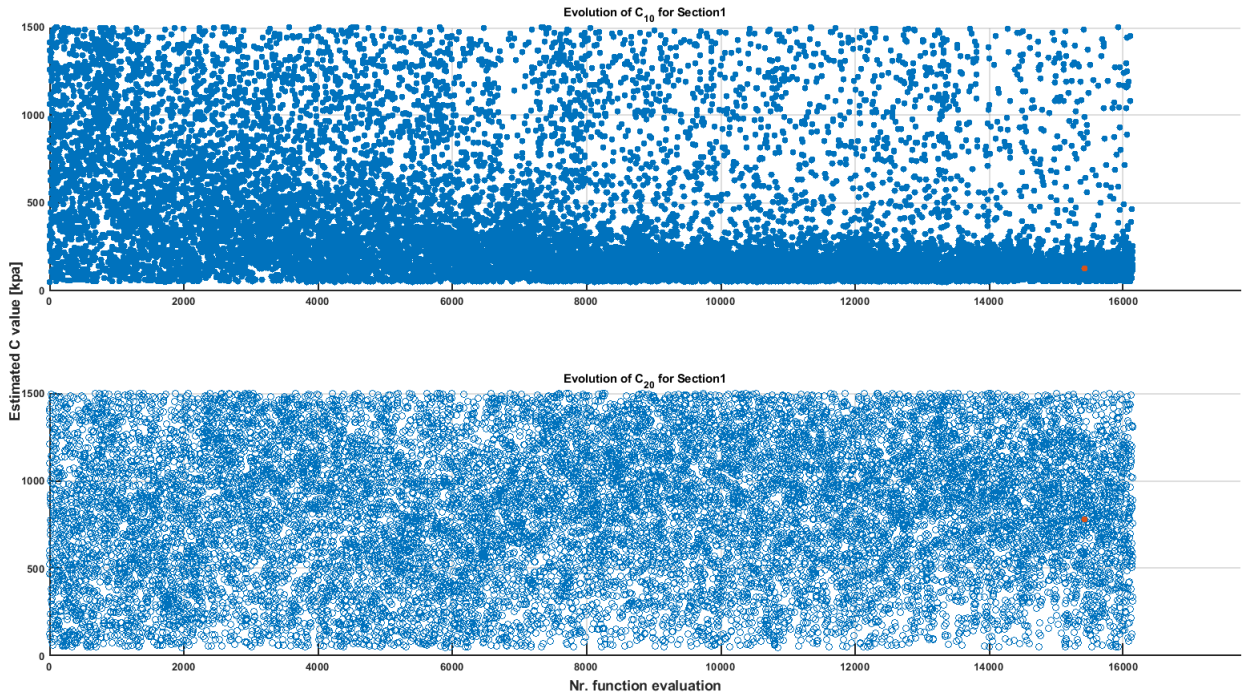


Figure 93: Evolution of material properties during the section study using 6 Sections. Material properties belong to Section 1.

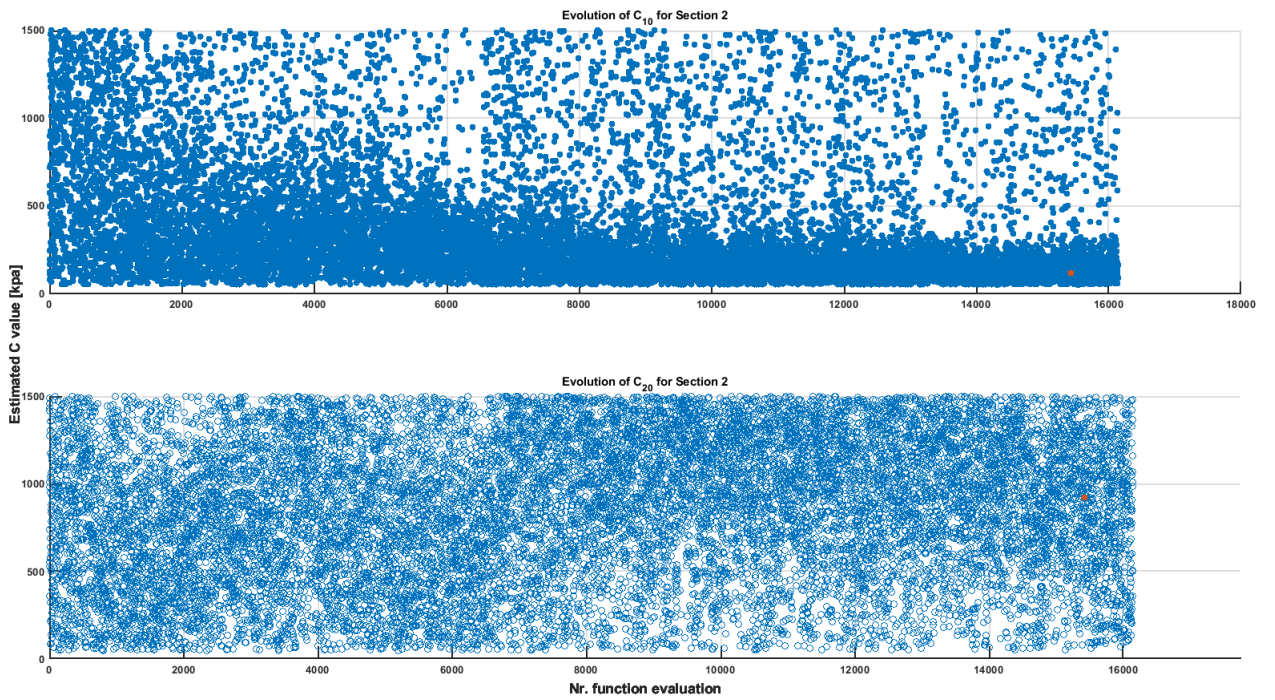


Figure 94: Evolution of material properties during the section study using 6 Sections. Material properties belong to Section 2.

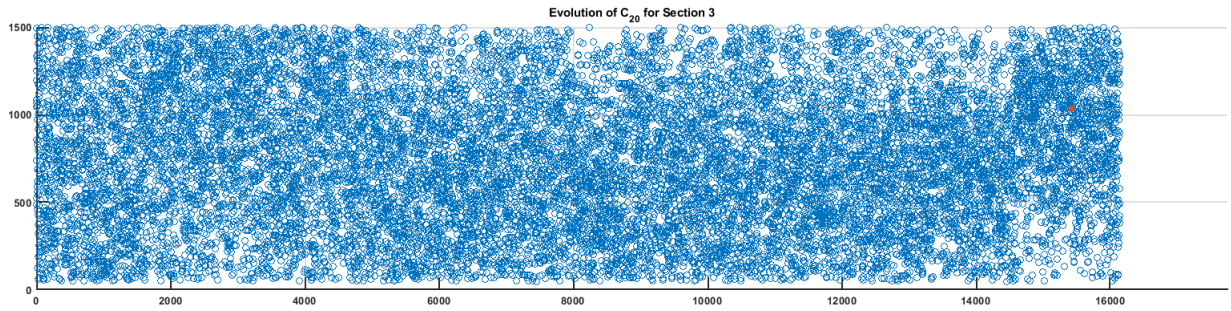
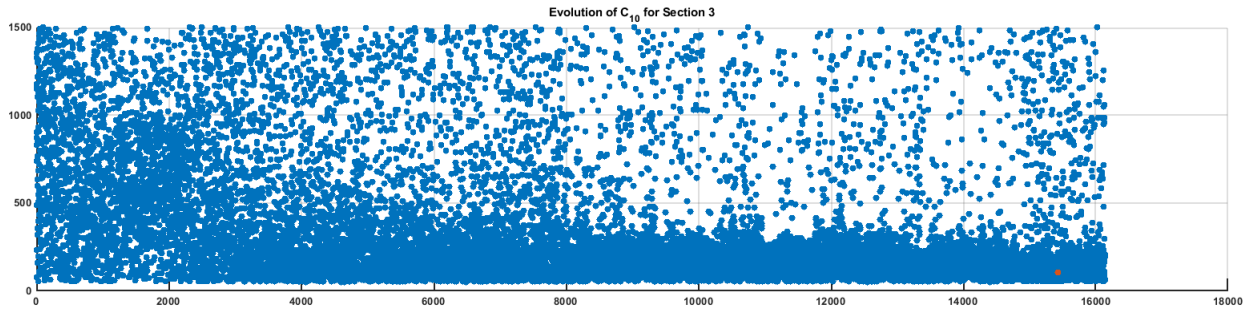


Figure 95: Evolution of material properties during the section study using 6 Sections. Material properties belong to Section 3.

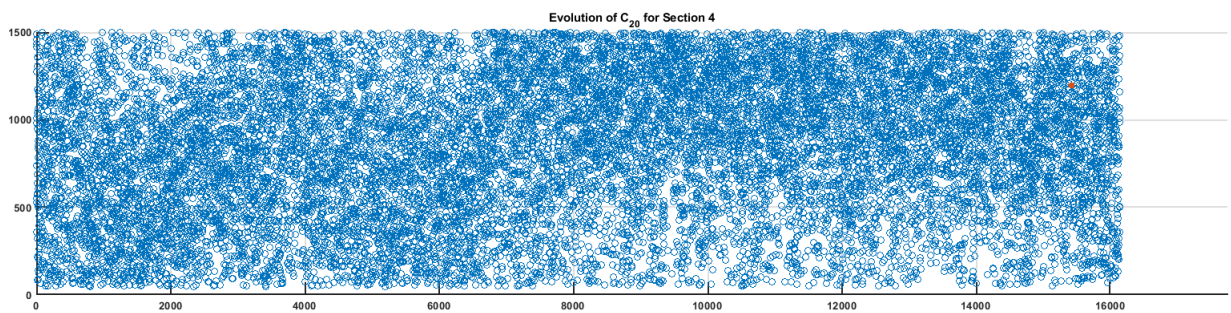
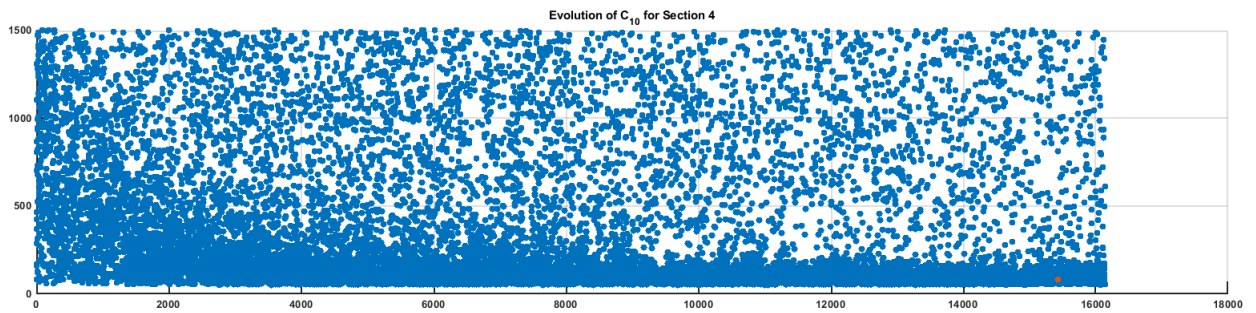


Figure 96: Evolution of material properties during the section study using 6 Sections. Material properties belong to Section 4.

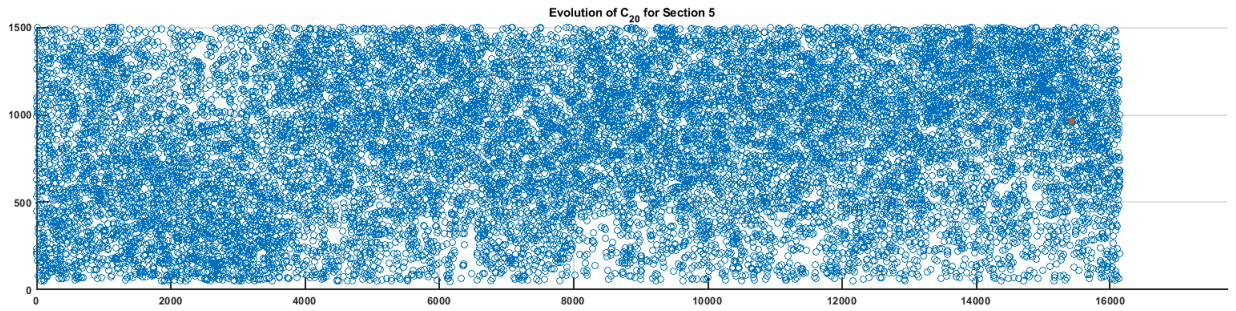
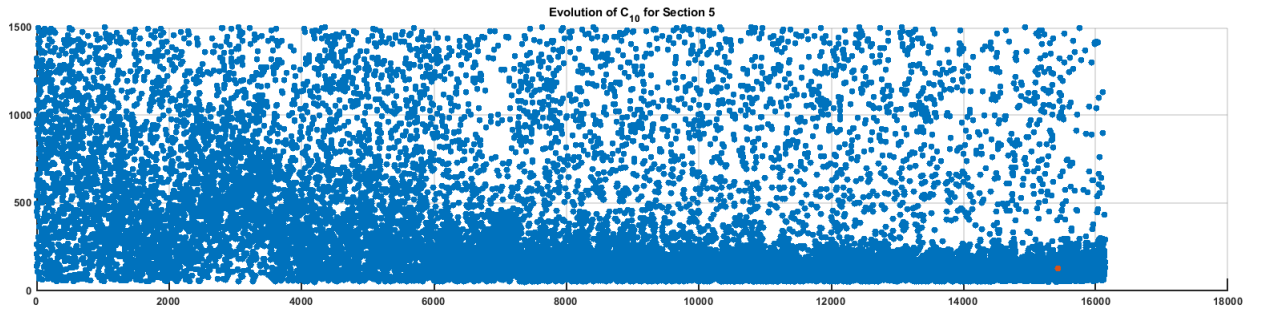


Figure 97: Evolution of material properties during the section study using 6 Sections. Material properties belong to Section 5.

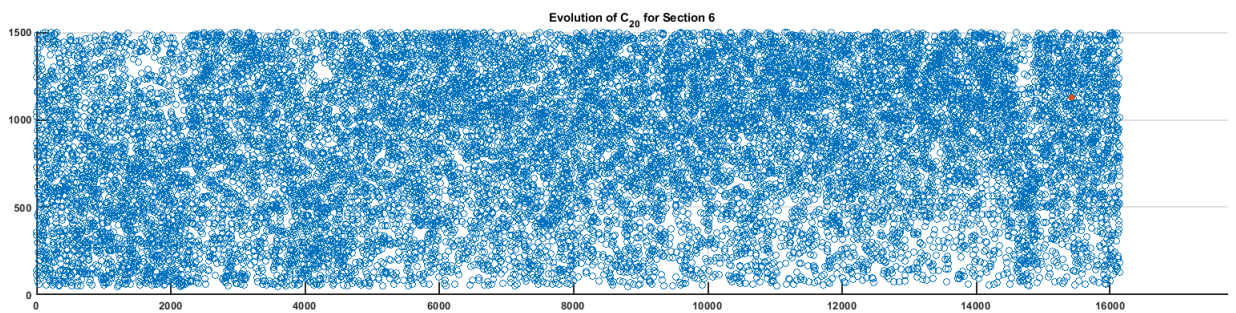
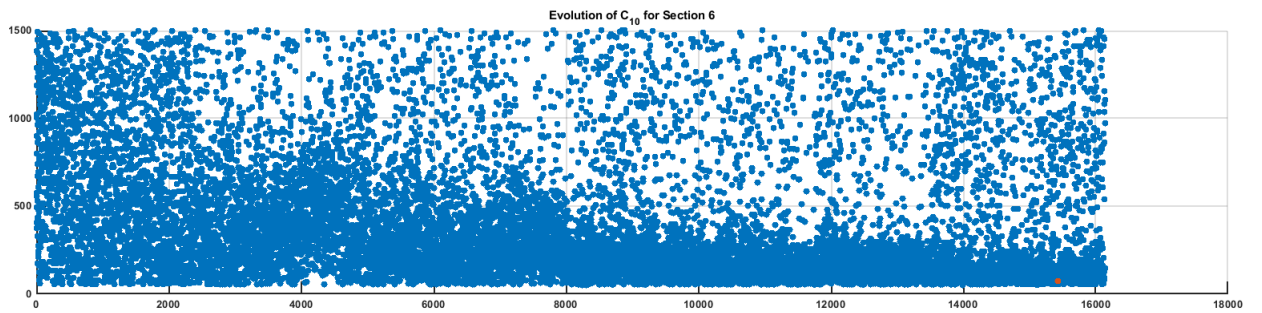


Figure 98: Evolution of material properties during the section study using 6 Sections. Material properties belong to Section 6.

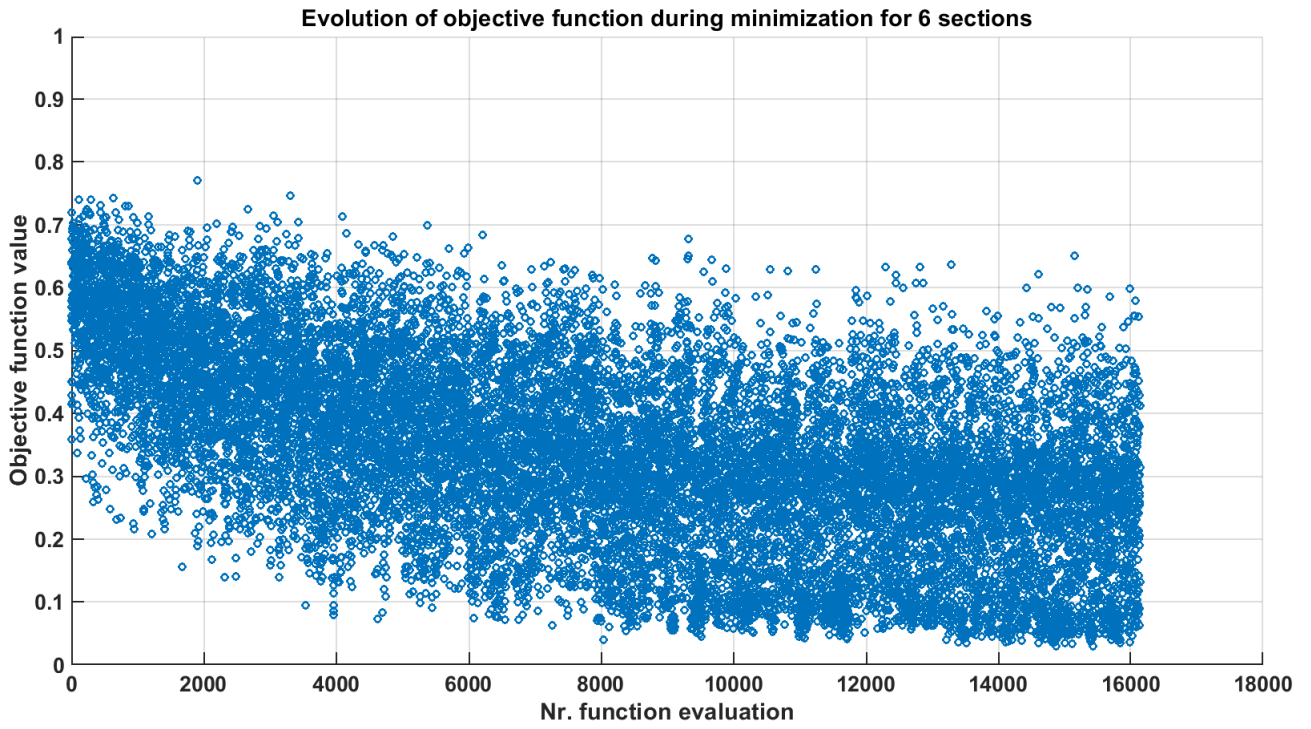


Figure 99: Evolution of the objective function during the section study using 6 Sections.

## K.2 Resulting displacement fields

### 2 Sections

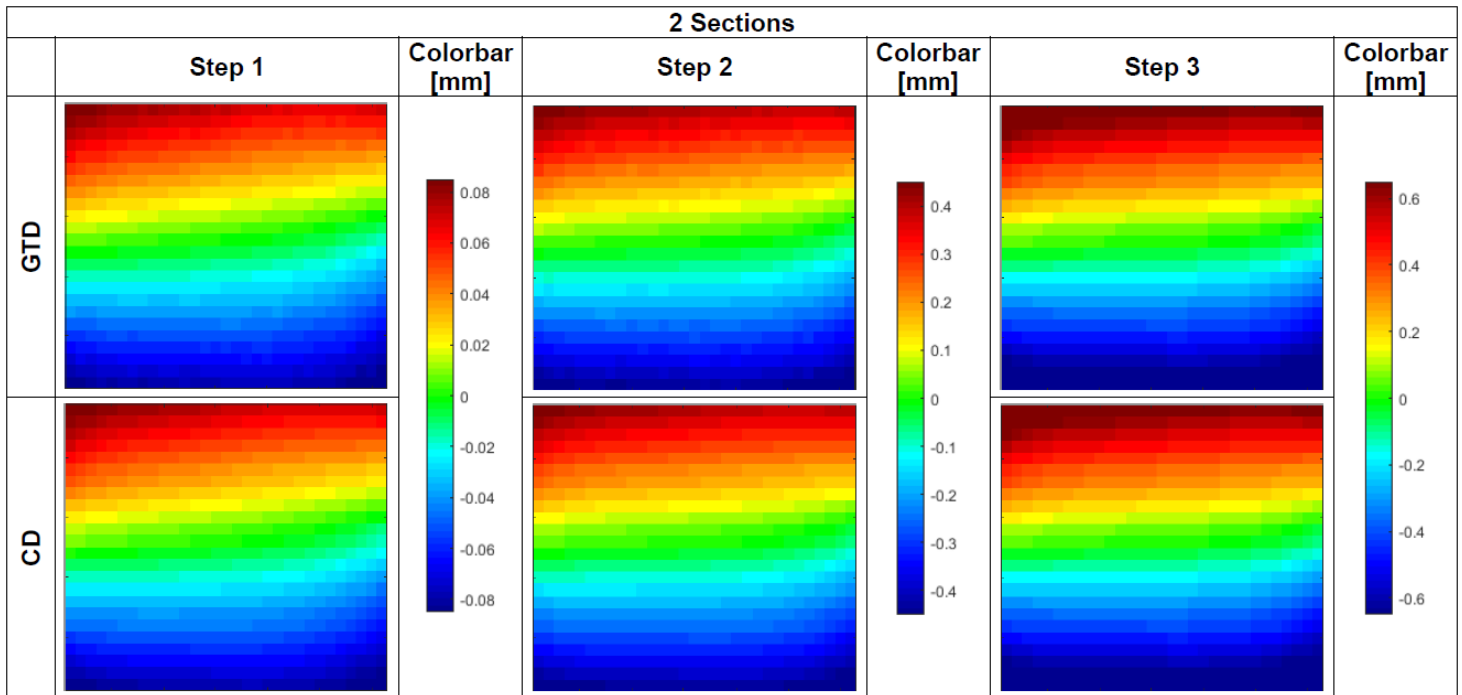


Figure 100: The displacement fields for the models including 2 Sections. Top row shows the GTD displacement fields for the three loading steps and bottom row shows the CD displacement fields with the estimated material properties.

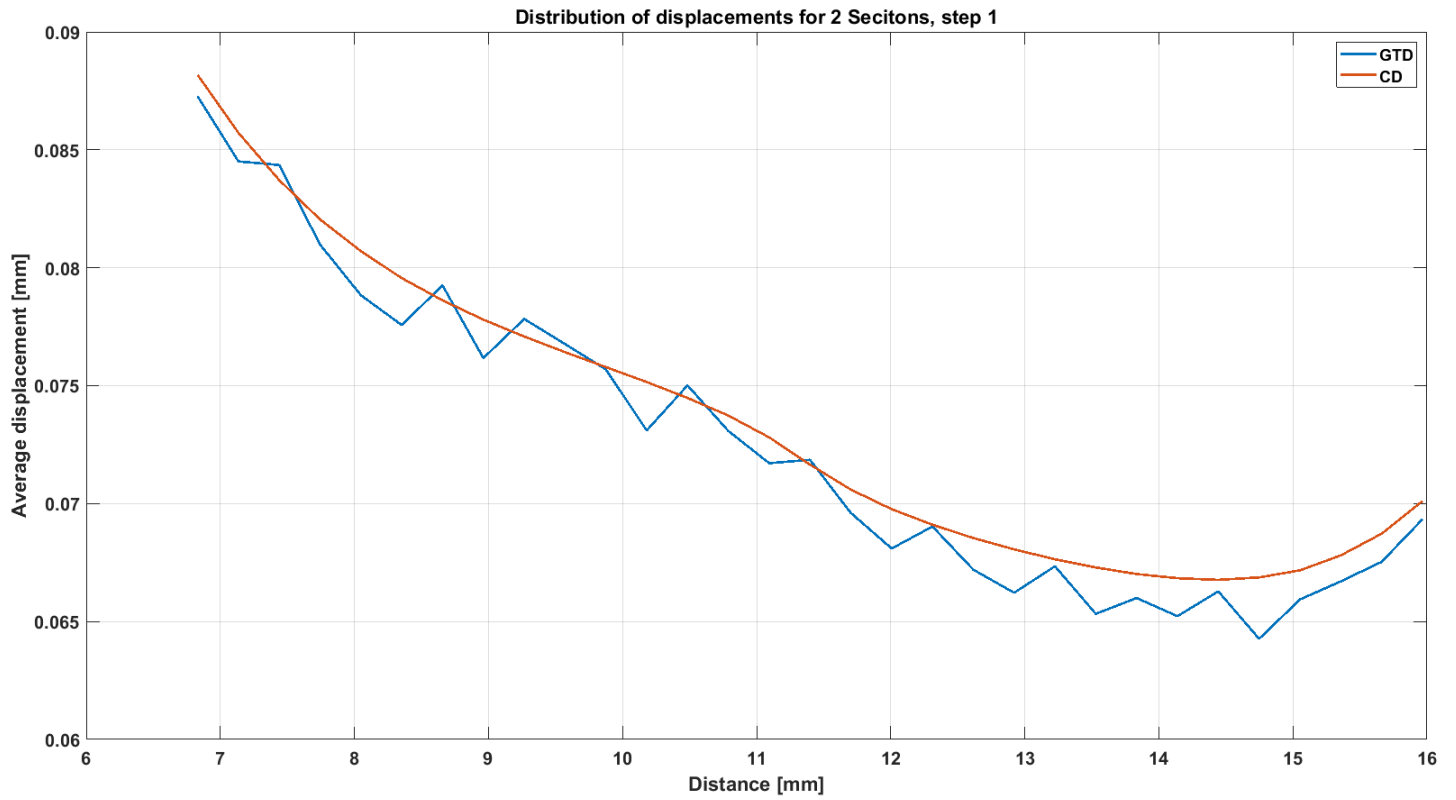


Figure 101: The distribution of displacement along the top edge of the ROI for the GTD and the CD, using 2 Sections model. The distributions belong the loading step 1.

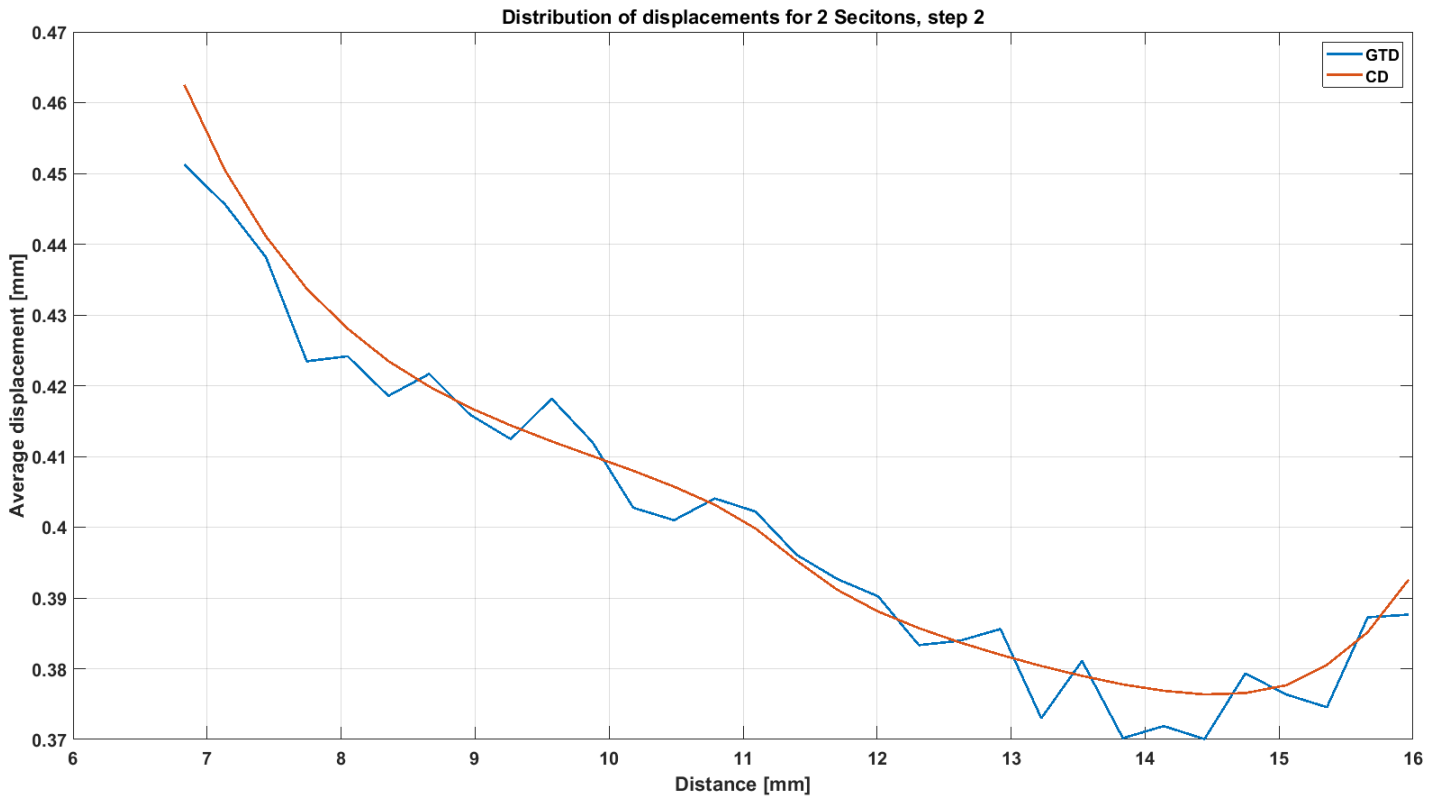


Figure 102: The distribution of displacement along the top edge of the ROI for the GTD and the CD, using 2 Sections model. The distributions belong the loading step 2.

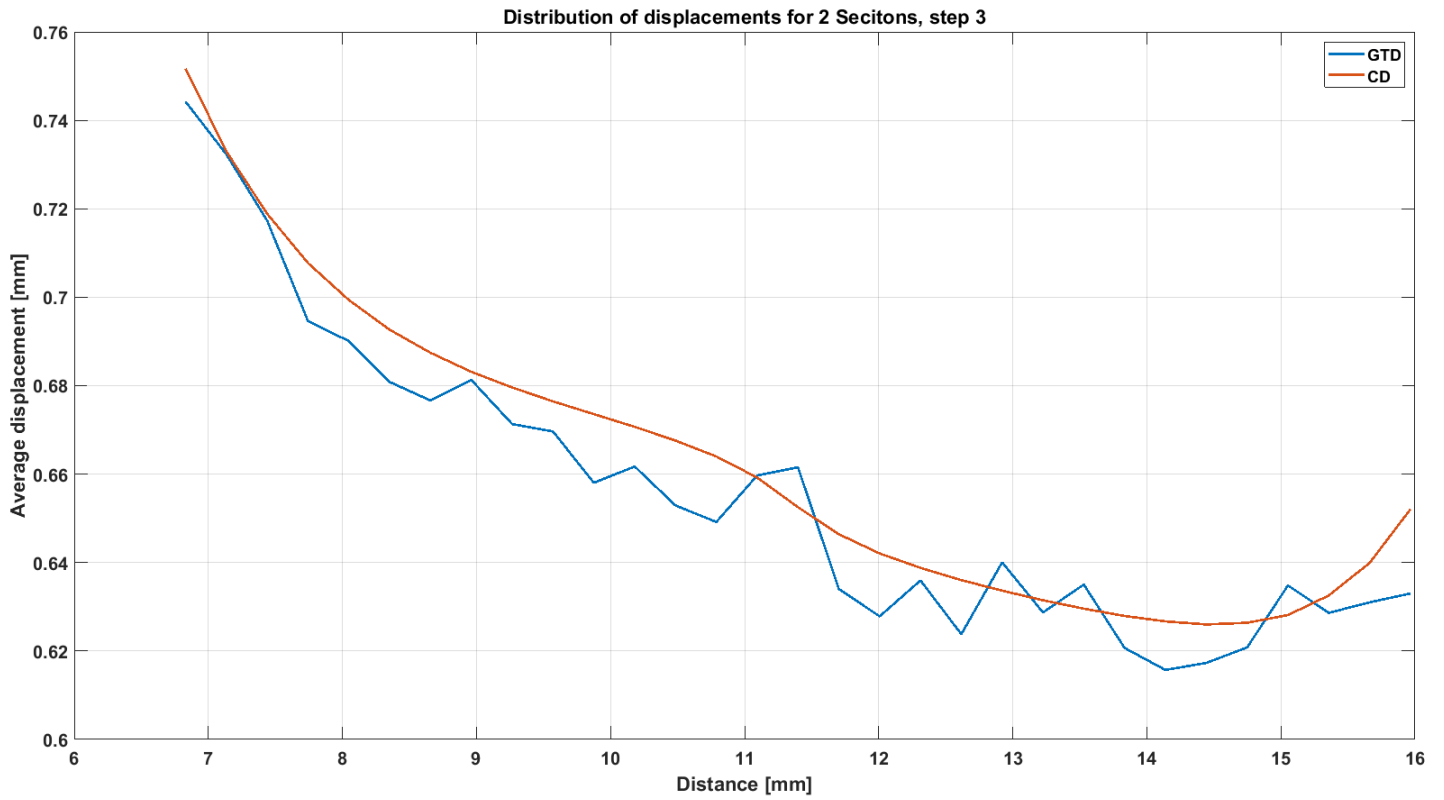


Figure 103: The distribution of displacement along the top edge of the ROI for the GTD and the CD, using 2 Sections model. The distributions belong to the loading step 3.

## 4 Sections

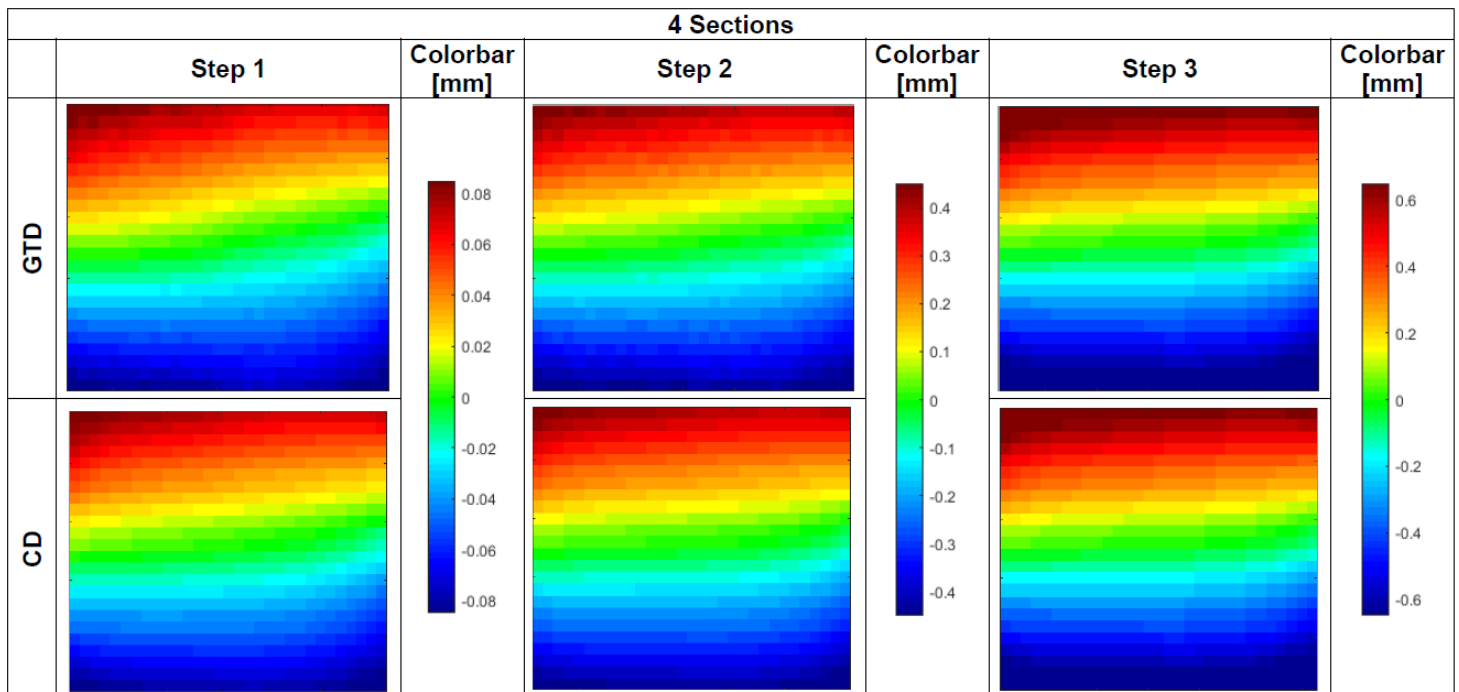


Figure 104: The displacement fields for the models including 4 Sections. Top row shows the GTD displacement fields for the three loading steps and bottom row shows the CD displacement fields with the estimated material properties.

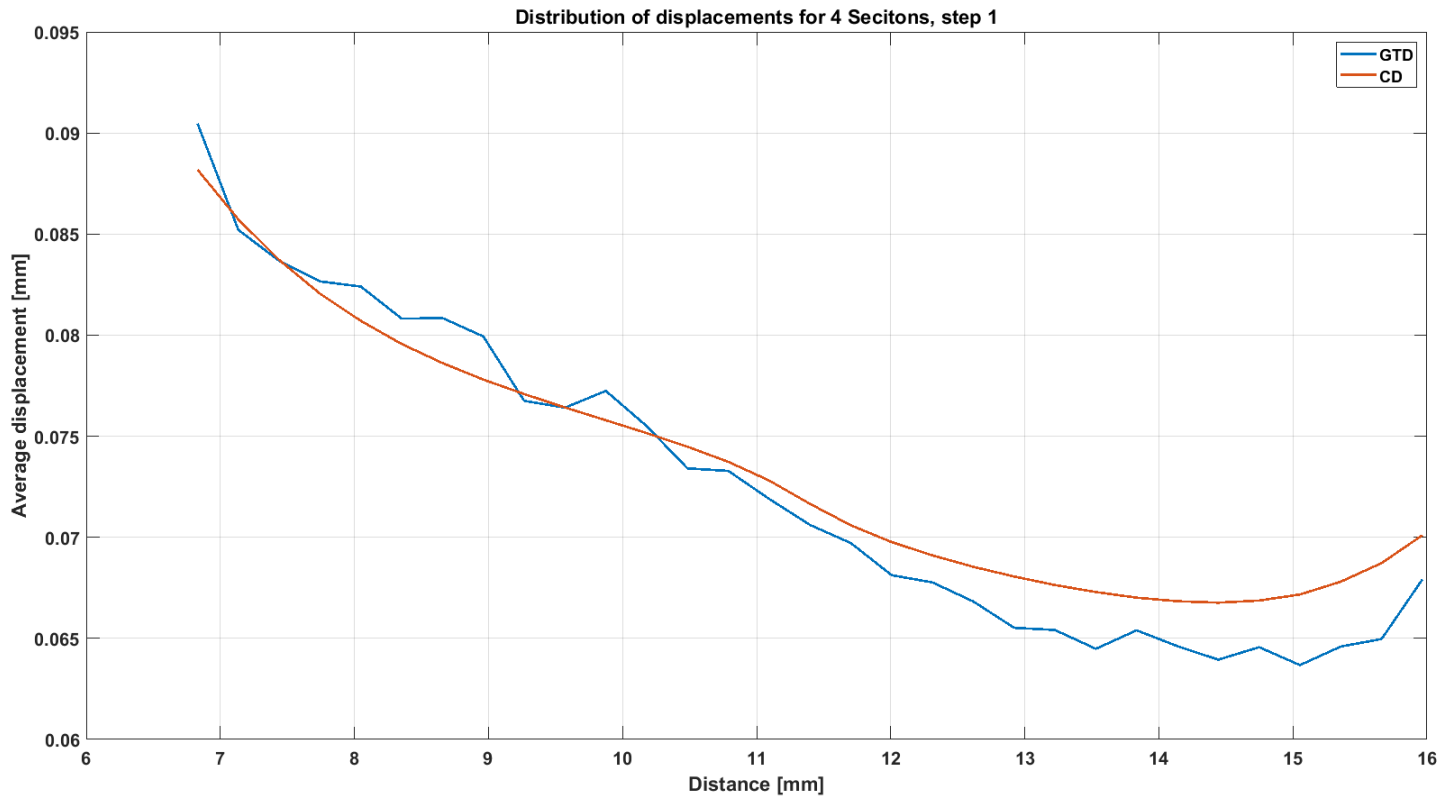


Figure 105: The distribution of displacement along the top edge of the ROI for the GTD and the CD, using 4 Sections model. The distributions belong the loading step 1.

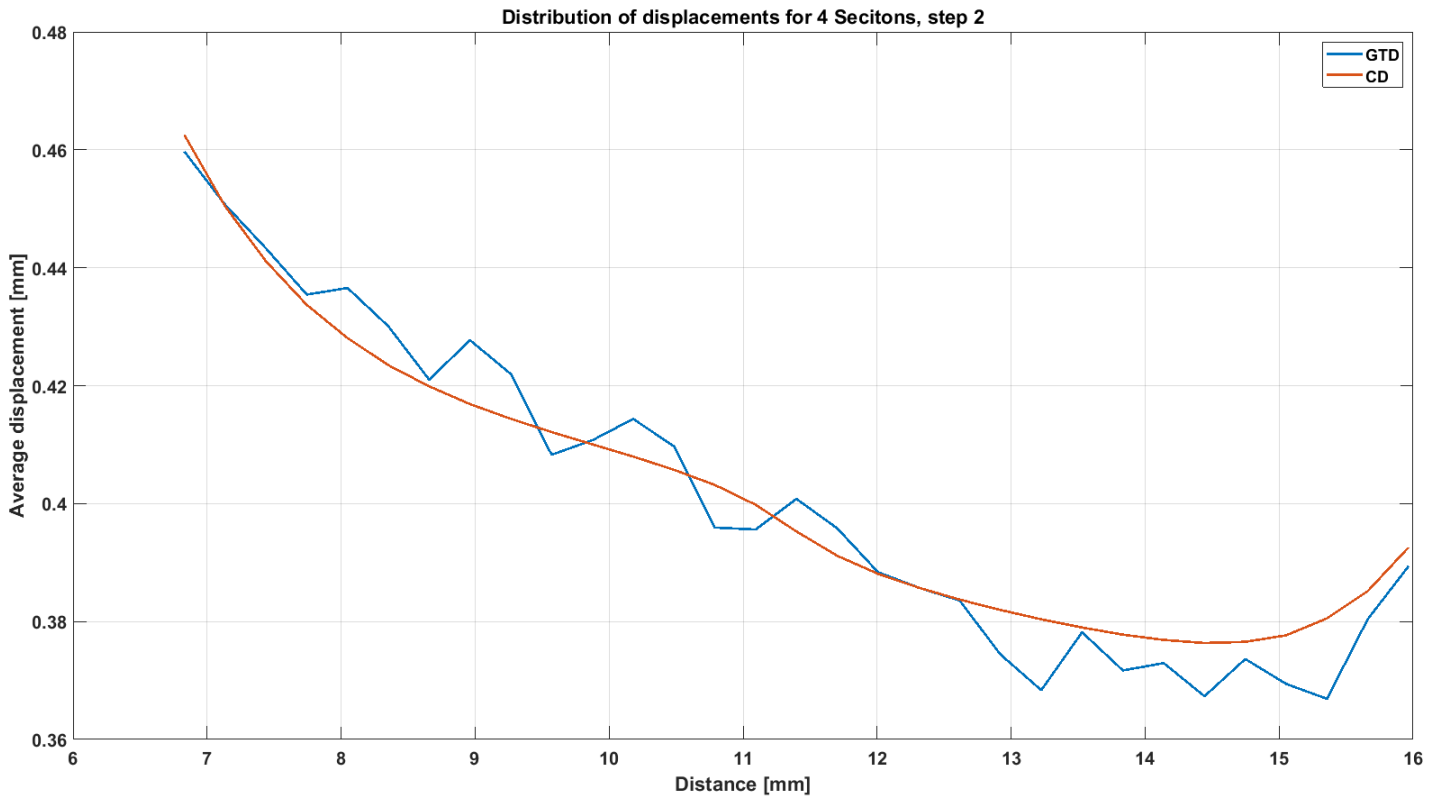


Figure 106: The distribution of displacement along the top edge of the ROI for the GTD and the CD, using 4 Sections model. The distributions belong the loading step 2.

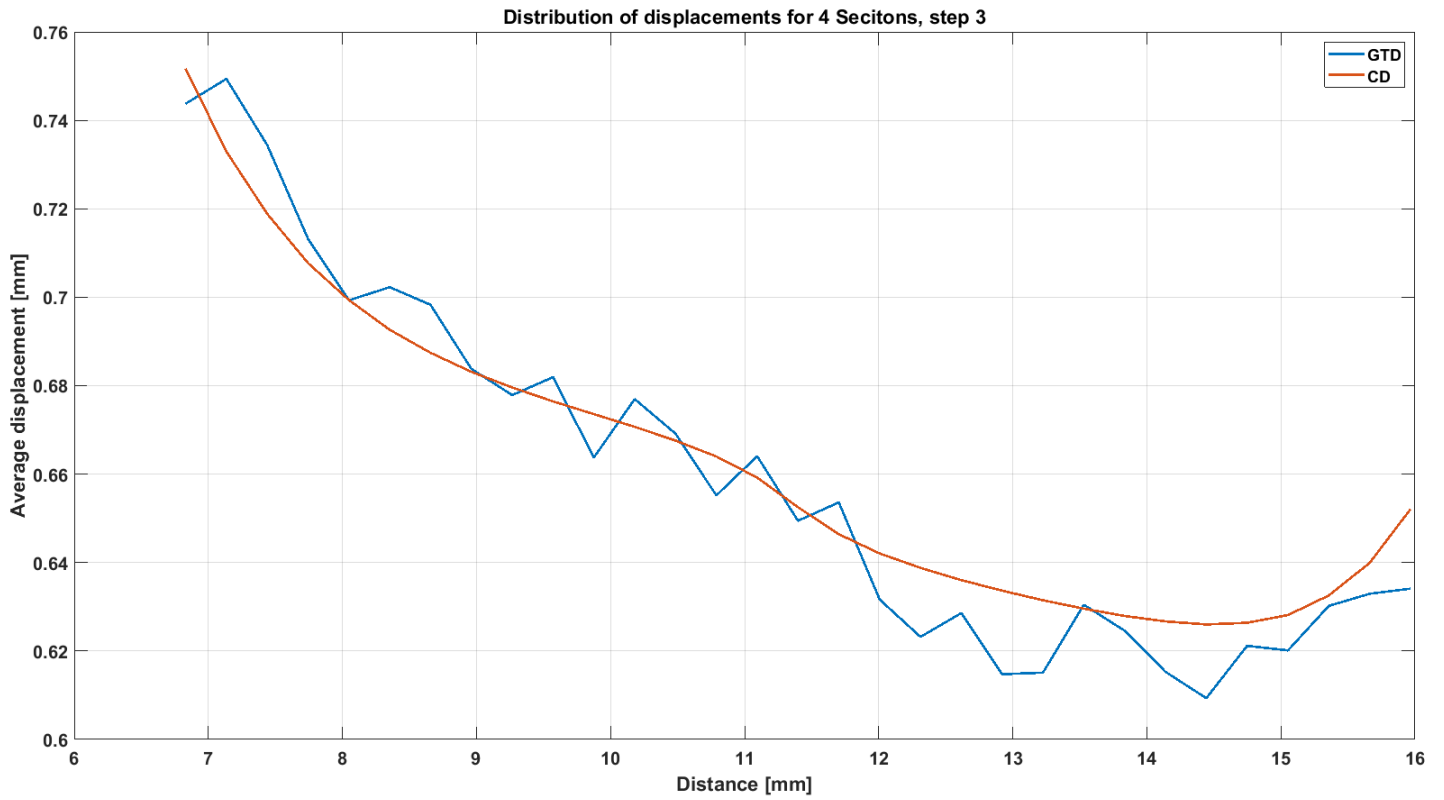


Figure 107: The distribution of displacement along the top edge of the ROI for the GTD and the CD, using 4 Sections model. The distributions belong to the loading step 3.

## 6 Sections

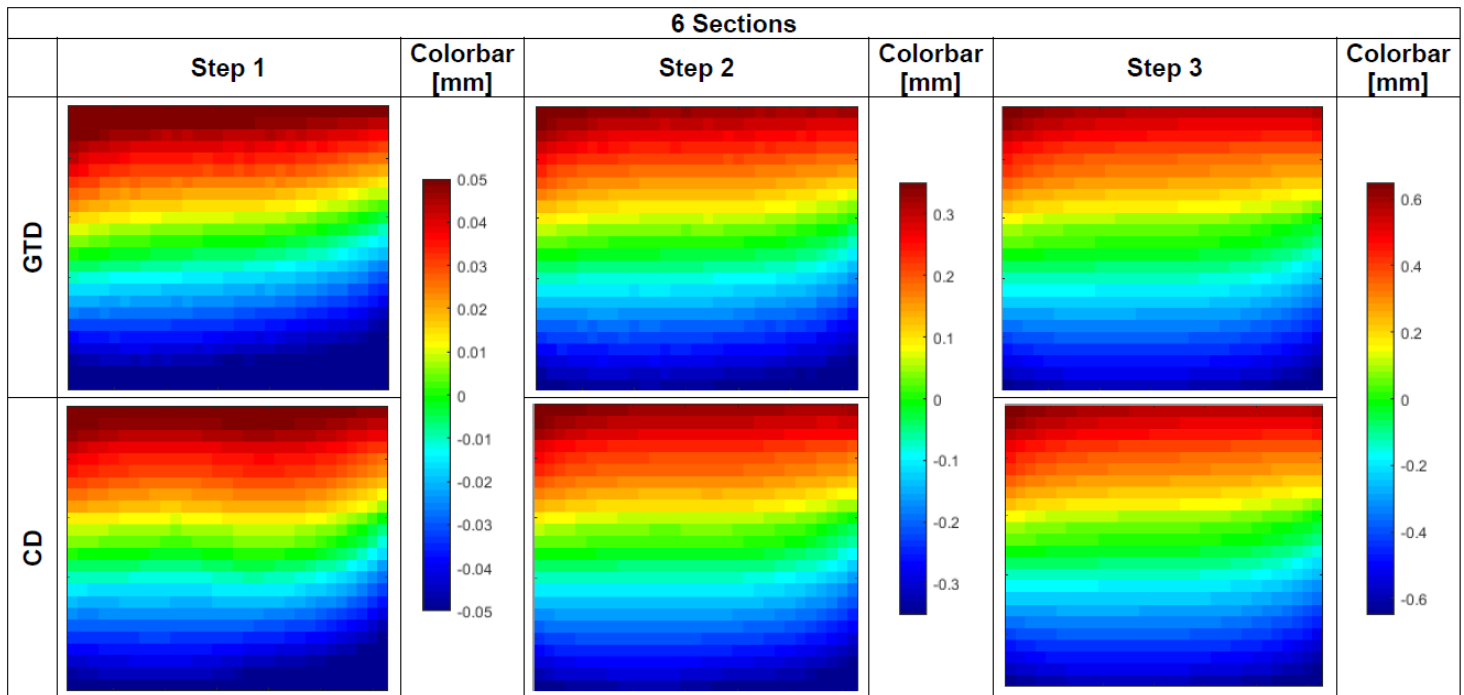


Figure 108: The displacement fields for the models including 6 Sections. Top row shows the GTD displacement fields for the three loading steps and bottom row shows the CD displacement fields with the estimated material properties.

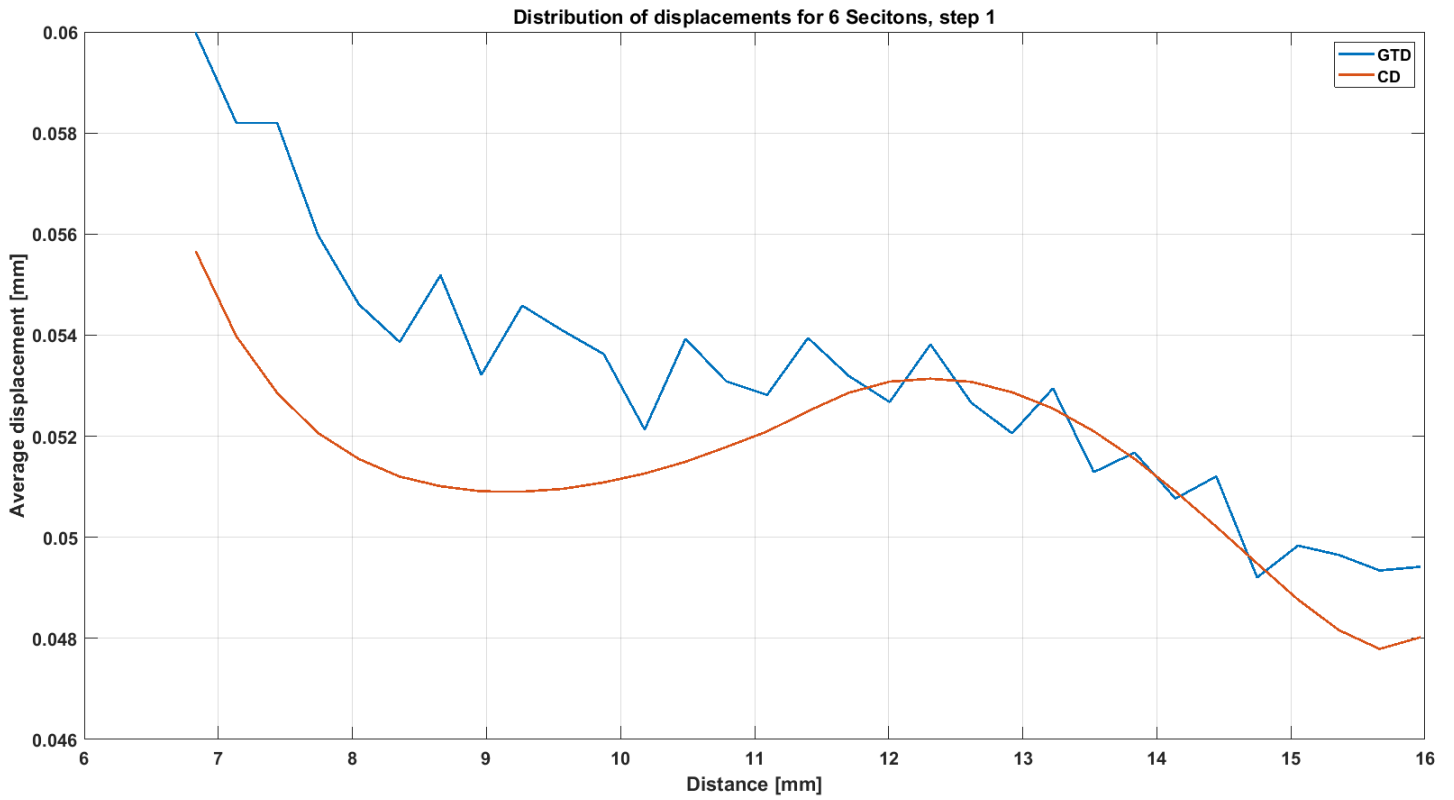


Figure 109: The distribution of displacement along the top edge of the ROI for the GTD and the CD, using 6 Sections model. The distributions belong to the loading step 1.

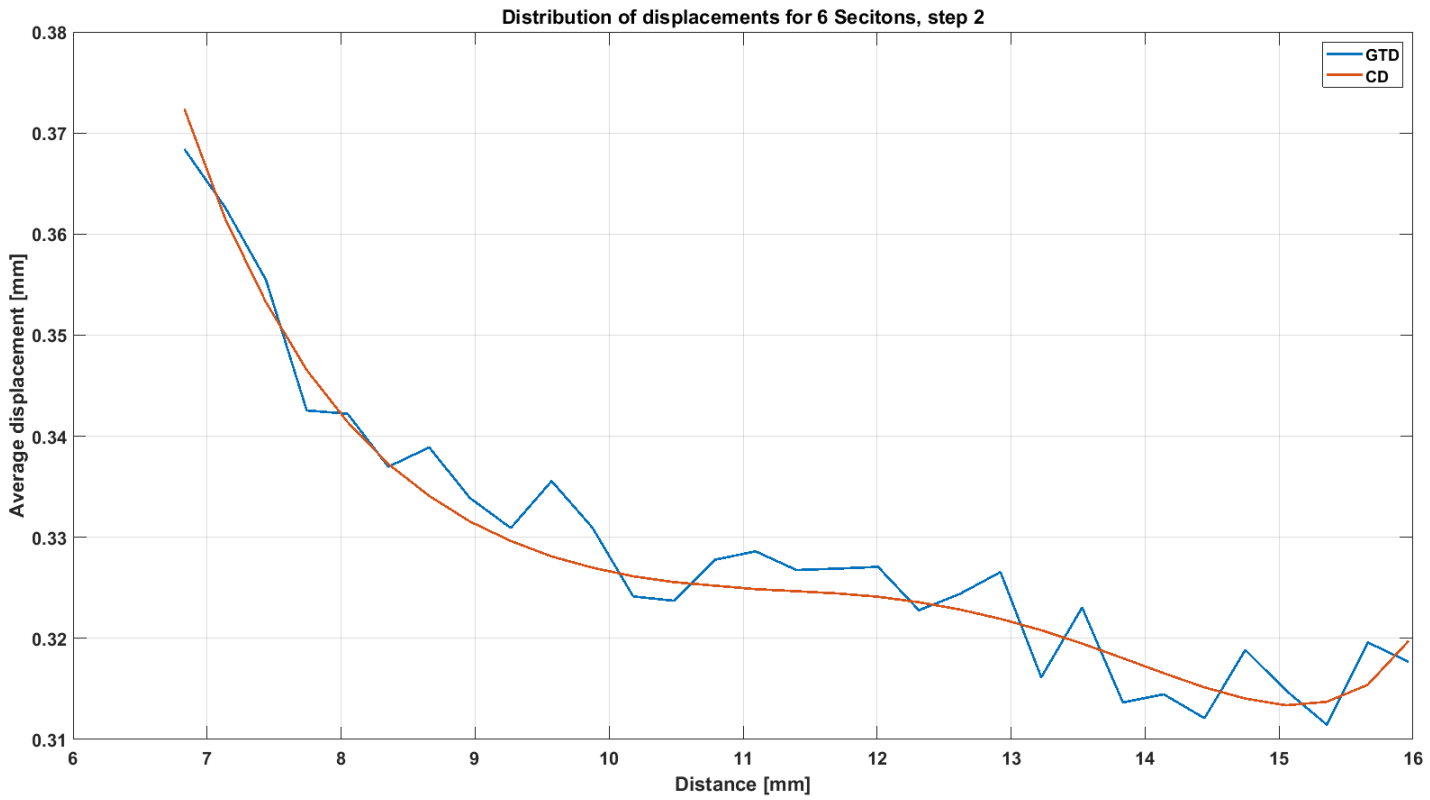


Figure 110: The distribution of displacement along the top edge of the ROI for the GTD and the CD, using 6 Sections model. The distributions belong the loading step 2.

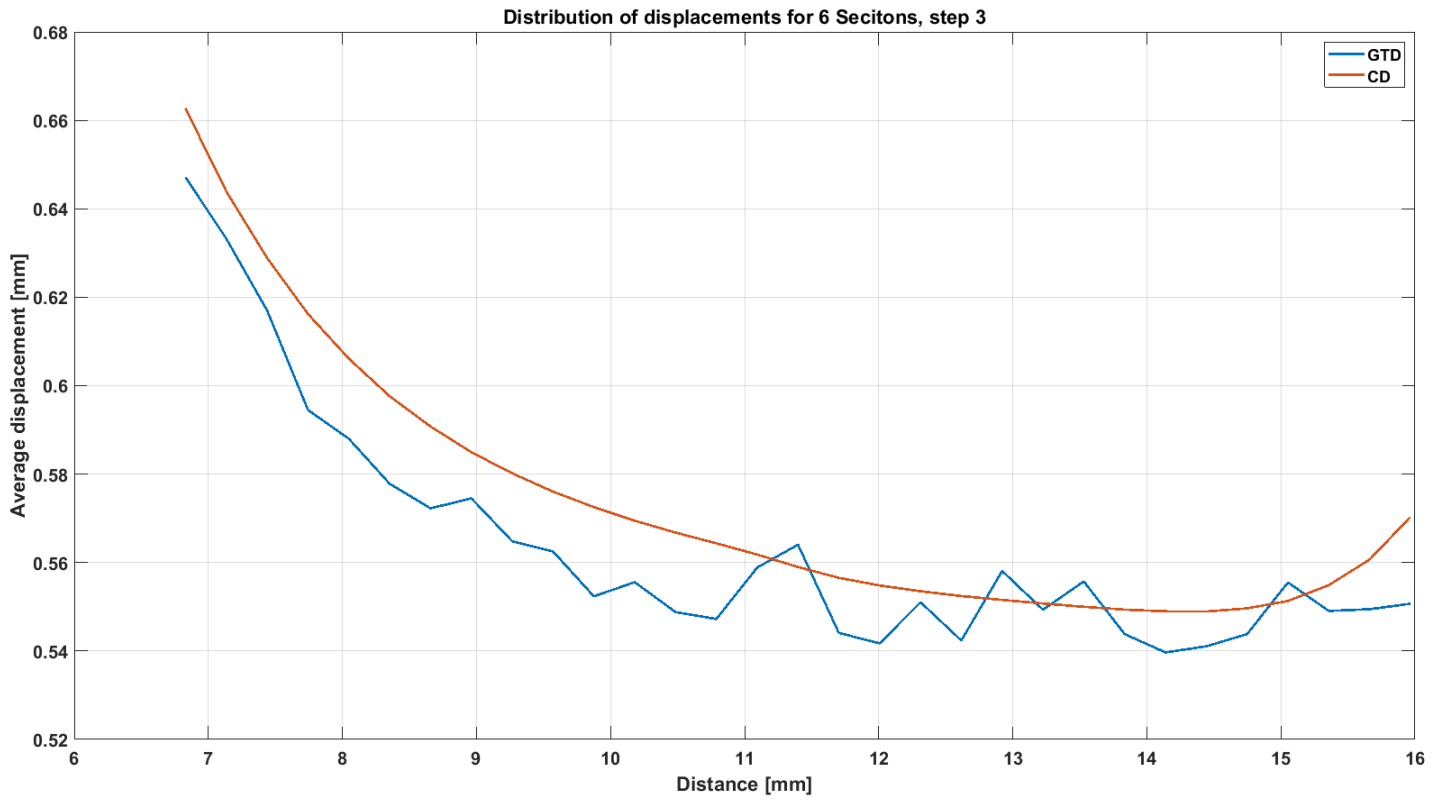


Figure 111: The distribution of displacement along the top edge of the ROI for the GTD and the CD, using 6 Sections model. The distributions belong to the loading step 3.

# L DE control parameters

## L.1 Estimation procedure

Mutation factor [0.2 1.5]

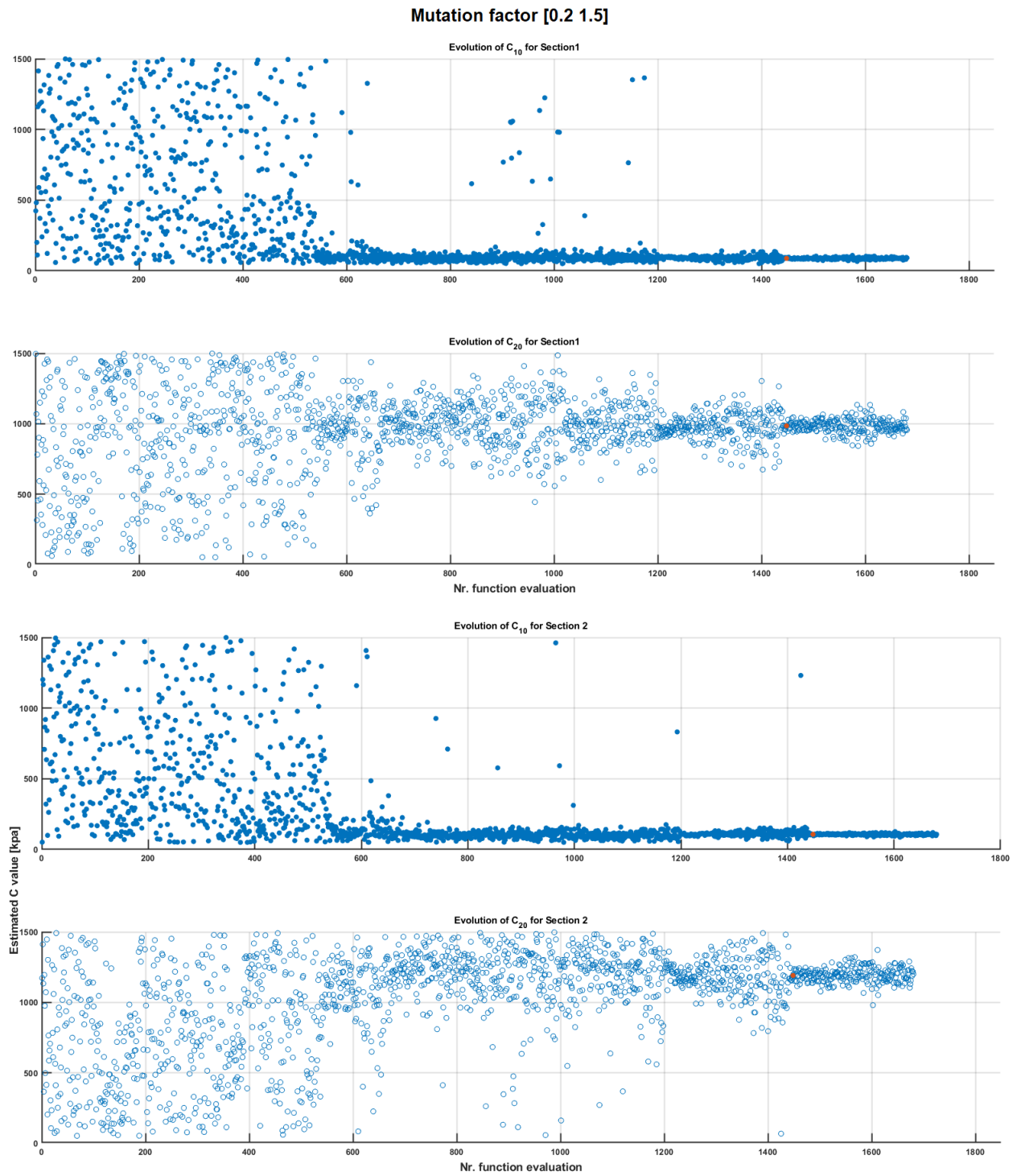


Figure 112: Evolution of material parameters for  $F = [0.21.5]$

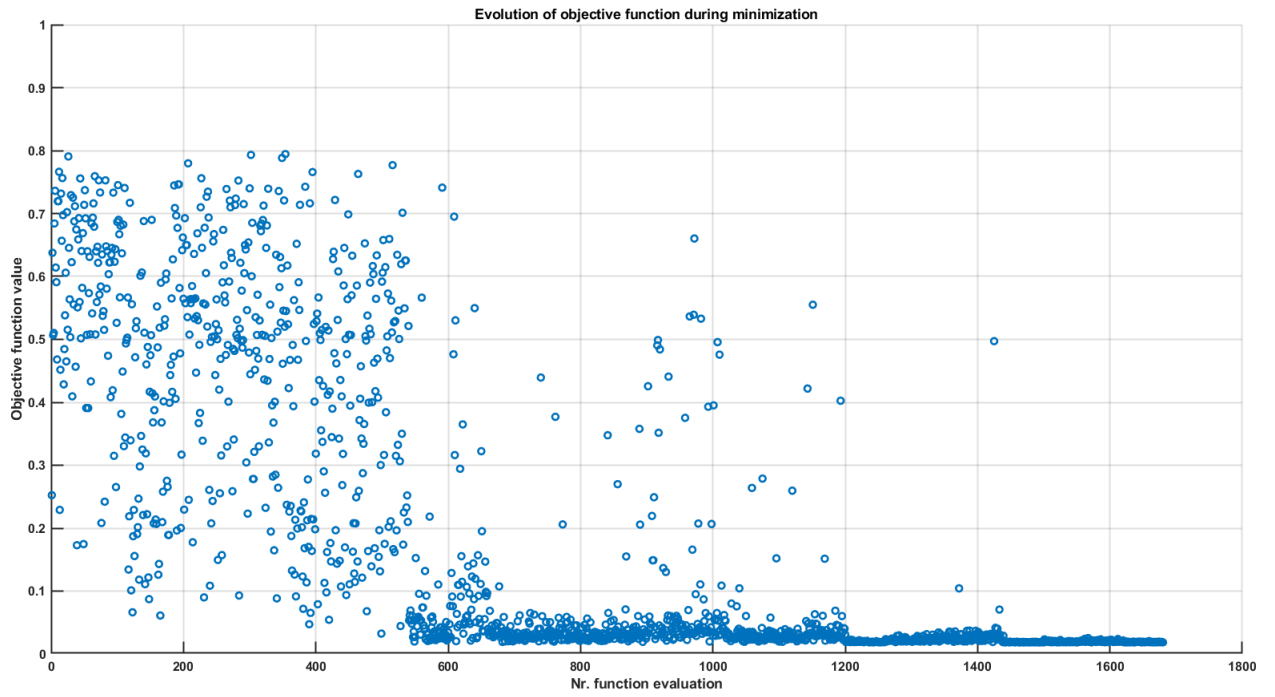


Figure 113: Evolution of objective function for  $F = [0.21.5]$

Crossover probability  $P = 0.5$



Figure 114: Evolution of material parameter for  $P = 0.5$

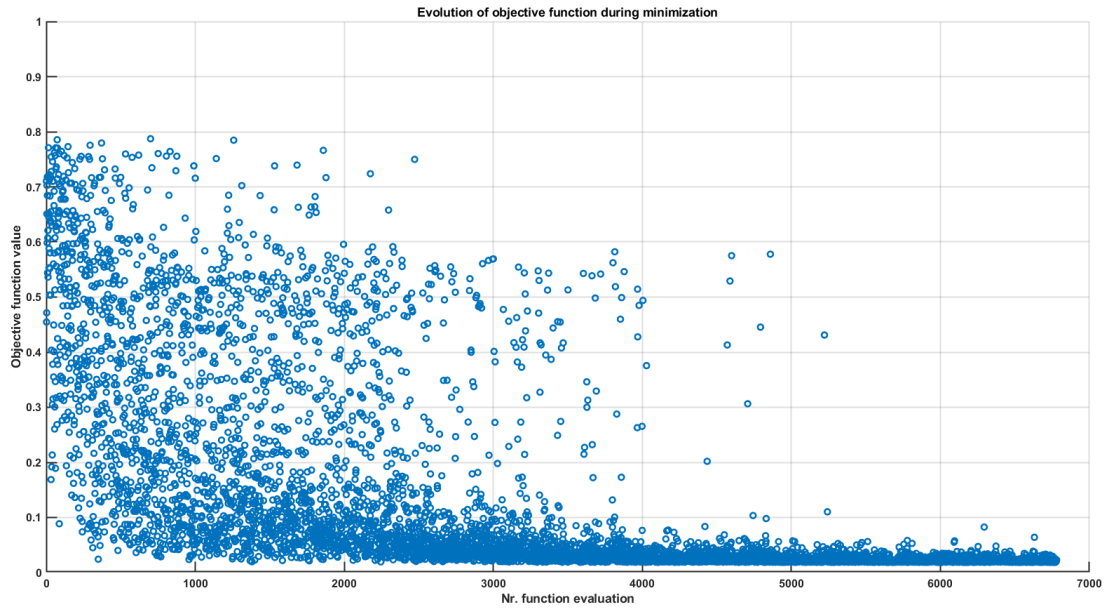


Figure 115: Objective function for  $P = 0.5$

# Mutation strategy rand1bin



Figure 116: Material property estimation using mutation strategy rand1bin

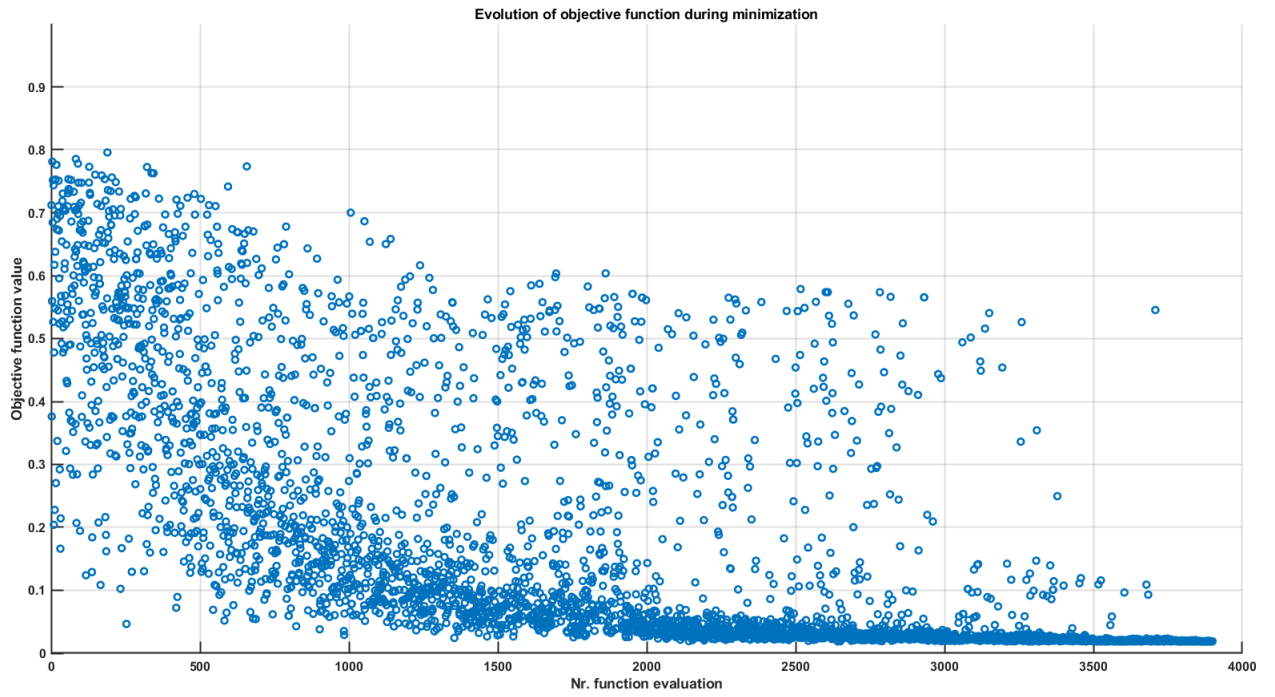


Figure 117: Objective functions of the estimation belonging to rand1bin mutation strategy

## L.2 Resulting displacement fields

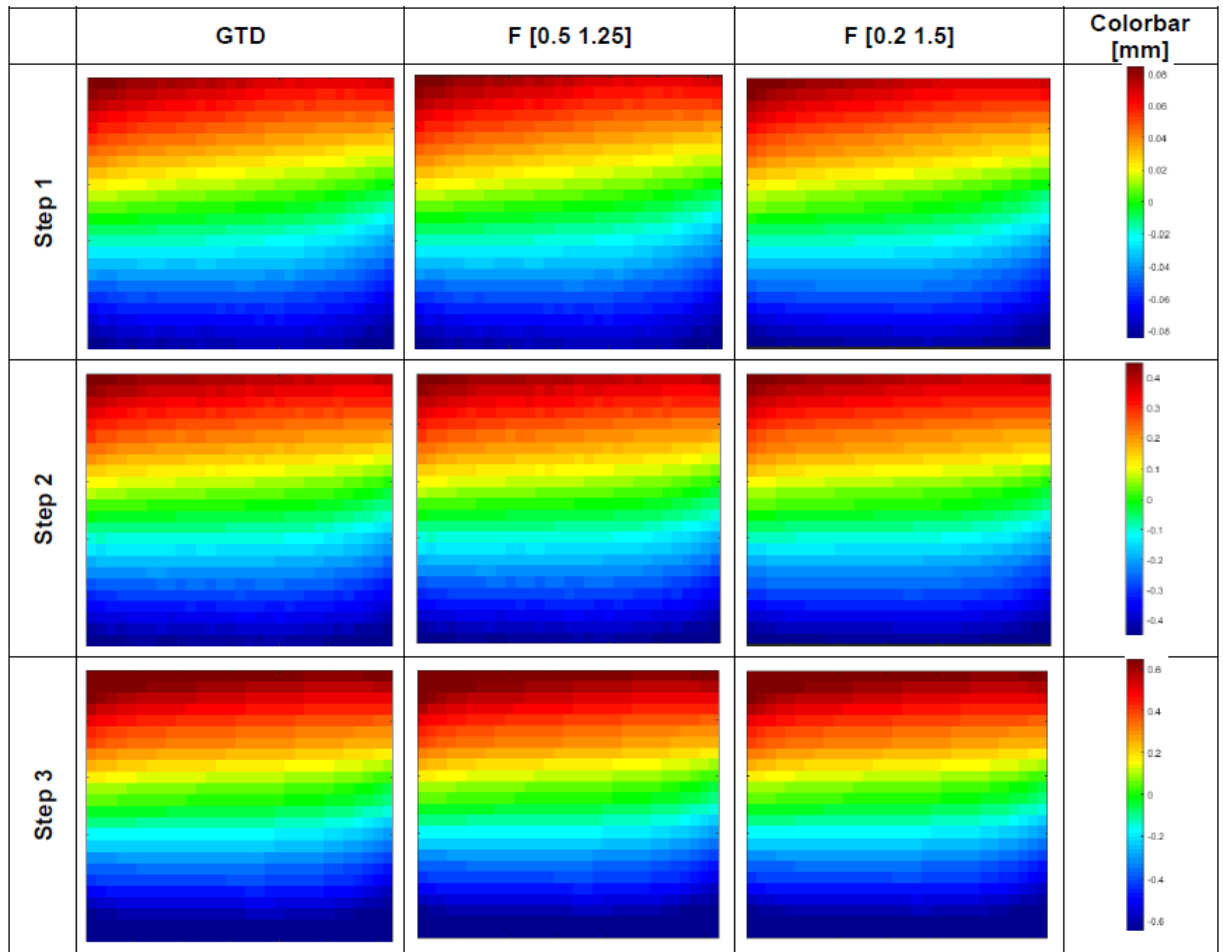


Figure 118: Visual comparison between the GTD (left), and the resulting CD using Mutation factor [0.5 1.25] (middle) and [0.2 1.5] (right). Different step levels are included, step 1 top, step 2 middle and step 3 bottom.

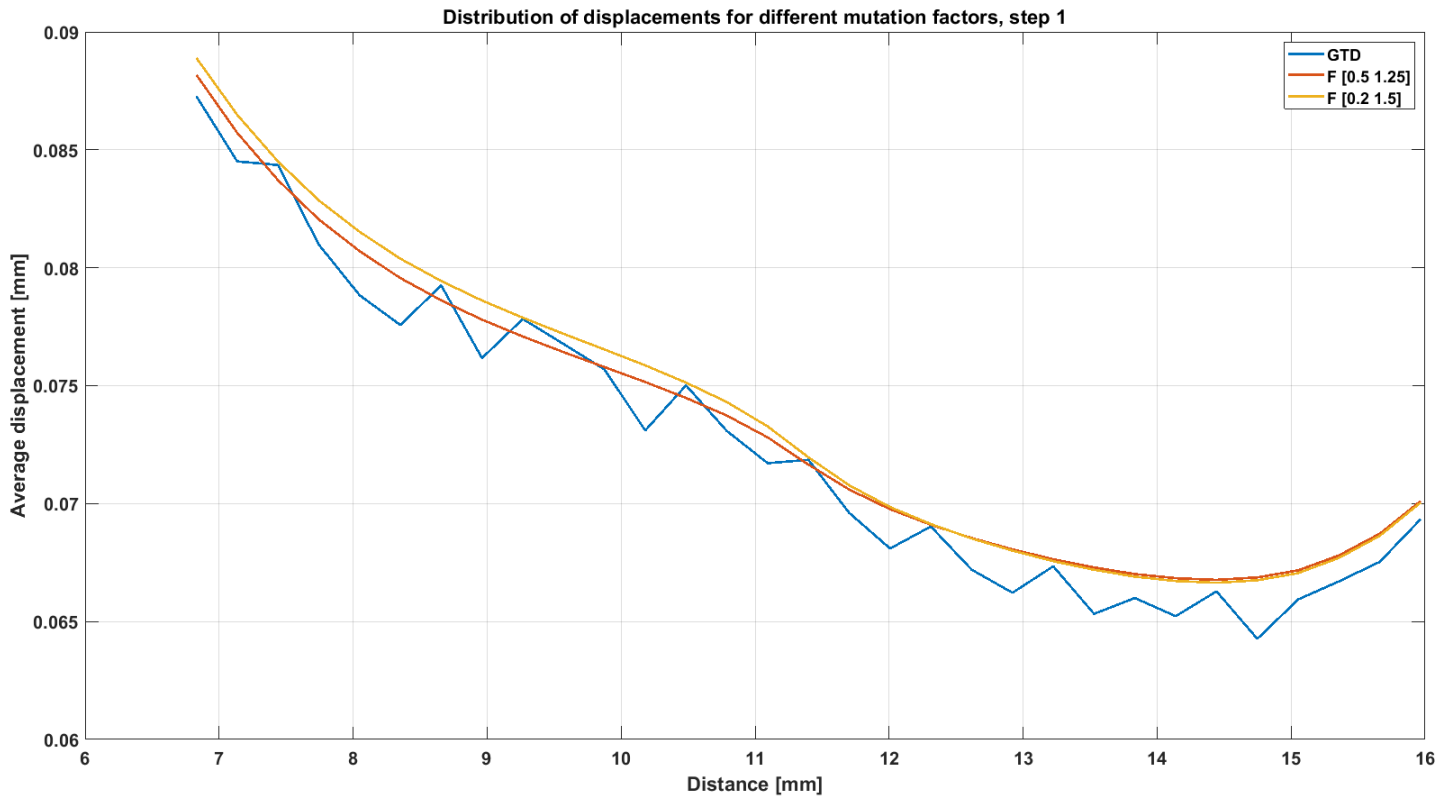


Figure 119: Comparing the distribution of displacements along the top of the ROI. Blue line represents the GTD, red line belongs to the displacement field estimated with mutation factor [0.5 1.25], and yellow line represents the distribution of the displacement after the estimation procedure with mutation factor [0.2 1.5]. The distributions belong to the loading step 1.

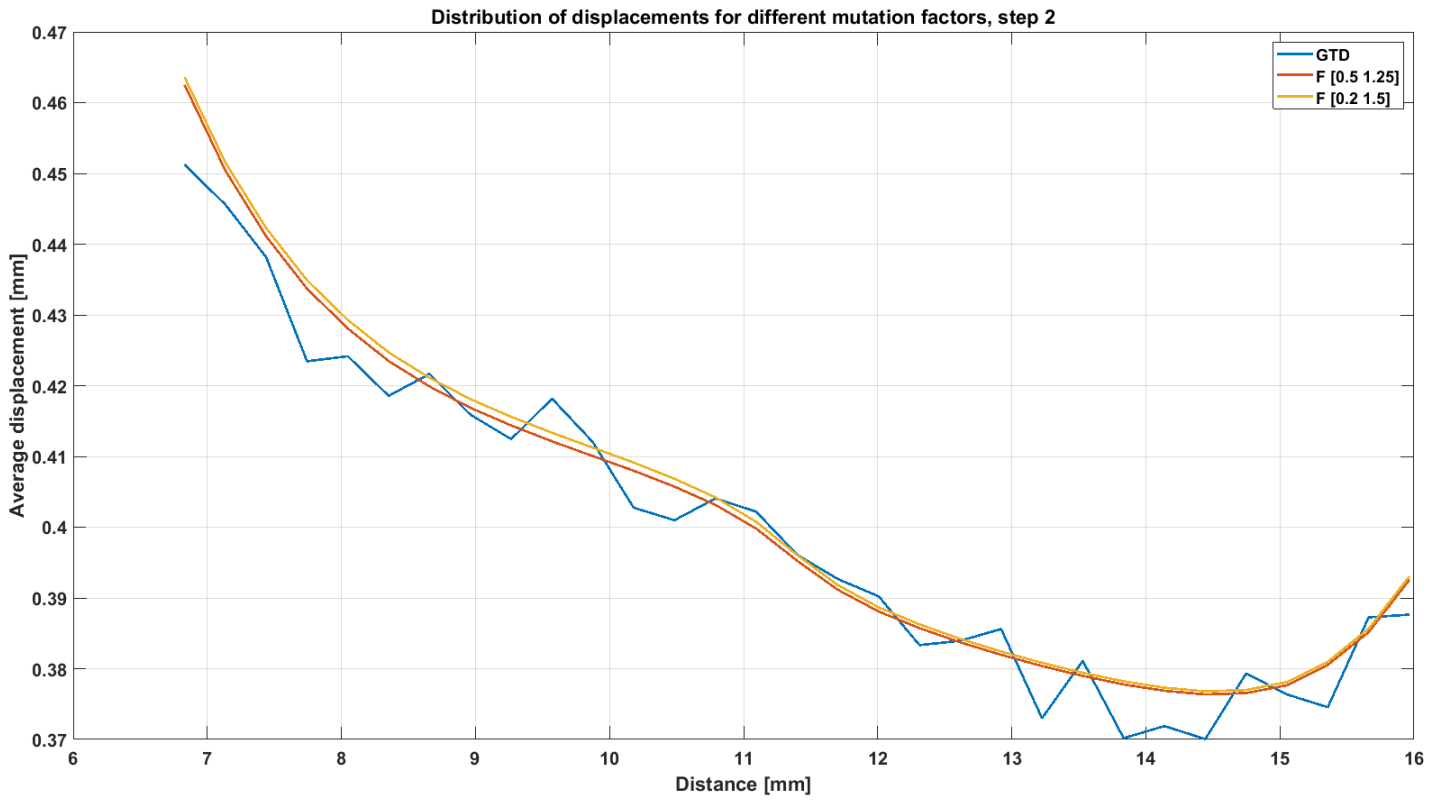


Figure 120: Comparing the distribution of displacements along the top of the ROI. Blue line represents the GTD, red line belongs to the displacement field estimated with mutation factor [0.5 1.25], and yellow line represents the distribution of the displacement after the estimation procedure with mutation factor [0.2 1.5]. The distributions belong the loading step 1.

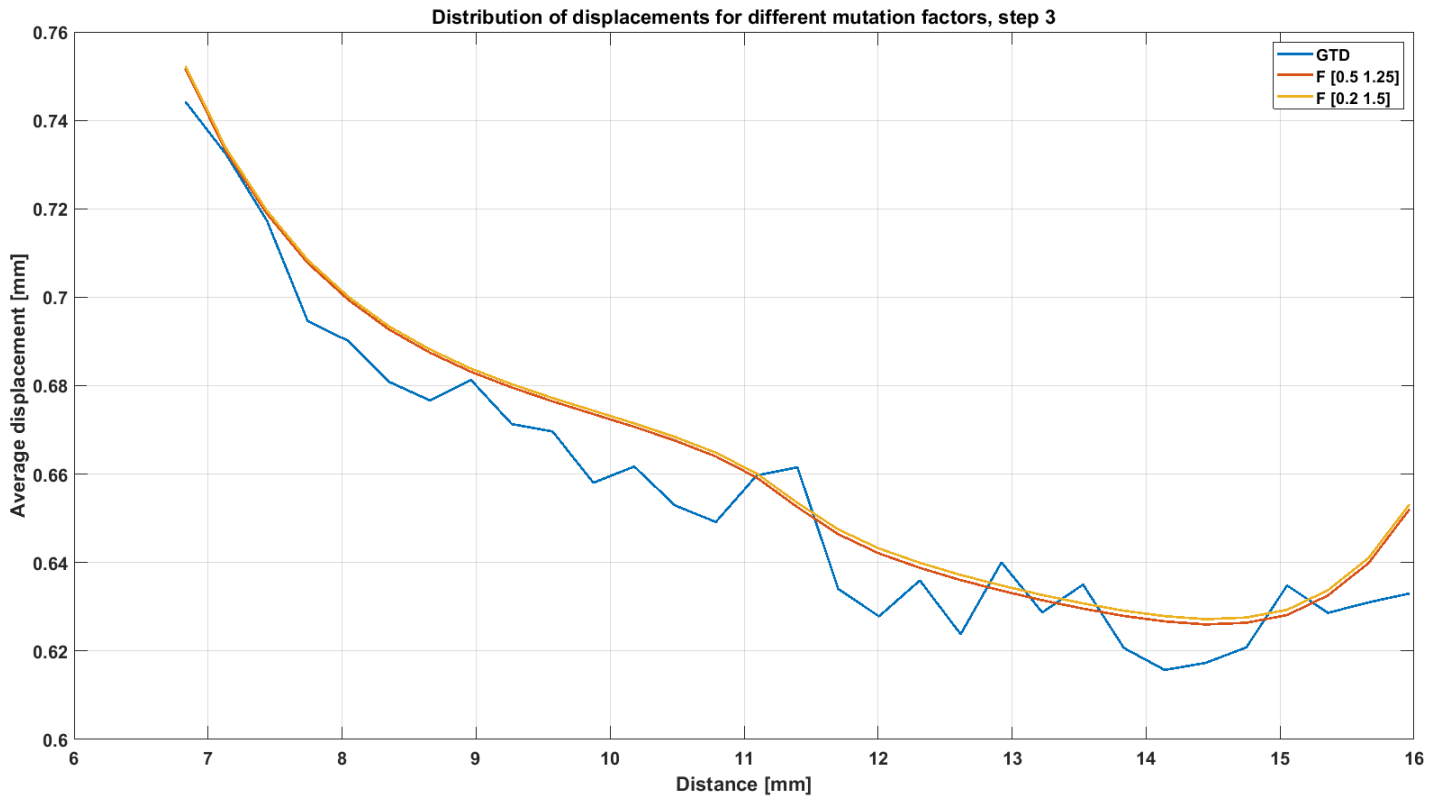


Figure 121: Comparing the distribution of displacements along the top of the ROI. Blue line represents the GTD, red line belongs to the displacement field estimated with mutation factor [0.5 1.25], and yellow line represents the distribution of the displacement after the estimation procedure with mutation factor [0.2 1.5]. The distributions belong to the loading step 1.

## Crossover probability

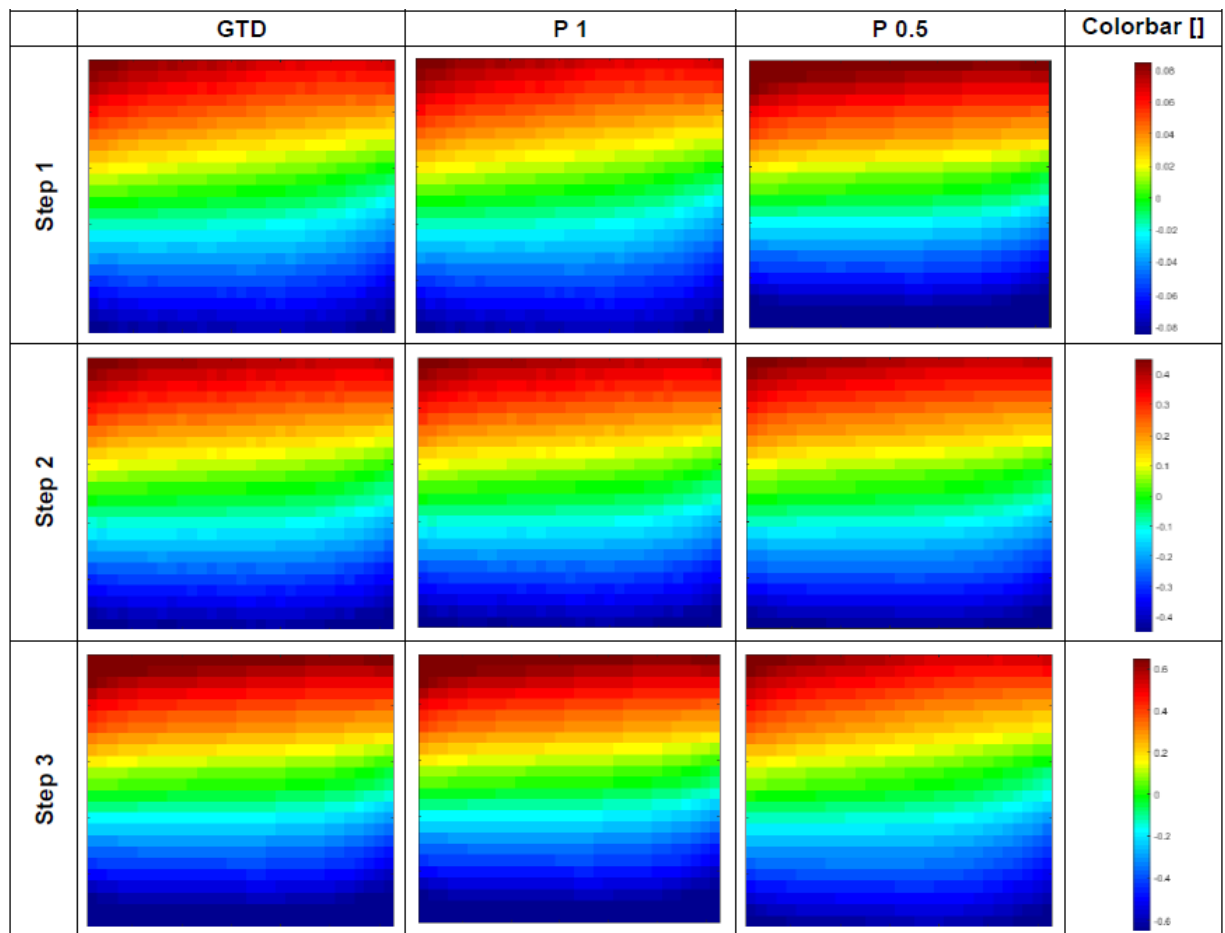


Figure 122: Visual comparison between the GTD (left), and the resulting CD using crossover probability  $P=1$  (middle) and  $P=0.5$  (right). Different step levels are included, step 1 top, step 2 middle and step 3 bottom.

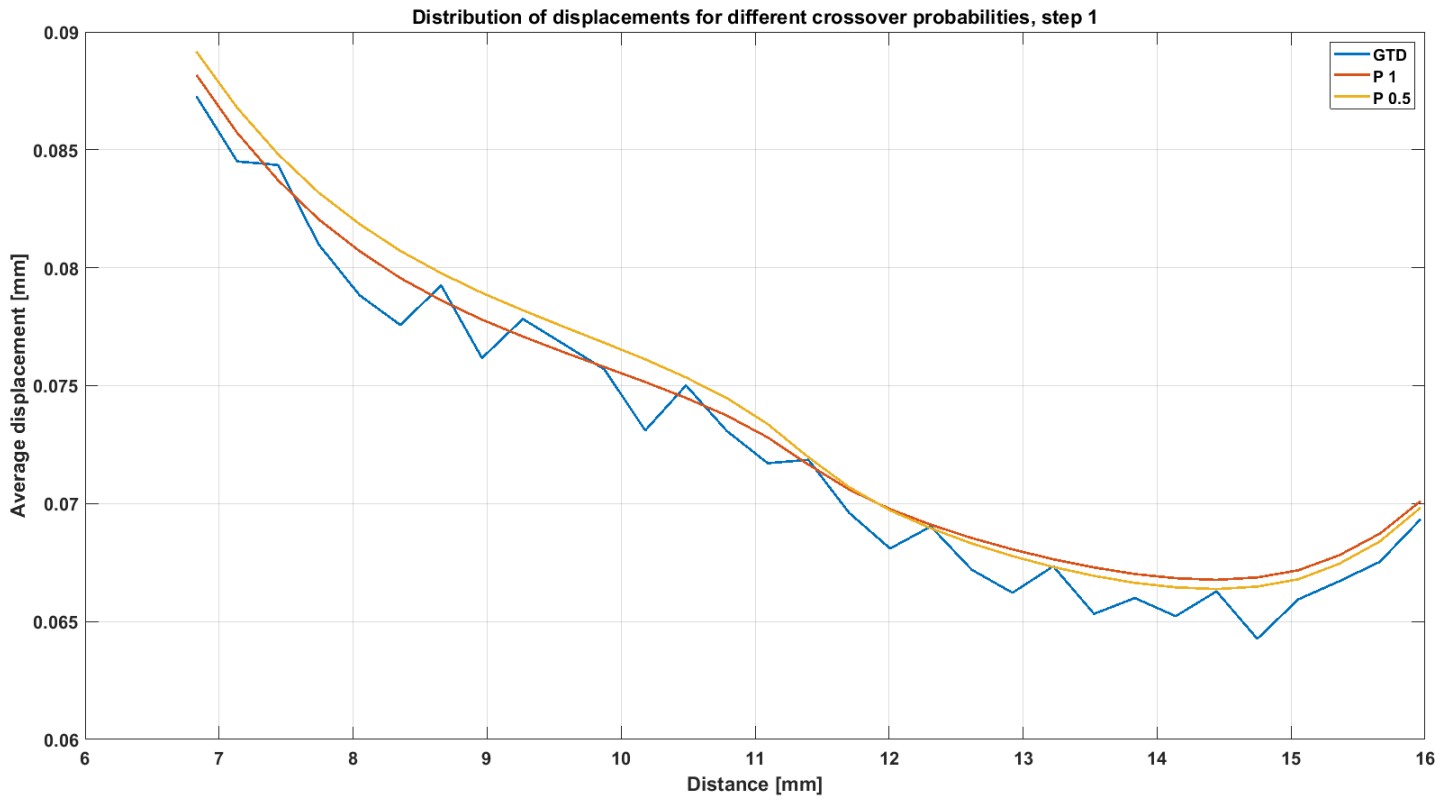


Figure 123: Comparing the distribution of displacements along the top of the ROI. Blue line represents the GTD, red line belongs to the displacement field estimated with crossover probability  $P=1$ , and yellow line represents the distribution of the displacement after the estimation procedure with crossover probability  $P=0.5$ . The distributions belong to the loading step 1.

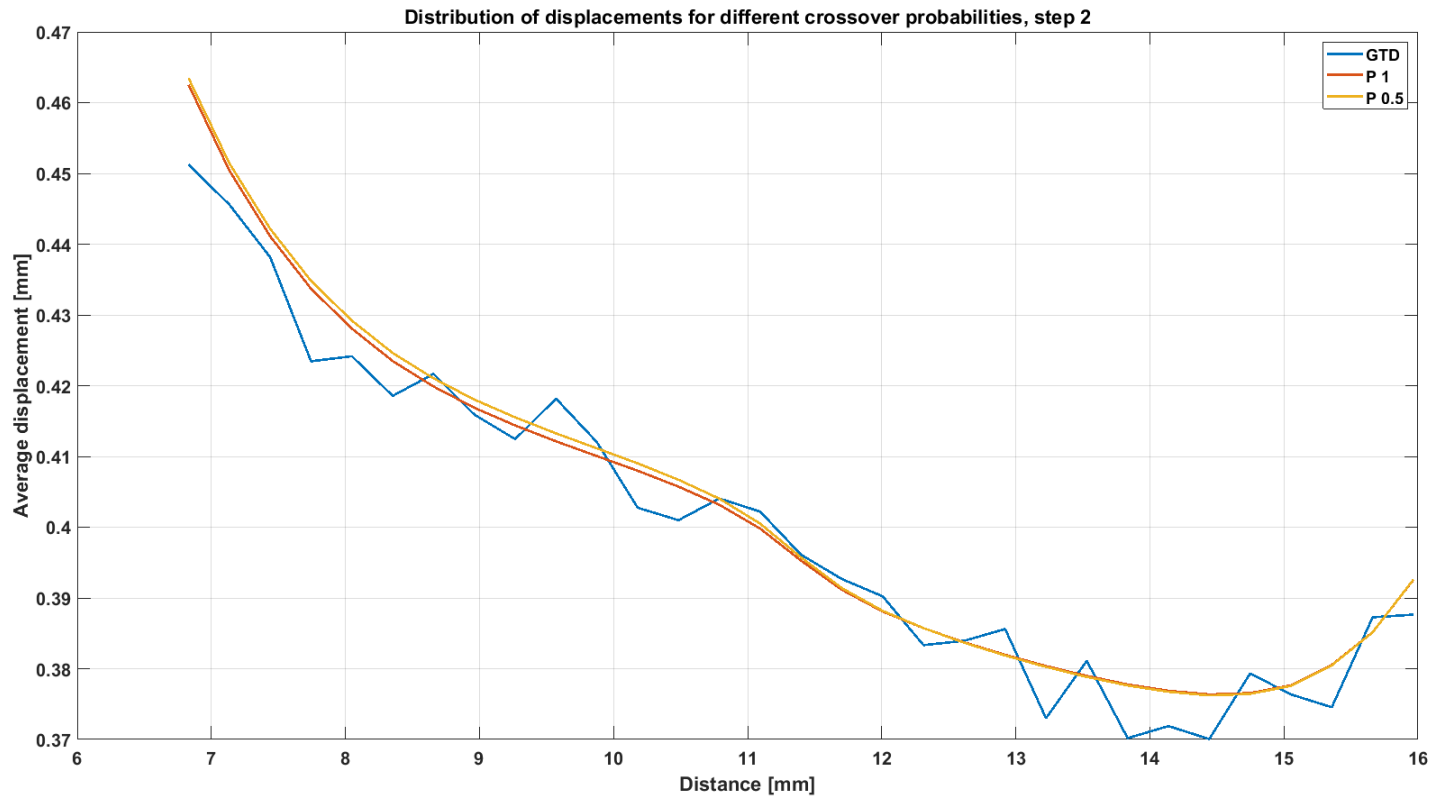


Figure 124: Comparing the distribution of displacements along the top of the ROI. Blue line represents the GTD, red line belongs to the displacement field estimated with crossover probability  $P=1$ , and yellow line represents the distribution of the displacement after the estimation procedure with crossover probability  $P=0.5$ . The distributions belong to the loading step 2.

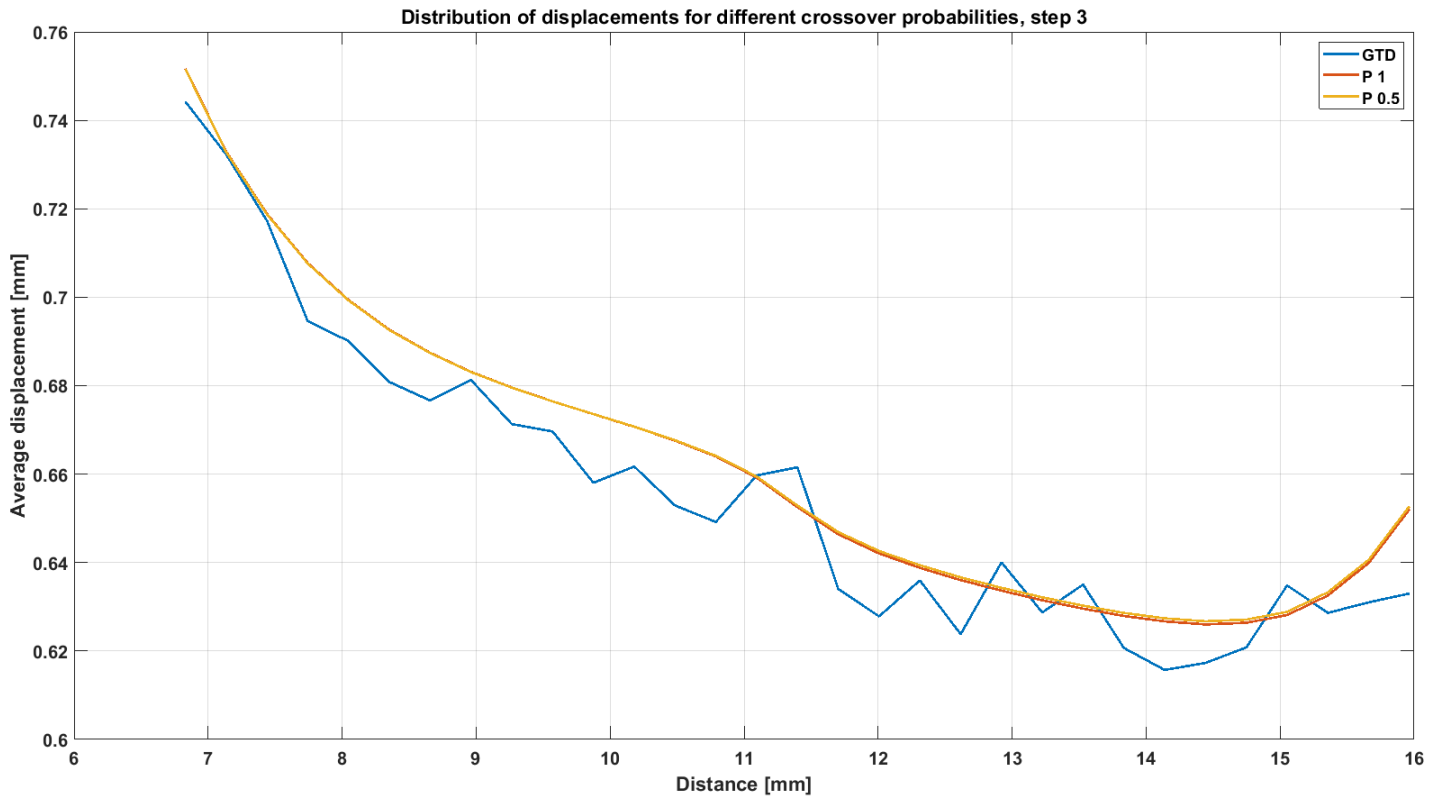


Figure 125: Comparing the distribution of displacements along the top of the ROI. Blue line represents the GTD, red line belongs to the displacement field estimated with crossover probability  $P=1$ , and yellow line represents the distribution of the displacement after the estimation procedure with crossover probability  $P=0.5$ . The distributions belong to the loading step 3.

## Mutation strategy

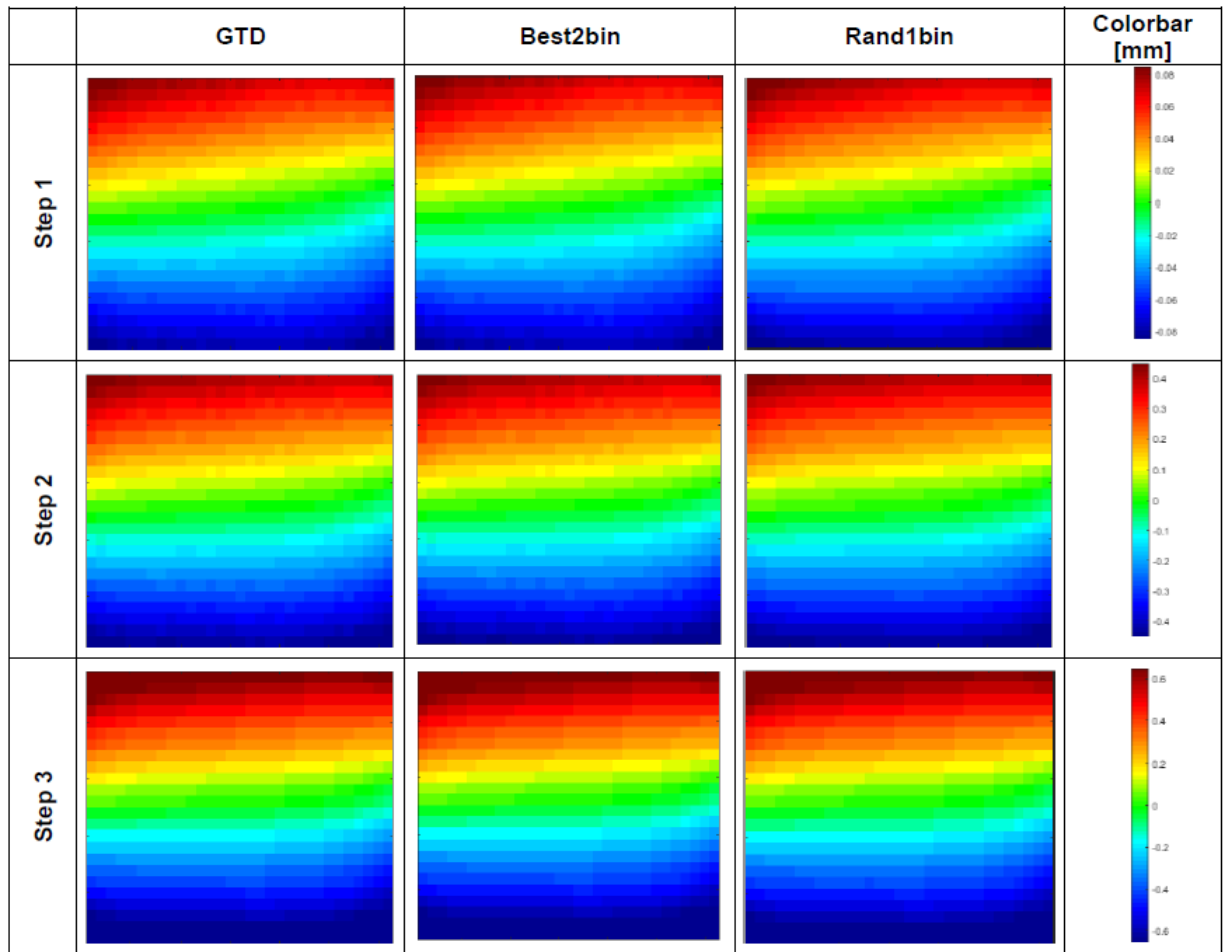


Figure 126: Visual comparison between the GTD (left), and the resulting CD using mutation strategy best2bin (middle) and rand1bin (right). Different step levels are included, step 1 top, step 2 middle and step 3 bottom.

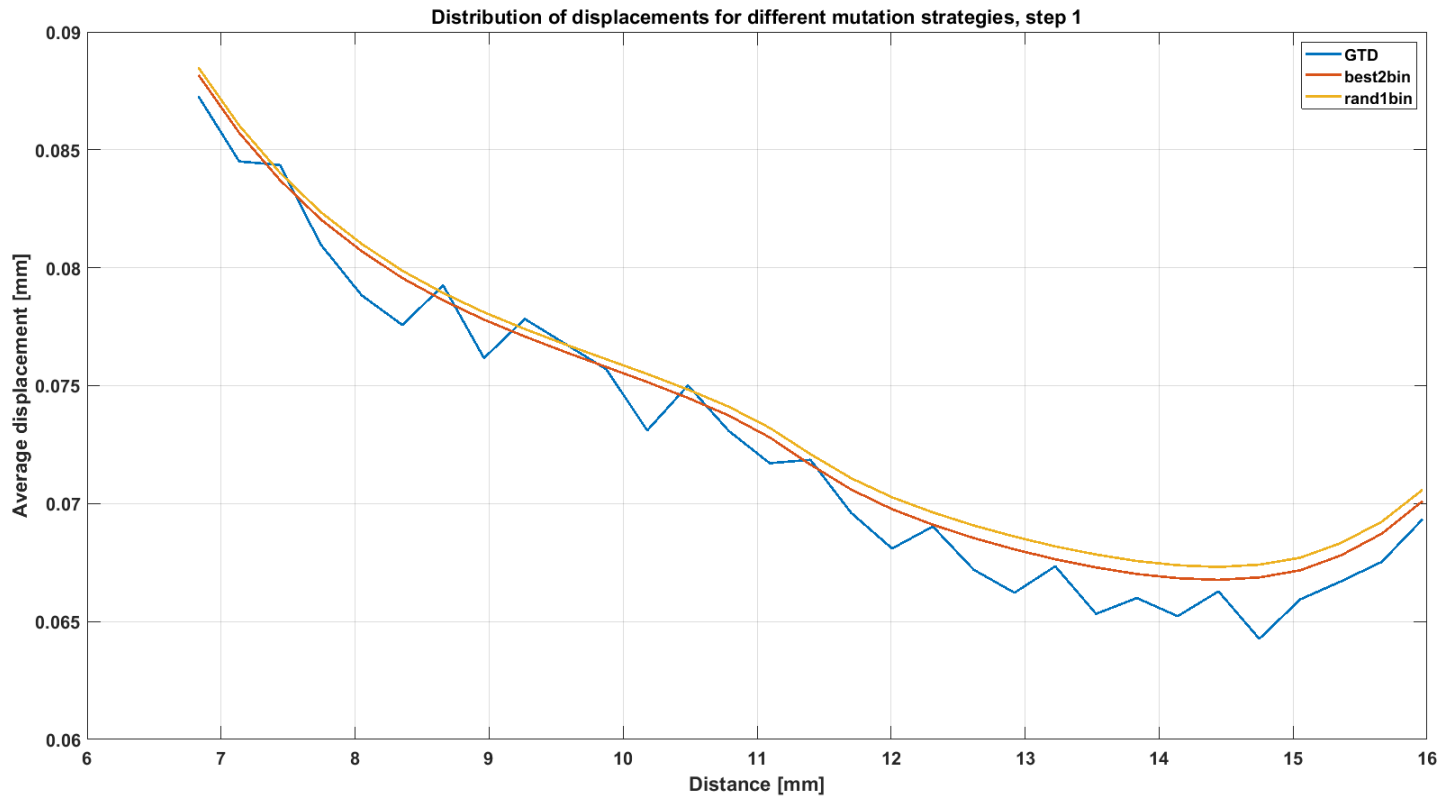


Figure 127: Comparing the distribution of displacements along the top of the ROI. Blue line represents the GTD, red line belongs to the displacement field estimated with mutation strategy best2bin, and yellow line represents the distribution of the displacement after the estimation procedure with mutation strategy rand1bin. The distributions belong the loading step 1.

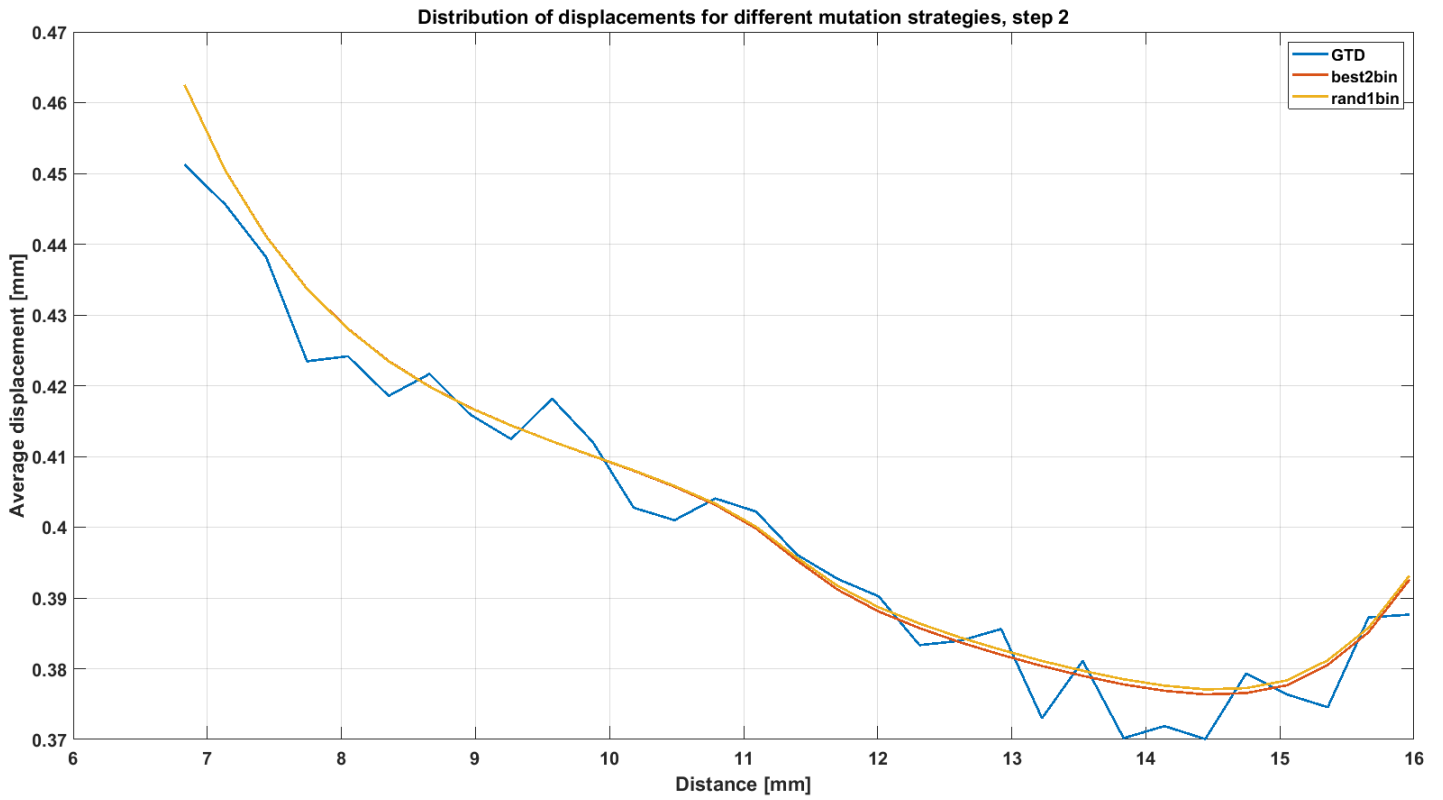


Figure 128: Comparing the distribution of displacements along the top of the ROI. Blue line represents the GTD, red line belongs to the displacement field estimated with mutation strategy best2bin, and yellow line represents the distribution of the displacement after the estimation procedure with mutation strategy rand1bin. The distributions belong the loading step 2.

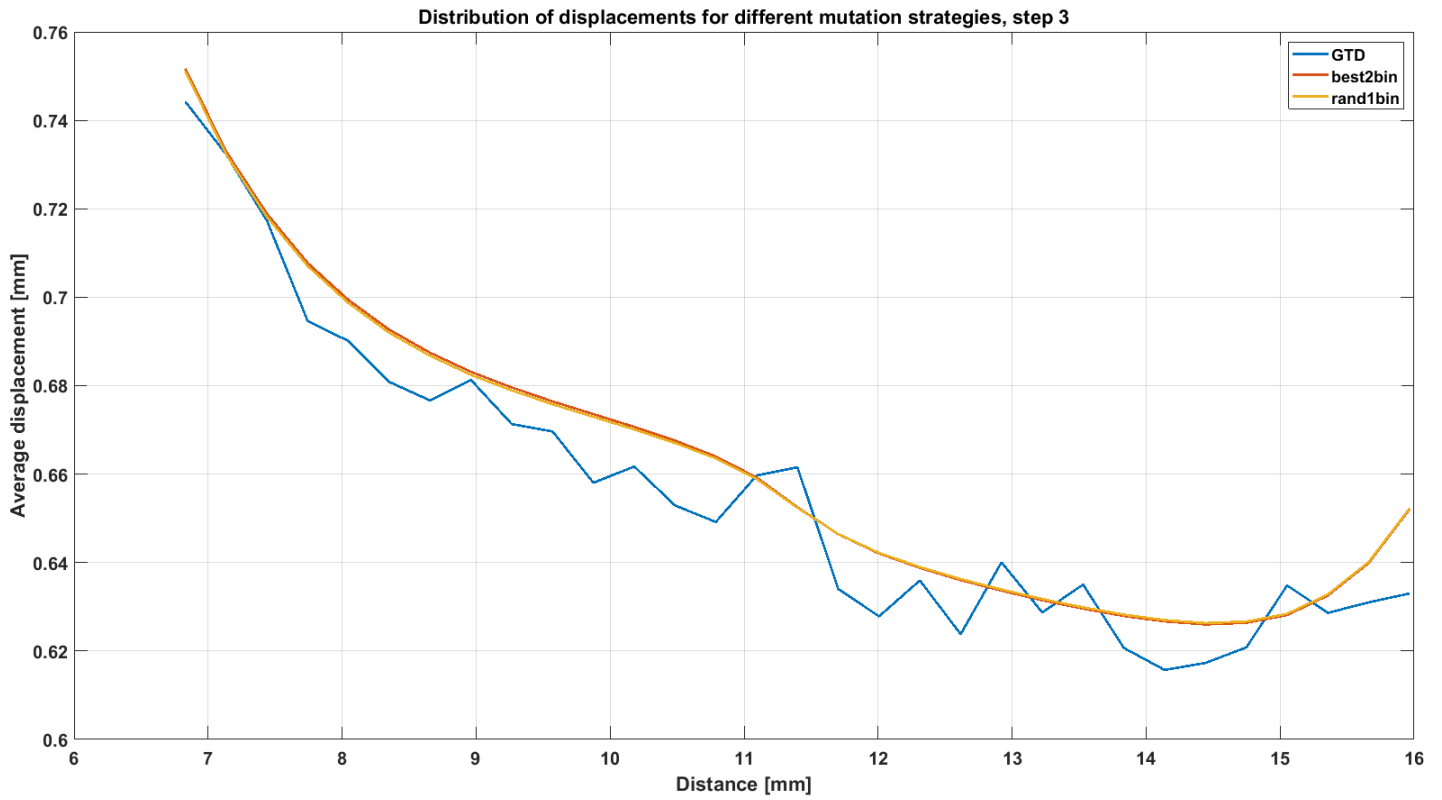


Figure 129: Comparing the distribution of displacements along the top of the ROI. Blue line represents the GTD, red line belongs to the displacement field estimated with mutation strategy best2bin, and yellow line represents the distribution of the displacement after the estimation procedure with mutation strategy rand1bin. The distributions belong the loading step 3.

# Appendix V - Supplementary results to the experimental study

## M Global estimation procedure

### M.1 Fibrous cap

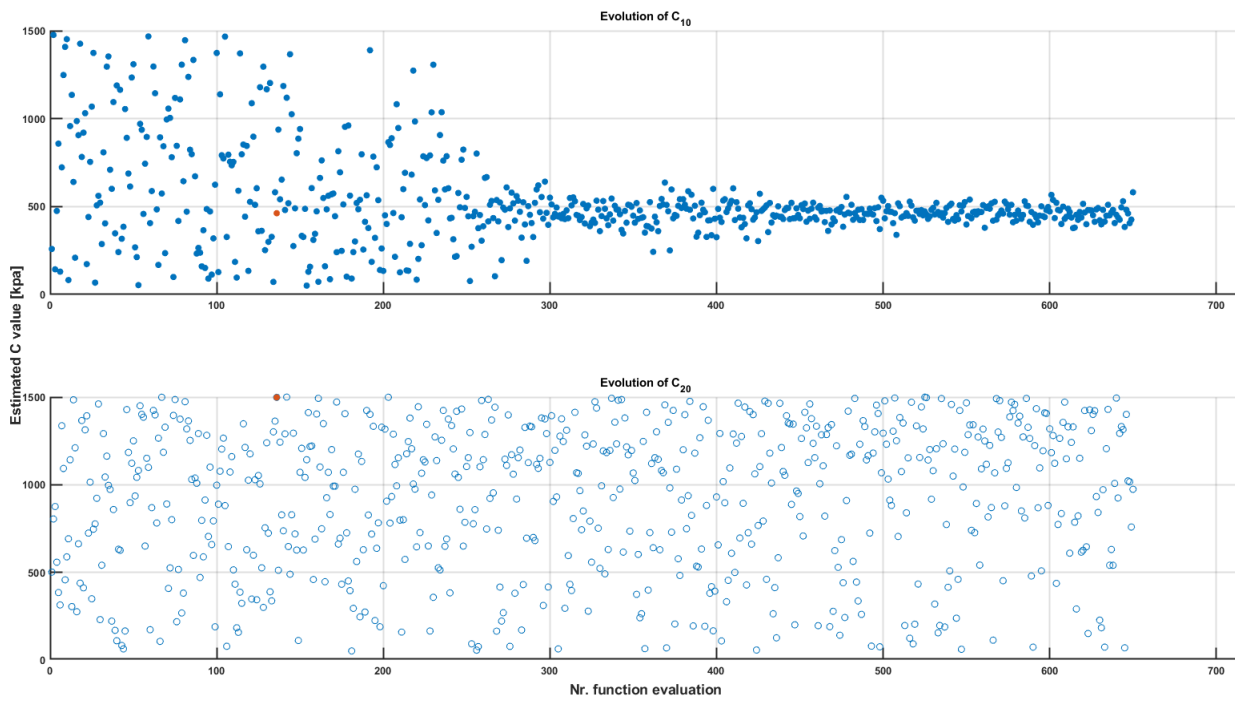


Figure 130: Evolution of material properties throughout global estimation for fibrous cap model

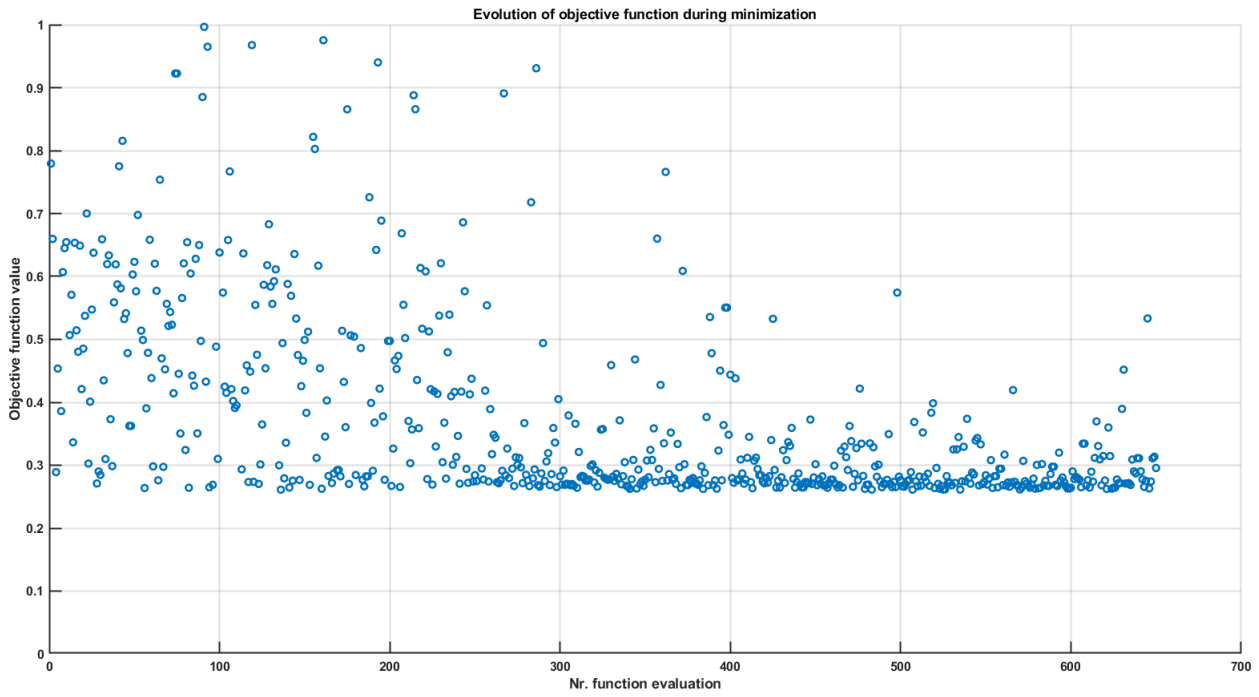


Figure 131: Objective function during global estimation for fibrous cap model

## M.2 Fibrous cap + SI

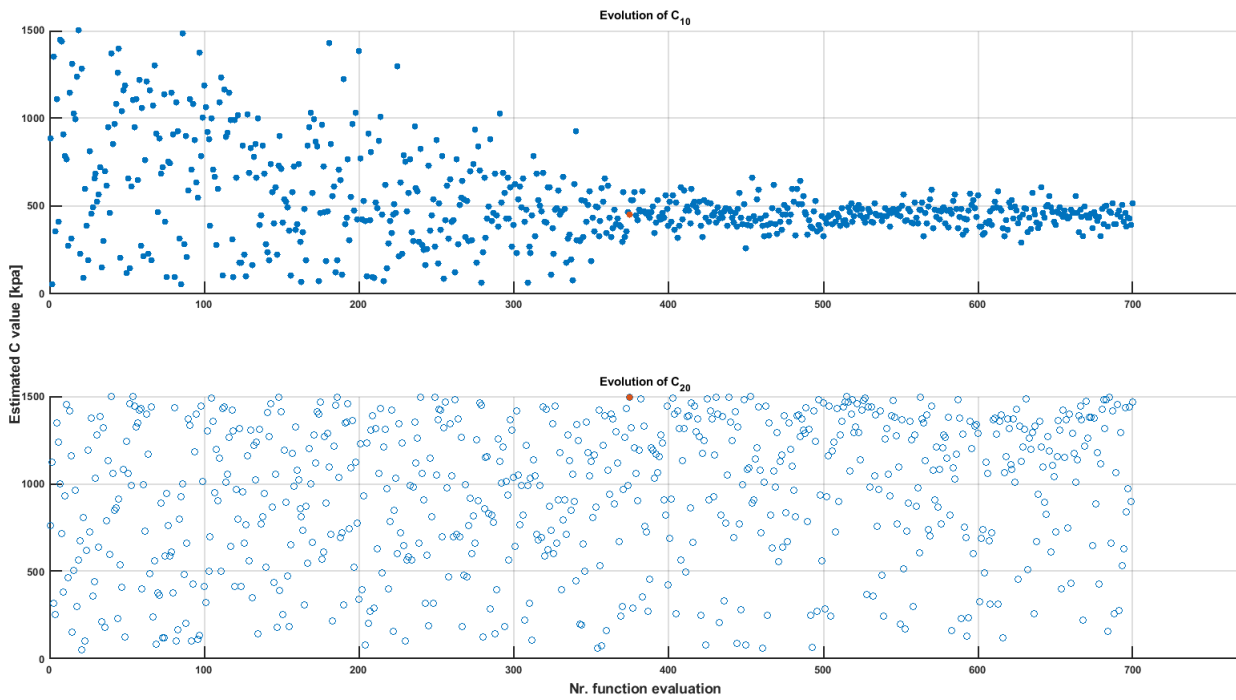


Figure 132: Evolution of material properties throughout global estimation for fibrous cap + SI model.

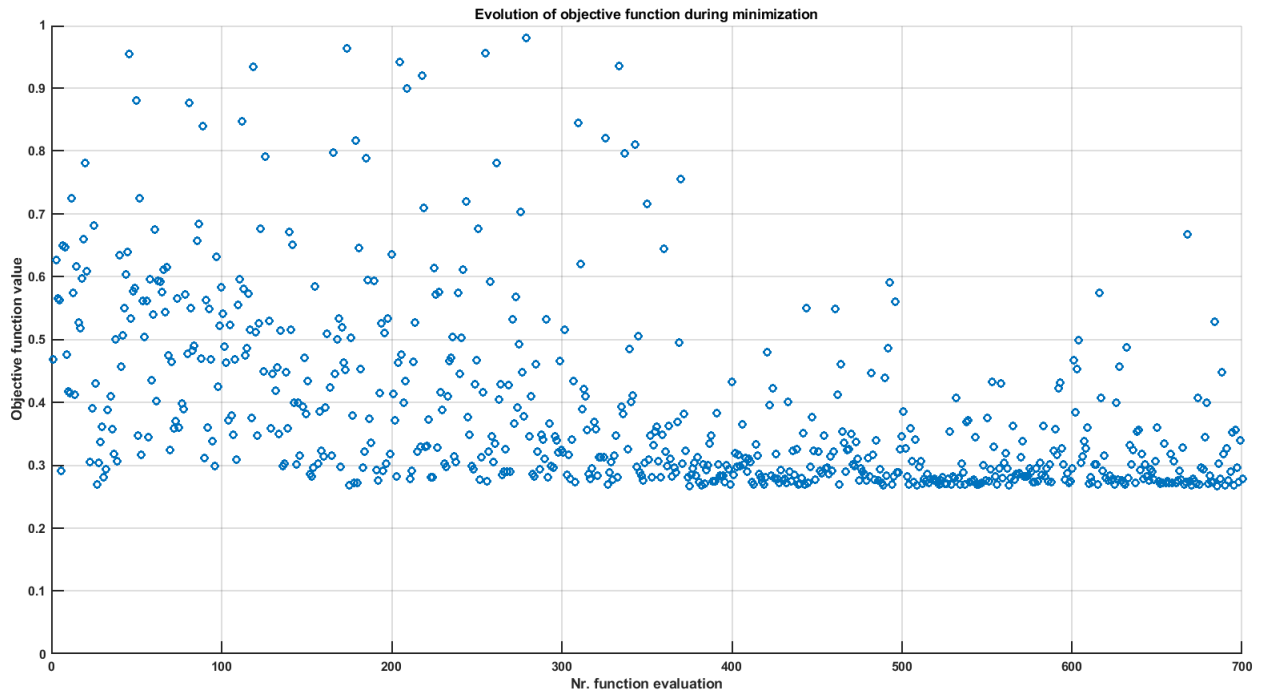


Figure 133: Objective function during global estimation of fibrous cap + SI model

## N Local estimation

### N.1 Fibrous cap

#### Estimation procedure

*2 Sections*

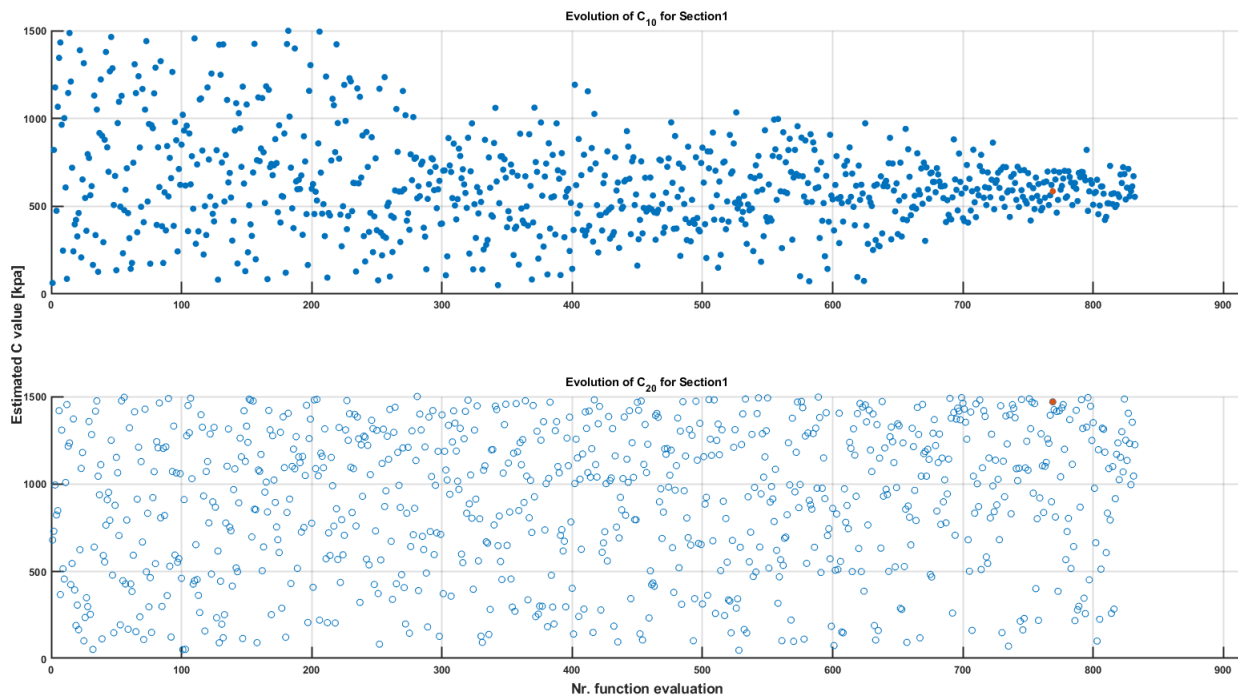


Figure 134: Evolution of material properties during the local estimation procedure using 2 Sections in the fibrous cap model. Material properties belong to Section 1.

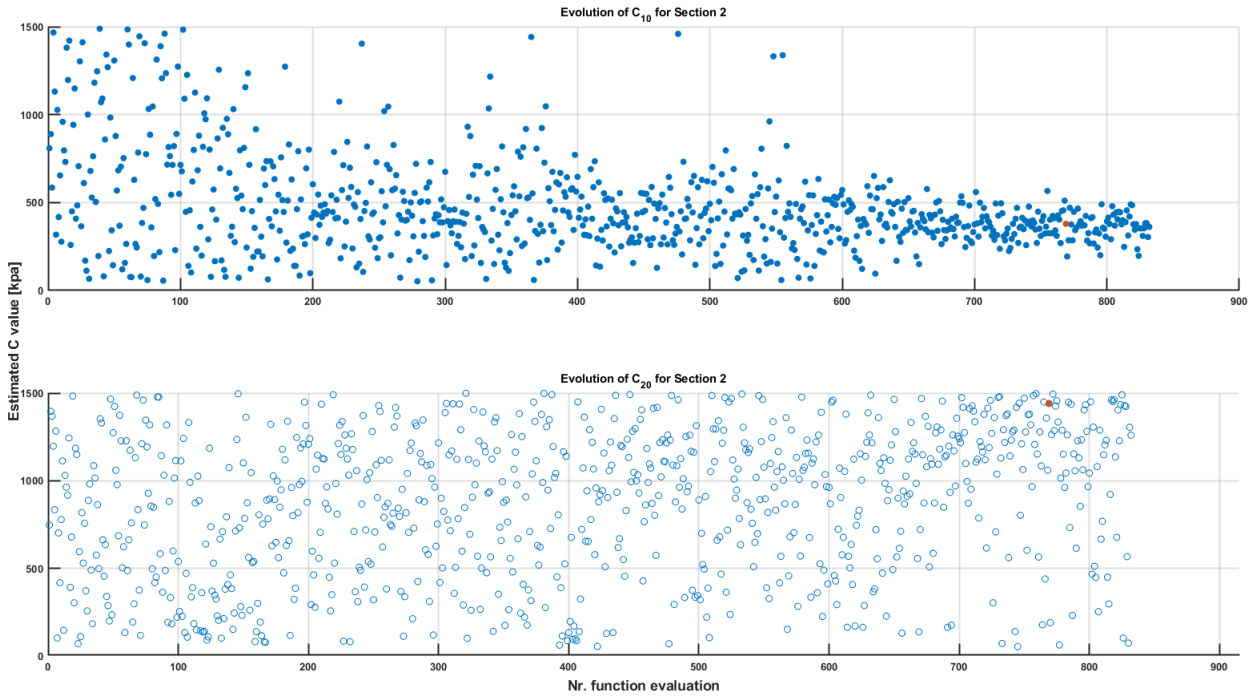


Figure 135: Evolution of material properties during the local estimation procedure using 2 Sections in the fibrous cap model. Material properties belong to Section 2.

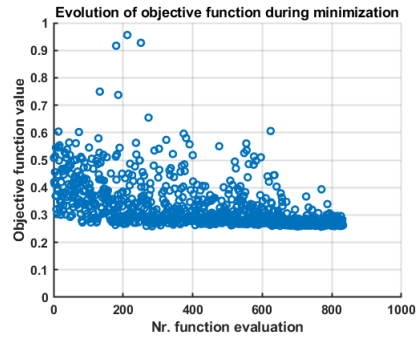


Figure 136: Evolution of objective function during the local estimation procedure using 2 Section in the fibrous cap model.

*4 Sections*

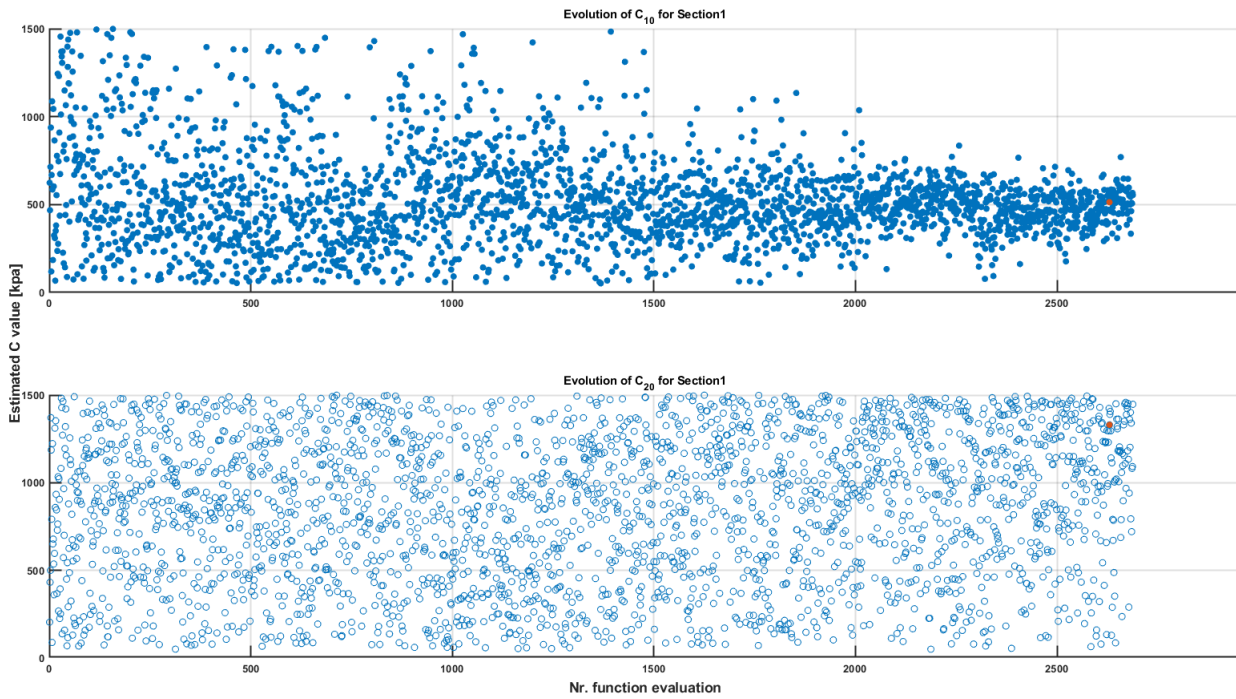


Figure 137: Evolution of material properties during the local estimation procedure using 4 Sections in the fibrous cap model. Material properties belong to Section 1.

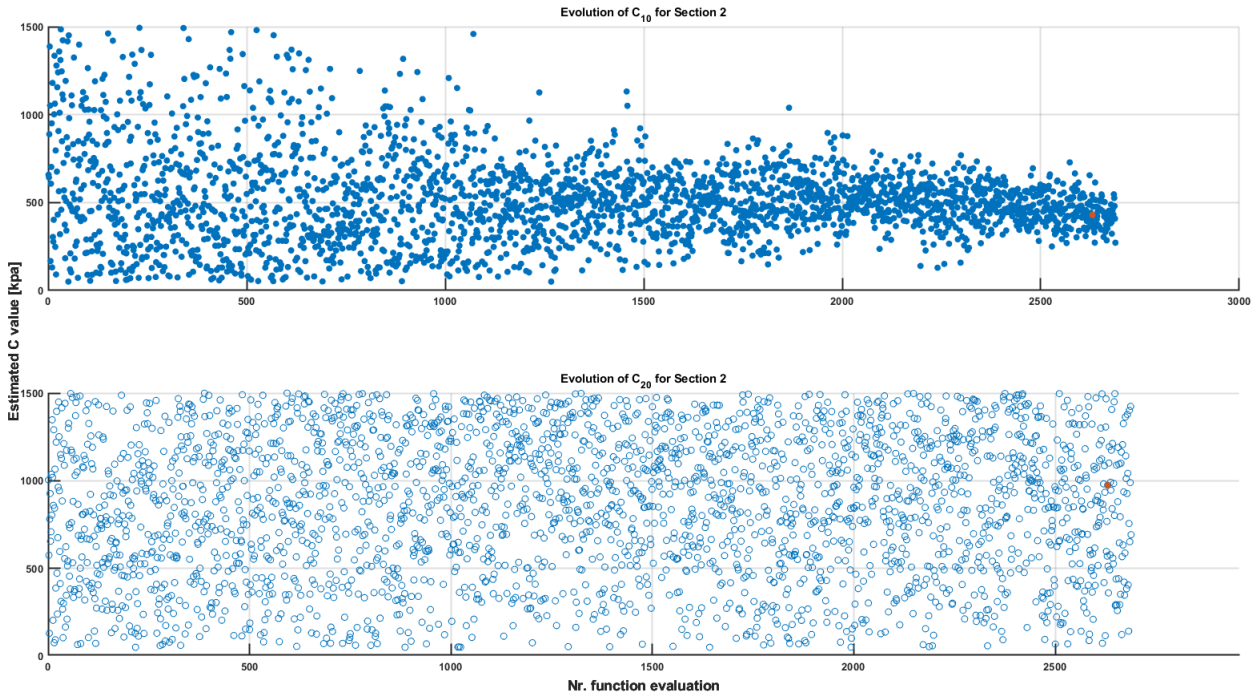


Figure 138: Evolution of material properties during the local estimation procedure using 4 Sections in the fibrous cap model. Material properties belong to Section 2.

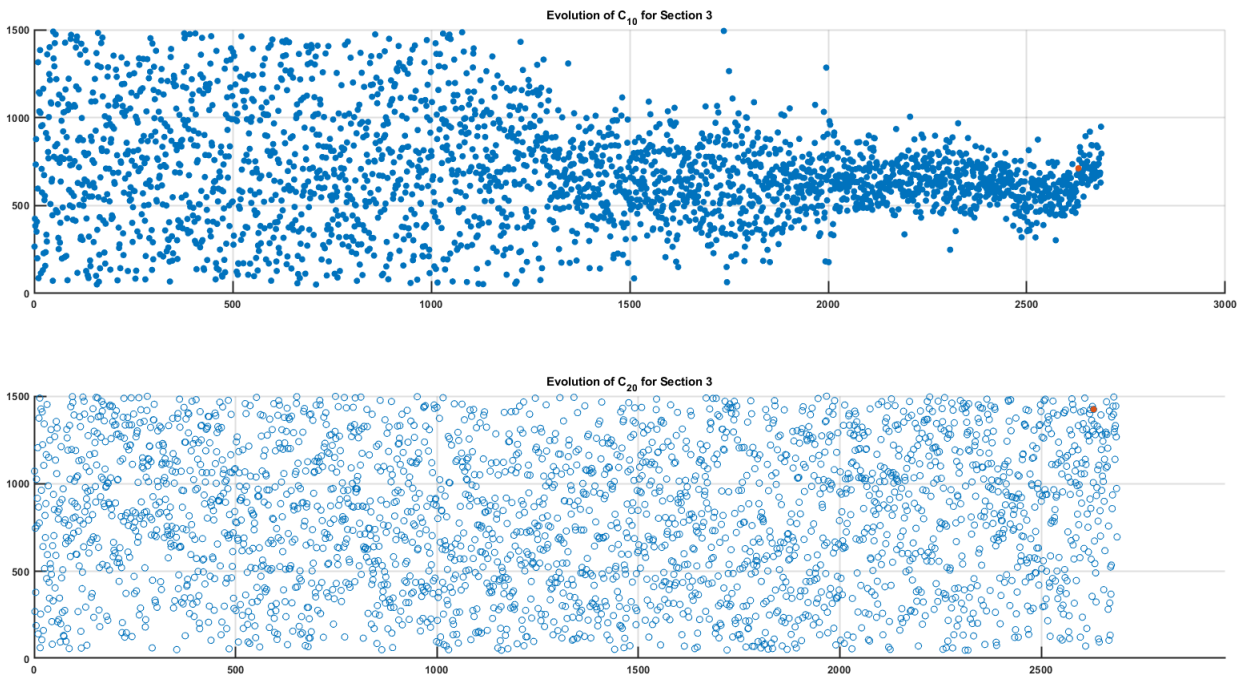


Figure 139: Evolution of material properties during the local estimation procedure using 4 Sections in the fibrous cap model. Material properties belong to Section 3.

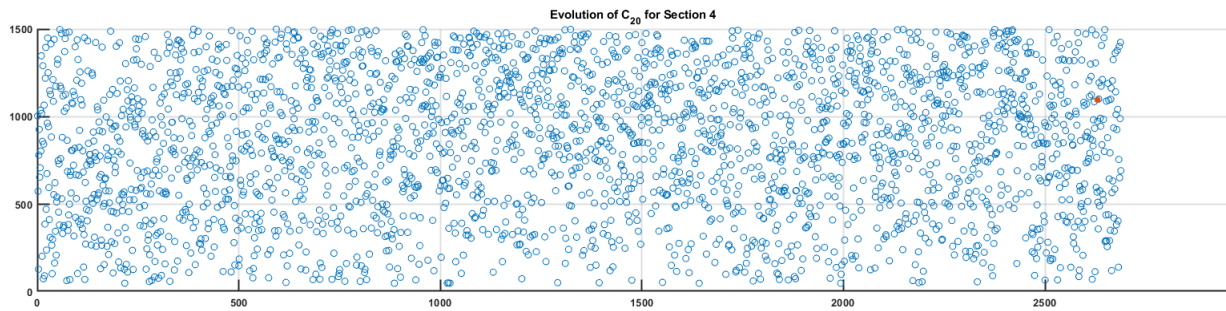
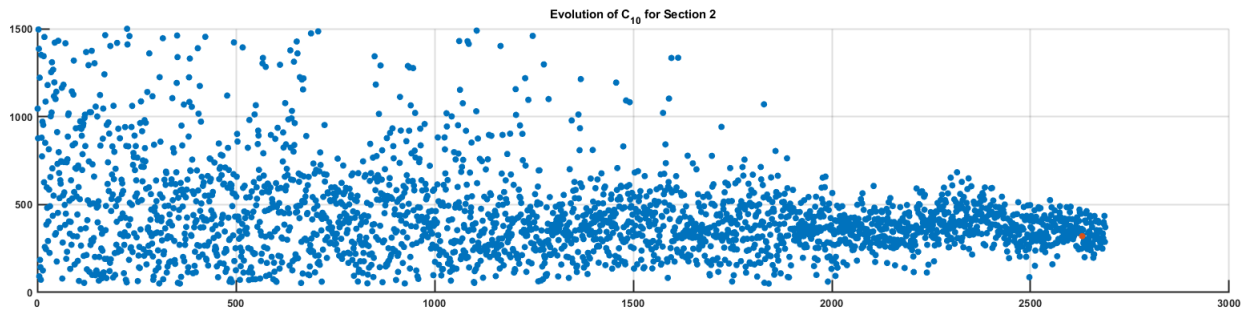


Figure 140: Evolution of material properties during the local estimation procedure using 4 Sections in the fibrous cap model. Material properties belong to Section 4.

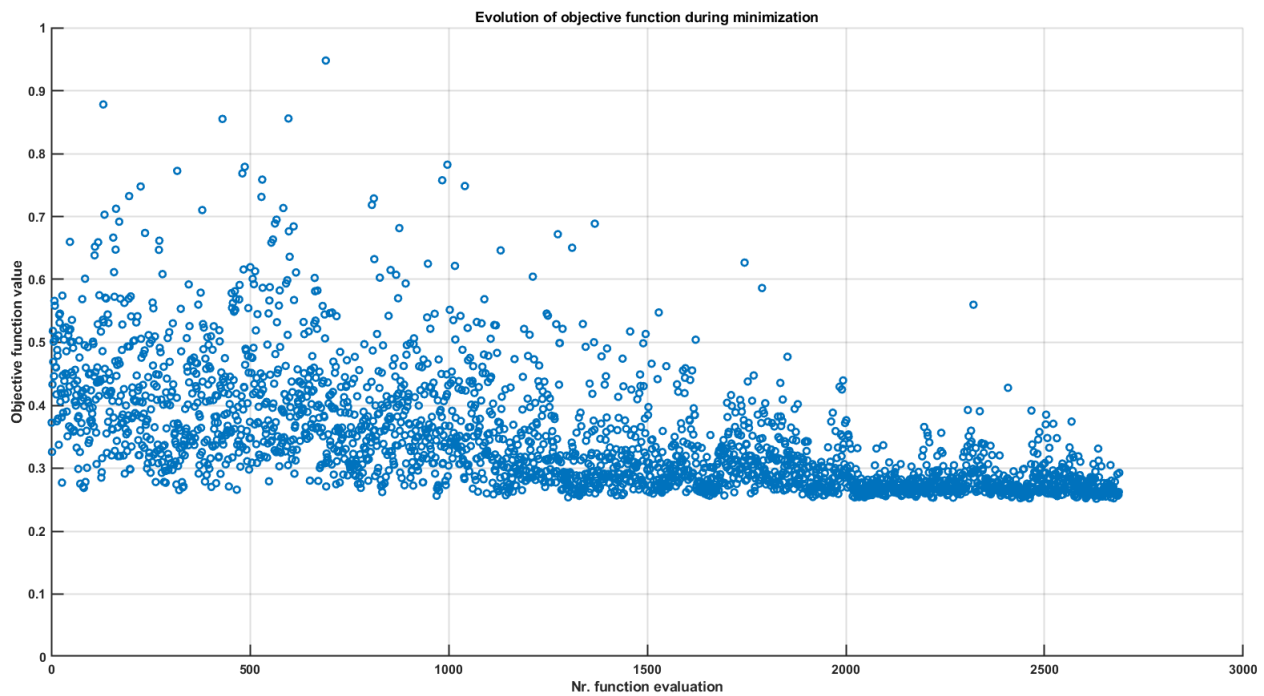


Figure 141: Evolution of objective function during the local estimation procedure using 4 Section in the fibrous cap model.

6 Sections

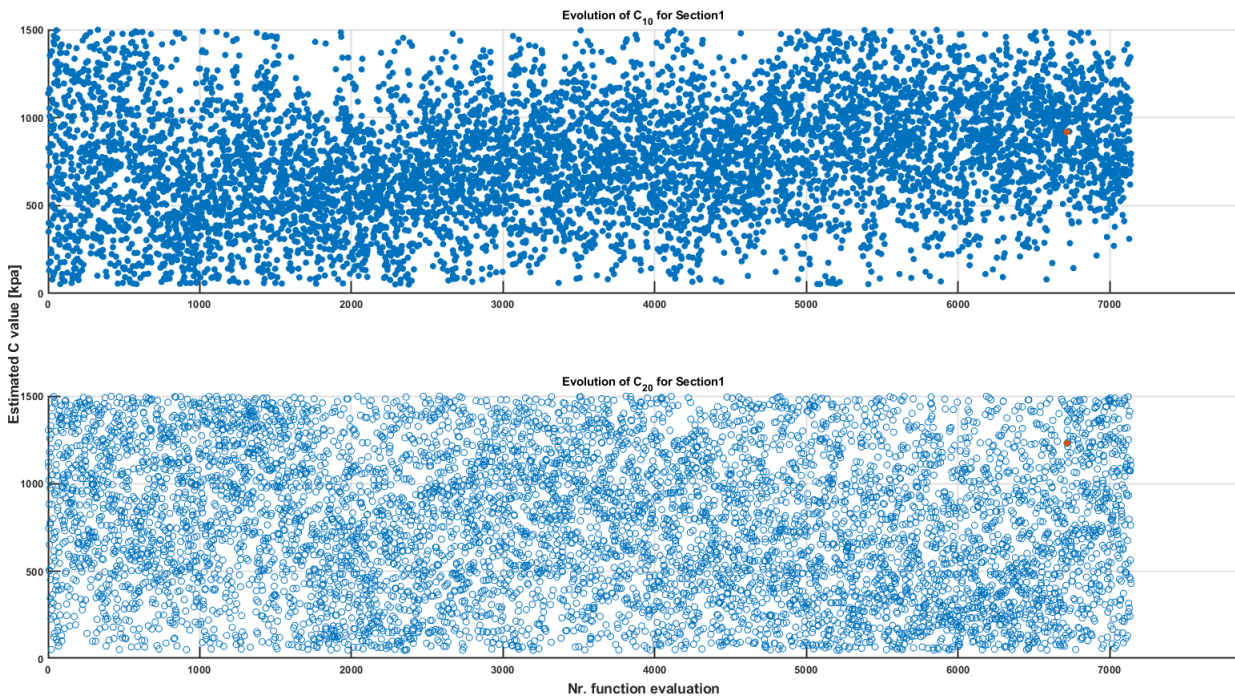


Figure 142: Evolution of material properties during the local estimation procedure using 6 Sections in the fibrous cap model. Material properties belong to Section 1.

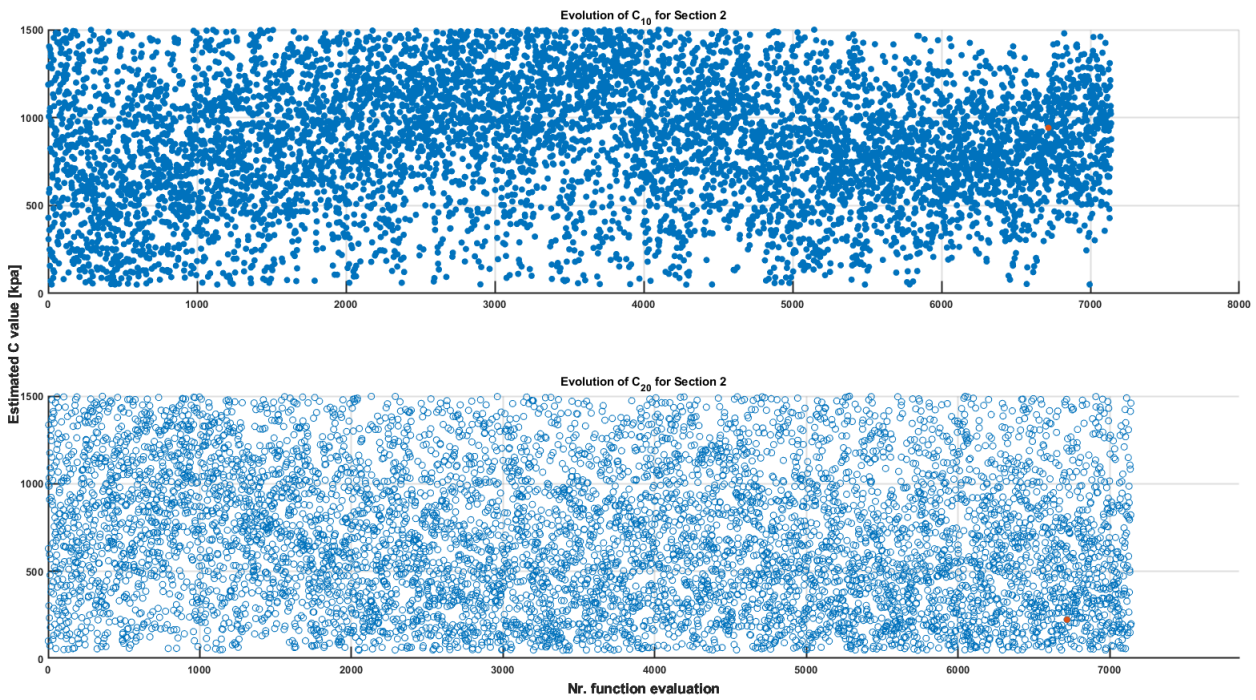


Figure 143: Evolution of material properties during the local estimation procedure using 6 Sections in the fibrous cap model. Material properties belong to Section 2.

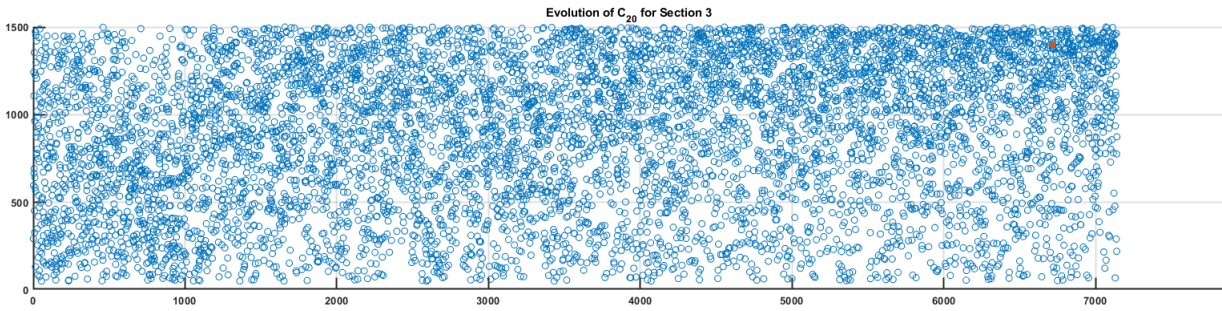
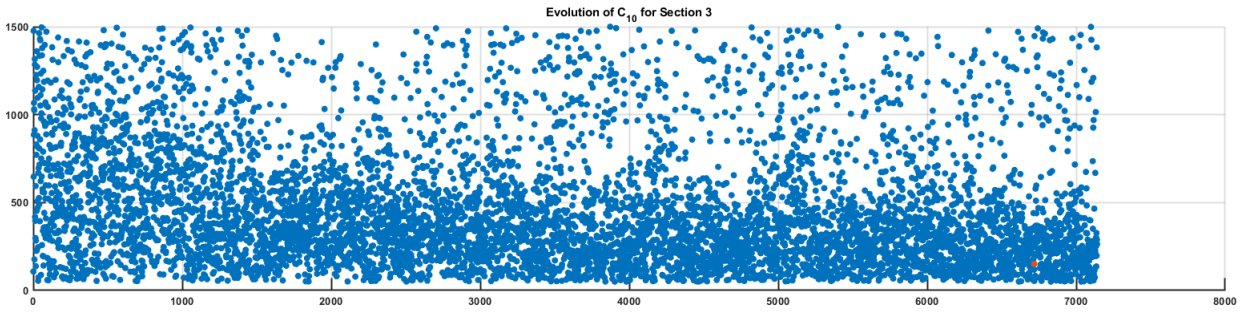


Figure 144: Evolution of material properties during the local estimation procedure using 6 Sections in the fibrous cap model. Material properties belong to Section 3.

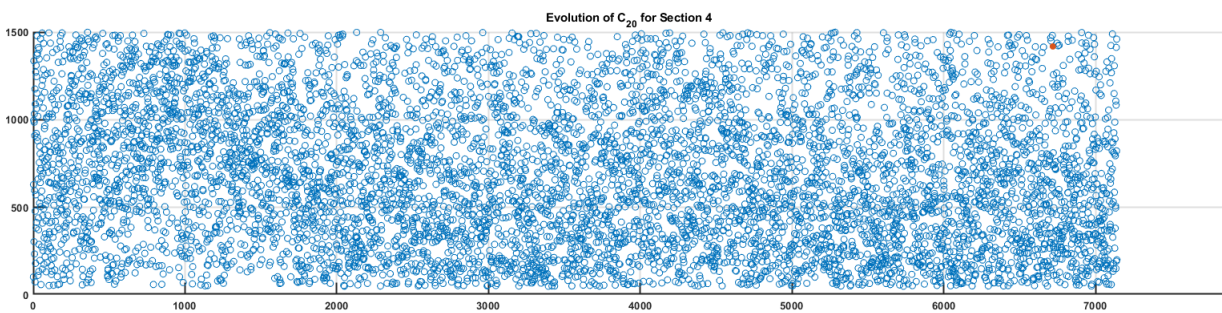
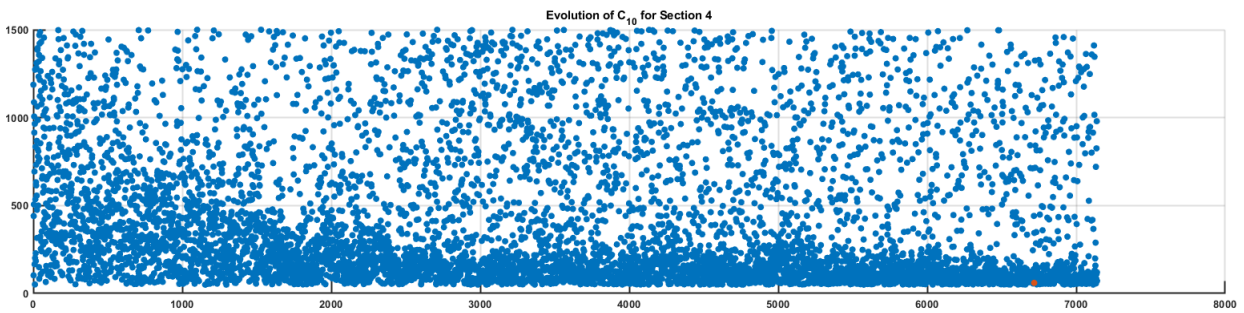


Figure 145: Evolution of material properties during the local estimation procedure using 6 Sections in the fibrous cap model. Material properties belong to Section 4.

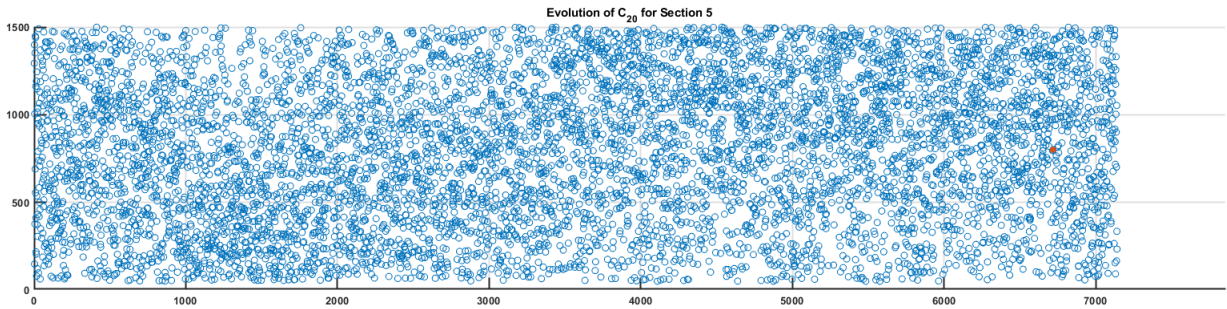
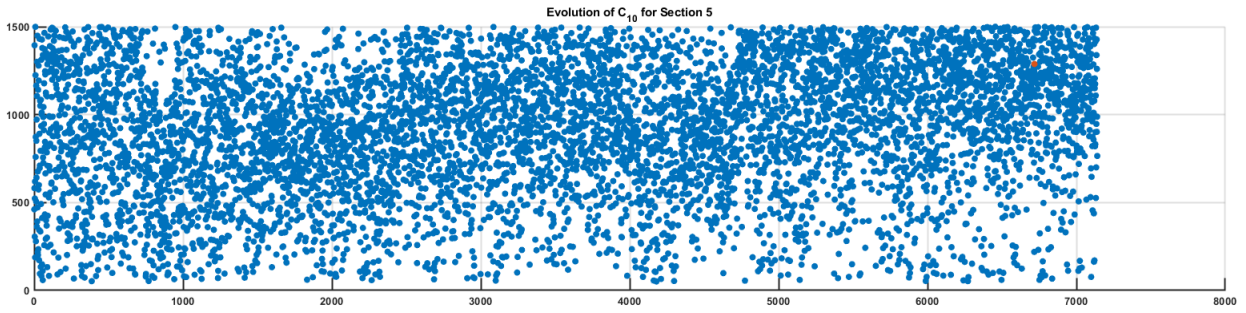


Figure 146: Evolution of material properties during the local estimation procedure using 6 Sections in the fibrous cap model. Material properties belong to Section 5.

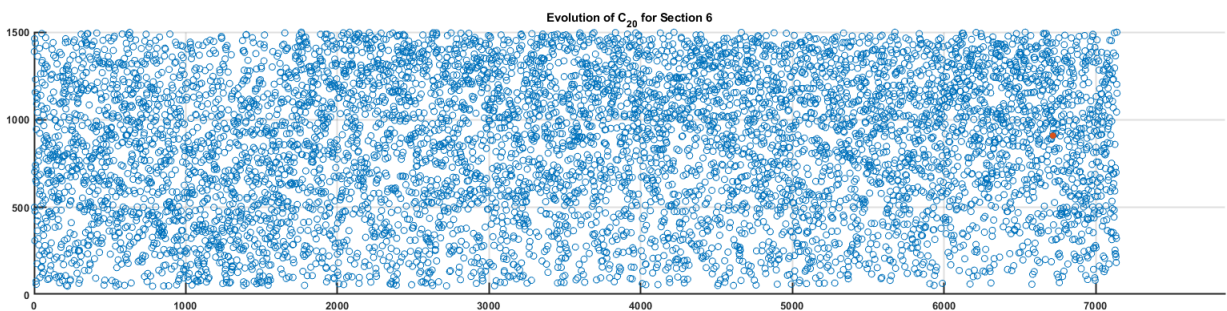
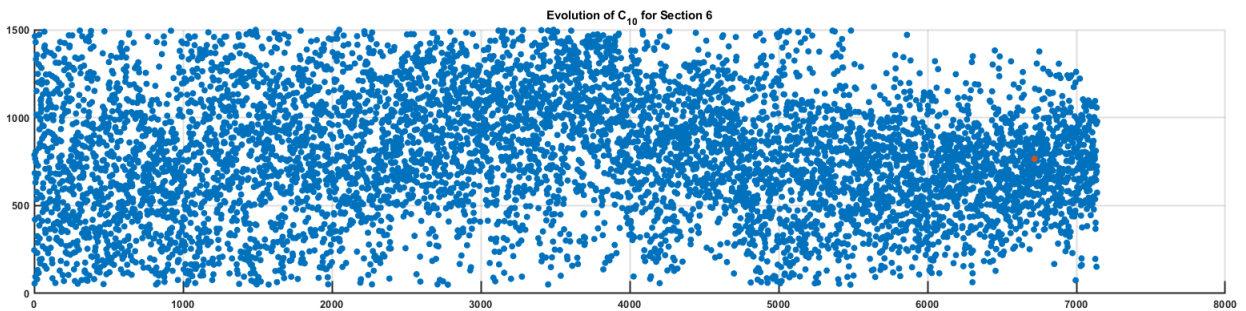


Figure 147: Evolution of material properties during the local estimation procedure using 6 Sections in the fibrous cap model. Material properties belong to Section 6.

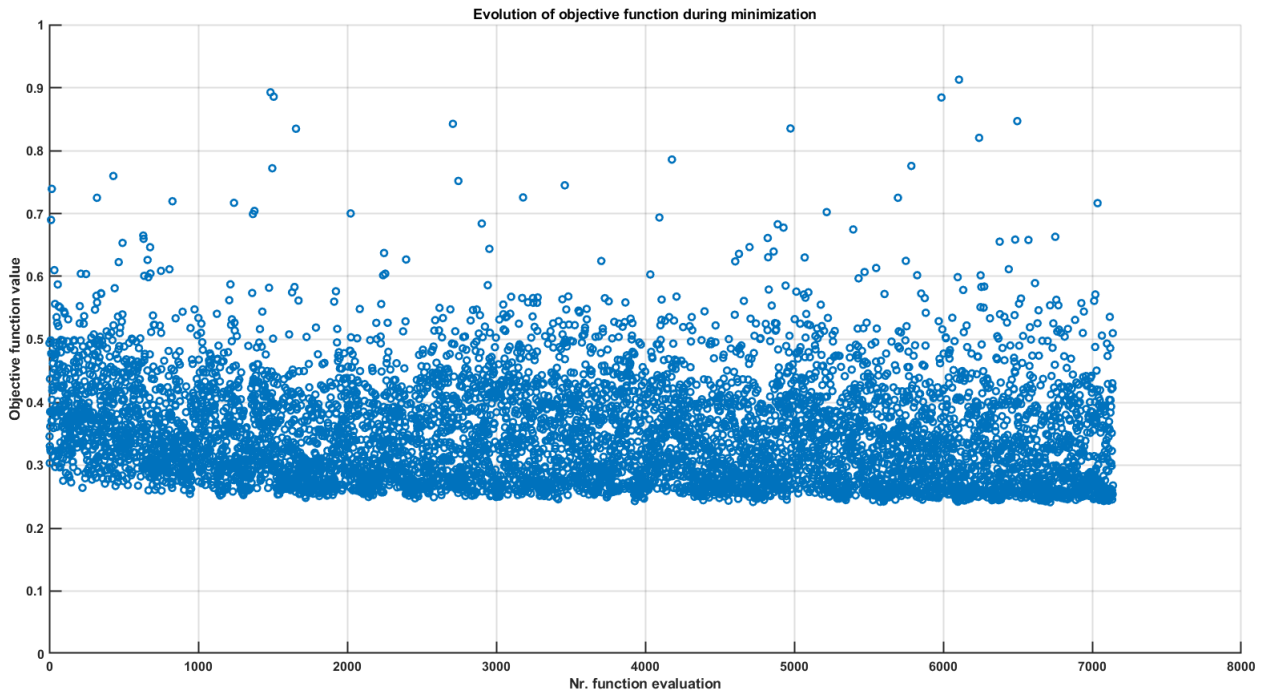


Figure 148: Evolution of objective function during the local estimation procedure using 6 Section in the fibrous cap model.

## N.2 Fibrous cap + SI

### Estimation procedure *2 Sections*

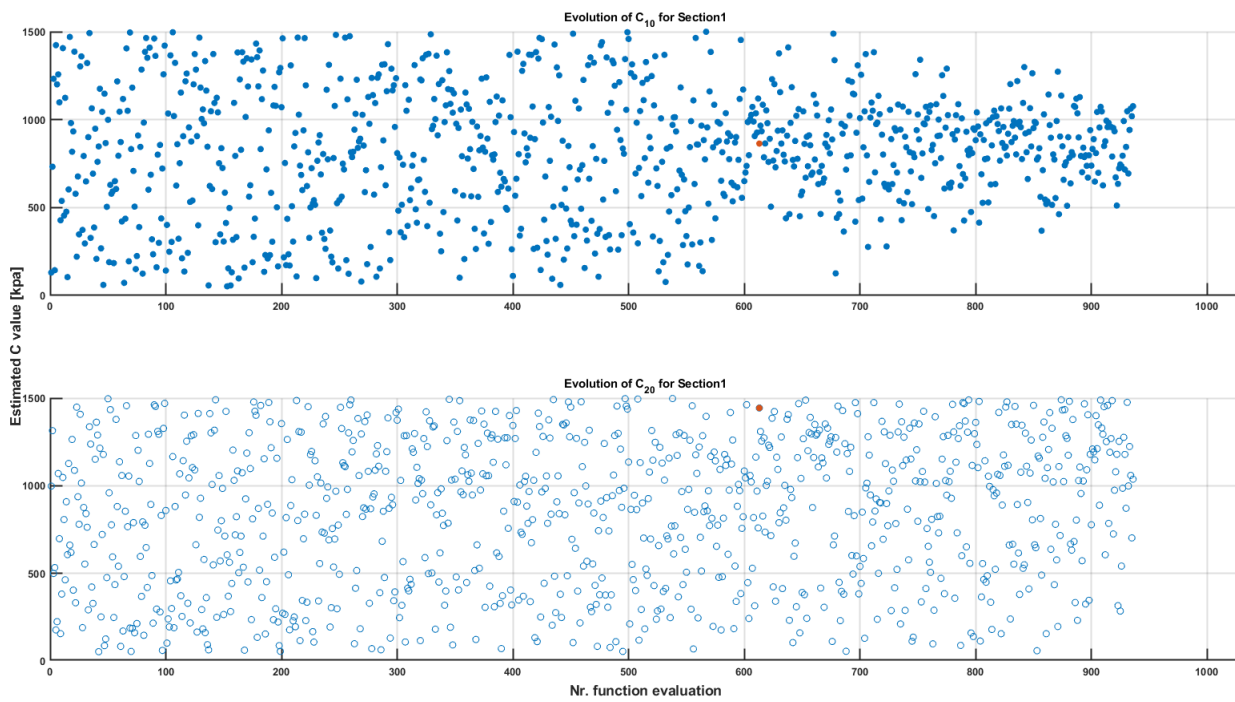


Figure 149: Evolution of material properties during the local estimation procedure using 2 Sections in the fibrous cap + SI model. Material properties belong to Section 1.

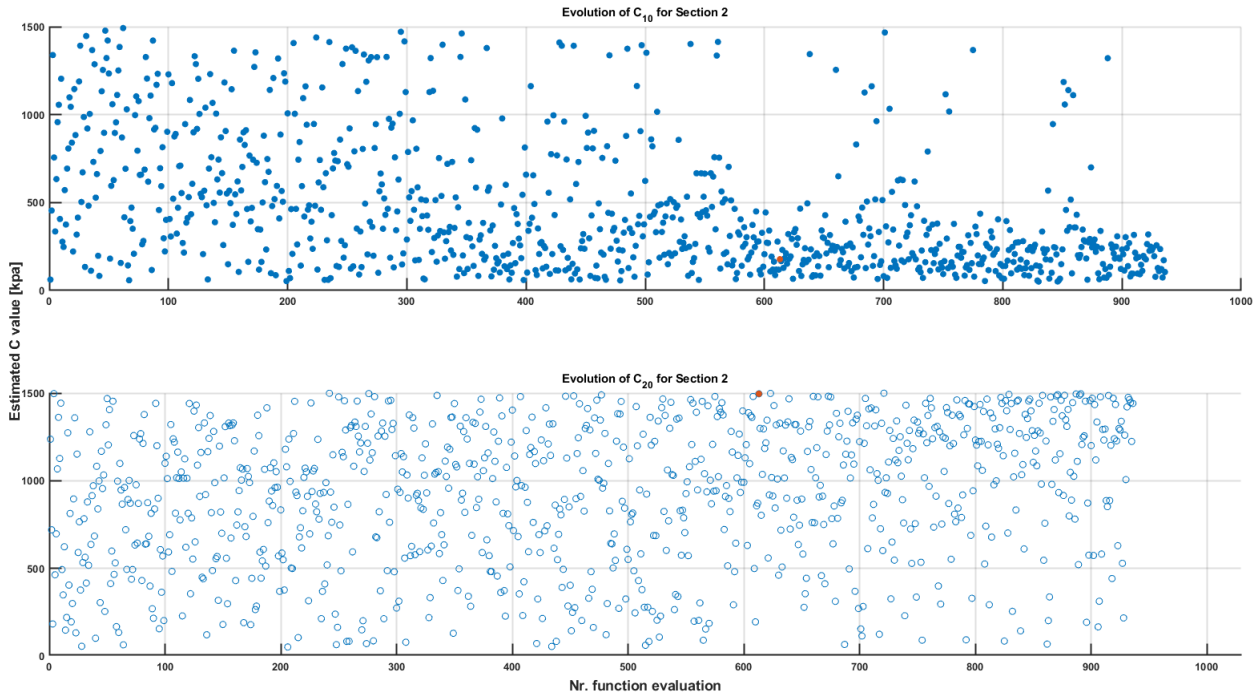


Figure 150: Evolution of material properties during the local estimation procedure using 2 Sections in the fibrous cap + SI model. Material properties belong to Section 2.

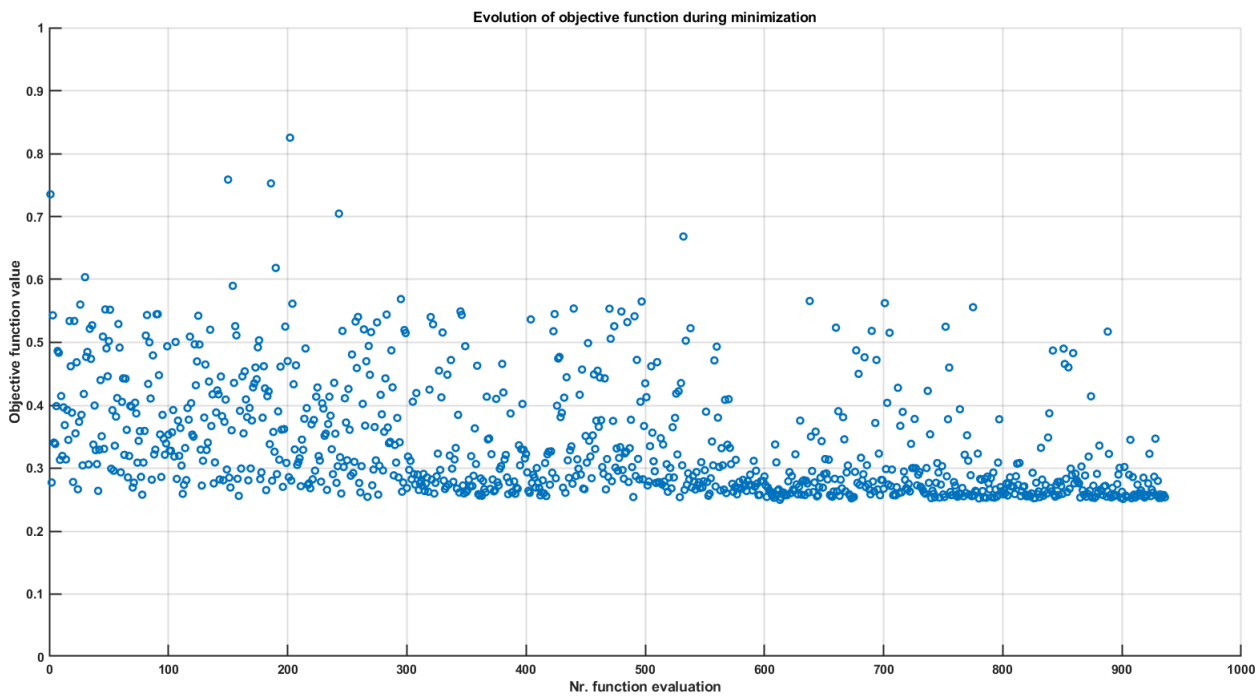


Figure 151: Evolution of objective function during the local estimation procedure using 2 Section in the fibrous cap + SI model.

4 Sections

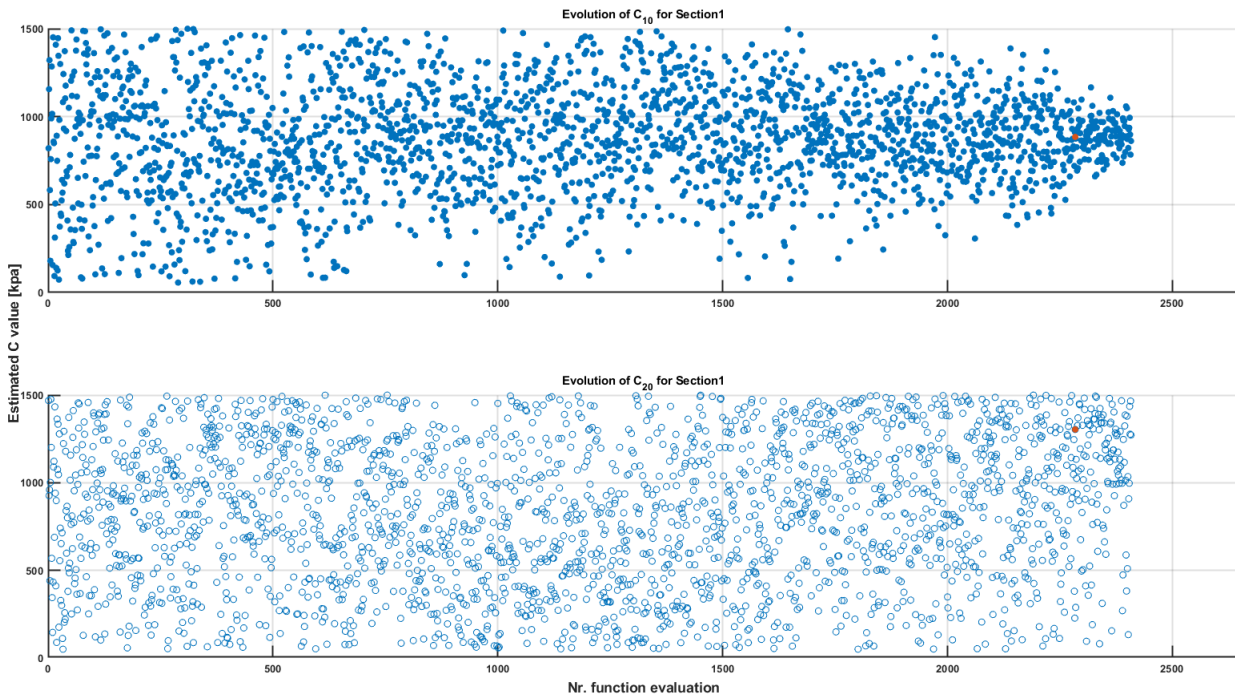


Figure 152: Evolution of material properties during the local estimation procedure using 4 Sections in the fibrous cap + SI model. Material properties belong to Section 1.

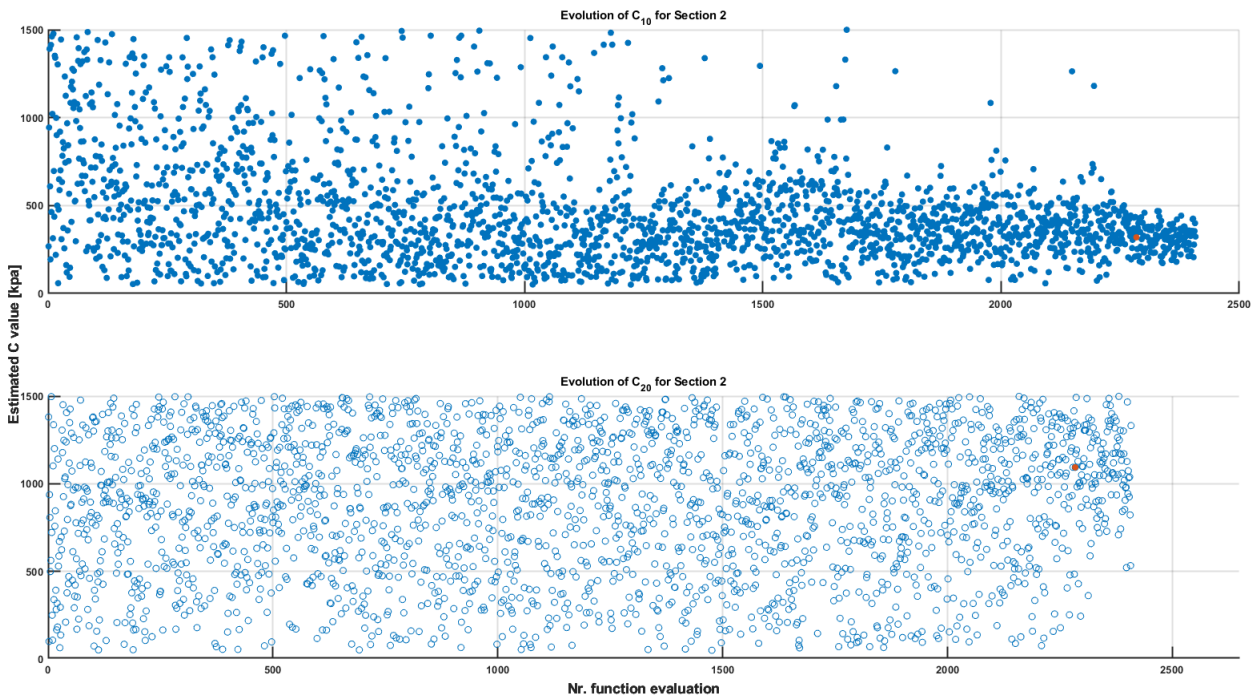


Figure 153: Evolution of material properties during the local estimation procedure using 4 Sections in the fibrous cap + SI model. Material properties belong to Section 2.

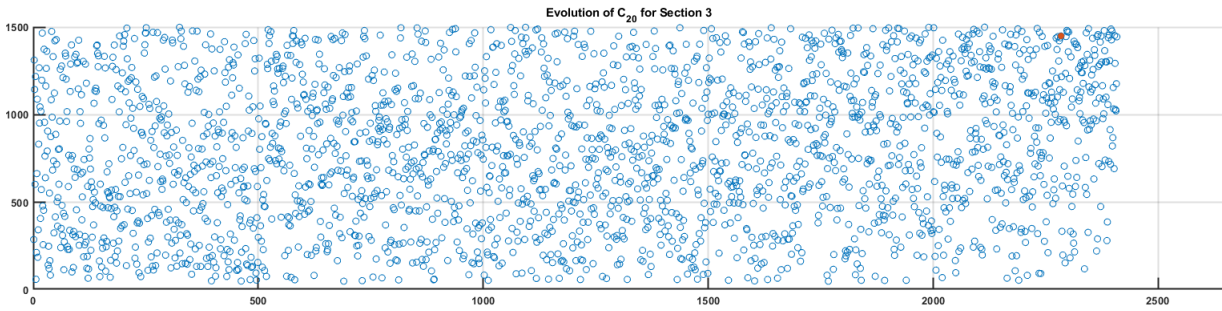
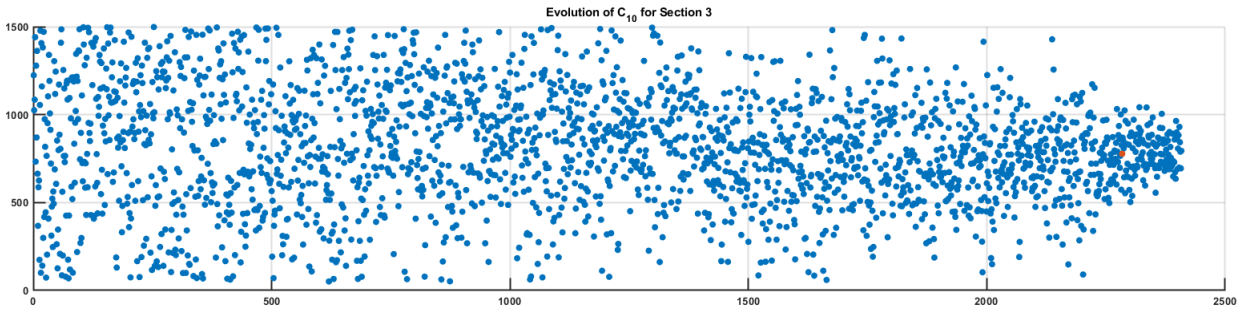


Figure 154: Evolution of material properties during the local estimation procedure using 4 Sections in the fibrous cap + SI model. Material properties belong to Section 3.

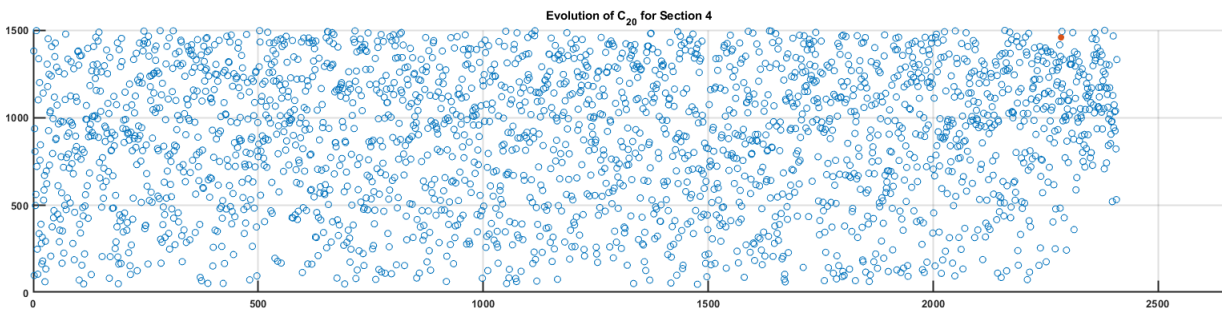
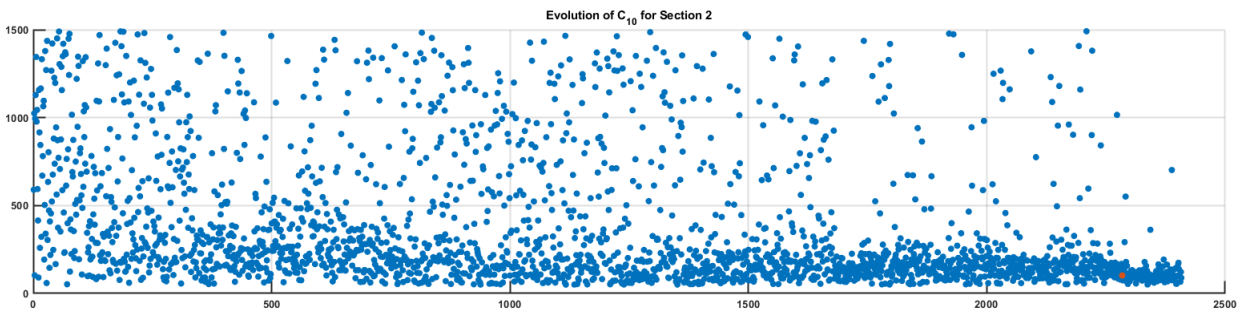


Figure 155: Evolution of material properties during the local estimation procedure using 4 Sections in the fibrous cap + SI model. Material properties belong to Section 4.

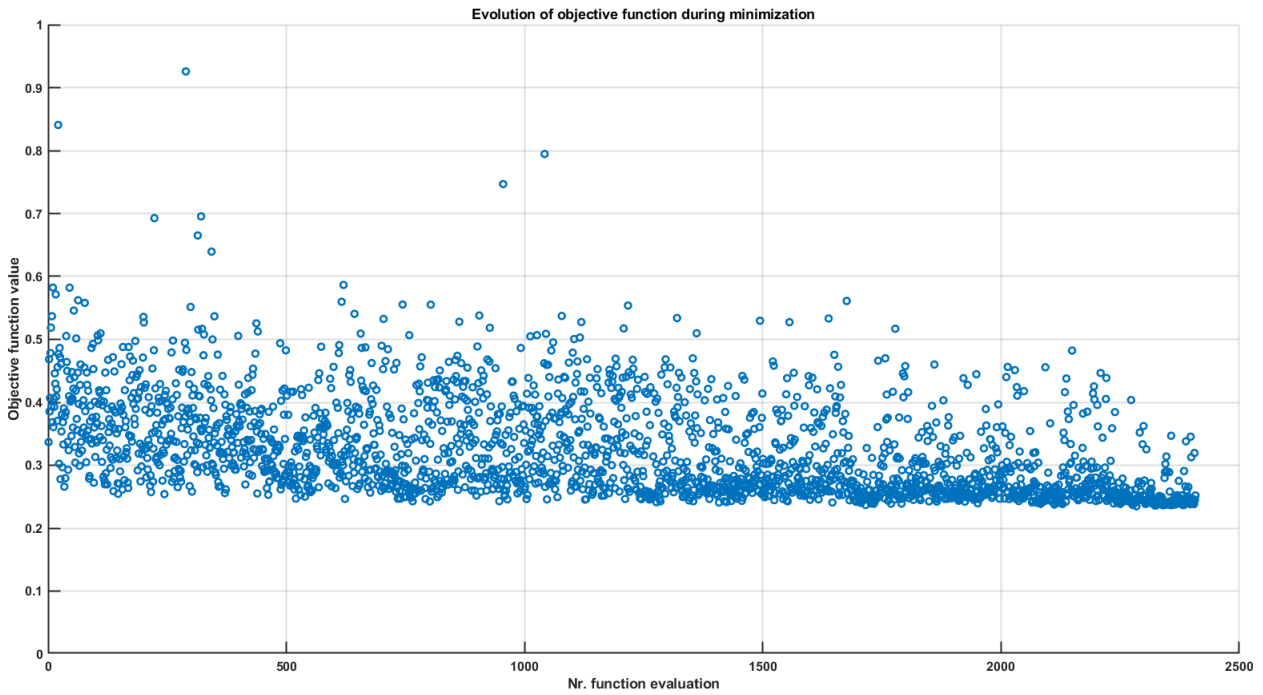


Figure 156: Evolution of objective function during the local estimation procedure using 4 Section in the fibrous cap + SI model.

*6 Sections*

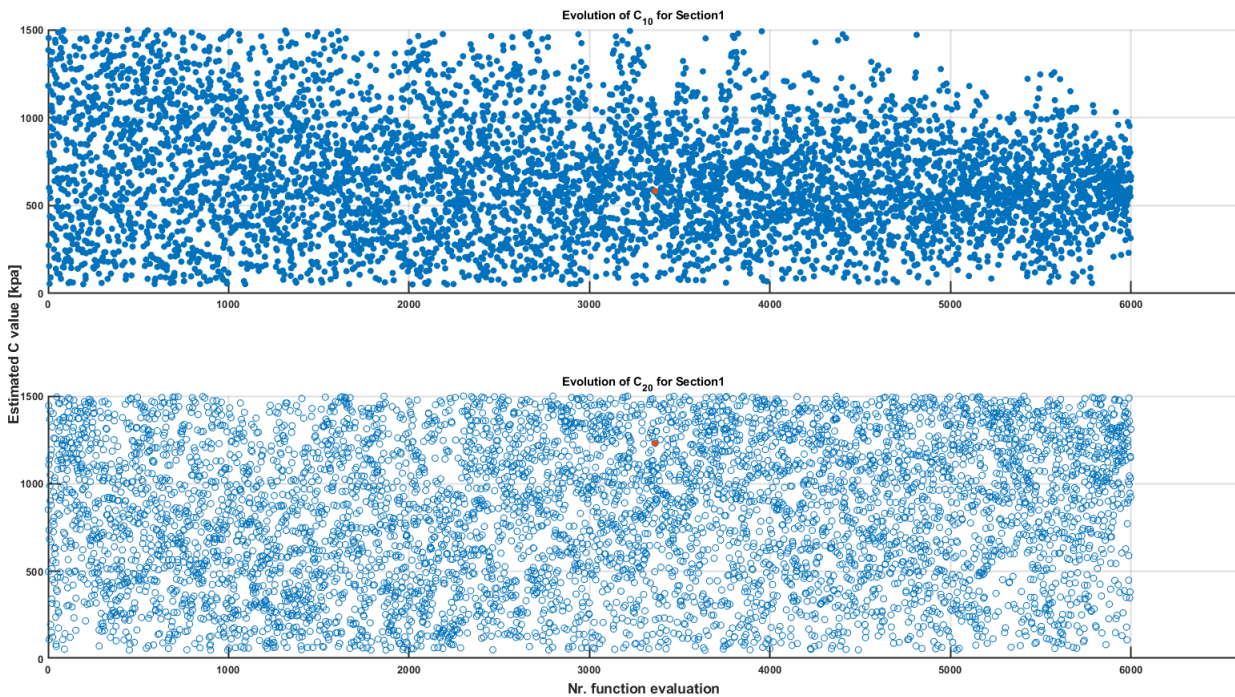


Figure 157: Evolution of material properties during the local estimation procedure using 6 Sections in the fibrous cap + SI model. Material properties belong to Section 1.

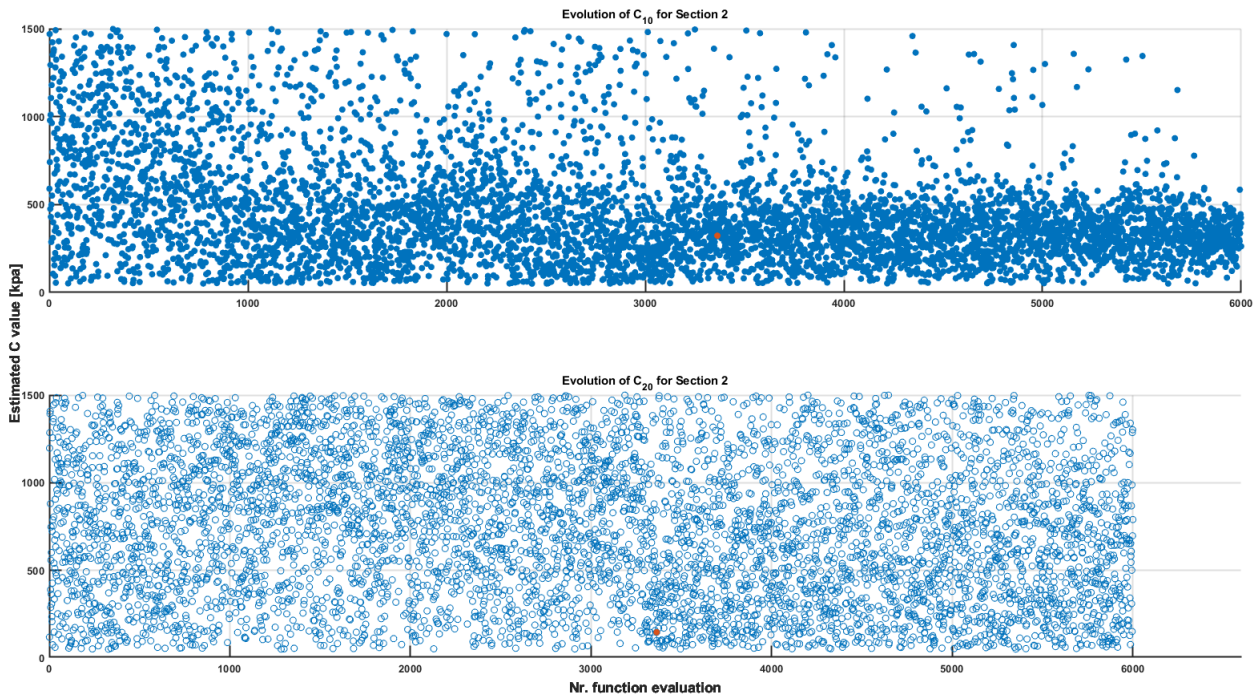


Figure 158: Evolution of material properties during the local estimation procedure using 6 Sections in the fibrous cap + SI model. Material properties belong to Section 2.

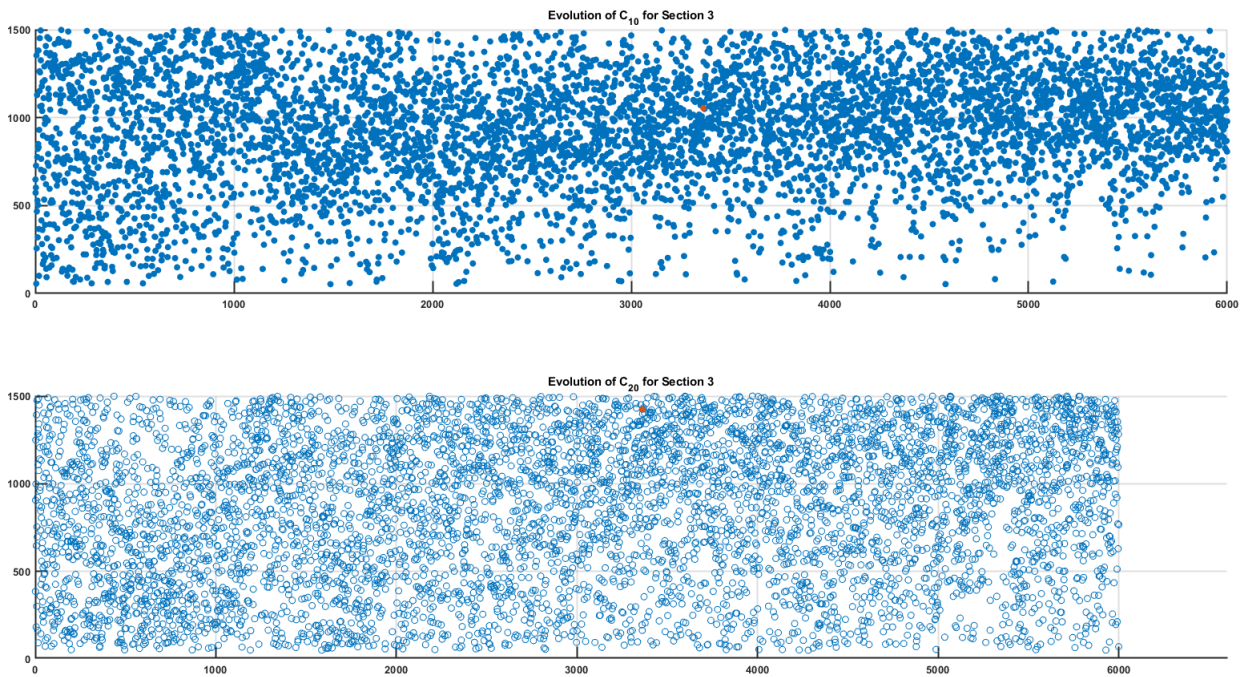


Figure 159: Evolution of material properties during the local estimation procedure using 6 Sections in the fibrous cap + SI model. Material properties belong to Section 3.

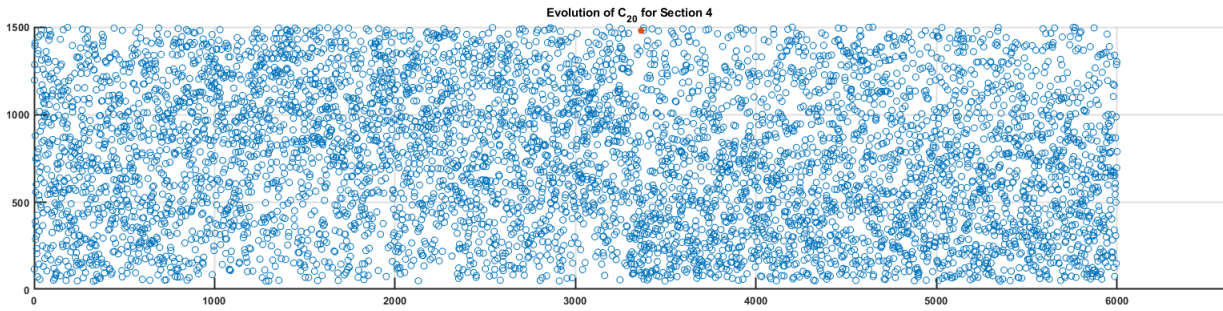
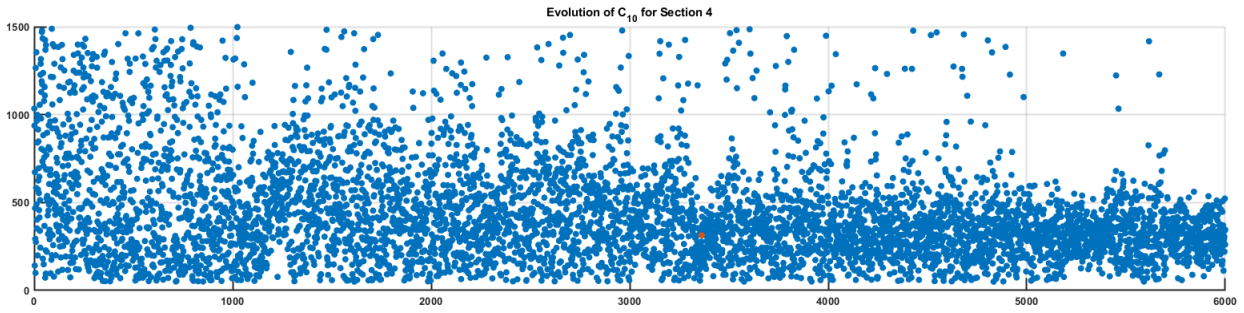


Figure 160: Evolution of material properties during the local estimation procedure using 6 Sections in the fibrous cap + SI model. Material properties belong to Section 4.

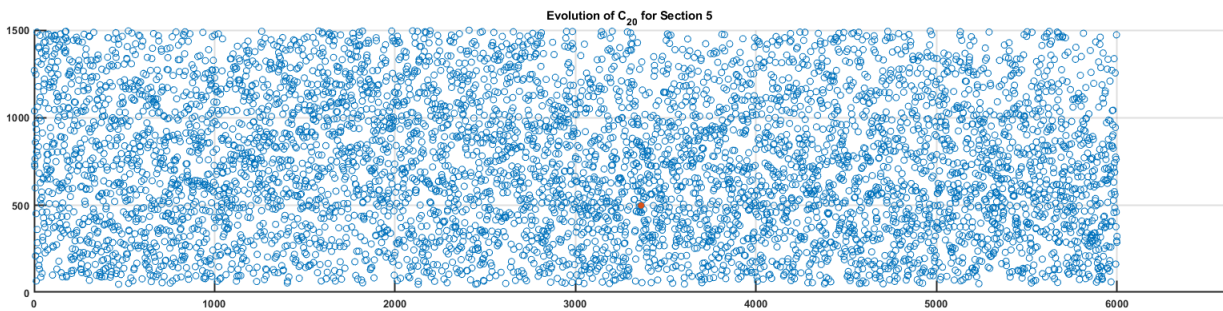
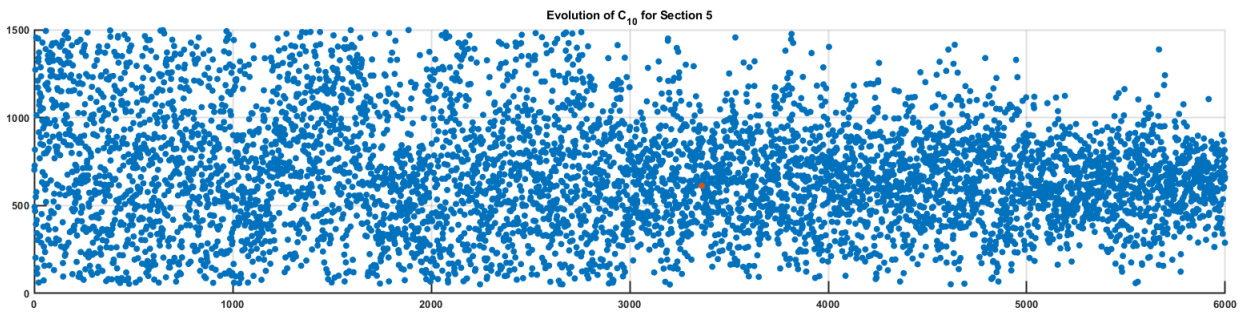


Figure 161: Evolution of material properties during the local estimation procedure using 6 Sections in the fibrous cap + SI model. Material properties belong to Section 5.

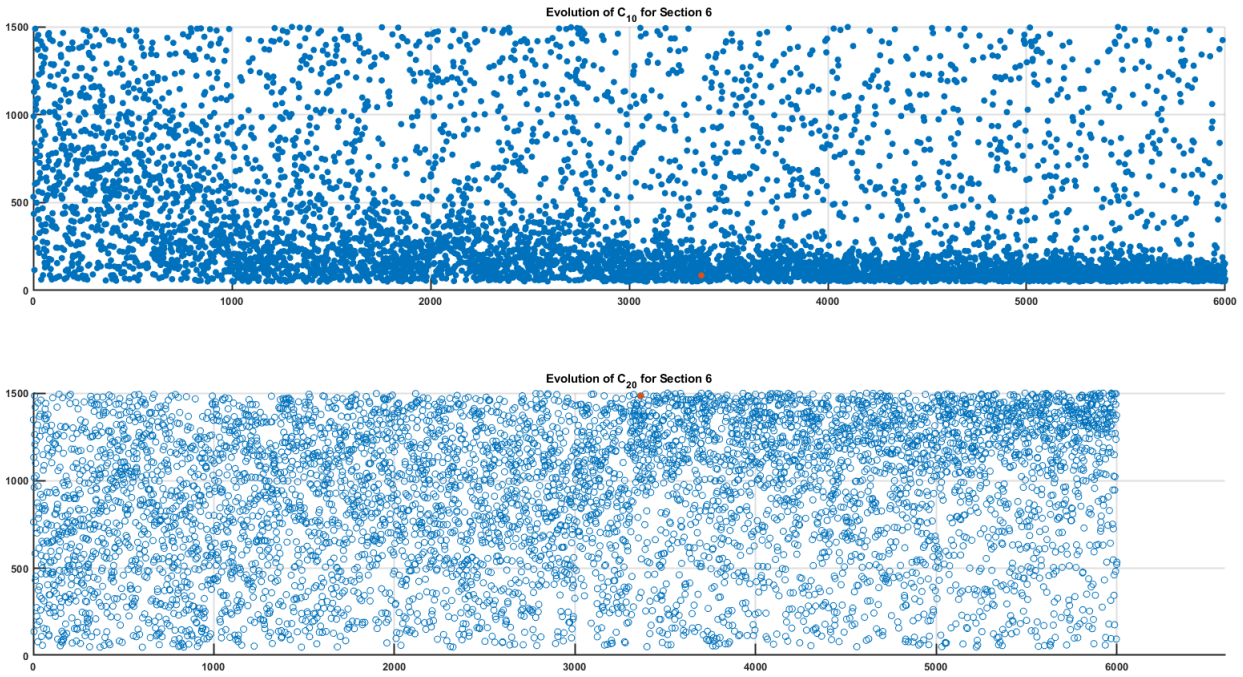


Figure 162: Evolution of material properties during the local estimation procedure using 6 Sections in the fibrous cap + SI model. Material properties belong to Section 6.

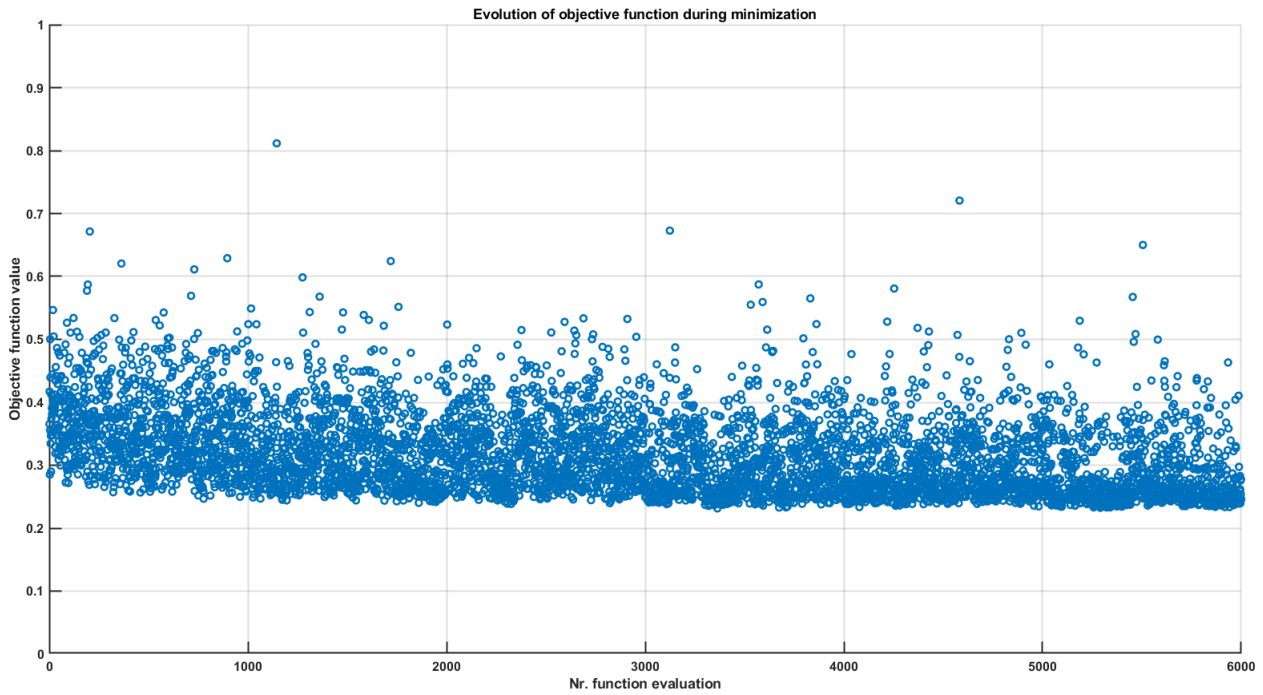


Figure 163: Evolution of objective function during the local estimation procedure using 6 Section in the fibrous cap + SI model.

### N.3 Resulting displacement fields

#### Step 1

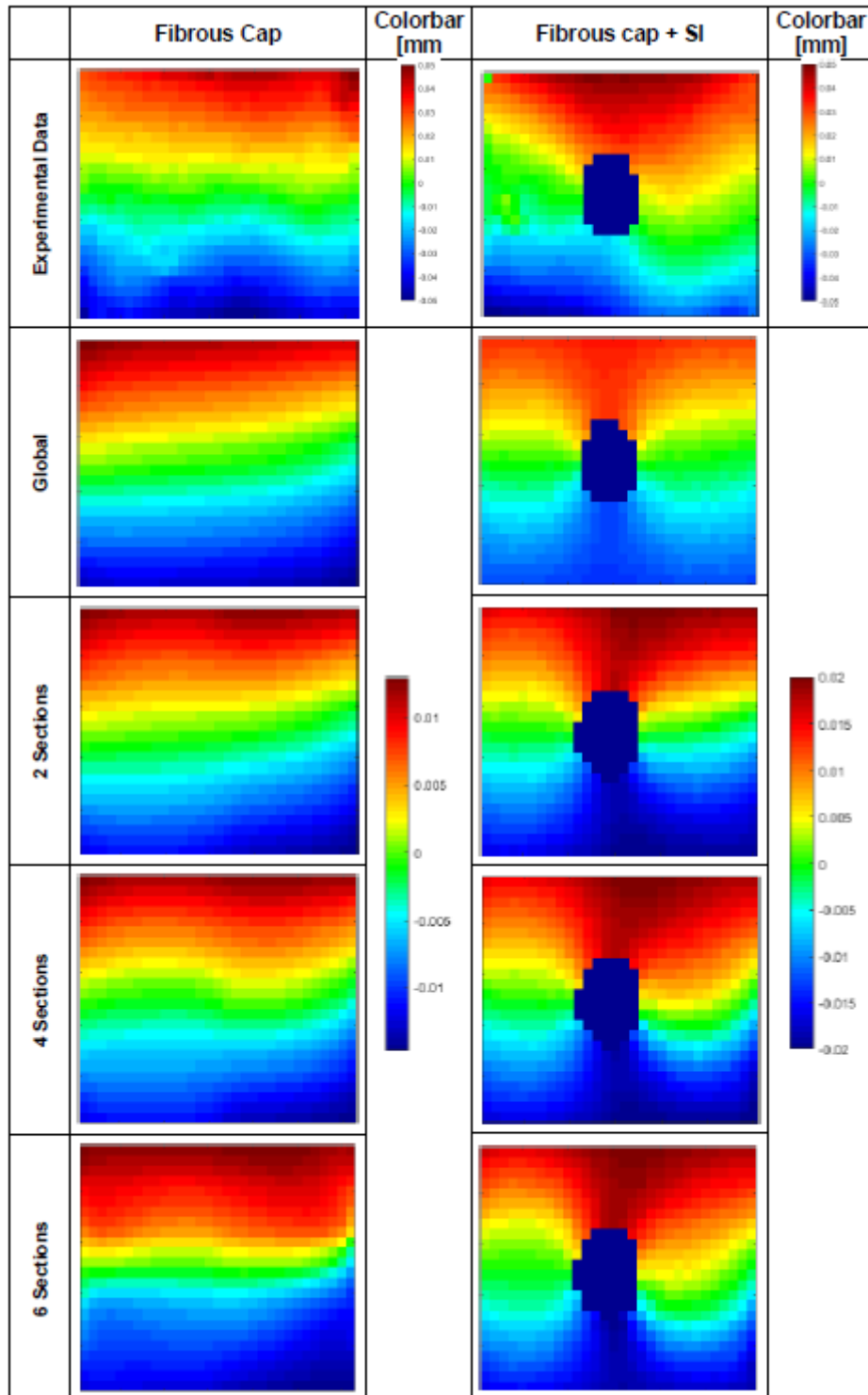


Figure 164: Visual comparisons between the displacement fields after local estimations. Figure contains the fibrous cap models (left) and the fibrous cap + SI models (right). The displacement fields belong to loading step 1.

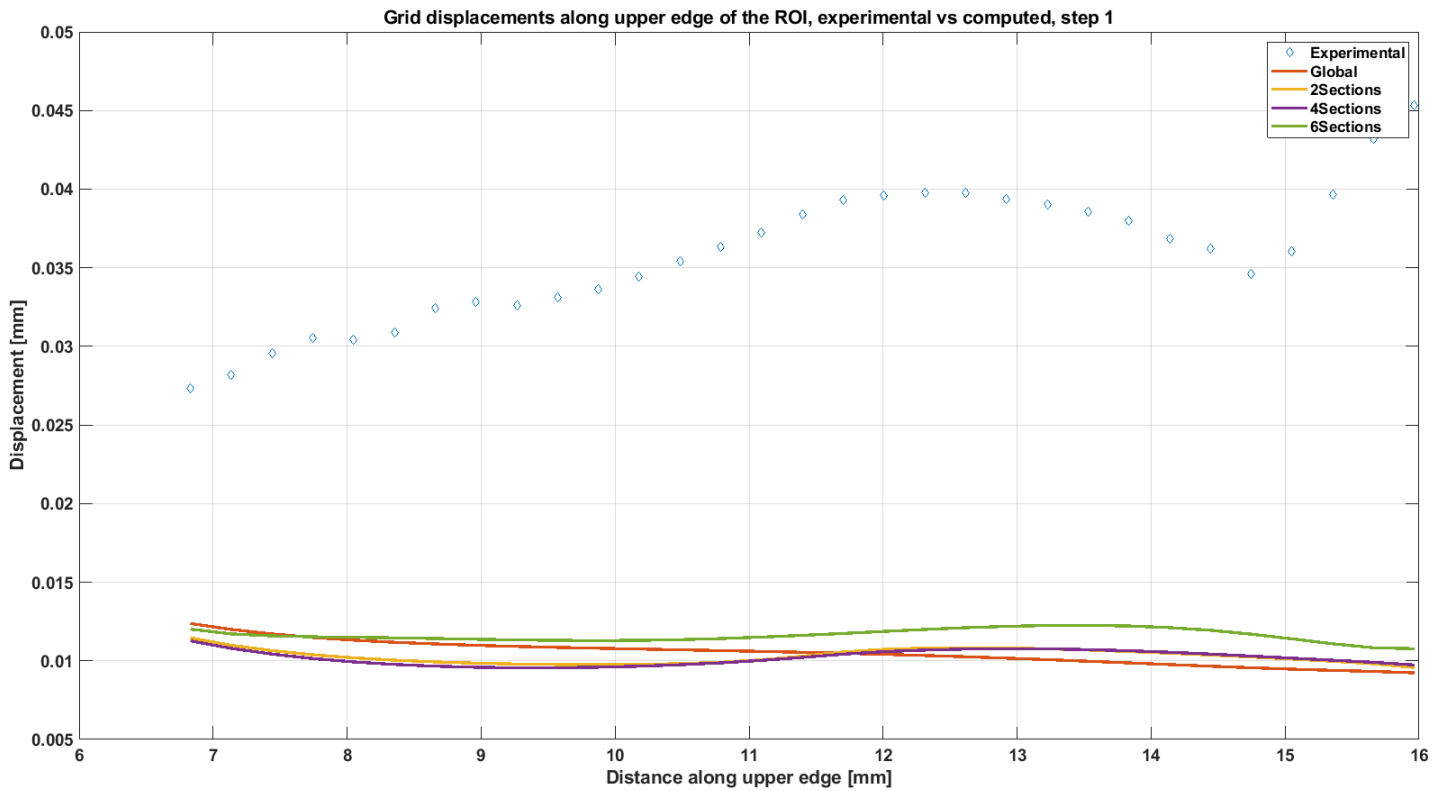


Figure 165: Comparing the distribution of displacement values along the upper edge of the ROIs for the fibrous cap models with different number of sections. The displacements belong to loading step 1. X axis shows the distance along the upper edge in mm and Y axis shows the average grid displacement values for models with different number of sections. The result from the experimental data is included as reference.

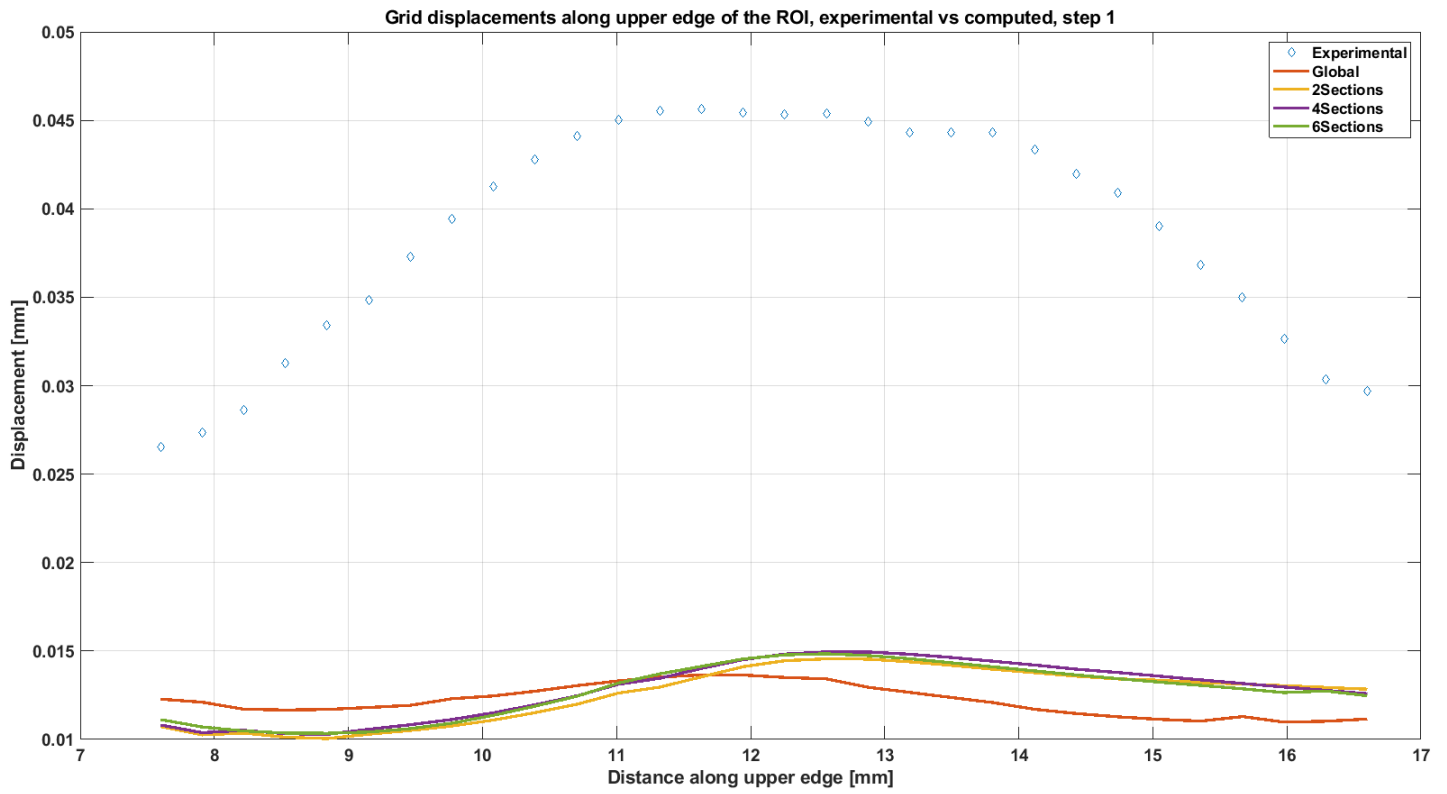


Figure 166: Comparing the distribution of displacement values along the upper edge of the ROIs for the fibrous cap + SI models with different number of sections. The displacements belong to loading step 1. X axis shows the distance along the upper edge in mm and Y axis shows the average grid displacement values for models with different number of sections. The result from the experimental data is included as reference.

Step 2

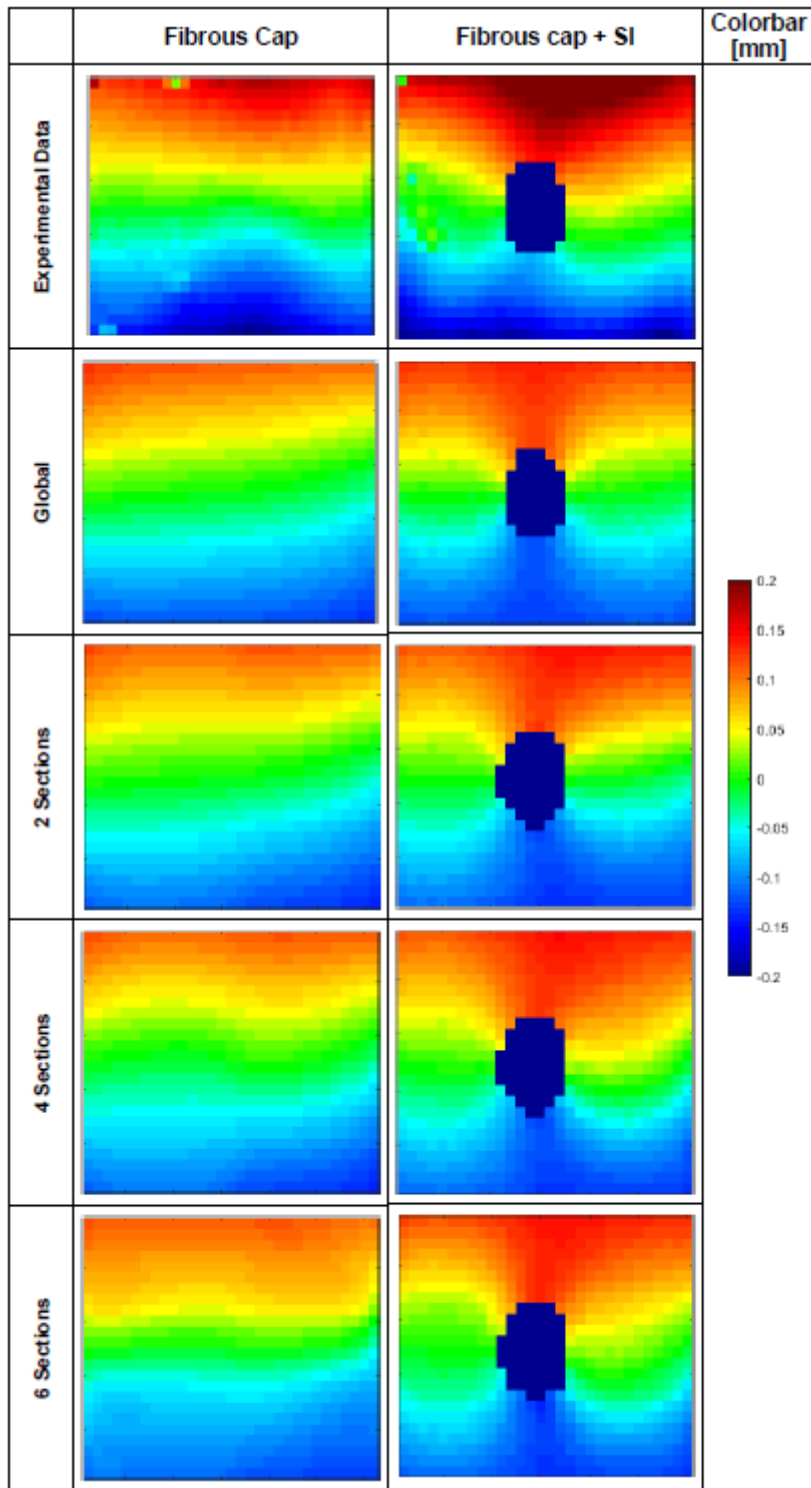


Figure 167: Visual comparisons between the displacement fields after local estimations. Figure contains the fibrous cap models (left) and the fibrous cap + SI models (right). The displacement fields belong to loading step 2.

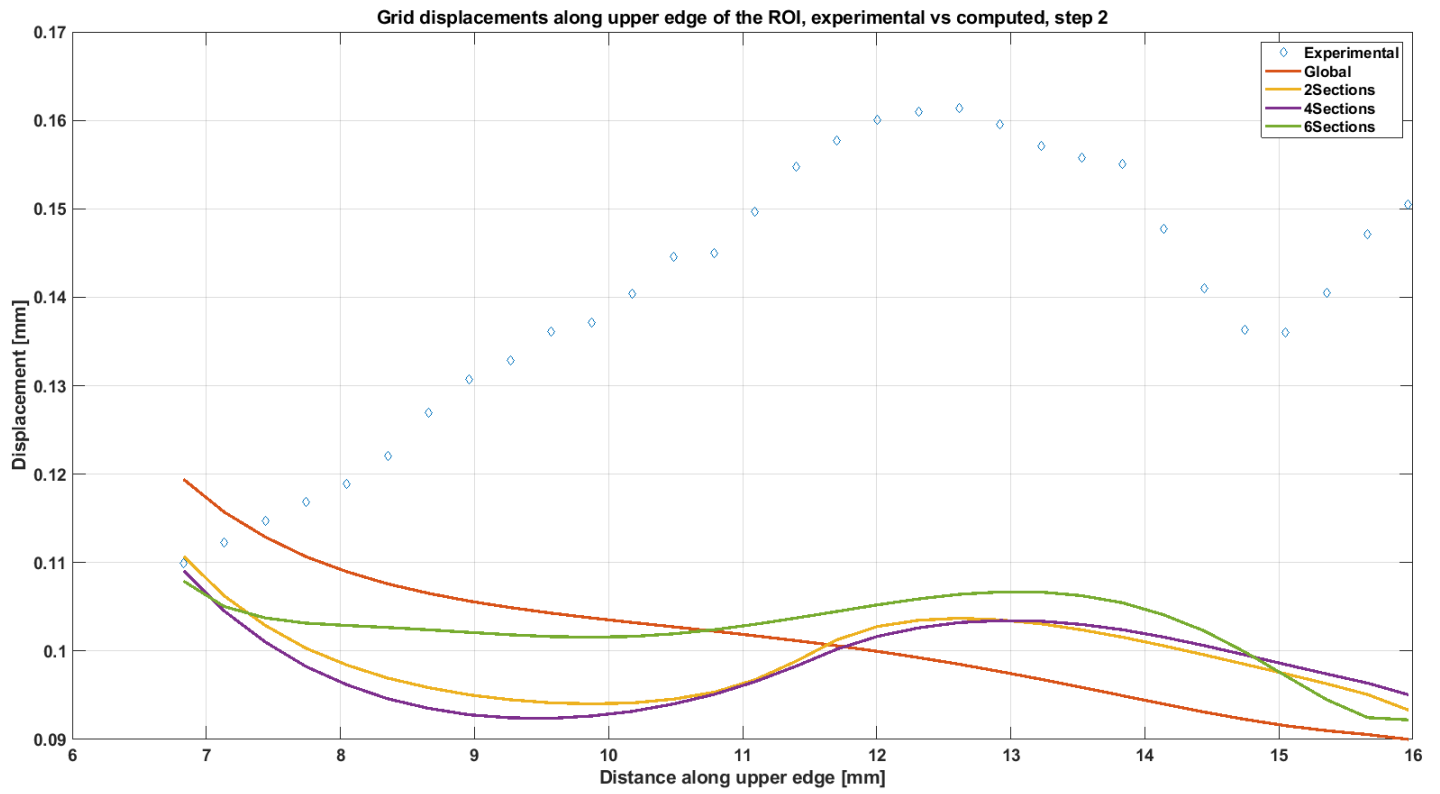


Figure 168: Comparing the distribution of displacement values along the upper edge of the ROIs for the fibrous cap models with different number of sections. The displacements belong to loading step 2. X axis shows the distance along the upper edge in mm and Y axis shows the average grid displacement values for models with different number of sections. The result from the experimental data is included as reference.

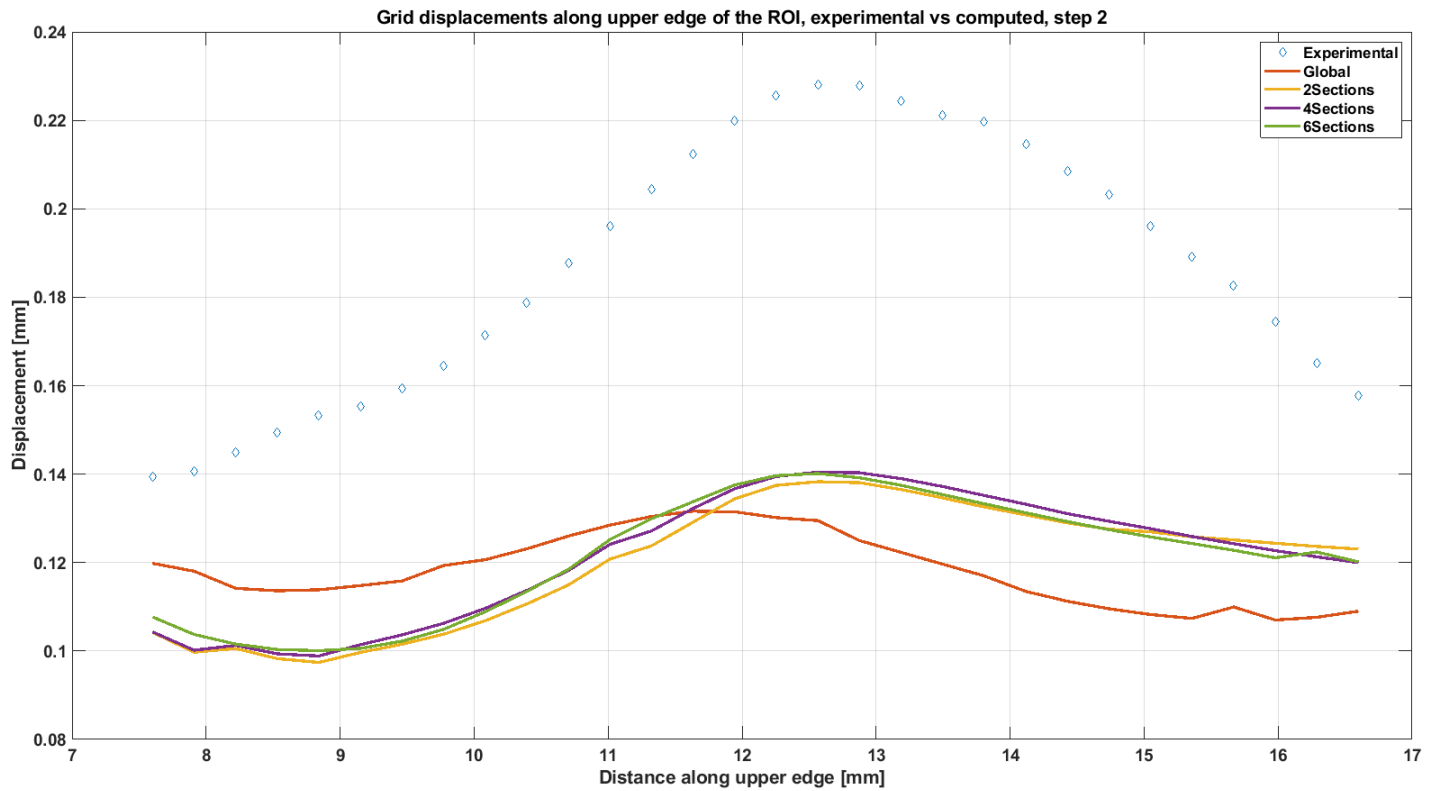


Figure 169: Comparing the distribution of displacement values along the upper edge of the ROIs for the fibrous cap + SI models with different number of sections. The displacements belong to loading step 2. X axis shows the distance along the upper edge in mm and Y axis shows the average grid displacement values for models with different number of sections. The result from the experimental data is included as reference.